ARTIFICIAL INTELLIGENCE IN NONDESTRUCTIVE TESTING OF CIVIL ENGINEERING MATERIALS

EDITED BY: Juncai Xu, Wen Deng and Jun Wu

PUBLISHED IN: Frontiers in Materials

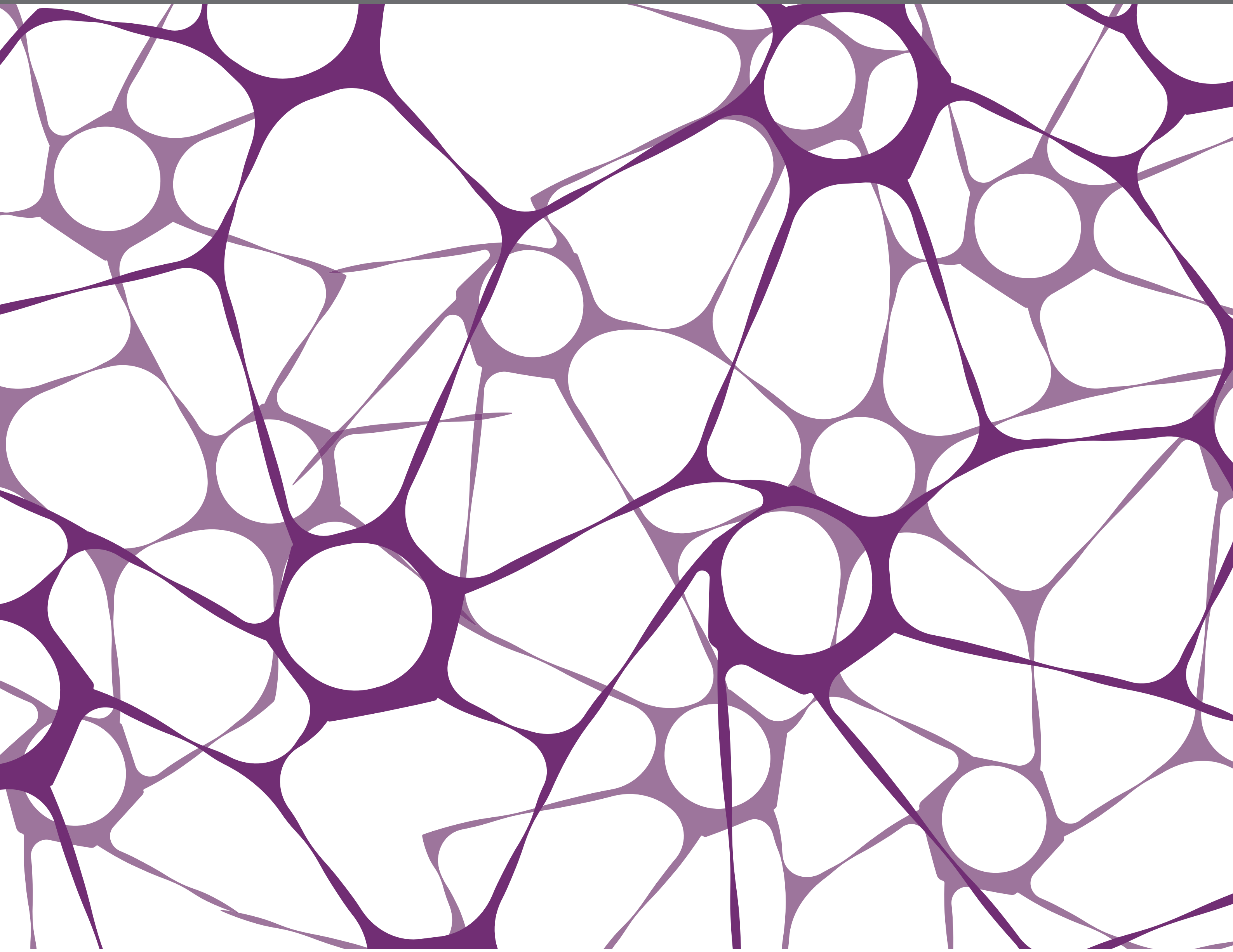

frontiers Research Topics

ISSN 1664-8714
ISBN 978-2-88971-669-2
DOI 10.3389/978-2-88971-669-2

About Frontiers

Frontiers is more than just an open-access publisher of scholarly articles: it is a pioneering approach to the world of academia, radically improving the way scholarly research is managed. The grand vision of Frontiers is a world where all people have an equal opportunity to seek, share and generate knowledge. Frontiers provides immediate and permanent online open access to all its publications, but this alone is not enough to realize our grand goals.

Frontiers Journal Series

The Frontiers Journal Series is a multi-tier and interdisciplinary set of open-access, online journals, promising a paradigm shift from the current review, selection and dissemination processes in academic publishing. All Frontiers journals are driven by researchers for researchers; therefore, they constitute a service to the scholarly community. At the same time, the Frontiers Journal Series operates on a revolutionary invention, the tiered publishing system, initially addressing specific communities of scholars, and gradually climbing up to broader public understanding, thus serving the interests of the lay society, too.

Dedication to Quality

Each Frontiers article is a landmark of the highest quality, thanks to genuinely collaborative interactions between authors and review editors, who include some of the world's best academicians. Research must be certified by peers before entering a stream of knowledge that may eventually reach the public - and shape society; therefore, Frontiers only applies the most rigorous and unbiased reviews.
Frontiers revolutionizes research publishing by freely delivering the most outstanding research, evaluated with no bias from both the academic and social point of view.
By applying the most advanced information technologies, Frontiers is catapulting scholarly publishing into a new generation.

What are Frontiers Research Topics?

Frontiers Research Topics are very popular trademarks of the Frontiers Journals Series: they are collections of at least ten articles, all centered on a particular subject. With their unique mix of varied contributions from Original Research to Review Articles, Frontiers Research Topics unify the most influential researchers, the latest key findings and historical advances in a hot research area! Find out more on how to host your own Frontiers Research Topic or contribute to one as an author by contacting the Frontiers Editorial Office: frontiersin.org/about/contact

ARTIFICIAL INTELLIGENCE IN NONDESTRUCTIVE TESTING OF CIVIL ENGINEERING MATERIALS

Topic Editors:
Juncai Xu, Case Western Reserve University, United States
Wen Deng, Missouri University of Science and Technology, United States
Jun Wu, Huazhong University of Science and Technology, China

Citation: Xu, J., Deng, W., Wu, J., eds. (2021). Artificial Intelligence in Nondestructive Testing of Civil Engineering Materials. Lausanne: Frontiers Media SA. doi: 10.3389/978-2-88971-669-2

Table of Contents

frontiers in Materials

ORIGINAL RESEARCH
published: 13 August 2020
doi: 10.3389/fmats.2020.00227

Influence of Aggregates in Concrete on Fiber-Optic Based Thermal Integrity Profiling Analysis of Concrete Structures

Ruoyu Zhong and Wen Deng*

Department of Civil, Architectural and Environmental Engineering, Missouri University of Science and Technology, Rolla, MO, United States

Fiber-optic sensor has drawn wide attention in the non-destructive testing and evaluation of civil engineering materials due to its high accuracy and resolution as well as cost-efficiency. Currently, using optical fiber as the temperature sensor is proposed to conduct the thermal integrity profiling (TIP) of concrete structures. However, concrete is not a thermally homogeneous material as assumed in current studies of concrete TIP. Its essential components, such as aggregates may cause thermal inhomogeneity problems when implementing fiber-optic sensors for TIP. In this paper, we use the concrete structures with different grades of aggregates to conduct numerical simulation for non-destructive thermal testing. The goal is to investigate how the thermal inhomogeneity caused by aggregates would influence the testing result. Firstly, we establish three concrete structure models with three different grades of aggregates based on the scenarios where these concrete structures will be used. Then, we numerically simulate the thermal process on these models and extract the temperature at the location where optical fiber would be installed. The influence caused by the inhomogeneity of aggregate size and distribution as well as the possible method to minimize the effect are evaluated in the paper. Overall, aggregates of concrete have a significant influence on the accuracy of TIP analysis, and defects could be veiled if no proper treatment to the data is implemented for TIP analysis.

Keywords: fiber-optic sensing, drilled shaft, concrete beam, thermal integrity profiling, concrete aggregates

Edited by:
Antonio Caggiano,
Darmstadt University of Technology, Germany

Reviewed by:
Wenxiang Xu,
Hohai University, China
GuiYun Tian,
Newcastle University, United Kingdom

****Correspondence:***
Wen Deng
wendeng@mst.edu

Specialty section:
This article was submitted to Structural Materials, a section of the journal Frontiers in Materials

Received: *03 April 2020*
Accepted: *22 June 2020*
Published: *13 August 2020*

Citation:
Zhong R and Deng W (2020) Influence of Aggregates in Concrete on Fiber-Optic Based Thermal Integrity Profiling Analysis of Concrete Structures. Front. Mater. 7:227. doi: 10.3389/fmats.2020.00227

INTRODUCTION

Concrete is one of the most important civil engineering materials across the world. From residential houses to transportation superstructures, numerous concrete structures are constructed and maintained every day. A key indicator of the structural safety is the integrity of the concrete. Thus, the integrity of the concrete structure should be monitored from its construction process throughout its service time. During the construction process, concrete could be foiled due to inappropriate procedures, especially for a cast-in-site concrete shaft. Concrete shafts, which bear and transfer the loading to the ground, play an important role in superstructure construction. However, slump, soft soil, misplacement of rebar cage, and other multiple factors could cause defects when pouring the concrete (O'Neill, 1991). 15% of 5,000 to 10,000 tested concrete shafts had the indication of potential defects, and 5% of the tested shafts showed indisputable defect signals

(Klingmüller and Kirsch, 2004; Brown and Schindler, 2007). Defects cannot be prevented during the construction completely since the excavation and concrete pouring are both blind processes. Thus, the integrity test to determine whether defects exist within the concrete shaft is critical for the evaluation of concrete structural safety. On the other hand, the concrete structure could be intact after construction, but it would still degrade over time. For example, during a fire hazard, extreme high temperature could cause cracking of the concrete, which leads to degradation of mechanical property and integrity of concrete structures (Kodur and Sultan, 2003; Kodur et al., 2009). An appropriate method of monitoring concrete structures helps evaluation of remaining capacity.

Recently, the thermographic approach for the material integrity and damage analysis becomes promising as the non-destructive testing technique (Ciampa et al., 2018; Wang et al., 2018, 2019). The current state of practice in thermal integrity analysis of civil engineering materials is to measure temperature using thermocouples or infrared probes, then estimate the temperature distributions within the structures. However, these methods are usually costly, time-consuming, easily affected by electromagnetic interference, moisture, and unanticipated junction problems (Smalcerz and Przylucki, 2013). Recent studies in thermographic approach has aroused interest of using optical fiber as an alternative for the concrete material integrity testing and monitoring due to its durability, accuracy, immunity to electromagnetic interference, resistance to harsh environment and cost-efficiency. Zhong et al. (2018) as the first explored using the optical fiber in thermal integrity profiling (TIP) for drilled shafts to acquire higher resolution spatial data. TIP, as a non-destructive method, makes use of cement hydration heat to test the integrity of a concrete shaft. Any defect such as inclusion and necking, will be shown as temperature anomaly in temperature measurement (Mullins, 2010, 2013; Johnson, 2016). Compared to the conventional method by using cross-hole sonic logging or sonic pulse echo, the TIP can cover a larger area and provide a more comprehensive result. However, the accuracy of the TIP is limited by the number of sensors when using thermocouples or access tubes within the concrete shaft when using infrared probes. Thus, it was proposed to use Rayleigh scattering within optical fiber to replace thermocouples or thermal probes to improve data quality (Zhong et al., 2018). The optical fibers can be wrapped spirally around the rebar cage due to its flexibility which reduces horizontal interval significantly and provides a more comprehensive temperature distribution within the concrete shaft. On the other hand, Bao et al. (2017) proposed using pulse pre-pump Brillouin optical time domain analysis (PPP-BOTDA) as a temperature sensing method to measure spatially-distributed temperatures in reinforced concrete specimens exposed to fire. The remaining capacity of a concrete structure can be evaluated through thermo-mechanical analysis when the temperature distributions *in situ* are known (Usmani et al., 2001).

However, none of above fiber-optic based thermal integrity research took the influence of thermal inhomogeneity caused by concrete aggregates into account. Concrete is a multi-components composite material, which consists of aggregate and cement. Up to 60–80% of the volume of concrete is aggregate. Generally, aggregates are classified into two groups: fine-grained aggregates with grain size smaller than 4.75 mm and coarse aggregates with grain size larger than 4.75 mm. Due to economic reasons, lower usage of cement is preferred in order to lower the cost, which requires the aggregates to consist of a range of sizes rather than a uniform size. While this fulfills the economic and mechanical purpose, a range of sizes of aggregate introduces material-heterogeneity to concrete. Various sizes of aggregates cause variation in bulk composition which leads to macro heterogeneity in concrete (Kreijger, 1990). Properties of concrete are related to the size, geometry, and distribution of aggregates (Shahbazi and Rasoolan, 2017). The properties differences between cement and aggregates, like thermal conductivity and heat capacity, cause uneven temperature distribution after heated. Since the thermal integrity testing method relies on temperature anomalies to identify defects that exist or occur within the concrete structure, the variation of temperature caused by random aggregate distribution may lead to an overestimation or a misjudgement of defects. However, the uniform fine-grained aggregate was adopted when testing the feasibility of fiber-optic sensor applications in the laboratory integrity test. While the test results were promising, the specimens were less realistic. The influence of aggregates should be tested thoroughly before introducing fiber-optic sensor into real applications to avoid any misjudgement of defects.

The objective of this paper is to investigate the influence of thermal inhomogeneity caused by concrete aggregates on the fiber-optic based thermal integrity analysis of concrete structures. To remain problem focused, the superiority of fiber-optic sensor with applications in non-destructive thermal testing over other thermographic approaches will not be discussed. In this study, two engineering scenarios are analyzed: the concrete beam exposed to fire hazards and the concrete shaft installation. Three concrete structure models are established, two of which are for concrete beams and one is for concrete shaft. Each model has different sizes of aggregates randomly distributed within the structures. The size of aggregates is based on the scenarios these concrete structures will be poured. We simulate the thermal testing on these models and extract the temperature at the location where optical fibers would be installed. The influence caused by the thermal inhomogeneity of concrete aggregates with different sizes and distribution is investigated, and the method used to minimize the effect is also proposed in this paper.

METHODOLOGY

Governing Equation

The thermal integrity testing method for either concrete beams or concrete shafts predicts the existence of crack or the defect shape of foiled concrete structure based on the temperature distribution inside the material. We makes use of finite element method based commercial software COMSOL Multiphysics® to simulate the temperature distribution within concrete structures.

The governing equation of heat transfer process in solid is:

$$\frac{\rho C_p \partial T}{\partial t} = [\frac{\partial}{\partial \mathrm{x}}\left(k\frac{\partial T}{\partial \mathrm{x}}\right) + \frac{\partial}{\partial \mathrm{y}}\left(k\frac{\partial T}{\partial \mathrm{y}}\right) + \frac{\partial}{\partial \mathrm{z}}\left(k\frac{\partial T}{\partial \mathrm{z}}\right)] + Q \quad (1)$$

where T is the temperature; Q is the heat generation rate of the material; C_p is the heat capacity of the material; k is the thermal conductivity of the material; ρ is the density of the material.

Heat Transfer in Air

In beam models, concrete beams are not directly heated by an internal heat source such as the hydration process but heated in a fire hazard scenario as an external heat source. The heat source is set with a certain distance away from the concrete beam. Thus, the heat transfer is not limited to a conduction which is the primary heat transfer way within a solid object. Conduction and radiation in air are two primary ways to transfer heat from the source to concrete beams. Conduction and radiation in air can be determined by Equations (2–7):

$$\begin{aligned}
\rho C_p u \cdot \nabla T + \nabla \cdot q &= Q + Q_p + Q_{vd} && (2)\\
q &= -kNu\nabla T && (3)\\
(1-\varepsilon)\, G &= J - \varepsilon e_b(T) && (4)\\
G &= G_m\,(J) + G_{amb} + G_{ext} && (5)\\
G_{amb} &= F_{amb} e_b(T_{amb}) && (6)\\
e_b\,(T) &= n^2 \sigma T^4 && (7)
\end{aligned}$$

where u represents the velocity of the fluid; Nu represents the Nusselt number; Q_p represents the pressure work; Q_{vd} represents the viscous dissipation; n represents the refractive index; ε represents the emissivity of the surface. G represents surface irradiation; G_{amb} represents ambient irradiation; G_{ext} represents external irradiation; G_m represents mutual surface irradiation; F_{amb} represents ambient view factor; e_b represents blackbody total emissive power; J represents the surface radiosity; σ represents Stefan-Boltzmann constant.

Heat Generation

In the drilled shaft model, the hydration heat generated during the concrete curing process is the key to the TIP test. Thus, it is necessary to determine the heat generation of concrete before simulation. The gross heat production and generation rate are two significant factors of temperature distribution. Two factors together determine the temperature of the shaft and the performance of TIP. Both factors are related to the ingredient of cement. Changing the proportion of cement would generate a different amount of heat. The total heat production can be calculated by Equations (8–10), (Schindler and Folliard, 2005):

$$\begin{aligned}
Q_0 &= Q_{cem}p_{cem} + 461p_{slag} + Q_{FA}p_{FA} && (8)\\
Q_{cem} &= 500p_{C_3S} + 260p_{C_2S} + 866P_{C_3A} + 420p_{c_4AF}\\
&\quad + 624p_{SO_3} + 1186p_{FreeCaO} + 850p_{MgO} && (9)\\
Q_{FA} &= 1800p_{FACaO} && (10)
\end{aligned}$$

where p with different subscripts represents the weight fraction of each compound; Q with different subscripts represents the heat generated according to each compound of the concrete. The subscript represents the name of each compound. The chemical composition of cement and fly ash are usually available from the supplier.

The rate of hydration can be calculated using the following equations provided by Schindler and Folliard (2005):

$$\begin{aligned}
\alpha\,(t) &= \alpha_u \exp(-\left[\frac{\tau}{t}\right]^{\beta}) && (11)\\
\alpha_u &= \frac{(1.031w/cm)}{(0.194 + w/cm)} + 0.5p_{FA} + 0.3p_{SLAG} < 1 && (12)\\
\beta &= p_{C_3S}^{0.227} \cdot 181.4 \cdot p_{C_3A}^{0.146} \cdot Blaine^{-0.535} \cdot p_{SO_3}^{0.558}\\
&\quad \cdot \exp(-0.647p_{SLAG}) && (13)\\
\tau &= p_{C_3S}^{-0.401} \cdot 66.78 \cdot p_{C_3A}^{-0.154} \cdot Blaine^{-0.804} \cdot p_{SO_3}^{-0.758}\\
&\quad \cdot \exp(2.187 \cdot p_{SLAG} + 9.5 \cdot p_{FA} \cdot p_{FACaO}) && (14)
\end{aligned}$$

where $\alpha(t)$ represents the degree of hydration of cement at time t; and w/cm is a water-cement ratio; β and τ are determined by the cementitious constituent fractions. According to ASTM D7949-14, the recommended timing to perform TIP would be 12 h after concrete pouring until the number of days equivalent to foundation diameter in meters divided by 0.3 m.

Heat Transfer in Soil

Heat is dissipated into surrounding soil after the heat is generated due to the hydration process. Since the predominant material in soil is solid, conduction plays the most important role in heat dissipation in the shaft simulation. Aside from the temperature and density of the material, two factors control the conduction process: thermal conductivity and heat capacity.

Soil is a composite material consisting of solid, air, and water. The effective thermal conductivity depends on the constitution of soil and the thermal conductivity of each phase. The thermal conductivity can be calculated by Equation (15), (Liu et al., 2002; Barry-Macaulay et al., 2013; Sáez Blázquez et al., 2017):

$$k_1 = k_s - n[k_s - S_w k_w - (1 - S_w)k_a] \quad (15)$$

where k with subscripts represents the thermal conductivity of each phase of soil; n represents porosity; S_w represents the degree of saturation. The subscript s denotes solid phase; w denotes water phase; a denotes air phase.

The shape of void inside of soil has an effect on heat transfer as well. To take that effect into account, the shape factor $\chi = \sqrt{S_w}$ is introduced into the equation. Now the equation becomes:

$$k = \sqrt{S_w}\left\{k_s - n\left[k_s - S_w k_w - (1 - S_w)\,k_a\right]\right\} + (1 - \sqrt{S_w})k_a \quad (16)$$

The temperature of the soil is assumed to be the same among the three phases. The heat required to raise the temperature of soil one degree can be calculated by the sum of three phases: $C_s m_s + C_w m_w + C_g m_a$. The total mass of the soil is: $m_s + m_w + m_a$. Therefore, the effective heat capacity of soil can be calculated as follow:

$$C_p = \frac{C_s m_s + C_w m_w + C_g m_a}{m_s + m_w + m_a} \quad (17)$$

where C with subscripts represents the heat capacity of each phase of soil; m with subscripts represents the mass of each phase of soil.

Considering that the mass of air is negligible, the equation can be simplified as:

$$C_p = \frac{C_s + C_w w}{1 + w} \tag{18}$$

where w is the water content.

Aggregate Distribution

The aggregate distribution method used in the simulation is referenced to Qian et al. (2016). Concrete is considered as a composite geometrical structure where aggregates such as sands and gravels are embedded in a mortar matrix. Although using non-spherical particles is more realistic, the temperature fluctuation caused by the shape of aggregates is less significant compared to other factors such as size and distribution. To simplify the calculation, thermal inhomogeneity caused by the shape of aggregates is not considered. Spherical shape aggregates are adopted in this study. An aggregate particle is generated with a random radius at each time. The radius is determined by a pseudo-random number generator within a given radius range. Then, the aggregate particles are placed at a random coordinate within a given range of coordinates which is the size of the model. The key algorithm required in the particle placing procedure is to check whether aggregate particles are overlapped. Since the shape of the particle is not considered, the overlap algorithm simply consists of equations to check whether the distance between particles and the distance between particle and boundaries are smaller than zero. A variable is assigned to count the failure of placement. When the total amount of aggregate for a certain radius range is reached or the failure count exceeds the limit, the next radius range would be used for a new round of placement. The placement procedure will stop after all radius ranges are finished.

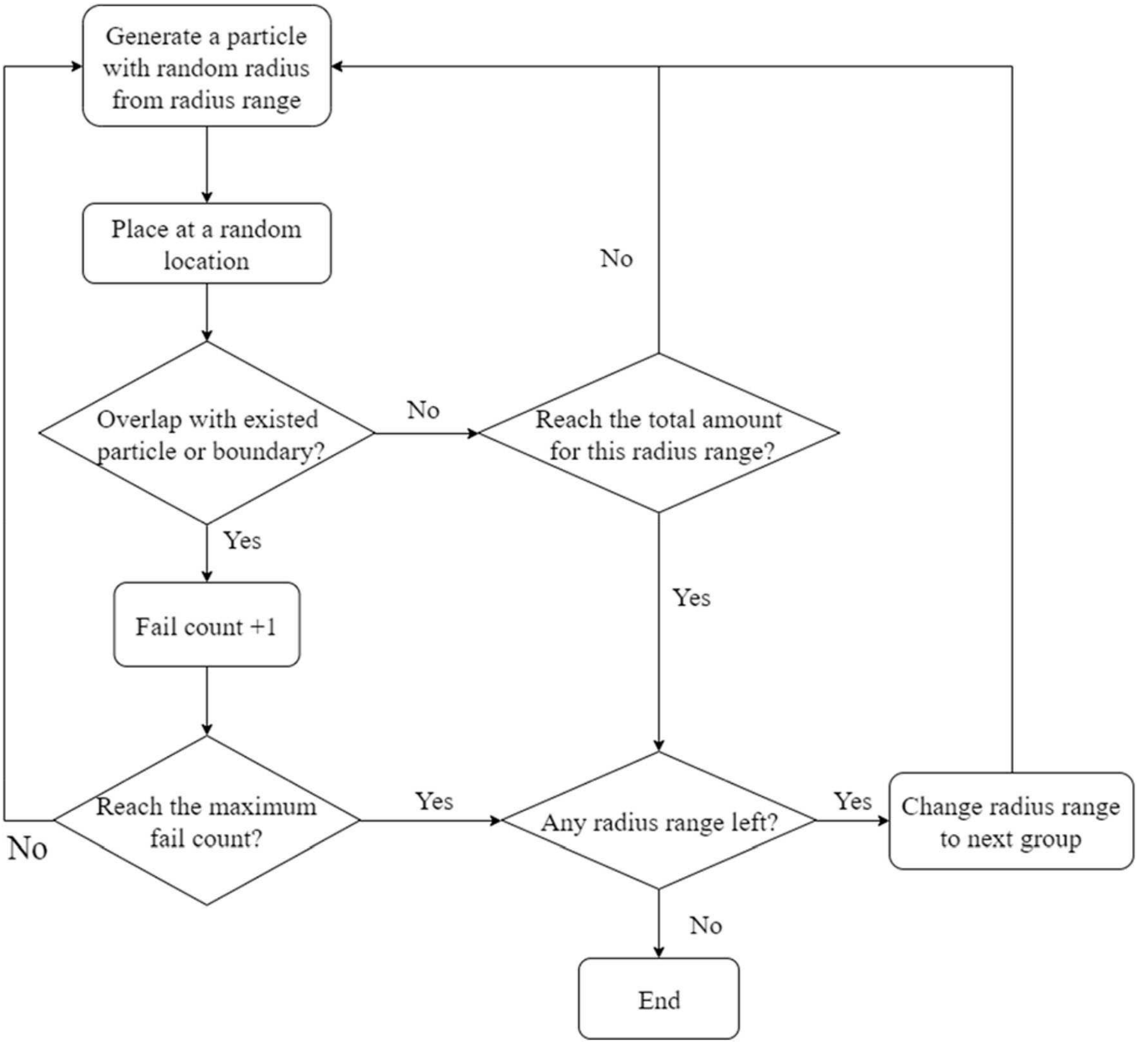

FIGURE 1 | Flow chart of aggregate placement.

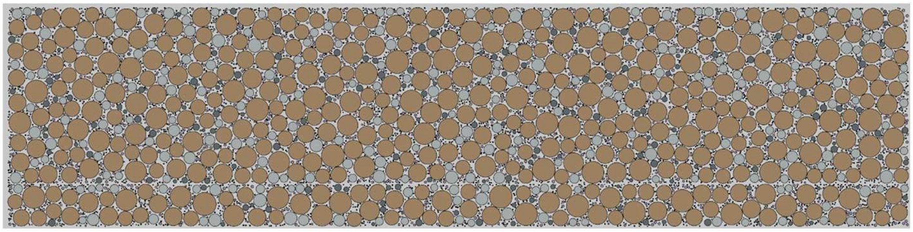

FIGURE 2 | Demonstration of aggregates distribution within a 2-D beam. A void gap line represents the location of optical fiber placed in the beam. Different colors of the aggregates represent certain size ranges.

TABLE 1 | Properties of each component in beam model.

	Volumetric fraction	**Density (kg/m^3)**	**Heat capacity [kJ/(kg × K)]**	**Thermal conductivity [W/(m × K)]**
HCP	0.204	2,160	1.55	1.163
Coarse aggregate	0.7	2,660	0.84	2.5
Fine aggregate	0.082	2,660	0.80	2
Air	0.014	1.225	1	0.0333

TABLE 2 | Heat rate and duration.

Heat rate	25 *kW*	40 *kW*	80 *kW*
Duration	45 min	10 min	10 min

The flow chart in **Figure 1** demonstrates the procedure of aggregate placement.

Simulation Parameters and Model for Beam

To simulate the temperature distribution within the beam exposed to a fire hazard environment, a two-dimensional (2-D) model is established. The model is shown in **Figure 2**. The reason for adopting a 2-D model rather than a three-dimensional (3-D) model is that the computation stress using a 3-D model is too high. Since we mainly focus on vertical heat transfer, to simplify the model without loss of generality, a 2-D model is employed. The size of the model is 610 × 152 mm. The model consists of three elements: gravel, sand, and cement. The aggregates particles are input to the model following the procedures illustrated in **Figure 1**. The circles with multiple colors represent aggregates, and each color represents a radius range. The gray section represents the cement surrounding aggregates. The small gap between aggregate represents the location of the fiber optic sensor. Rebar is not established in this model since the main focus is the effect of aggregate. Although is not shown in the figure, the beam model is surrounded by air with default properties in COMSOL. The heat source is set at the bottom of the air section to simulate fire. The heart rate is set at several given rates. Temperature distribution data is acquired at the gap with a space interval of 1 cm. The properties of each component can be found in **Table 1**, and the heat rate and duration can be found in **Table 2**.

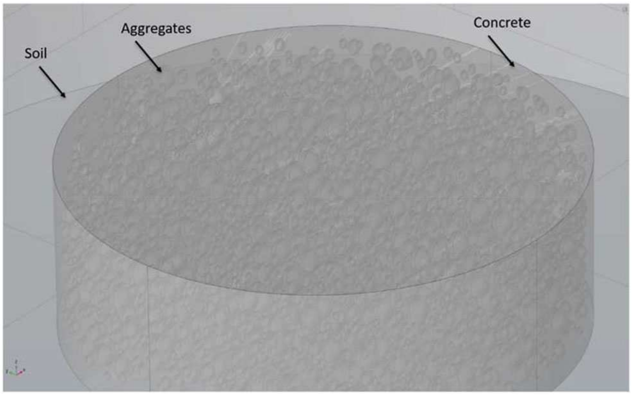

FIGURE 3 | Shaft-soil model. Aggregates are embedded in the concrete shaft.

Simulation Parameters and Model for Shaft

To simulate the temperature evolution and distribution within the shaft, a 3-D model is established as shown in **Figure 3**. **Figure 3** shows the composition of a concrete shaft model. We made two simplifications to the model. Firstly, the rebar cage is not reconstructed in the model. Rebar has relatively low heat capacity and high thermal conductivity, and the heat that transfers into rebar cage is negligible. Moreover, the volume of the rebar cage is relatively small compared to the concrete shaft. Therefore, to simplify the model, no rebar cage geometry is input to the model. However, it is still necessary to point out the location of the rebar cage. Secondly, aggregates of which diameter is smaller than 5 mm are removed due to the high requirement of computational resources for 3-D simulation. According to our preliminary study, the influence of thermal inhomogeneity caused by small aggregates on the integrity analysis is relatively insignificant. Therefore, in our simulation, the volume ratio of aggregates actually cannot reach 60% or above. Since our goal is not to study the mechanical properties of concrete but the thermal process within the concrete, current packing of aggregates by neglecting the small aggregates can still meet the goal of the study.

In the paper proposed using fiber-optic sensor as means to acquire temperature distribution data for TIP, the optical fiber is proposed to be wrapped spirally around rebar cage (Zhong

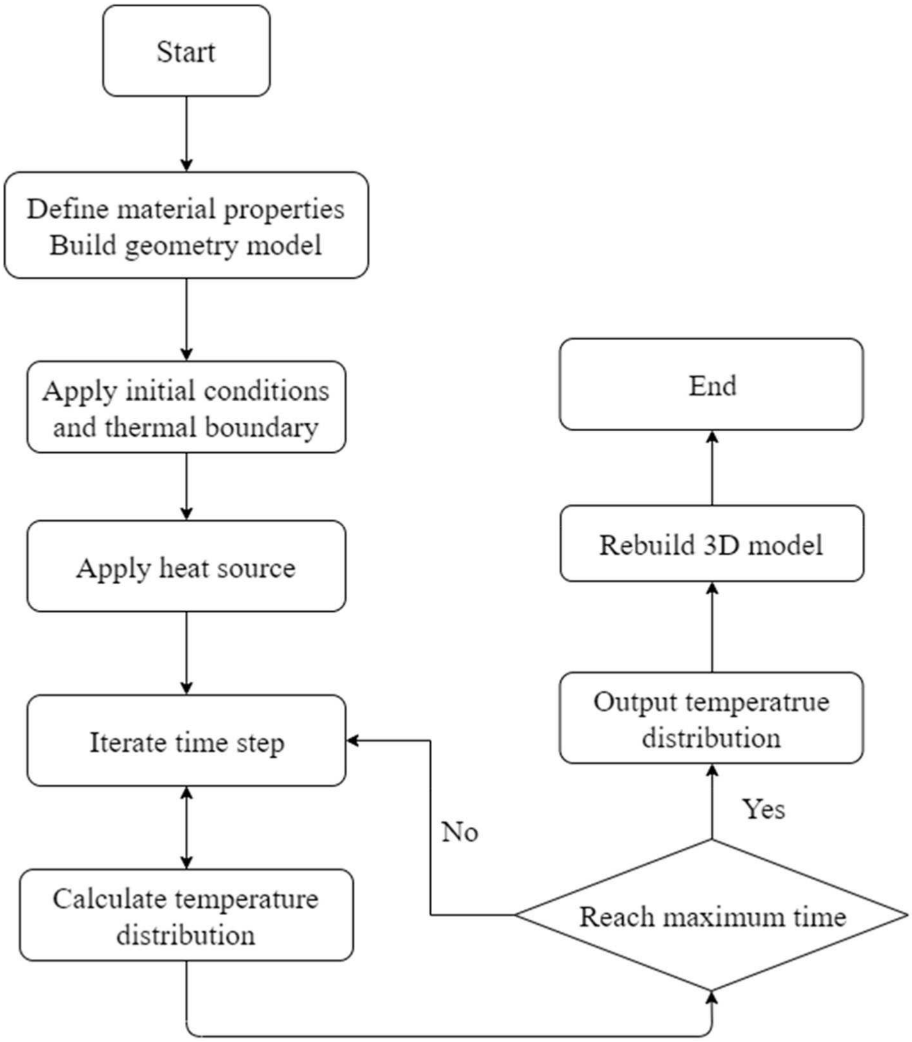

FIGURE 4 | Simulation flow chart (Zhong et al., 2018).

et al., 2018). In the realistic scenario, the optical fiber is wrapped on the outside of rebar cage before the rebar cage is placed into the drilled pit and location of the optical fiber relative to rebar cage is calibrated. The location of the rebar cage in the model is where the temperature distribution data would be extracted. Optical fiber is not input to the geometry for a similar reason. The properties of concrete can be found in **Table 1**. The properties of soil can be found in **Table 3**. The flow chart of simulation is given in **Figure 4**.

TABLE 3 | Soil properties.

Properties	Unit	Value
Soil solid thermal conductivity	$W/m \cdot K$	5.2
Water thermal conductivity	$W/m \cdot K$	0.55
Air thermal conductivity	$W/m \cdot K$	0.05
Density	kg/m^3	1,830
Soil solid heat capacity	$J/(kg \cdot K)$	850
Water heat capacity	$J/(kg \cdot K)$	4,190
Water content	%	39.8
Saturation	%	97
Porosity	%	51.1

RESULTS AND DISCUSSION

The simulation results of two beam-models and one shaft model are presented in this section along with the discussion of the influence of thermal inhomogeneity caused by aggregates. First, we present the result of a beam model of self-consolidating concrete (SCC) following with another model of conventional concrete (CC). Then, the results from a concrete shaft model with maximum grain size of 80 mm and minimum grain size of 5 mm are presented. The influence of aggregates on thermal integrity analysis is discussed separately in the other section.

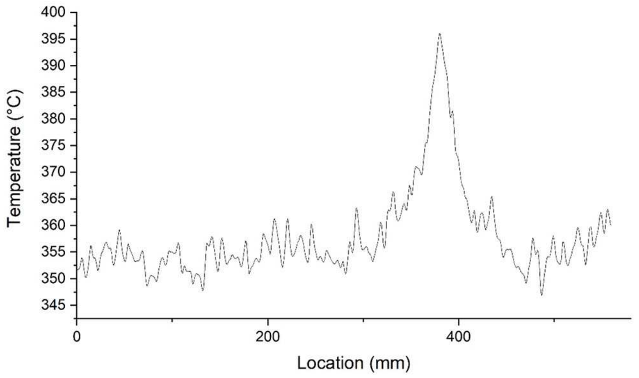

FIGURE 5 | Temperature distribution of beam model I for SCC.

Results of SCC Beam

SCC is a type of concrete of which predominant aggregate type is the fine aggregate. This type of concrete sacrifices economic efficiency for higher workability. Its high workability gives it the ability to flow into intricate spaces and congested reinforcement. Moreover, SCC does not require vibrators to compact concrete which improves safety and reduces noise at the site. Since SCC has wide applications in the construction, SCC would be a standard material to study the influence of aggregates on the thermal integrity analysis with relatively small-size aggregates.

The SCC in the simulation has a maximum grain size of 12 mm. The beam model is heated at the given heat rate as given in **Table 2**. After 65 min of heating and crack occurs, temperature data are extracted at the location of the virtual fiber-optic sensor. Since our main focus is not the temperature distribution of the whole beam structure, only temperature distribution at a straight-line direction is extracted. Temperature distribution data along the fiber-optic sensor are shown in **Figure 5**.

As shown in **Figure 5**, the temperature data plot has a main peak along with multiple minor fluctuations at other locations. The main peak, according to the paper published by Bao et al. (2017), indicates the location of cracks which occurred due to extremely high temperatures. The predominant heat transfer way in concrete is conduction before a crack appears. However, after crack appears, the void space in the crack is filled with hot air, which means the predominant heat transfer at that location would be convection in the air and radiation. The heat transfer at crack location has higher efficiency compared with the intact concrete cover. Therefore, the temperature rises dramatically around the crack and the fiber-optic sensor can catch this temperature change. The temperature fluctuation shown in **Figure 5** demonstrates the thermal inhomogeneity of concrete caused by the aggregate distribution. Assuming that concrete is homogeneous, temperature distribution should be a flat line along the intact concrete cover. However, the thermal properties of cement are not the same as those of aggregates. Moreover, the spatial distribution of aggregates is not perfect uniform. These two factors make the heat conduction has a different rate in different directions, resulting in temperature fluctuation. The temperature increment is distinct compared to the fluctuation. This is because the size of the crack is considerably larger than the maximum grain size and the grain size is relatively small in SCC. The temperature increment due to cracking outgrows the effect caused by the thermal inhomogeneity due to aggregates. In the case of SCC, the influence of aggregates on the thermal integrity analysis is relatively insignificant.

Results of CC Beam

Compared to SCC beam, CC beam is more commonly used. The second case uses CC as a study example. The maximum grain size in the CC is 26 mm. In this model, the CC beam is heated at the same condition as in the SCC model, and the temperature is also extracted at the same location at different time. The temperature data are shown in **Figure 6A**. The temperature fluctuation is considerably pronounced compared to the SCC model. The effect of aggregates increases with the increment of the maximum size of the aggregates. The fluctuation is almost twice as the one in the SCC model. The location of cracks is pointed in **Figure 6A**, and almost undetectable from the data. On the one hand, the size of the crack is slightly smaller compared to the SCC model, which decreases the increment caused by crack. On the other hand, the larger fluctuation due to larger aggregates makes it harder to distinguish the thermal effect due to the crack from the temperature fluctuation due to the thermal inhomogeneity. These two factors together result in a non-distinctive temperature increment as shown in **Figure 6A**. The existence of coarse aggregates could be problematic for the application of the fiber-optic sensor in concrete structures exposed to fire hazards.

Although the location of defects cannot be detected based on the data at a certain time, there could be still a solution to that problem. It should be noted that cracks are not naturally existed in the concrete structure. The crack in the model usually develops due to the exposure to extremely high temperatures. Therefore, we can make use of the temporal temperature logging to solve this problem of non-distinguishable data. Firstly, we divide temperature data into groups based on the time collected. Then we divide the temperature data at each group by the average temperature (T_{avg}) of that group. The outcome is shown in **Figure 6B**. We have a more direct comparison of temperature distribution at a different time compared to **Figure 6A**. The temperature increment caused by cracking can easily be detected with the help of reference data of intact concrete. The temperature distribution of a damaged concrete outside of the damaged region is lower than the intact concrete beam. This is because the temperature increment caused by crack rises the average temperature, which leads to a lower ratio at the intact region. By subtracting the reference data from each group, we can further diminish the effect of thermal inhomogeneity caused by aggregates. The result is shown in **Figure 6C**. The only peak in **Figure 6C** is the temperature increment caused by crack. The intact region has an almost flat line by diminishing the effect of aggregates. Therefore, this method can be further used to detect the cracking of CC beam when the concrete structure is exposed to fire hazards.

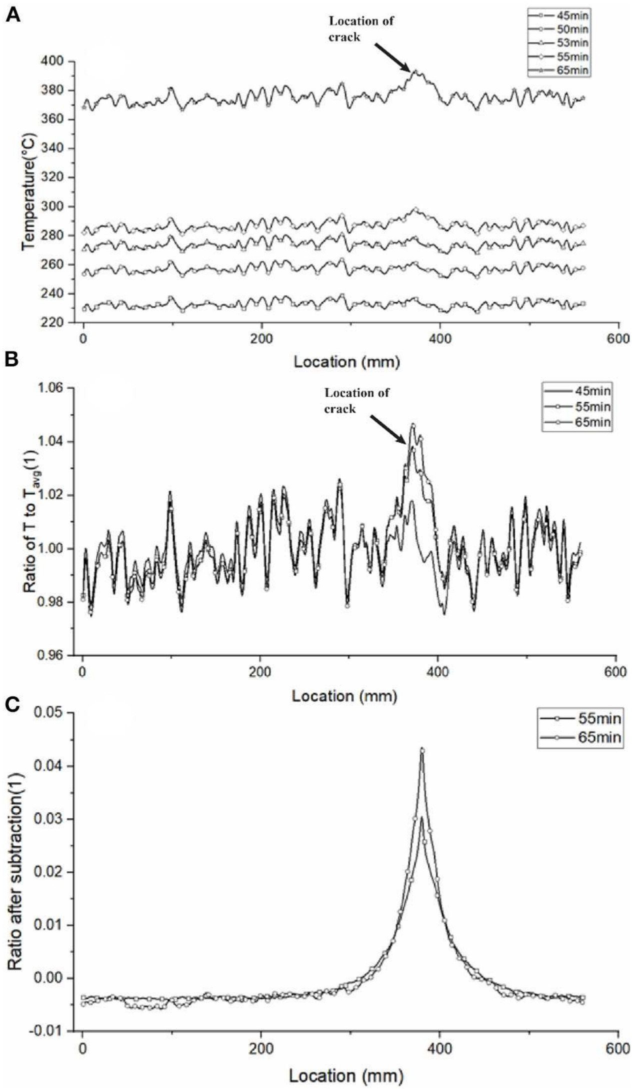

FIGURE 6 | (A) Temperature distribution of beam model II, **(B)** normalized temperature by T_{avg}, and **(C)** normalized temperature after subtraction of temporal temperature data.

Shaft Model

The maximum grain size used in the current production shafts could be as large as 160 mm. Although 40 mm may be the most common case for concrete shaft, the maximum size used in the shaft model is 80 mm to better study the influence of larger aggregates. To simulate the TIP test of concrete shaft, we establish a 6-foot concrete shaft with a longitudinal length of 1 m. Since the temperature anomaly is only restricted in the vicinity of the defect region, only part of the concrete shaft nearby the defect is simulated in the model to save the computational resources. The model geometry is shown in **Figure 3**. To simulate the inclusion defect in the concrete shaft, a 15×15×10 inch sand block as inclusion defect is placed at the edge of concrete shaft in the circumferential direction. The concrete shaft would generate heat during the curing process. Any location that has a shortage of concrete would generate less heat and be recognized as a thermal sink region at the plot. We simulate the 5-day curing process starting from pouring with 1-day interval. The temperature on the third day is recorded. The result is shown in **Figure 7**.

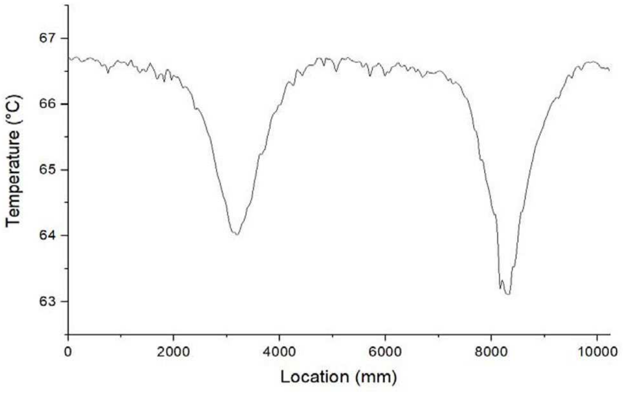

FIGURE 7 | Third-day temperature distribution for concrete shaft with coarse aggregates. The x-axis is the corresponding length of optical fiber spirally wrapped on the rebar cage.

The fiber-optic sensor is wrapped around a rebar cage spirally, and the sensor may pass the defective region several times. Each local minimum on the temperature plot represents the location of the defective region. As shown in the **Figure 7**, two local minima indicate the fiber-optic sensor passes the defective region for two times. The location that measures the local minimum temperature represents the spot that is closest to the center of the anomaly. Even though it is not pronounced, temperature fluctuations can be found in the plot. The temperature anomalies outgrows the fluctuation even more than the case of SCC beam. The explanation would be that the defect size is much greater than the maximum size of aggregates. If we consider that each aggregate as a small inclusion, and the sand block as a single large inclusion, and temperature will change according to the size of inclusion. The ability to detect anomaly in the concrete shaft or other structure would be affected by aggregates only when the size of anomaly is comparable or smaller than the maximum size of aggregates. By considering the required detectable defects of concrete shaft installation, it can be concluded that the influence of thermal inhomogeneity caused by aggregates is insignificant to practical application of fiber-optic based TIP of concrete shafts.

CONCLUSION

Within this paper, it is demonstrated that the thermal inhomogeneity due to the aggregates could cause temperature fluctuation during the non-destructive thermal integrity testing. This fluctuation may conceal the temperature anomaly caused by the damaged or defective region which is the essential mechanism for non-destructive thermal integrity testing. The larger the maximum aggregate size is, the larger the fluctuation would be due to thermal property contrast between aggregates and concrete cement. The ability to detect damaged or defective region in the concrete shaft or other structure could be affected by aggregates when the size of defects is comparable or smaller than the maximum size of aggregates. For the case of SCC beam and concrete shaft as we study in this paper, the influence of aggregate on the thermal integrity analysis is insignificant.

Even though temperature anomaly due to defects might be veiled by temperature fluctuation due to thermal inhomogeneity caused by aggregates, with proper treatment provided within this paper, the effect of aggregates can still be diminished by using the temperature data of intact structure as a reference.

The result indicates that the aggregates could have significant influence on the thermal integrity analysis of concrete structures when pouring with CC. However, proper treatment of the temperature data can diminish such an influence.

All of current conclusions are based on our explorative numerical simulation, the further verification by laboratory and *in situ* testing is suggested in the future study.

DATA AVAILABILITY STATEMENT

The raw data supporting the conclusions of this article will be made available by the authors, without undue reservation.

AUTHOR CONTRIBUTIONS

RZ conducted the research and wrote the paper. WD funded and supervised the research and edited the paper. All authors contributed to the article and approved the submitted version.

ACKNOWLEDGMENTS

The support of this research was provided by the Geotechnical Engineering program of Missouri University of Science and Technology. The authors would like to thank the Associate Editor Dr. Antonio Caggiano and two reviewers for their constructive comments to improve the early version of this paper.

REFERENCES

Bao, Y., Hoehler, M. S., Smith, C. M., Bundy, M., and Chen, G. (2017). Temperature measurement and damage detection in concrete beams exposed to fire using PPP-BOTDA based fiber optic sensors. *Smart Mater. Struct.* 26:105034. doi: 10.1088/1361-665X/aa89a9

Barry-Macaulay, D., Bouazza, A., Singh, R. M., Wang, B., and Ranjith, P. (2013). Thermal conductivity of soils and rocks from the Melbourne (Australia) region. *Eng. Geol.* 164, 131–138. doi: 10.1016/j.enggeo.2013.06.014

Brown, D., and Schindler, A. (2007). "High performance concrete and drilled shaft construction," in *Contemporary Issues in Deep Foundations*, eds W. Camp, R. Castelli, D. F. Laefer, and S. Paikowsky (Denver, CO: American Society of Civil Engineers), 1–12. doi: 10.1061/40902(221)31

Ciampa, F., Mahmoodi, P., Pinto, F., and Meo, M. (2018). Recent advances in active infrared thermography for non-destructive testing of aerospace components. *Sensors* 18:609. doi: 10.3390/s18020609

Johnson, K. R. (2016). Analyzing thermal integrity profiling data for drilled shaft evaluation. *DFI J.* 10, 25–33. doi: 10.1080/19375247.2016.1169361

Klingmüller, O., and Kirsch, F. (2004). "A quality and safetyissue for cast-in-place piles-25 years of experience with low-strain integrity testing in Germany: from scientific peculiarity to day-to-day practice," in *Current Practices and Future Trends in Deep Foundations*, eds J. A. DiMaggio, and M. H. Hussein (Los Angeles, CA: American Society of Civil Engineers), 202–221. doi: 10.1061/40743(142)12

Kodur, V., Dwaikat, M., and Raut, N. (2009). Macroscopic FE model for tracing the fire response of reinforced concrete structures. *Eng. Struct.* 31, 2368–2379. doi: 10.1016/j.engstruct.2009.05.018

Kodur, V., and Sultan, M. (2003). Effect of temperature on thermal properties of high-strength concrete. *J. Mater. Civ. Eng.* 15, 101–107. doi: 10.1061/(ASCE)0899-1561(2003)15:2(101)

Kreijger, P. (1990). "Inhomogeneity in concrete and its effect on degradation: a review of technology," in *Protection of Concrete: Proceedings of the International Conference, University of Dundee, September 1990* (Dundee: CRC Press).

Liu, W., He, P., and Zhang, Z. (2002). A calculation method of thermal conductivity of soils. *J. Glaciol. Geocryol.* 24, 770–773. Available online at: http://www.bcdt.ac.cn/EN/Y2002/V24/I6/770

Mullins, G. (2010). Thermal integrity profiling of drilled shafts. *DFI J.* 4, 54–64. doi: 10.1179/dfi.2010.010

Mullins, G. (2013). Advancements in drilled shaft construction, design, and quality assurance: the value of research. *Int. J. Pavement Res. Technol.* 6, 93–99. doi: 10.6135/ijprt.org.tw/2013.6(2).93

O'Neill, M. W. (1991). Construction practices and defects in drilled shafts. *Transp. Res. Rec.* 1331, 6–14.

Qian, Z., Garboczi, E., Ye, G., and Schlangen, E. (2016). Anm: a geometrical model for the composite structure of mortar and concrete using real-shape particles. *Mater. Struct.* 49, 149–158. doi: 10.1617/s11527-014-0482-5

Sáez Blázquez, C., Farfán Martín, A., Martín Nieto, I., and Gonzalez-Aguilera, D. (2017). Measuring of thermal conductivities of soils and rocks to be used in the calculation of a geothermal installation. *Energies* 10:795. doi: 10.3390/en10060795

Schindler, A. K., and Folliard, K. J. (2005). Heat of hydration models for cementitious materials. *ACI Mater. J.* 102:24. doi: 10.14359/14246

Shahbazi, S., and Rasoolan, I. (2017). Meso-scale finite element modeling of non-homogeneous three-phase concrete. *Case Stud. Constr. Mater.* 6, 29–42. doi: 10.1016/j.cscm.2016.10.002

Smalcerz, A., and Przylucki, R. (2013). Impact of electromagnetic field upon temperature measurement of induction heated charges. *Int. J. Thermophys.* 34, 667–679. doi: 10.1007/s10765-013-1423-1

Usmani, A., Rotter, J., Lamont, S., Sanad, A., and Gillie, M. (2001). Fundamental principles of structural behaviour under thermal effects. *Fire Saf. J.* 36, 721–744. doi: 10.1016/S0379-7112(01)00037-6

Wang, Z., Tian, G., Meo, M., and Ciampa, F. (2018). Image processing based quantitative damage evaluation in composites with long pulse thermography. *NDT&E Int.* 99, 93–104. doi: 10.1016/j.ndteint.2018.07.004

Wang, Z., Zhu, J., Tian, G., and Ciampa, F. (2019). Comparative analysis of eddy current pulsed thermography and long pulse thermography for damage detection in metals and composites. *NDT&E Int.* 107:102155. doi: 10.1016/j.ndteint.2019.102155

Zhong, R., Guo, R., and Deng, W. (2018). Optical-fiber-based smart concrete thermal integrity profiling: an example of concrete shaft. *Adv. Mater. Sci. Eng.* 2018:9290306. doi: 10.1155/2018/9290306

Conflict of Interest: The authors declare that the research was conducted in the absence of any commercial or financial relationships that could be construed as a potential conflict of interest.

frontiers in Materials

ORIGINAL RESEARCH
published: 31 August 2020
doi: 10.3389/fmats.2020.00300

Improved Kalman Filtering-Based Information Fusion for Crack Monitoring Using Piezoelectric-Fiber Hybrid Sensor Network

Yishou Wang[1], **Mengyue He**[1], **Lei Sun**[1], **Di Wu**[2], **Yue Wang**[2]* and **Li Zou**[3,4]*

[1] *School of Aerospace Engineering, Xiamen University, Xiamen, China,* [2] *China Academy of Launch Vehicle Technology, Beijing, China,* [3] *State Key Laboratory of Structural Analysis for Industrial Equipment, School of Naval Architecture, Dalian University of Technology, Dalian, China,* [4] *Collaborative Innovation Center for Advanced Ship and Deep-Sea Exploration, Shanghai, China*

Edited by:
Jun Wu,
Huazhong University of Science and Technology, China

Reviewed by:
Lingling Lu,
Institute of Mechanics (CAS), China
Cheng Liu,
Stanford University, United States
Bo Ye,
Kunming University of Science and Technology, China

***Correspondence:**
Yue Wang
wangjk1977@vip.sina.com
Li Zou
lizou@dlut.edu.cn

Specialty section:
This article was submitted to Structural Materials, a section of the journal Frontiers in Materials

Received: *28 June 2020*
Accepted: *11 August 2020*
Published: *31 August 2020*

Citation:
Wang Y, He M, Sun L, Wu D, Wang Y and Zou L (2020) Improved Kalman Filtering-Based Information Fusion for Crack Monitoring Using Piezoelectric-Fiber Hybrid Sensor Network. Front. Mater. 7:300. doi: 10.3389/fmats.2020.00300

Multifunctional sensor network has become a research focus in the field of structural health monitoring. To improve the reliability and stability of the diagnosis results, it is necessary to fuse heterogeneous signals under the interference of the external load and damage. In this paper, a piezoelectric-fiber hybrid sensor network is integrated to monitor the crack growth around the hole in the aviation aluminum plate. The effect of the load change on the signals of piezoelectric transducers (PZTs) and optical fiber sensors is analyzed. To improve the damage diagnosis result obtained by ultrasonic guided wave imaging diagnosis based on PZTs and strain damage identification based on distributed optical fiber sensor, a fusion strategy of heterogeneous signals based on a two-stage Kalman filtering algorithm is proposed. In the first stage, the features extracted from two types of sensors are fused at a specific time at the feature level, and then the location of the damage center is predicted. Then, the second fusion is to fuse the predicted damage location results at multiple specific times at the decision level. Crack growth monitoring experiments in hot spots of metallic material under bending moment loading is carried out to verify the feasibility of the proposed fusion method. The experimental results indicate that the fusion damage diagnosis results are more stable, moreover, the accuracy of damage location and quantification is improved than the single signal diagnosis results.

Keywords: structural health monitoring, multi-sensor information fusion, Kalman filtering, piezoelectric transducers, guided waves, optical fiber sensor

INTRODUCTION

In recent years, structural damage and failure have led to some dramatic accidents in the field of aeronautical and ocean engineering. With the complexity of the structural load and the harsher environment, the demand for obtaining real-time information on the structural state becomes more and more urgent. Structural health monitoring (SHM) techniques have been widely used to assess the structural state and improve the structural safety of aircraft (Qing et al., 2012) and ocean platform (Tang et al., 2020) in recent years. Different types of lightweight sensor networks are permanently integrated on the surface or embedded within the structure to obtain information on load, deformation, and damage expansion of key structural regions. Many advanced SHM techniques have emerged, such as ultrasonic guided waves (Villegas, 2019; Wang et al., 2019), optical fiber gratings (Lau, 2014), vibration-based (Zhang et al., 2018), eddy current (Bohacova, 2013), acoustic emission (Michalcová and Růžek, 2016), and mechanical impedance (Min et al., 2012). However, most of these techniques are based on single-type sensors, which is difficult to meet the requirements of complex structure and multi-physical field monitoring. The monitoring results are also easily disturbed by the surrounding environment and external scenarios such as temperature, vibration, and different forms of the load.

Recently, a multi-functional sensor network composed of different kinds of sensors has become a research focus (Qing et al., 2005; Wu et al., 2009). However, the research of multi-source sensor interaction in the multi-physics field is still insufficient. To improve the reliability and stability of the diagnosis results, it is necessary to make full use of various sensor information (data or signals) when the structural load and damage are considered comprehensively (Wu et al., 2017; Sun et al., 2018). Multi-sensor information fusion technology integrates the redundant or complementary information of each sensor in space or time. The reliability and robustness of the system can be improved by overcoming the uncertainty and limitation of single-type sensors and obtaining consistent interpretation or description of the structure. Information fusion can be carried out at different levels, including data level, feature level, and decision level, which correspond to three fusion methods. Among them, data-level fusion is mainly used to preprocess multi-source information such as strain, modal parameters, acceleration, temperature, and pressure. Feature-level fusion is to extract characteristic indices by damage sensitivity analysis and data mining. Decision-level fusion is used to predict the state characteristics of the structure. Gravina et al. (2017) provided a comprehensive and systematic review of the latest technologies from three levels: data-level, feature-level, and decision-level. They pointed out that multiple homogeneous sensors can be directly fused, while for heterogeneous sensors, feature-level or decision-level fusion techniques are required. Besides, common fusion methods were listed, including the Kalman filtering method (Kalman, 1960), weighted average method, Bayesian estimation method, Dempster-Shafer evidence theory, artificial neural network, fuzzy theory, genetic algorithm, support vector machine and so on. Su et al. (2009) evaluated mono- and multi-delamination of carbon fiber-epoxy (CF/EP) composite structures using three fusion schemes, namely disjunctive, conjunctive, and compromise fusion. The difference between the three fusion schemes lies in whether the signal feature extraction and pattern recognition are carried out at single-type sensors or the whole network. They found that disjunctive and conjunctive fusion might exaggerate and minimize the possibility of damage, respectively, while compromise fusion scheme showed high robustness and reliability.

The Multi-sensor system is the hardware foundation of data fusion. In the field of SHM, an ultrasonic guided wave technique based on piezoelectric transducers (PZTs) (Liu et al., 2016b; Memmolo et al., 2016; Miniaci et al., 2019) and optical fiber sensing (Liang and Yuan, 2015) have been widely used. The guided wave monitoring technique has high monitoring efficiency and sensitivity and can realize large area active monitoring. It is mainly used to monitor fatigue crack, fracture, delamination, and other damages. However, the guide wave signal is easily restricted by actuator-sensor paths, which makes the signal interpretation very complicated. Besides, temperature, stress, and other external environmental factors have a greater impact on the signal fluctuations. In contrast, the optical fiber sensor is light in weight, small in size, and easy to install, it can realize multi-point continuous passive monitoring relatively stably. Especially, a distributed optical fiber sensor can replace multiple strain gauges to realize high-density monitoring, thus greatly reducing the weight of connecting cables and sensor networks. However, the monitoring area of optical fiber sensors is limited, which can only be detected after temperature changes and structural deformation, and only the signal along the fiber length direction can be monitored. Therefore, based on the above advantages and disadvantages of guided wave and optical fiber monitoring, it is important to fuse ultrasonic guided wave signals with optical fiber signals to make up for the shortage of single-type sensors. The accuracy and stability of SHM can be improved by constructing a hybrid sensor network and integrating multi-source sensor information to monitor the load state, damage state, and other information of the structure.

In this paper, a two-stage Kalman filtering-based heterogeneous signal fusion of the piezoelectric-fiber hybrid sensor network is proposed to monitor crack growth at the feature level and decision level. The remaining work is organized as follows. Section "Sensing Principle of Damage Monitoring" describes the damage monitoring principle of the piezoelectric transducer and the optical fiber sensor, respectively. Section "Heterogeneous Signal Fusion based on Kalman Filtering" depicts the heterogeneous signal fusion technology based on Kalman filtering. Section "Experiment" conducts a crack growth monitoring experiment in the hot spot area of metal material under bending moment loading. In section "Two-Stage Fusion of Kalman Filtering for Damage Location Monitoring," a Kalman filtering fusion algorithm based on two-stage fusion is proposed, which firstly fuses the multi-sensor signals at a specific time at the feature level and predicts the damage location, and then fuses the prediction results at multiple specific times at the decision level. The whole process of two-stage heterogeneous signal fusion of multi-sensing is shown in **Figure 1**.

SENSING PRINCIPLE OF DAMAGE MONITORING

Structural health monitoring (SHM) is mainly concerned with the diagnosis of damage in large and local areas. It is very important to select sensors with reliable performance and high-cost performance. Piezoelectric transducers (PZTs) and optical fiber sensors were commonly used because of their small size and lightweight. In sections "Guided Wave Method

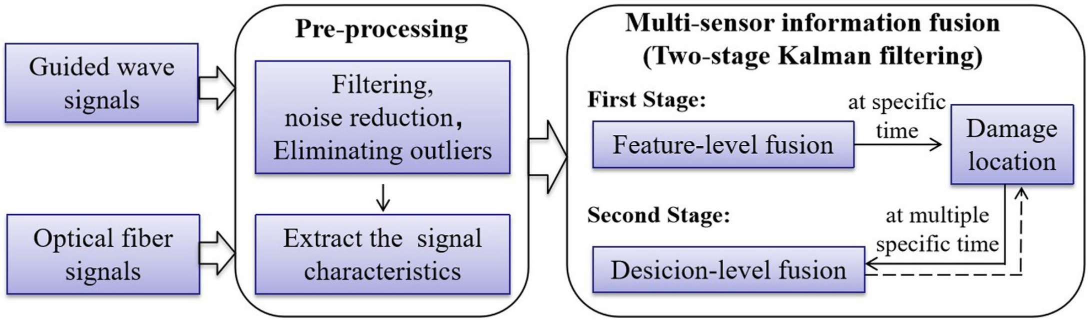

FIGURE 1 | The heterogeneous signal fusion process based on a piezoelectric-fiber hybrid sensor network.

based on Piezoelectric Transducers" and "Optical Fiber Sensing," the sensing theory of PZTs and the optical fiber sensors are introduced, corresponding to the elliptic probabilistic weighted damage imaging method and the damage diagnosis method based on strain change, respectively.

Guided Wave Method Based on Piezoelectric Transducers

Guided wave damage monitoring is suitable for both large and local areas with the advantages of high detection efficiency and damage sensitivity. Different types of damage such as fatigue crack, fracture, and delamination can be monitored. As is shown in **Figure 2**, the ultrasound signals are excited by the actuator on the surface of the detected structure and the other sensors receive the structural response signal at one or more locations of the structure (Qing et al., 2019). When the structure is damaged, the structure boundary changes accordingly, which leads to the scattering and energy absorption of the ultrasonic guided waves propagating in the structure. Therefore, the structural health state can be judged by analyzing the signal changes of each actuator-sensor path before and after damage (Wu et al., 2015). PZTs are often used to excite and receive guided wave signals and can be regarded as exciter and receiver due to their positive and negative piezoelectric effects.

Damage imaging diagnosis methods based on guided waves mainly include the probability weighting method (Wu et al., 2015), phase control array method, time of flight method, delay superposition method, time-reversal method, etc. Considering that damage diagnosis cannot be realized only based on the change of the guided wave signal in the single actuator-sensor path, the change of the wave signal in the multi-actuator-sensor path is needed. Therefore, the elliptic probability weighting method was used in this paper because of its high efficiency and strong applicability (Wu et al., 2015; Liu et al., 2016a). The damage indicator (DI) of each actuator-sensor path was first calculated. Then the damage probability of each point on the

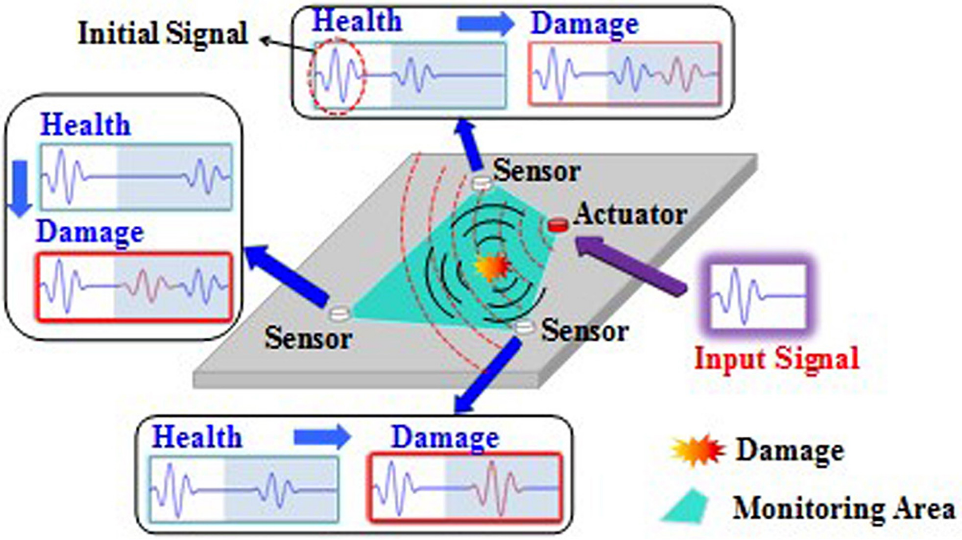

FIGURE 2 | The monitoring principle of the Guided wave method (Wu et al., 2015; Liu et al., 2016a).

structure was obtained by integrating the DI information of all actuator-sensor paths with the weighted function, thus the damage diagnosis and imaging of the whole monitoring area can be carried out.

DI has a great influence on the sensitivity of damage diagnosis and can be expressed in the time domain, frequency domain, and other characteristic forms, such as wave velocity, amplitude, and energy. The time-domain energy of the scattered signal not only contains the attenuation information of the ultrasonic guided wave caused by damage but also reflects the phase delay information of the guided wave signal, so it is highly sensitive to damage. Therefore, the time-domain energy (i.e., *eng*) of the direct wave, S_0 scattered signal was selected to represent DI of the guided wave monitoring method. The form of *eng* and DI are as follows:

$$eng = \int_{t_0}^{t_f} u^2(t)dt \tag{1}$$

$$DI = \frac{eng_C - eng_B}{eng_B} \tag{2}$$

Where t_0 and t_f represent the range of time-domain signals used for signal comparison, u is the signal amplitude, the subscripts C and B of *eng* represent the measured signal and the baseline signal of the guided wave, respectively.

Optical Fiber Sensing

Optical fiber sensor monitoring is to judge the damage state of the structure according to the change of strain field and its correlation with the damage. The damage near the actuator-sensor path of the optical fiber sensor can be determined by accurate strain field measurement (Shan et al., 2019). The location and severity of damage can be determined by comparing the signal differences of optical fiber sensing before and after the damage. Optical fiber sensor has the characteristics of lightweight, flexibility, strong anti-interference, and high sensitivity, and can realize long-distance measurement. The most commonly used optical fiber sensors are fiber Bragg gratings (FBGs) and distributed optical fiber sensors. In this paper, a distributed fiber sensor was selected because the strain information at any point along the length of the fiber can be obtained.

When strain or temperature is measured by the distributed fiber sensor, the variation of temperature or strain will cause the deviation of the Raleigh scattering spectrum of backscattering in the fiber. By observing the spectrum of the scattered light, it can be determined which part of the fiber has changed in temperature or strain (Kreger et al., 2009). The relationship among the backscatter spectral shift (similar to the wavelength λ), the strain ε, and the temperature T in fiber Bragg gratings (Kreger et al., 2009) is:

$$\frac{\Delta\lambda}{\lambda} = K_\varepsilon \varepsilon + K_T \Delta T \tag{3}$$

Where K_ε and K_T are the calibration constants of strain and temperature respectively, whose values are related to the characteristics of the optical fiber.

For optical fiber monitoring, the variation of strain before and after the damage is usually taken as the DI, which is specifically expressed as follows:

$$DI = \varepsilon - \varepsilon_0 \tag{4}$$

Where ε and ε_0 are the strain values collected after and before the damage. The higher the DI value, the greater the probability or severity of the damage.

HETEROGENEOUS SIGNAL FUSION BASED ON KALMAN FILTERING

Kalman Filtering is an important and widely used information fusion algorithm based on the theory of closed-loop feedback information estimation (Kalman, 1960). In the field of damage identification, Kalman filtering is commonly used to detect large civil and mechanical structures. By establishing the Kalman filtering system model, the sensor data are predicted and corrected recursively, so that the system processing does not need a large number of data storage and calculation. Especially, the Kalman filter can estimate the state of a dynamic system from a series of data with measurement noise when measurement variance is known. It is convenient for computer programming and can update and process the data collected on-site in real-time. These advantages are conducive to information fusion of piezoelectric plate and optical fiber sensor, especially their complementary advantages (global detection and local detection). By monitoring different information such as load state and damage state of the structure at the same time, the deficiency of the damage diagnosis method based on a single-type sensor is avoided, and thus have a more comprehensive understanding of structure state.

However, for other common fusion methods, such as weighted average method, Kalman filtering method, Bayesian estimation method, Dempster-Shafer (D-S) evidence theory, artificial neural network, fuzzy theory, genetic algorithm, support vector machine, etc., they all have various disadvantages. For example, the weighted average method is not suitable for complex signal processing, Bayesian estimation requires the prior probability to be given, D-S evidence theory's exponent is extremely complex, the artificial neural network has a large amount of computation and is difficult to find the local optimal solution.

Kalman filtering (Kalman, 1960) is an optimal state estimation method, mainly including prediction and correction (Woods and Radewan, 1977). The current state is predicted according to the previous state and control quantity, and then the credibility of sensor data and overall estimate is judged by correction, and the current state is updated by repeated prediction and correction. Assume that the system state is expressed by a state vector X ($X \in R^n$), and the state equation of the system at time k is (Cui and Huang, 2001):

$$X_k = AX_{k-1} + BU_k + W_k \tag{5}$$

Where U_k and W_k are the control input and state noise of the system respectively, and A and B are the state transition matrices.

The observation equation of the system at the corresponding time k is:

$$Z_k = HX_k + V_k \tag{6}$$

TABLE 1 | The material properties of the 7075 aircraft aluminum plate.

Density (kg/m^3)	Tensile strength (MPa)	Yield strength (MPa)	Poisson ratio	Thermal expansion coefficient	Elasticity modulus (GPa)	Elongation (%)
2810	572	503	0.33	23.6	71	11

Where $Z \in R^{\mathrm{m}}$, H and V_{k} are the observation matrix and the observation noise, respectively. W_{k} and V_{k} are two independent white noises with a mean value of zero and a covariance matrix of Q and R, respectively.

The state estimation at time k is divided into a prior estimate and a posterior estimate. The prior estimate is to estimate the state at time k according to the state before time k, while the posterior estimate is an estimate of the state at time k given the observed quantity Z_{k} at time k.

The prior estimate $\widehat{X}_{\mathrm{k\_pre}}$ and its error $E_{\mathrm{k\_pre}}$ and covariance $P_{\mathrm{k\_pre}}$ of the system at time k are:

$$\widehat{X}_{k\_pre} = A\widehat{X}_{k-1} + BU_k \tag{7}$$

$$E_{k\_pre} = X_k - \widehat{X}_{k\_pre} \tag{8}$$

$$P_{k\_pre} = A\widehat{P}_{k-1}A^T + Q = EE_{k\_pre}E^T_{k\_pre} \tag{9}$$

Where $\widehat{X}_{\mathrm{k}-1}$ is the posterior estimate of time $k-1$, $\widehat{P}_{\mathrm{k}-1}$ is the covariance of the posterior estimate of time $k-1$, E is a unit matrix, $E^{\mathrm{T}}_{\mathrm{k\_pre}}$ is the transposed matrix of $E_{\mathrm{k\_\ pre}}$.

The posterior estimate $\widehat{X}_{\mathrm{k}}$, error E_{k}, and covariance P_{k} of the posterior estimate at time k are:

$$\widehat{X}_k = \widehat{X}_{k\_pre} + K_kZ_k - \widehat{X}_{k\_pre} \tag{10}$$

$$E_k = X_k - \widehat{X}_k \tag{11}$$

$$P_k = P_{k\_pre} - K_kHP_{k\_pre} = EE_kE^T_k \tag{12}$$

Where E^T_{k} is the transpose matrix of E_{k}, K_{k} is the Kalman gain at time k, and the expression of K_{k} is:

$$K_k = P_{k\_pre}H^THP_{k\_pre}H^T + R^{-1} \tag{13}$$

The common multi-sensor Kalman filtering fusion needs to calculate the Kalman factor of each sensor at each time, which is a huge amount of computation. In this paper, when the Kalman filtering fusion algorithm is used to fuse the signals of the PZTs and optical fiber signals, assume that the sensor error conforms to the normal distribution. The measurement error of the PZTs is M, and the measurement error of the optical fiber sensor is N. When piezoelectric and optical fiber sensors are used to measure the same damage, the measurement values of the two sensors are weighted and averaged to obtain the best measurement value. Taking Eqs (7)–(13), Kalman optimal estimated weight can be obtained by:

$$\begin{cases} W_{PZT} = \frac{N^2}{M^2+N^2} \\ W_{OP} = \frac{M^2}{M^2+N^2} \\ W_F = \frac{M^2N^2}{M^2+N^2} \end{cases} \tag{14}$$

Where W_{PZT} and W_{OP} are the fusion weights of the measured values of the PZTs and the optical fiber sensors, respectively during the first fusion. W_{F} is the covariance of the estimated value after the first fusion.

EXPERIMENT

The experiment is to monitor the crack growth in the hot spot area of metal materials under bending moment loading. The specimen is a 300 mm × 300 mm × 2 mm 7075 aircraft aluminum plate with a 10 mm diameter through-hole in the center specimen. The material properties of the specimen are shown in **Table 1**. As is shown in **Figure 3**, the crack growth of the specimen starts from the point (155, 150) and extends along the positive direction of the X-axis.

As is shown in **Figure 4**, eight circular PZTs and a distributed optical fiber sensor with a length of one meter were set on the surface of the same aluminum plate by high-temperature AB glue. For PZTs sensing, the diameter and thickness of the circular piezoelectric sensor are 8 and 0.48 mm, respectively, and each PZT acted as excitation or receiver. For optical fiber sensing, the distributed optical fiber sensor was used to monitor the strain information at predefined points. The effective strain monitoring path of the optical fiber sensor consists of four parts, i.e., AB, CD, EF, and GH segments. The AB and EF segments of the fiber monitored the strain in the X direction and the

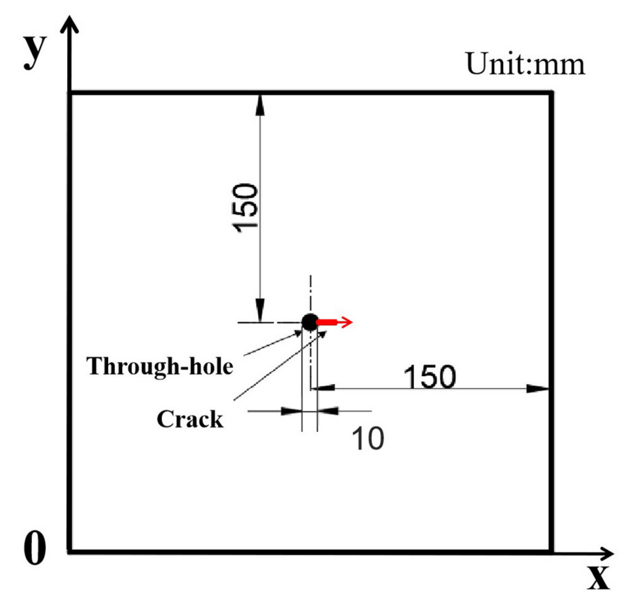

FIGURE 3 | The schematic diagram of through-hole on the aluminum plate.

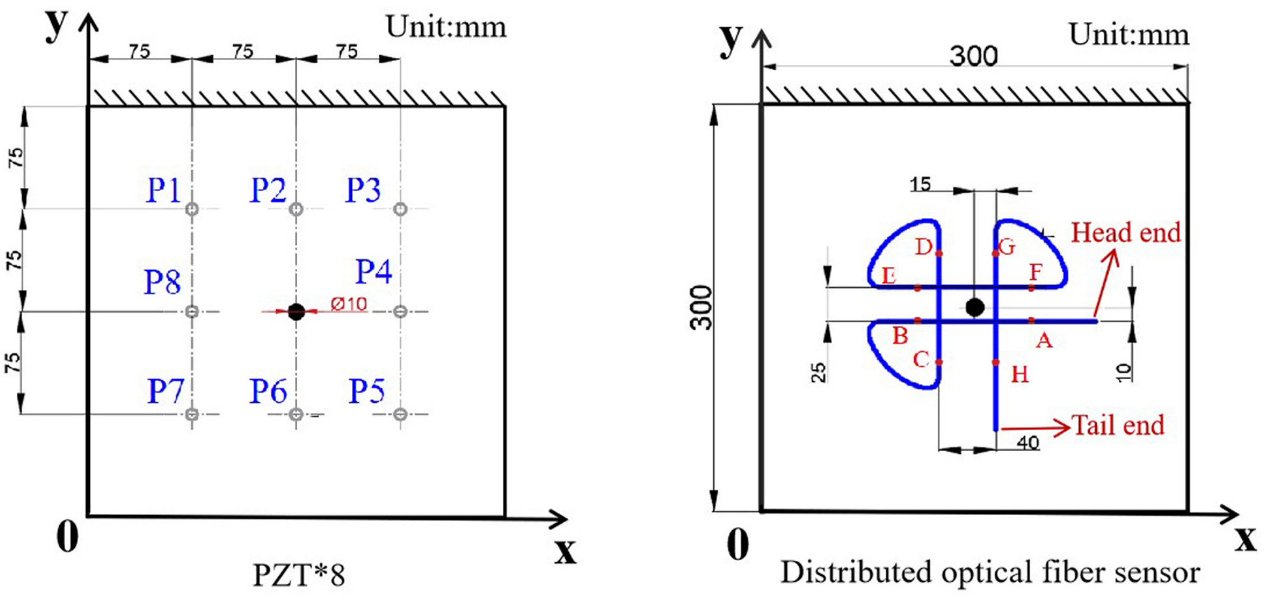

FIGURE 4 | The sensor layout of the PZTs and distributed optical fiber sensor on the same aluminum plate.

CD and GH segments monitored the strain in the Y direction. **Table 2** lists the positions of initial points of four segments in the coordinate system and on the entire distributed optical fiber sensor (relative to head end). There are seventeen equispaced strain measuring points for each segment on the optical fiber sensor. The position range of strain measuring points in AB, CD, EF, and GH segments are 205–285, 435–515, 690–770, and 905–985 mm, respectively. The distance between two adjacent measurement points is 5 mm.

Figure 5 shows the layout of the piezoelectric-fiber hybrid sensor network of the aluminum alloy plate. To simulate the stress scenario of the wing skin, the bending test was conducted with five G-clamp fixed the aluminum plate evenly on the experimental rack. Five loading points distributed uniformly by magnets hooks at the free end of the aluminum plate. The baseline signal of the structure under the health state without load and the damage signal under crack growth were collected, respectively. Considering the magnet and hook will change the structure of the specimen, which will affect the propagation of the ultrasonic guided wave, the state of the magnet hook was served as the baseline of no load.

The specific loading process mainly includes four steps:

Step 1: Collect the signals when the load is 0 g;

Step 2: Load weights in turn from 250 to 1500 g with intervals of 250 g for sampling;

Step 3: Prefabricate 1 mm long cracks at the edge of the circular hole, then repeat Steps 1 and 2;

Step 4: After the crack generated in Step 3 extended by 1 mm, repeat Step 1 and 2 until the crack extended to 6 mm.

In **Figure 6A**, the ScanGenie II monitoring system developed by Acellent was adopted as the monitoring system of ultrasonic guided waves, mainly completing the generation of excitation signals required by sensors and the collection of sensing signals. The signal of ultrasonic guided wave adopts the five-cycle sinusoid Hanning-modulated tone bursts, the frequency range of the excitation signal is 160–260 kHz with an interval of 20 kHz, and the amplitude of the excitation is 30 V. The selection of excitation signal frequency was mainly based on the quality of the direct S_0 signal received by the sensor. For signals of multiple excitation frequencies, the S_0 signal with little or no crosstalk was selected for analysis. In **Figure 6B**, the strain monitoring based on distributed optical fiber sensor was conducted by high-resolution fiber sensor interrogating system ODiSI-A (Optical Distributed Sensor Interrogator) of the American Luna Technology company. The optical fiber signal with a resolution of 0.5 cm/point was selected. It should be noted that since the two sensors are based on different working principles, data acquisition can be carried out simultaneously without affecting each other. During the experiment, all the tests were conducted within

TABLE 2 | The starting points of each optical fiber monitoring path (Unit: mm).

Initial points of sensing paths	A	B	C	D	E	F	G	H
X coordinate	190	110	125	125	165	165	190	110
Y coordinate	140	140	110	190	110	190	165	165
Position on the entire optical fiber (relative to head end)	205	285	435	515	690	770	905	985

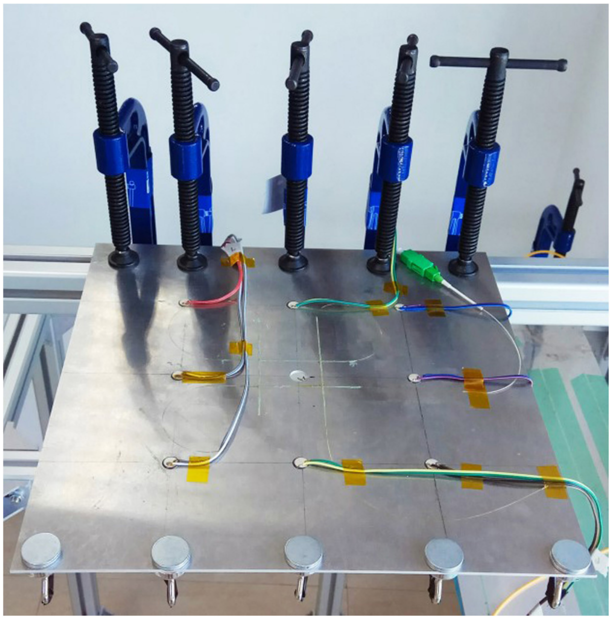

FIGURE 5 | The layout of the fiber-piezoelectric hybrid sensor network.

10 min after the system was loaded to avoid the impact of vibration on the signal. To avoid the occurrence of accidental abnormal signals, outliers were removed from all signals, and the average value is taken for three times. Besides, the air conditioner was used to adjust the temperature of the laboratory, and a thermometer was placed around the specimen to control the temperature change in the range of 24.9–25.1℃.

TWO-STAGE FUSION OF KALMAN FILTERING FOR DAMAGE LOCATION MONITORING

According to the advantages and disadvantages of PZTs and optical fiber sensors, a two-stage Kalman filtering fusion was proposed to achieve damage location monitoring. The first stage is to fuse the features extracted from two types of sensors at a specific time at the feature level and predict the damage location. Then, the predicted damage location results at multiple specific times are fused at the decision level in the second fusion. In sections "Guided Wave Signal Analysis" and "Optical Fiber Signal Analysis," the effects of load and crack length on the signals of PZTs and distributed optical fiber sensors were analyzed, respectively. In section "Multi-sensor Information Fusion Based on Two-Stage Kalman Filtering," two-stage multi-sensor heterogeneous signal fusion for damage monitoring was conducted, and the monitoring results were compared with those of single-type sensors.

Guided Wave Signal Analysis

The guided wave signal based on PZTs was analyzed by the elliptic probability weighting method. It is easier to distinguish the damaged area from the healthy area by using the square value of DI for damage imaging. **Figure 7** shows the damage diagnostic imaging of guided wave signals for 5 mm crack under the load from 0 to 1500 g. Different colors in the figure represent different DI squared values and correspond to different damage probabilities. The seven imaging results were all based on the health signal, and the maximum of DI was regarded as the position of damage center. Take 250 g as an example, the predicted damage was obtained by analyzing the difference between health signal and damage signal under the 250 g load. It can be seen that the position of the damage center does not change with the load.

To compare DI values of different crack lengths under different loads, **Figure 8** shows the DI value of optical fiber sensor for 1–8 mm crack under the load of 0–1500 g. It can be seen intuitively that the DI value of the 6 mm crack increases by leaps and bounds under different loads, and the damage is easily predicted. However, when the crack length is less than or equal to 5 mm, the DI value fluctuates within a lower range. Therefore, the sensitivity of the guided wave to the monitoring results with small damage is not high in this actuator-sensor path.

Considering that different loads have different effects on ultrasound guided wave diagnostic imaging, **Table 3** lists four cases with a different combination of load and guided wave signals, corresponding to the guided wave imaging results in **Figure 9**. Take Case 1 as an example, the baseline signal is the health signal with no load, and the diagnostic signal is the damage signal with no load. However, the special reason for Case 3 is that the aluminum plate has not been damaged with no load, so it only corresponds to the health signal. It can be seen from **Figure 9** that the change of baseline of guided

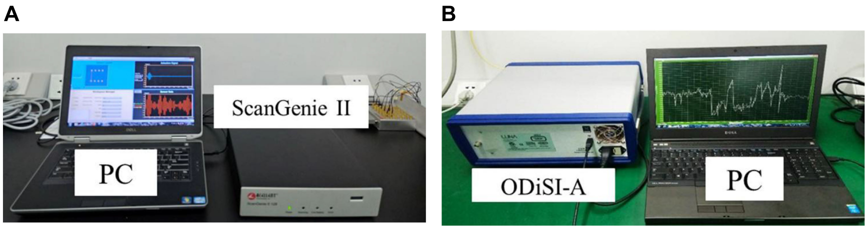

FIGURE 6 | Experimental monitoring system for measuring signals of optical fibers and guided waves: **(A)** ScanGenie II, **(B)** ODiSI.

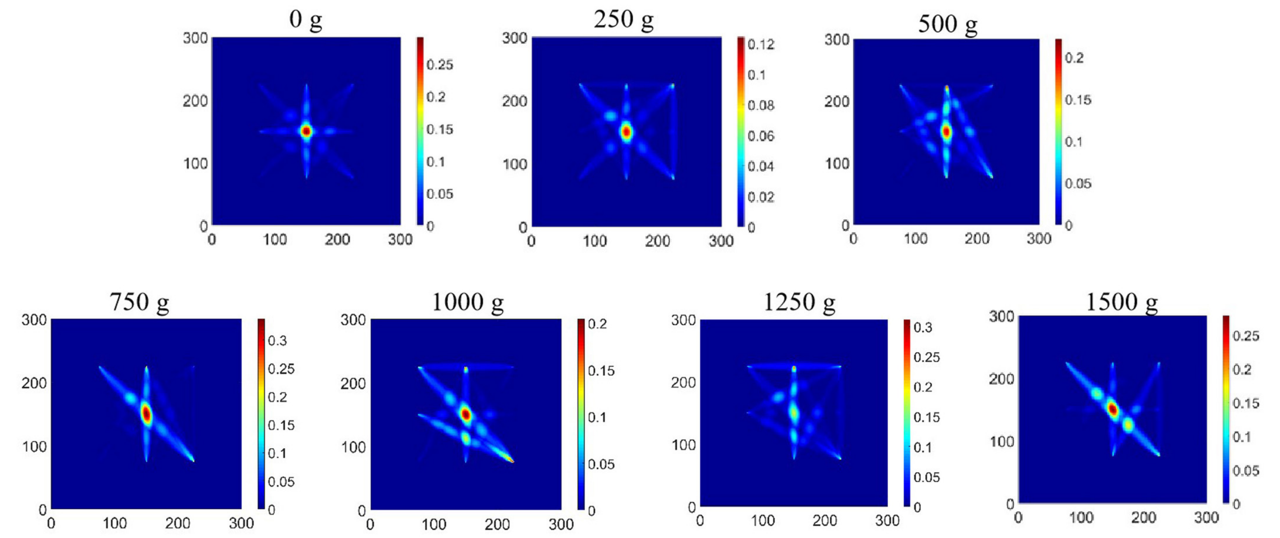

FIGURE 7 | Guided wave damage imaging diagnosis under different loading quality (Load from 0 g to 1500 g at intervals of 250 g).

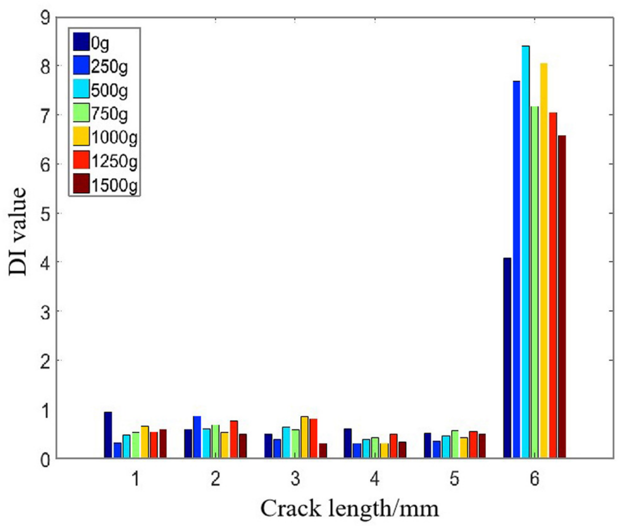

FIGURE 8 | The effect of load and crack length on the guided wave damage imaging.

wave damage imaging seriously affects the diagnosis result, and even leads to the misdiagnosis of damage location and number especially in Case 2. From Case 1–3, it can be seen that under the same baseline signal, i.e., no-load healthy signal, different diagnostic signals lead to completely different imaging diagnosis results. However, by comparing Case 3 and Case 4, no matter the no-load health signal or the 150 0g health signal as the baseline signal, the imaging results of the 1500 g damage signal are similar.

Optical Fiber Signal Analysis

The DI values of optical fiber monitoring with crack growth in different segments were monitored under the load from 0 to 1500 g. **Figure 10** shows the DI value of four segments (AB, CD, EF, and GH) with an undamaged and 1–6 mm crack under the load 1500 g. The points on the *X*-axis represent the position of each strain measurement point on the entire length of the distributed optical fiber sensor, which can be referred to in **Table 2**. The DI value of optical fiber monitoring is calculated by Equation (4), and the larger the DI value is, the greater the probability of damage or the more serious the damage is. It can be seen that with the increase of crack length, the DI values monitored by the four-segment optical fiber sensor increases. The changes of DI near the damage was more obvious than in the undamaged area, especially for AB and GH segments. This is because AB and GH segments are closer to the damage in the X direction than EF and CD segments in the X and Y direction.

Figure 11 shows the DI values of optical fiber monitoring under the load from 0 to 1500 g under the 5 mm crack. The green marked area corresponding to the *X*-axis is the circular hole position in the center of the specimen, and the red marked signal area is the crack damage at the edge of

TABLE 3 | The baseline and diagnostic signals of different cases.

	Case 1	Case 2	Case 3	Case 4
Baseline signal	No-load; healthy signal	No-load; healthy signal	No-load; healthy signal	1500 g load; healthy signal
Diagnostic signal	No-load; damage signal	1500 g load; healthy signal	1500 g load; damage signal	1500 g load; damage signal

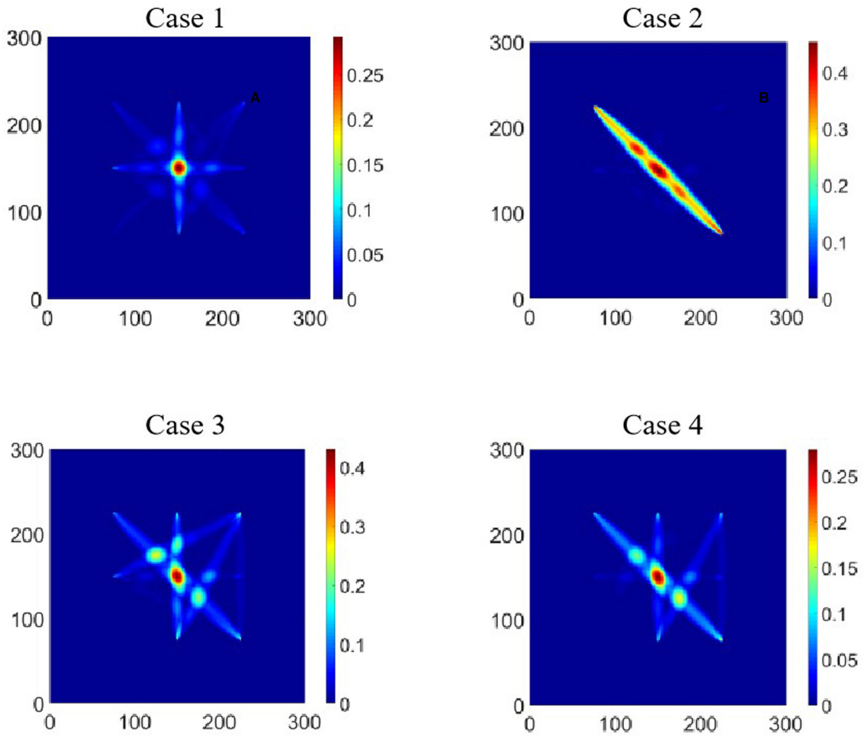

FIGURE 9 | Damage location based on guided wave damage diagnosis in Cases 1–4.

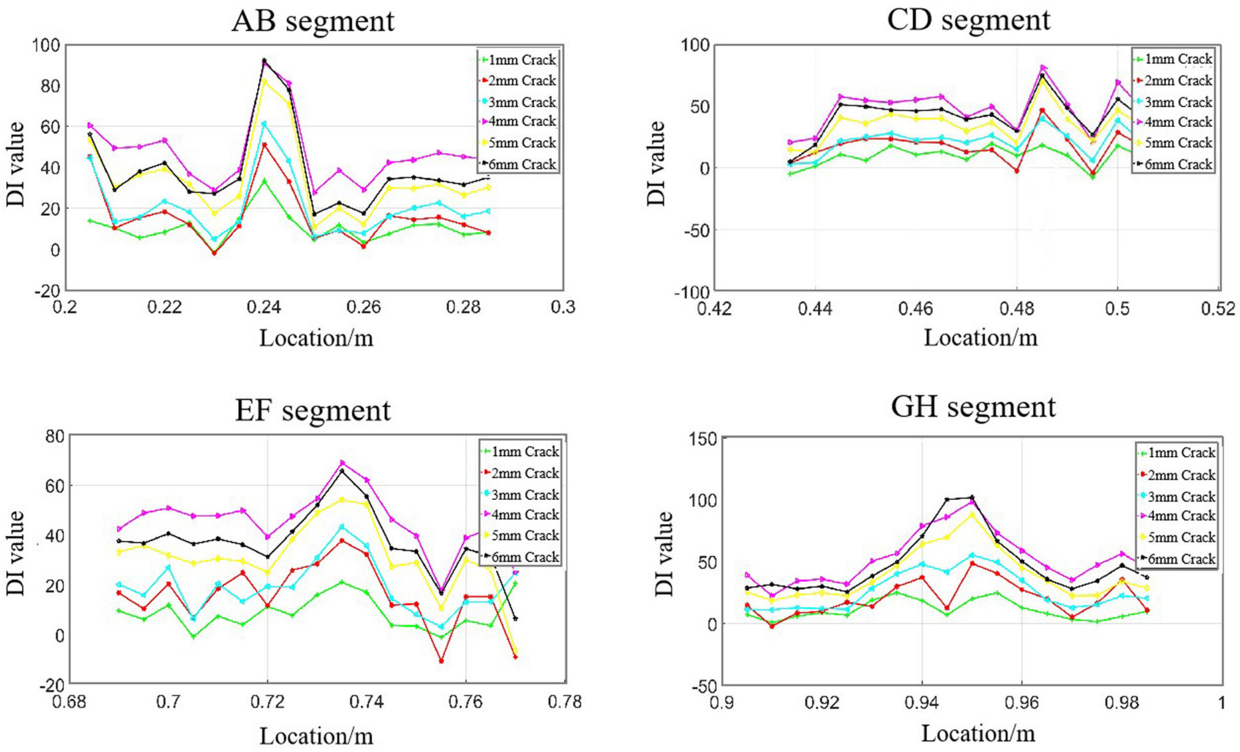

FIGURE 10 | The DI changes of distributed optical fiber signal segments (AB, CD, EF, GH) with crack growth.

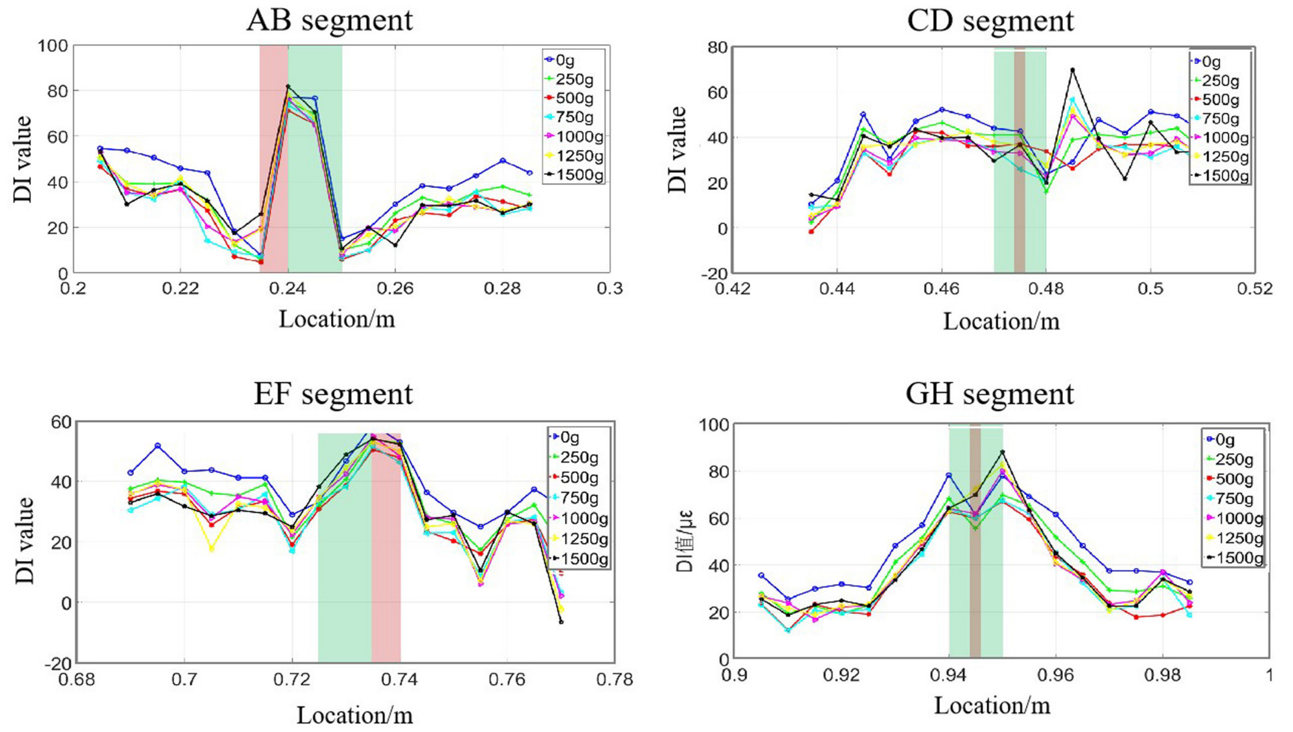

FIGURE 11 | The effect of load under 5 mm crack on the DI value of distributed optical fiber segments (AB, CD, EF, GH).

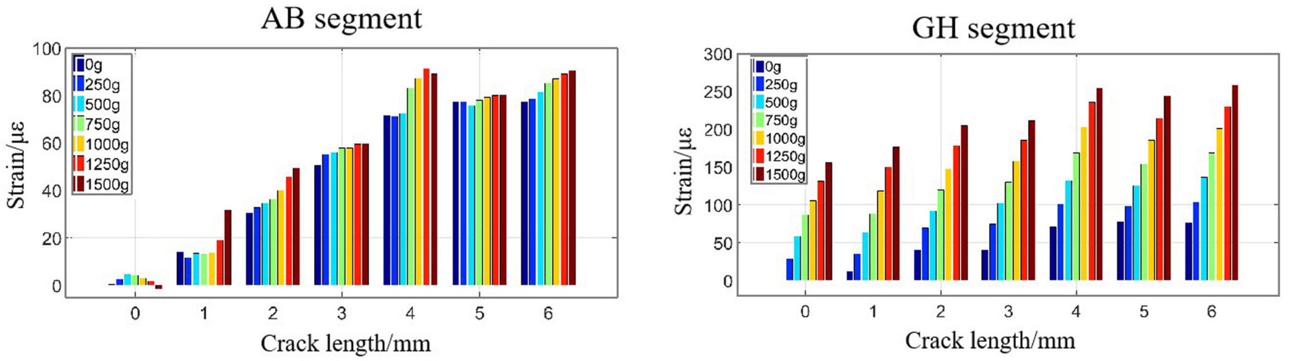

FIGURE 12 | The effect of load and crack length on the strain of the distributed optical fiber segments (AB, GH) near the hole.

the hole. Combined with the crack growth extending from point (155, 150) to the positive direction of the *X*-axis in **Figure 3**, the relative position relationship between the green region and the red region in **Figure 11** can be verified. For the X direction of AB and EF segments, the crack is close to point A and F and away from point B and E, so the red areas are to the left and right of the green range. For the Y direction of CD and GH segments, the crack is in the middle of the circular hole, so the red area is within the green range. It can be seen from **Figure 11** that the DI variation of AB, CD, and EF segments has a peak near the damage, while the DI value of the CD segment changes irregularly. This phenomenon indicates that the strain method based on optical fiber sensors has the shortcoming of monitoring area limitation. Therefore, a further fusion of optical fiber signals with other technology is necessary.

According to **Figure 4**, AB and GH segments are closer to the damage center than CD and EF segments, the severity of damage can be represented by strain values at the damage center of the AB segment and GH segment. **Figure 12** shows the strain value of the AB and GH segments of distributed optical fiber near the hole varies with load and crack length. It can be seen that the strain of damage center in AB and GH segment increases with the increase of load and crack length. The difference between AB and GH segment is that the strain value of the GH segment is relatively larger with better linearity, which

TABLE 4 | The predicted damage center location and location error of single-type sensors and two-stage Kalman filtering fusion.

Load (g)	Actual damage location (mm)	Damage location monitored by Single-type sensors (mm)		Two-stage Kalman filtering fusion predicted (mm)/error*
		Single-type PZTs monitoring/error*	Single-type optical fiber sensor monitoring/error*	
0	(157.5, 150.0)	(151.0, 151.0)/6.5765	(152.5, 144.0)/7.8102	(151.7017, 147.7256)/6.2285
250	(157.5, 150.0)	(151.0, 151.0)/6.5765	(153.0, 143.5)/7.9057	(151.9356, 147.4917)/6.1037
500	(157.5, 150.0)	(151.0, 151.0)/6.5765	(153.0, 144.5)/7.1063	(151.9356, 147.9595)/5.9268
750	(157.5, 150.0)	(151.0, 151.0)/6.5765	(153.0, 144.0)/7.5000	(151.9356, 147.7256)/6.0113
1000	(157.5, 150.0)	(151.0, 151.0)/6.5765	(153.0, 144.5)/7.1063	(151.9356, 147.9595)/5.9268
1250	(157.5, 150.0)	(151.0, 151.0)/6.5765	(153.0, 145.5)/6.3640	(151.9356, 148.4272)/5.7824
1500	(157.5, 150.0)	(151.0, 151.0)/6.5765	(153.0, 145.0)/6.7268	(151.9356, 148.1933)/5.8504

*Error means the distance between the predicted damage center and the actual damage center.

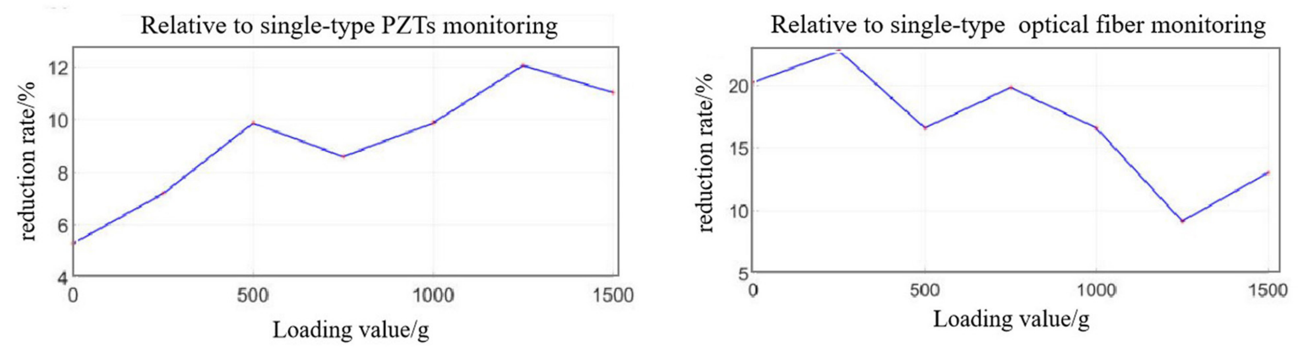

FIGURE 13 | The location error reduction rate of the two-stage fusion relative to single-type PZTs and single-type optical fiber sensor monitoring.

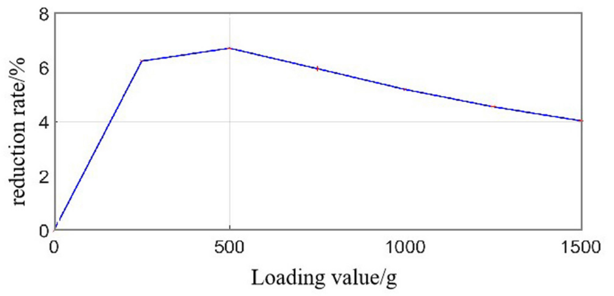

FIGURE 14 | The location error reduction rate of second-stage fusion relative to the first-stage fusion.

is attributed to the strain change in Y direction mainly caused by the bending load.

Multi-Sensor Information Fusion Based on Two-Stage Kalman Filtering

By analyzing the effects of loads and crack length on guided wave imaging and optical fiber strain in sections "Guided Wave Signal Analysis" and "Optical Fiber Signal Analysis," it is found that both guided wave and fiber monitoring methods have advantages and disadvantages. For example, guided wave imaging diagnosis based on PZTs is prone to misjudgment due to baseline signal, and the monitoring area of fiber sensor monitoring is limited, only the signal along the fiber length direction can be monitored, etc. Therefore, the fusion of these two heterogeneous signals is very significant. However, the common multi-sensor Kalman filtering fusion needs to calculate the Kalman factor of each sensor at each moment, which requires a huge amount of computation. In this paper, an improved Kalman filtering, i.e., two-stage Kalman filtering fusion was proposed to achieve damage location monitoring at the feature level and decision level. In the first stage, the characteristics of the heterogeneous signal of PZTs and optical fiber sensors at time k were fused by Kalman filtering at the feature level, and predict the damage location which is also known as the weighted least square method. Then the second stage is to fuse the predicted damage location by the Kalman filtering at the decision level.

Table 4 shows a comparison of the damage center location predicted by single-type sensors and two-stage Kalman filtering fusion under different loads. Among them, the distance between the predicted damage center and the actual damage center is regarded as location error. It can be seen that the location error of the two-stage fusion method is less than that of the single-type sensors, and the location error of the single-type PZTs monitoring is less than that of single-type optical fiber monitoring. Besides, by comparing the location errors under different loads, it is found that the location errors of single-type PZTs monitoring remain unchanged, which confirms the conclusion in **Figure 7**. However, the location errors of single-type optical fiber sensor monitoring under high load are more accurate than those under low load, which means that the larger the structure deformation is, the more favorable it is for optical fiber monitoring.

To further verify the accuracy of the proposed two-stage Kalman filtering fusion method, the reduction rate of location error was used, as shown in Formula (15). The higher the location error reduction rate means the higher the damage monitoring accuracy. **Figure 13** shows the location error reduction rate of piezoelectric-fiber information fusion compared with single-type PZTs and single-type optical fiber sensor monitoring under different loads. It can be seen that the location error reduction rate of two-stage piezoelectric-fiber fusion is 5–12% compared with that of the single-type PZTs monitoring, and 9–23% compared with that of single optical fiber sensor monitoring. This indicates that the damage monitoring accuracy by two-stage fusion is higher, and the accuracy of optical fiber monitoring is greatly improved than that of PZTs monitoring.

$$R_E = \frac{E_i - E_f}{E_i} \times 100\% \tag{15}$$

Where R_{E} is the reduction rate of the location error, R_{i} is the location error of the single-type sensors monitoring, and E_{f} is the location error by two-stage fusion.

Besides, to compare the predicted results of second-stage fusion with the first-stage fusion, **Figure 14** shows the location error reduction rate of second-stage fusion relative to the first-stage fusion. The location error reduction rate of the second-stage fusion is within 0–7%, which is the highest when the load is 500g. This indicates that the predicted location is more accurate than that of the first-stage fusion. Therefore, the two-stage Kalman filtering fusion method reduces the damage misjudgment and the damage location error effectively.

CONCLUSION

In this paper, a two-stage Kalman filtering fusion method for crack growth location monitoring of the aviation aluminum plate is proposed. The heterogeneous signals are collected by piezoelectric-fiber hybrid sensor networks composed of piezoelectric transducers (PZTs) and distributed optical fiber sensors. The first stage is to fuse the features extracted from two types of sensors at a specific time at the feature level, and then predict the damage location. In the second fusion, the predicted damage location results at multiple specific times are fused at the decision level. The proposed two-step fusion method is verified by the experiment of hole edge crack growth monitoring under the bending moment load, and the effect of load on two kinds of sensor signals is analyzed. The experimental results show that, compared with single-type PZTs and single-type optical fiber sensor monitoring, multi-source sensing information fusion based on the two-stage Kalman filtering can reduce the damage misjudgment and improve the damage monitoring accuracy. The proposed two-step fusion method is expected to fuse other heterogeneous signals, such as acoustic emission, impedance, and eddy current signals, and can be extended to the fusion of more than two types of signals. Furthermore, multi-sensor data fusion can be further combined with artificial intelligence technology.

DATA AVAILABILITY STATEMENT

The original contributions presented in the study are included in the article/supplementary material, further inquiries can be directed to the corresponding author.

AUTHOR CONTRIBUTIONS

YSW, LS, and MH designed the experiments and conducted the data analysis. LS and MH carried out the experiments. YW, LZ, and DW contributed to the planning and coordination of the project. YSW, MH, and LS wrote and edited the manuscript. All authors participated in a discussion about the results and the manuscript.

FUNDING

The present work was supported by the National Key Research and Development Program of China (2019YFC0312400 and 2017YFE0132000) and the State Key Laboratory of Structural Analysis for Industrial Equipment (S18408).

REFERENCES

Bohacova, M. (2013). Methodology of short fatigue crack detection by the eddy current method in a multi-layered metal aircraft structure. *Eng. Failure Anal.* 35, 597–608. doi: 10.1016/j.engfailanal.2013.06.009

Cui, P. Y., and Huang, X. R. (2001). Multi-sensor information fusion algorithm based on federal Kalman filter and its application. *Electr. Mach.Control* 5, 204–207.

Gravina, R., Alinia, P., Ghasemzadeh, H., and Fortino, G. (2017). Multi-sensor fusion in body sensor networks: state-of-the-art and research challenges. *Inform. Fusion.* 35, 68–80. doi: 10.1016/j.inffus.2016.09.005

Kalman, R. E. (1960). A new approach to linear filtering and prediction problems. *J. Basic. Eng.* 82, 35–45. doi: 10.1115/1.3662552

Kreger, S. T., Sang, A. K., Gifford, D. K., and Froggatt, M. E. (2009). "Distributed strain and temperature sensing in plastic optical fiber using Rayleigh scatter," in *Proceedings of SPIE - The International Society for Optical Engineering*, Orlando, FL, doi: 10.1117/12.821353

Lau, K. (2014). Structural health monitoring for smart composites using embedded FBG sensor technology. *Mater. Sci. Technol.* 30, 1642–1654. doi: 10.1179/1743284714Y.0000000608

Liang, D., and Yuan, S. F. (2015). Decision fusion system for bolted joint monitoring. *Shock Vib*. 2015, 1–11. doi: 10.1155/2015/592043

Liu, K., Ma, S., Wu, Z. J., Zheng, Y. B., Qu, X. X., Wang, Y. S., et al. (2016a). A novel probability-based diagnostic imaging with weight compensation for damage localization using guided waves. *Struct. Health Monit.* 15, 162–173. doi: 10.1177/1475921715627491

Liu, K., Wu, Z. J., Jiang, Y. Q., Wang, Y. S., Zhou, K., and Chen, Y. P. (2016b). Guided waves based diagnostic imaging of circumferential cracks in small-diameter pipe. *Ultrasonics* 65, 34–42. doi: 10.1016/j.ultras.2015.10.025

Memmolo, V., Maio, L., Boffa, N. D., Monaco, E., and Ricci, F. (2016). Damage detection tomography based on guided waves in composite structures using a distributed sensor network. *Opt. Eng.* 55:011007. doi: 10.1117/1.OE.55.1.011007

Michalcová, L., and Růžek, R. (2016). Fatigue test of an integrally stiffened panel: prediction and crack growth monitoring using acoustic emission. *Proc. Struct. Integr.* 2, 3049–3056. doi: 10.1016/j.prostr.2016.06.381

Min, J., Park, S., Yun, C. B., Lee, C. G., and Lee, C. (2012). Impedance-based structural health monitoring incorporating neural network technique for identification of damage type and severity. *Eng. Struct.* 39, 210–220. doi: 10.1016/j.engstruct.2012.01.012

Miniaci, M., Mazzotti, M., Radzienski, M., Kudela, P., Kherraz, N., Bosia, F., et al. (2019). Application of a laser-based time reversal algorithm for impact localization in a stiffened aluminum plate. *Front. Mater.* 6:30. doi: 10.3389/fmats.2019.00030

Qing, X. L., Kumar, A., Zhang, C., Gonzalez, I. F., Guo, G. P., and Chang, F. K. (2005). A hybrid piezoelectric/fiber optic diagnostic system for structural health monitoring. *Smart Mater. Struct.* 14:S98. doi: 10.1088/0964-1726/14/3/012

Qing, X. L., Li, W. Z., Wang, Y. S., and Sun, H. (2019). Piezoelectric transducer-based structural health monitoring for aircraft applications. *Sensors* 19:545. doi: 10.3390/s19030545

Qing, X. L., Wang, Y. S., and Zhao, L. (2012). Structural health monitoring technology and its application in aeronautics and astronautics. *J. Exp. Mech.* 27, 517–526.

Shan, Y. N., Xu, H., Zhou, Z. H., Yuan, Z. Y., Xu, X. S., and Wu, Z. J. (2019). State sensing of composite structures with complex curved surface based on distributed optical fiber sensor. *J. Intell. Mater. Syst. Struct.* 30, 1951–1968. doi: 10.1177/1045389X19849287

Su, Z. Q., Wang, X. M., Cheng, L., Yu, L., and Chen, Z. P. (2009). On selection of data fusion schemes for structural damage evaluation. *Struct. Health. Monit.* 8, 223–241. doi: 10.1177/1475921708102140

Sun, L., Wang, Y. S., Miao, B. R., Wu, D., Sun, H., and Qing, X. L. (2018). "Research on structural health monitoring method based on multi-source sensing information fusion," in *Proceedings of the 7th Asia-Pacific Workshop on Structural Health Monitoring, APWSHM 2018*, Hongkong, 670–681.

Tang, D., Chen, J., Wu, W. H., Jin, L. Y., Yue, Q. J., Xie, B., et al. (2020). Research on sampling rate selection of sensors in offshore platform shm based on vibration. *Appl. Ocean. Res.* 101, 102–192. doi: 10.1016/j.apor.2020.102192

Villegas, I. F. (2019). Ultrasonic welding of thermoplastic composites. *Front. Mater.* 6:291. doi: 10.3389/fmats.2019.00291

Wang, Y. S., Gao, T., Liu, D. B., Sun, H., Miao, B. G., and Qing, X. L. (2019). Propagation characteristics of ultrasonic weld-guided waves in friction stir welding joint of same material. *Ultrasonics* 102:106058. doi: 10.1016/j.ultras.2019.106058

Woods, J., and Radewan, C. (1977). Kalman filtering in two dimensions. *IEEE Trans. Inf. Theory.* 23, 473–482. doi: 10.1109/tit.1977.1055750

Wu, J., Su, Y., Zhu, Y., and Deng, C. (2017). Real-time remaining useful life prediction of cutting tool based on information fusion. *J. Huazhong Univ. Sci. Technol.* 45, 1–5. doi: 10.13245/j.hust.170401

Wu, Z. J., Liu, K. H., Wang, Y. S., and Zheng, Y. B. (2015). Validation and evaluation of damage identification using probability-based diagnostic imaging on a stiffened composite panel. *J. Intell. Mater. Syst. Struct.* 26, 2181–2195. doi: 10.1177/1045389X14549873

Wu, Z. J., Qing, X. L., and Chang, F. K. (2009). Damage detection for composite laminate plates with a distributed hybrid PZT/FBG sensor network. *J. Intell. Mater. Syst. Struct.* 20, 1069–1077. doi: 10.1177/1045389X08101632

Zhang, Z. F., He, M. Y., Liu, A. R., Singh, H. K., Ramakrishnan, K. R., Hui, D., et al. (2018). Vibration-based assessment of delaminations in FRP composite plates. *Composites Part B* 144, 254–266. doi: 10.1016/j.compositesb.2018.03.003

Conflict of Interest: The authors declare that the research was conducted in the absence of any commercial or financial relationships that could be construed as a potential conflict of interest.

frontiers in Materials

ORIGINAL RESEARCH
published: 25 September 2020
doi: 10.3389/fmats.2020.00301

Internal Damage Identification of Sandwich Panels With Truss Core Through Dynamic Properties and Deep Learning

Lingling Lu[1], *Yabo Wang*[1], *Jianquan Bi*[2], *Cheng Liu*[3], *Hongwei Song*[1]* *and Chenguang Huang*[4]

[1] *Key Laboratory for Mechanics in Fluid Solid Coupling Systems, Institute of Mechanics, Chinese Academy of Sciences, Beijing, China,* [2] *Department of Information Engineering, Army Academy of Armored Forces, Beijing, China,* [3] *Department of Aeronautics and Astronautics, Stanford University, Stanford, CA, United States,* [4] *Hefei Institutes of Physical Science, Chinese Academy of Sciences, Hefei, China*

For sandwich panels with truss core, the weakest part is the low-density core; therefore, some effective damage identification methods have been previously proposed for sandwich panels. However, these studies have mainly focused on damage location identification and only a few studies have discussed detection of the extent of the damage. In this study, a damage identification method integrating a deep learning technique with dynamic properties is proposed to identify both the location and extent of internal damage in sandwich panels with truss core. An analytical model verified by experiments based on a laser vibrometer is used to obtain raw data, which can generate various levels of damage inside the two face sheets. Instead of using surface photographs or raw data as the deep learning training dataset, the dataset is constructed using damage indices. By combining this with an analytical model, a dataset of specimens with various defects was collected and used as the input for the neural networks. The ability to identify the locations of damage and the extent of damage was used to evaluate the effectiveness of the proposed technique. The results show that the proposed method could be used to identify the location and extent of internal damage accurately.

Keywords: sandwich panel with truss core, damage identification, deep learning, vibration-based damage index, feature extraction

Edited by:
Jun Wu,
Huazhong University of Science and Technology, China

Reviewed by:
Xi Wang,
Beijing Jiaotong University, China
Dongyue Gao,
Sun Yat-sen University, China

Correspondence:
Hongwei Song
songhw@imech.ac.cn

Specialty section:
This article was submitted to Structural Materials, a section of the journal Frontiers in Materials

Received: *21 July 2020*
Accepted: *11 August 2020*
Published: *25 September 2020*

Citation:
Lu L, Wang Y, Bi J, Liu C, Song H and Huang C (2020) Internal Damage Identification of Sandwich Panels With Truss Core Through Dynamic Properties and Deep Learning. Front. Mater. 7:301. doi: 10.3389/fmats.2020.00301

INTRODUCTION

Structural safety and integrity cannot be overemphasized because a catastrophic structural failure may result in a significant loss of human life and wealth. Also, a more complicated service environment may bring about additional problems (Lai, 2019; Lai et al., 2019a,b). Sandwich structures with truss core (SPTCs) have been increasingly applied in industrial sectors, such as in ships, aircraft, civil engineering, and aerospace engineering (Hg, 1969; Chiras et al., 2002; Wadley et al., 2003). The lightweight cellular core can be in the form of a stochastic foam, a periodic honeycomb, a corrugated sheet, or a lattice truss (He et al., 2014; Liu et al., 2014). During the manufacturing process or during service, damage or defects are inevitable, such as buckling of the panel (Yuan et al., 2014, 2015), breakage of the truss, burn-through of the face sheets, or truss nodes that are not bound to the face sheet. Different damage features (style, extent, and location) have different influences on the structural vibration properties (Lou et al., 2014). Compared with traditional structure styles, such as beams or plates, internal damage identification of SPTCs is more difficult:

1) Internal damage, such as unbound nodes, is shielded by the face sheets, which hinders direct visible inspection, so a vibration-based identification method may be an important choice.
2) There is a wealth of damage features that vary in damage type, location, extent, and their combinations; these can, in turn, affect the structural vibration behavior.
3) Damage identification can be classified into inversion problems, and the solutions may be non-unique.
4) The final process of damage identification relies on human judgment, which is time-consuming and subjective.

In the literature, some methods have been proposed for the detection and localization of damage in sandwich structures. For surface cracks in composite laminates, Hu et al. (2006) proposed a strain-energy method to identify the surface crack location. The results revealed that the method could identify the location of the damage successfully. For honeycomb sandwich plates, Andrzej (2014) proposed a vibration-based non-destructive testing method with a post-processing algorithm based on wavelet analysis. The results revealed that different types of damage could be detected and localized accurately. For composite SPTCs, Li et al. (2015) proposed a baseline-free damage localization method based on uniform load surface curvature, a gapped smoothing method, and the Teager energy operator to detect truss bar damage. Lu et al. (2017a) proposed a damage identification method based on a flexural matrix of metallic SPTCs. Subsequently, an improved method was also developed to identify damage to unbounded nodes (Lu et al., 2017b). Seguel and Meruane (2018) proposed four damage indices, including mode shape curvatures, uniform load surface, modal strain energy, and gapped smoothing, to evaluate the debonding damage of an aluminum honeycomb sandwich panel. Sikdar et al. (2018) proposed an acoustic emission-based real-time health monitoring framework to efficiently identify the probable damage in sandwich composite structures. Zhu et al. (2016) proposed a torsional guided wave method to detect debonding damage in honeycomb sandwich beams. Klepka et al. (2013) used non-linear acoustics to detect impact damage in a composite chiral sandwich panel. High-frequency ultrasonic excitation and low-frequency model excitation were used to observe non-linear modulations in ultrasonic waves due to structural damage.

Most of these studies could detect and locate the damage accurately, but fewer studies have discussed quantification of the extent of damage (Kumar et al., 2009; Zhu et al., 2014; Khan et al., 2019). To detect the extent of damage more accurately, some intelligent techniques, such as a genetic algorithm (GA) or convolutional neural networks (CNNs), have been combined with traditional vibration-based methods or other methods (Zhu et al., 2014; Khan et al., 2019). In these studies, damage at different locations and of different extents are considered. Kumar et al. (2009) presented a model strain-energy two-step method for a composite sandwich beam. This method can identify both the location and extent of damage in the faces and the core. Using the frequency response function (FRF), Zhu et al. (2014) proposed a non-destructive evaluation method to identify debonding in a honeycomb sandwich beam. By combining this with a GA, the method could determine both damage location and size. When detecting damage in large structures, the method cannot effectively identify small debonding, which has little influence on the low-frequency range of an FRF. Khan et al. (2019) proposed a CNN-based approach for the classification and prediction of various types of in-plane and through-the-thickness delamination in smart composite laminates by using structural vibration information.

With the capacity of massive data processing, data mining, and fast training through the deep architecture of neural networks, machine learning gives an objective solution with quantitative accuracy. Chen and Jahanshahi (2018) proposed a deep learning (DL) framework to analyze individual video frames for crack detection. The proposed framework achieves a 98.3% hit rate. Cha et al. (2017) proposed a vision-based method by using the deep architecture of a CNN for detecting cracks in concrete. The trained CNN was combined with a sliding window technique to scan any image size. The results indicate that the proposed method performs well in finding cracks in concrete in realistic situations. Zhang et al. (2016) used deep CNN to detect cracks in roads. The training images were obtained by means of a low-cost smart mobile phone, demonstrating that DL has the potential to be applied in practical damage identification. Pathirage et al. (2018) proposed an autoencoder-based framework for damage identification, which could support deep neural networks and which could be used to obtain optimal solutions for pattern recognition problems of a highly non-linear nature. The method was applied on steel-frame structures. Guo et al. (2020) presented a DL-based method that extracts the damage features from mode shapes without utilizing any hand-engineered feature or prior knowledge. Datasets based on numerical simulations, along with two datasets based on laboratory measurements, were used. Zhang et al. (2020) used machine vision and DL for structural health monitoring by focusing on detecting bolt loosening. A dataset that contains 300 images was used. Huang et al. (2020) proposed a CNN-based method for detection of surface damage to a steel wire rope (SWR). In this work, only two different types of SWR surface defects were investigated. In this study, the authors mentioned that it is necessary to combine the method with other imaging techniques to detect SWR inner damage. Liu et al. (2020) reported that a novel damage identification framework was established in this study by integrating massive datasets constructed by structural transmissibility functions and a DL strategy based on one-dimensional convolutional neural networks (1D-CNNs). Avci et al. (2017) used 1D-CNNs to automatically extract damage-sensitive features from the raw acceleration signals and presented the preliminary experiments that were conducted to verify the proposed method.

Previous studies often dealt with damage to the structural surface that could be captured by a camera or that used the structural raw displacement or acceleration data captured in experiments directly as the input data. However, for SPTCs, the weakest part is the low-density truss core, and the inside damage is covered by the face sheets and cannot be directly detected in photographs. Also, compared with plates or beams, SPTCs consist of two face sheets and a truss core, meaning that the raw response data hardly reflect the structural damage information. Therefore, vibration-based methods, which involve many forms of damage indices that could reflect both the surface and internal damage, could be used in combination with DL for structural damage identification in SPTCs.

This work incorporates a DL technique with a vibration-based method to detect internal damage to SPTCs. Unlike previous studies, which used surface photographs or raw data as the DL training dataset, we construct a dataset by using damage indices instead of raw data. An analytical model is then used to obtain massive raw structural data, which are verified by experiments. Then two damage indices, one with a baseline and the other without a baseline, are used to construct the input to the neural networks. The effectiveness of the method is evaluated according to the accuracy of damage location and extent identification.

CONSTRUCTION OF THE DATASET

Outline of the Construction Process

Obtaining more data is always the best way to make a neural network model generalize better, although the amount of data is usually limited in practice. In this study, a vibration analytical model with random damage features, described previously by the authors (Lu et al., 2017c), was used to generate the raw data. Experiments were carried out to verify the proposed model. Two damage indices were applied to extract the internal damage features. Finally, the input dataset, including massive and diverse samples, was built.

SPTC Specimens

A sketch of the pyramidal SPTC model being simulated is provided in **Figure 1**. The SPTC is made of stainless steel. The boundary condition for the SPTC is fully clamped (CCCC). The unit cell of the pyramidal truss is shown in **Figure 1B**. The thickness of the face sheets is 1 mm. Parameter L_x is equal to L_y, which is 11.312 mm. There are 15 cells along the x- and y-directions, respectively. The details of the model are given in **Table 1**.

In the damage identification process, three types of damage features are considered, including damage location, damage style, and damage extent, denoted as D_L, D_S, and D_E, respectively. In this study, D_S, that is, cell missing damage, is used to simulate structural damage, which is a typical form of damage for SPTCs. Four D_E values are considered, including half-cell missing (HCM), one cell missing (OCM), two cells missing (TCM), and four cells missing (FCM). To consider all possible damage distributions, the parameter D_L is set as a random number, with its position inside the sandwich panels.

Analytical Models With Random Damage Features

The training dataset is often obtained through real videos or images. However, information from videos or images is normally very limited and cannot cover all possible damage features. In addition, for SPTCs, only the surface information can be obtained by videos or images, which does not reflect the internal damage features of SPTCs. Therefore, in this study, analytical models with random damage features, verified by experiments, are used as they are able to consider all possible damage features.

TABLE 1 | Material properties and geometrical information.

Material property		Geometrical parameter	
Young's modulus	200 GPa	h_c	8 mm
Poisson's ratio	0.3	t_c	1 mm
Mass density	7,800 kg/m^3	θ	45°

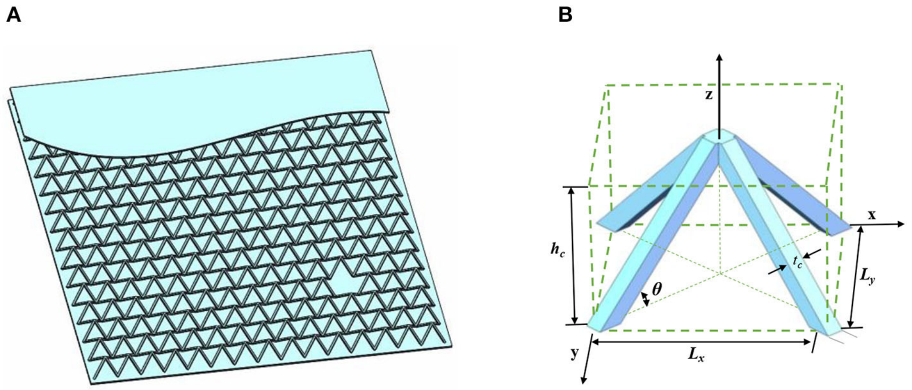

FIGURE 1 | Model information of sandwich panel with truss core (SPTC). **(A)** A damaged SPTC model. **(B)** A unit cell of a pyramidal truss.

Analytical Models

To build the rich dataset, two kinds of analytical models are presented. For single-damage cases, a step-by-step analytical model is proposed. In the model, for a given D_E and D_S, D_L moves step by step until all possible D_L values are used, as shown in **Figure 2A**. For multiple-damage cases, an analytical model with random damage features is used. In the analytical model, the parameters D_L, D_S, and D_E are set as variables. By

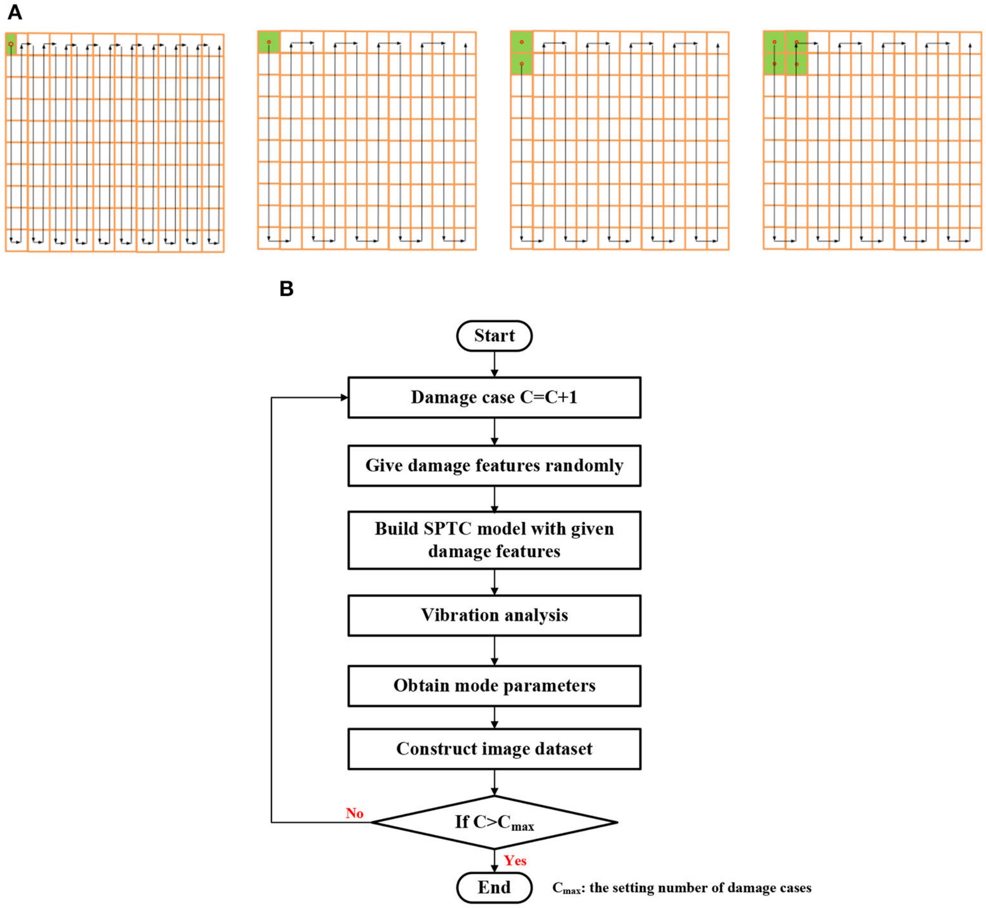

FIGURE 2 | Vibration analytical models of sandwich structure with truss core (SPTC). **(A)** Single-damage case. **(B)** Multiple-damage case.

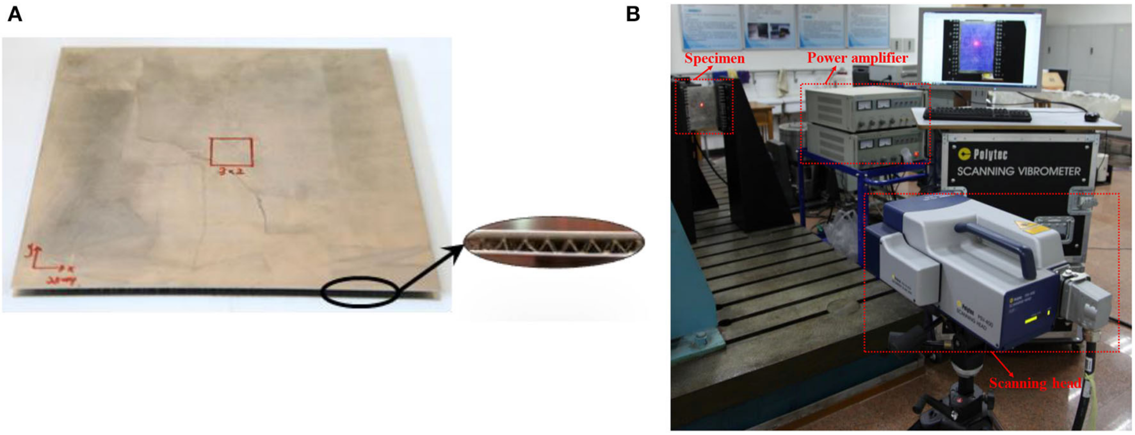

FIGURE 3 | Experimental information. **(A)** Damaged specimen (SD1). **(B)** Experimental set-up.

setting the values of D_L, D_S, and D_E, the damage features can be given randomly. D_E includes HCM, OCM, TCM, and FCM, and the corresponding parameter D_E is set to 1, 2, 3, and 4, respectively. D_L is the starting location of the damage, including D_{LX}, D_{LY}. The procedure used by the analytical model is shown in **Figure 2B**.

Experimental Validation

To verify the proposed analytical model, experiments were carried out in which pyramidal SPTCs (**Figure 3A**) were used. The relative density of the truss core was about 3%. The thicknesses of the face sheets and the truss core were 0.9 and 7 mm, respectively. The dimensions of the metallic SPTC specimen were 250 × 250 mm.

In the experiments, specimens with a single area of damage and multiple areas of damage were considered. For specimens with a single area of damage, three cases were used: SD1, SD2, and SD3. The corresponding D_E values were 2×3, 3×4, and 4×5, where $x\times y$ represents the D_E and x and y are the numbers of the missing cells by row and column, respectively. The defined single area of damage is in the center of the specimens. For specimens with areas of multiple damage, a specimen comprising two areas of damage at D_E 2×3 and 3×5, respectively (MD1), was used. The healthy specimen is denoted by SD0. For each damage case, repeated experiments of specimens with the same damage extent were conducted to verify the model.

The experimental set-up is shown in **Figure 3B**. The specimens were excited by a JZK-50 shaker. Two edges of the specimens were clamped. A laser Doppler vibrometer (Polytec, PSV-400) generated the excitation signal and measured the structural response. The structural modal information was obtained by analyzing the excitation and structural response signal.

Numerical models of the same dimensions as the experimental specimens were built to verify the analytical model. In contrast to the experimental specimens, in which the damage zone was prefabricated, the numerical model could simulate various cases with randomly distributed damage. The number of random damage cases $C_{\max}$ was set as 80.

To compare the numerical and experimental results, parameter η_i is defined as

$$\eta_i = \omega_i^D / \omega_i^U \tag{1}$$

where ω_i^D and ω_i^U are the i-th natural frequency of the damaged and undamaged specimens, respectively.

In the experiment, only the 1st order of mode is selected and i is set as 1. According to the results for η_1 shown in **Figure 4**, it can be seen that the trend of η_1 of simulation is in accordance with the experimental results as the D_E increases from 0 to 4×5. For a given D_E, D_L has a significant influence on the structural vibration properties. Taking SD3 for example, the largest η_1 is almost 1, and the smallest η_1 is 0.84, because the D_L is different. Therefore, in structural damage identification, various damage cases using different D_E and D_L values must be considered. When the damage case changes from SD3 to MD1, the trend of η_1 of simulation is also in accordance with experimental results. Although there are two areas of damage in the case of MD1, the effect of MD1 on the structural vibration properties is smaller than that of SD3, demonstrating that a number of areas of damage, D_L, D_E, and D_S, couple together and influence the structural vibration properties. This demonstrates that small changes in damage features may cause large variations in the structural properties. However, it is impractical to obtain massive data merely from experiments. Therefore, a simulation or numerical model is a very important way to obtain the data.

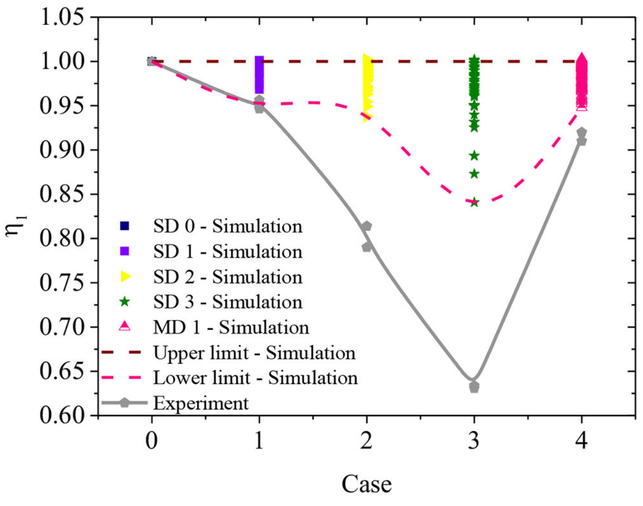

FIGURE 4 | Numerical and experimental results.

Damage Indices

Because of the difficulty in identifying internal damage in sandwich panels (as mentioned in section introduction), damage indices are used to extract damage features. Then, by combining these with a DL technique, the identification of damage features is more accurate.

Vibration-based damage indices are used to extract the internal damage features according to information gained from the face sheet. Two damage indices are used (Li et al., 2015; Le et al., 2019) and compared; these are denoted DI-1 and DI-2.

DI-1 is proposed for filled SPTCs, and needs information from a healthy structure as the baseline. When a specimen is damaged, its stiffness or mass changes. Therefore, the vibration characteristics (natural frequencies and mode shapes) change. According to the variations in the vibration characteristics, the damage features can be identified. The damage index $DIT_r(k)$ is defined as:

$$DIT_r\left(k\right) = \left|DI1_r^2\left(k\right) - DI1_r\left(k-1\right)DI1_r\left(k+1\right)\right| \tag{2}$$

where $DI\text{-}1_r$ is calculated according to the natural frequencies and mode shapes, expressed in Equation (3);

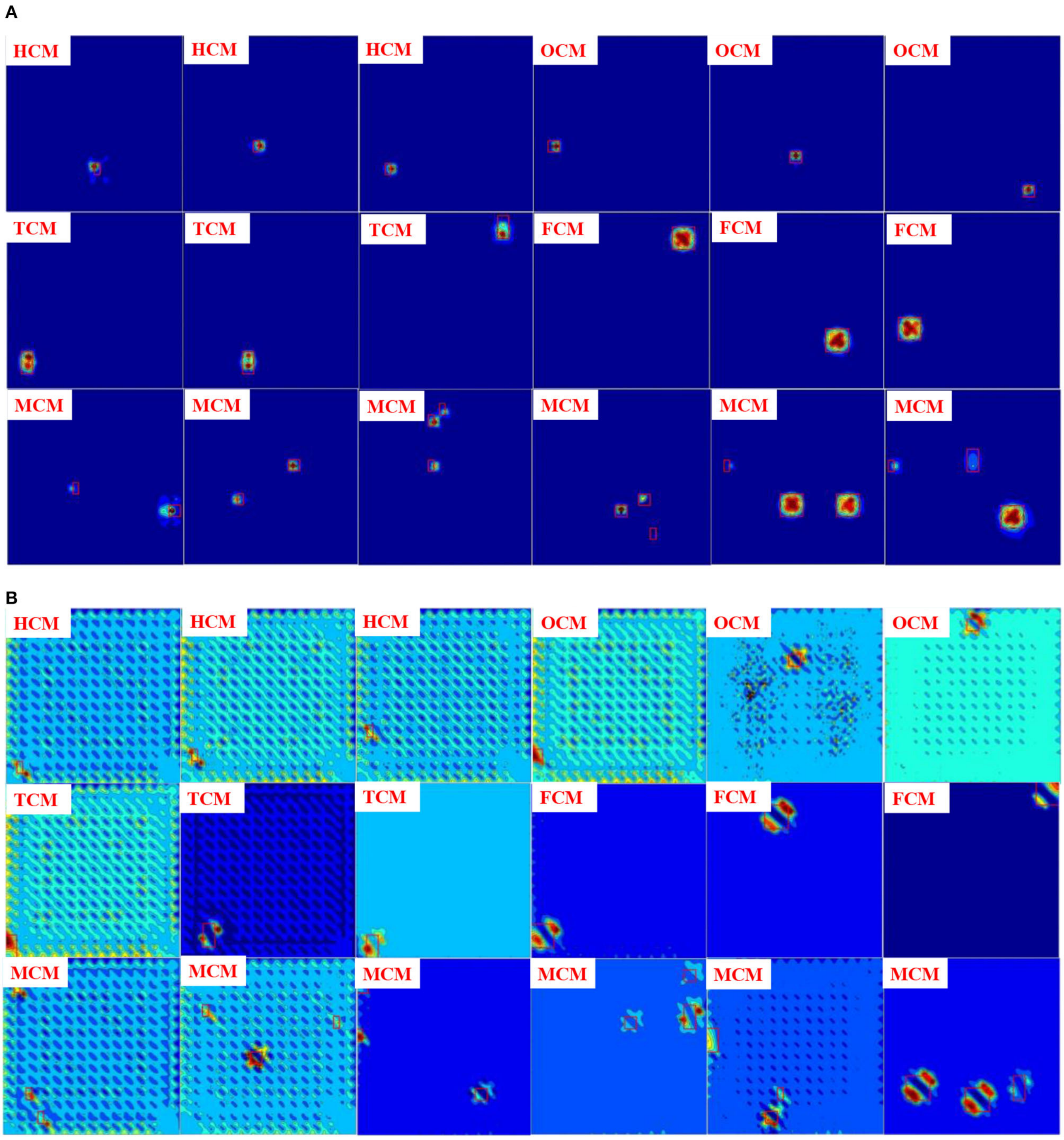

FIGURE 5 | Samples of datasets based on **(A)** DI-1 and **(B)** DI-2. HCM, half-cell missing; OCM, one cell missing; TCM, two cells missing; FCM, four cells missing.

k is the number of the selected node; and r is the weight coefficient.

$$DI1_r = \sqrt{\sum_{p=P_1}^{P_2} \frac{\omega_p^r}{\sum\limits_{p=P_1}^{P_2} \omega_p^r} \left(\left[F_p \cdot I \right]_D - \left[F_p \cdot I \right]_U \right)^2} \tag{3}$$

$$F_p = \frac{\Phi_p \Phi_p^T}{\omega_p^2} \tag{4}$$

where ω_p and Φ_p are the p-th natural frequency and mode shape, respectively; I is $\{1,\ldots,1\}T_{1\times n}$; P_1 and P_2 are the beginning and ending order modes, respectively, in the practical case; and D

and *U* denote the damaged and undamaged model, respectively. Parameter *r* is used to define the weight of low- and high-order modes in the damage index DI-1. Different damage features have different influences on different order modes: some damage has a great influence on low-order modes and some damage has a great influence on high-order modes.

However, in practice, it is hard to obtain information on a healthy status. Therefore, a baseline-free damage index DI-2 was also used in this study. A gapped smoothing method (GSM) was used to construct a baseline. If there was no damage in the structure, the mode shapes were smooth and continuous. When there was damage in the structure, the mode shapes at the damage were not smooth. We used a GSM to construct a baseline. By comparing the information before and after the GSM, the damage features could be extracted. DI-2 is expressed as:

$$DI_m^*(n) = T(DI2_m(n)) = DI2_m^2\,(n) - DI2_m\,(n+1)\,DI2_m\,(n-1) \tag{5}$$

where DI-2 is defined in Equation (6), *n* is the number of the selected node, and *m* is the weight coefficient.

$$DI2_m(x_i, y_j) = \sum_{p=P_1}^{P_2} \alpha_p^m \frac{\left(MDC_p(x_i, y_j) - MDC_p(x_i, y_j)'\right)^2}{\sum_{i=1}^{E}\sum_{j=1}^{F}\left(MDC_p(x_i, y_j) - MDC_p(x_i, y_j)'\right)^2} \tag{6}$$

$$\alpha_p^m = {}^{\omega_p^m}\Big/_{\sum_{p=K_1}^{K_2} \omega_p^m} \tag{7}$$

where *E* and *F* are the numbers of the columns and rows of the measuring points; P_1 and P_2 are the beginning and ending order modes, respectively, in the practical case; and α_p^m is defined as the weight coefficient of the *p*-th component and is expressed in Equation (7). The details of DI-2 can be found in our previous work (Le et al., 2019).

Dataset Building

Based on the proposed analytical models and the two damage indices, data in the cases of single and multiple damage are obtained. Some samples are shown in **Figure 5**. To detect damage of a different orientation and to increase the variety of the dataset, data enhancement was applied to increase the number of samples.

Comparing the first line of results for DI-1 (**Figure 5A**) and DI-2 (**Figure 5B**), it can be seen that the results for HCM or OCM identified by DI-1 are better than those identified by DI-2 because the influence of small areas of damage on the structural vibration properties is small; however, when D_E becomes significant, DI-2 also shows very good performance.

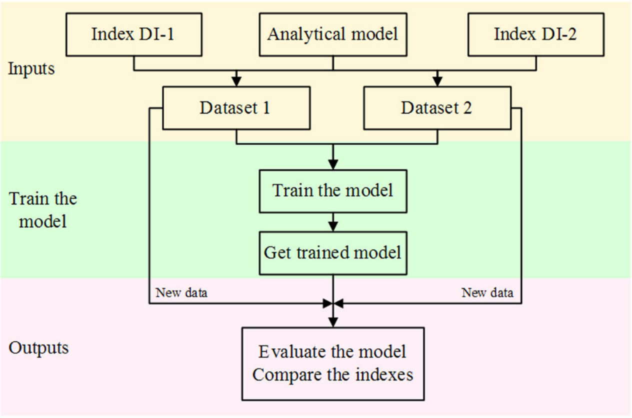

FIGURE 6 | Flowchart of the identification process.

TABLE 2 | Parameters of faster RCNN.

Parameter		Parameter	
Learning rate:	0.001	Average loss	100
Gamma	0.1	Momentum	0.9
Step size	30,000	Weight decay	0.0005
Learning rate policy	Step		

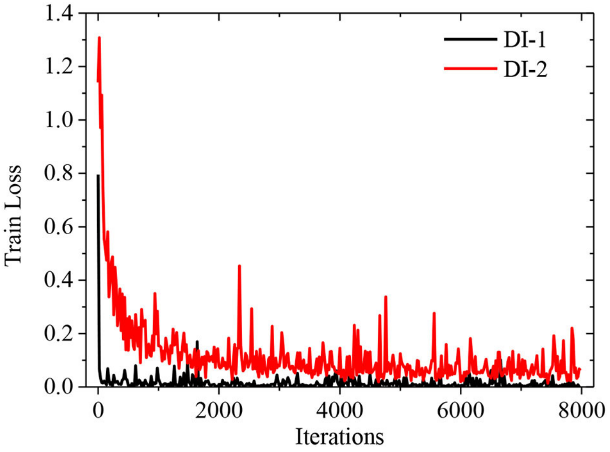

FIGURE 7 | The training loss curves of DI-1 and DI-2.

DL FRAMEWORK FOR INTERNAL DAMAGE IDENTIFICATION IN SPTCS

In this study, Faster RCNN (Ren et al., 2015), a framework for target recognition, is combined with a vibration-based method (section construction of the dataset) to identify internal damage features of SPTCs. The flowchart of the identification process is provided in **Figure 6**. The method can be summarized in four steps:

Step 1 Build dataset according to the damage indices and analytical model.
Step 2 Set the dataset as input and train the Faster RCNN model.
Step 3 Obtain the trained Faster RCNN model.
Step 4 Input the new data and evaluate the trained model.

In this study, a Zend Framework (ZF) CNN was selected. Before the training process, all images were normalized to 1,491 × 1,501 pixels. To detect damage of different orientations and increase the variety of the dataset, data enhancement was applied to increase the number of samples. Of the 2018 samples obtained, 50% were set as the training set and 50% were set as the testing set. The parameters of the Faster RCNN are shown in **Table 2**.

Caffe, a DL framework, was used to conduct the training process as it has been widely applied in DL and machine learning, such as computer vision, speech recognition, image feature coding, and information retrieval. The computing platform was Ubuntu 16.04, and all the codes were run on a server equipped with 12 Intel Core i7-6800K CPUs (3.40 GHz) and an NVIDIA GeForce GTX 1080 Ti with 11 GB of memory.

RESULTS AND DISCUSSION

As is well-known, in damage identification, the effectiveness of different damage indices for the same damage feature is different. Even for the same damage, one index could identify it and another one may not. Therefore, in this section, comparisons between DI-1 and DI-2 are conducted to investigate the capability and applications of the indices.

There are two steps in damage identification: first, detect if there is any damage in the structures and identify the D_L; second, identify the D_E and D_S. Compared with D_L, it is more difficult to identify the D_E and D_S. Most of the previous studies have focused on the identification of D_L, and few studies could identify all three damage features. In this study, only one D_S (truss core missing) is considered. Therefore, in section 4.1, the capacity of the proposed method to determine the D_L and D_E is discussed.

D_L and D_E Identification

Figure 7 shows the training loss results of DI-1 and DI-2. For DI-1, the loss value becomes stable very quickly. For DI-2, it can be seen that the loss value tends to be stable when the iteration is around 1,000 times, and the final loss value is stable at around 0.1. Because the proposed damage indices have extracted the damage feature effectively, the loss value becomes stable more quickly.

Figure 8 provides some identification results of DI-1 and DI-2. From **Figure 8**, it can be seen that the accuracy of damage feature identification is high, no matter whether the D_E is HCM, OCM, TCM, or FCM or whether the D_L is in the center of the model or on the boundary edge. From the middle and right-hand panels in **Figure 8A**, it can be seen that the features of HCM and OCM are similar; it is difficult for humans to identify the D_E accurately, but the DL-based method could identify the location and extent accurately.

To evaluate the proposed method, 100 figures were used to test the trained network, and the statistical results are provided in **Figure 9**. In **Figures 9A,B**, the x-axis is the D_E results identified by the trained network and the y-axis is the real D_E. When using the trained network to identify the damage, five cases may occur. Taking HCM as an example, the five cases are listed in **Table 3**. Cases 3–5 demonstrate that the damage location is

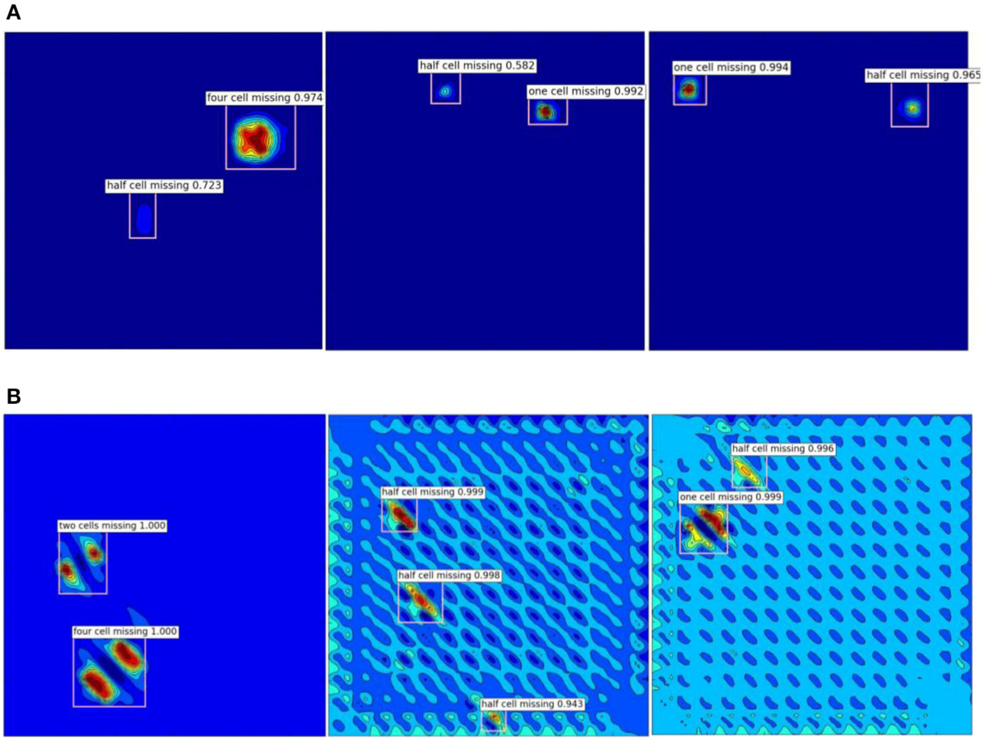

FIGURE 8 | Examples of the identified results. **(A)** DI-1 and **(B)** DI-2.

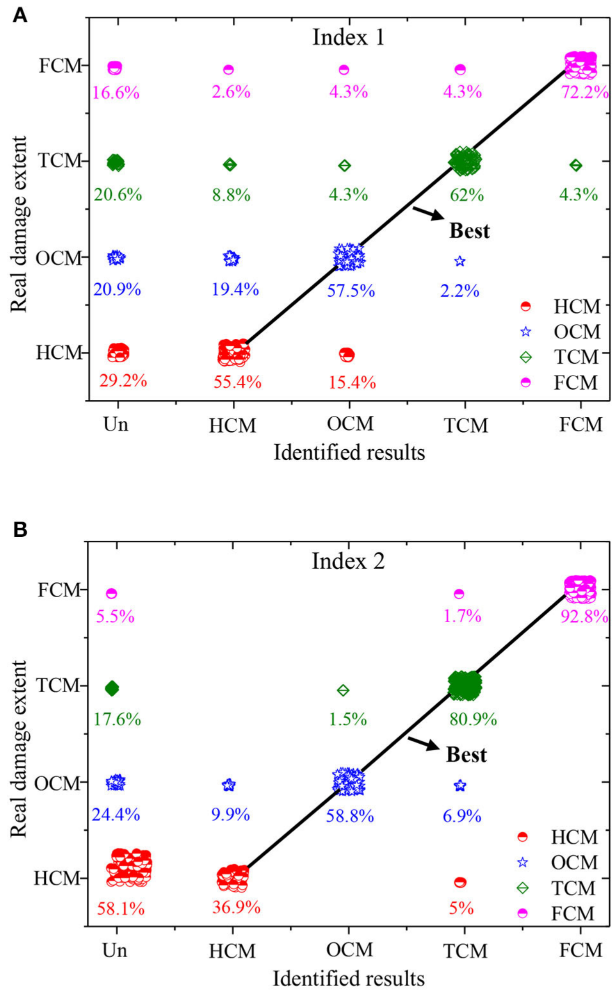

FIGURE 9 | The statistical results. **(A)** DI-1 and **(B)** DI-2. HCM, half-cell missing; OCM, one cell missing; TCM, two cells missing; FCM, four cells missing.

TABLE 3 | Five cases for HCM identification.

Case number	Detail	Status
1	HCM is not identified	×
2	HCM is identified as HCM	√
3	HCM is identified as OCM	×
4	HCM is identified as TCM	×
5	HCM is identified as FCM	×

HCM, half-cell missing; OCM, one cell missing; TCM, two cells missing; FCM, four cells missing.

TABLE 4 | Accuracy of damage location identification according to the statistical results.

Index \ Accuracy	HCM	OCM	TCM	FCM
DI1	70.8%	79.1%	79.4%	83.4%
DI2	41.9%	75.6%	82.4%	94.5%

HCM, half-cell missing; OCM, one cell missing; TCM, two cells missing; FCM, four cells missing.

TABLE 5 | Accuracy of damage extent identification according to the statistical results.

Index \ Accuracy	HCM	OCM	TCM	FCM
DI-1	55.4%	57.5%	62%	72.2%
DI-2	36.9%	58.8%	80.9%	92.8%

HCM, half-cell missing; OCM, one cell missing; TCM, two cells missing; FCM, four cells missing.

identified accurately, but the damage extent could not be detected accurately. Case 2 shows the best result, with both the location and extent identified.

The accuracies of damage location and extent identification based on DI-1 and DI-2 are listed in **Tables 4** and **5**, respectively. It can be seen that the identification accuracy increases as the D_E increases because the damaged feature identified by the indices becomes more obvious as the D_E increases.

From **Figure 10A**, it can be seen that there are three areas of damage in the SPTC, including one OCM and two HCMs. However, after identifying the network, only damage areas 1 and 2 are identified because the effects of damage area 3 on the structure vibration properties are hidden by those of damage areas 1 and 2. This demonstrates that the sensitivity of the damage index to the damage feature plays a very important role in D_L identification. This conclusion is in accordance with previous studies. From **Figure 10B**, there are three areas of damage, including FCM, TCM, and HCM. The trained network could only identify damage areas 1 and 3. The reason for damage area 2 in **Figure 10B** not being identified is that the D_E for damage area 2 is smaller than that for the other two damage areas. Damage area 3 (TCM) is identified as HCM, and the corresponding accuracy is about 0.352, meaning that the trained network could identify that there is damage at this location but the probability of identifying it as HCM is not high.

In conclusion, according to the results in **Figure 10**, it can be seen that the damage can be located if the damage can be characterized in the figure, and the damage cannot be located if the damage cannot be characterized. When there are multiple areas of damage in SPTCs, damage feature identification is more difficult. The small D_E value is easily covered by large D_E values, meaning that the small D_E values could not be identified or that the damage is mis-identified, as in cases 3, 4, or 5. Therefore, to identify the damage with small D_E values, it is better to combine more effective indices that are sensitive to the small D_E values.

Comparison of DI-1 and DI-2

In this study, a dataset based on two damage indices is used; this dataset has a significant influence on the effectiveness of the proposed method. Therefore, the effectiveness of the two damage indices is compared. Comparing **Figure 5A** with **Figure 5B**, it can be seen that the extracted feature based on DI-1 is more obvious than that based on DI-2 when D_E is small (HCM and

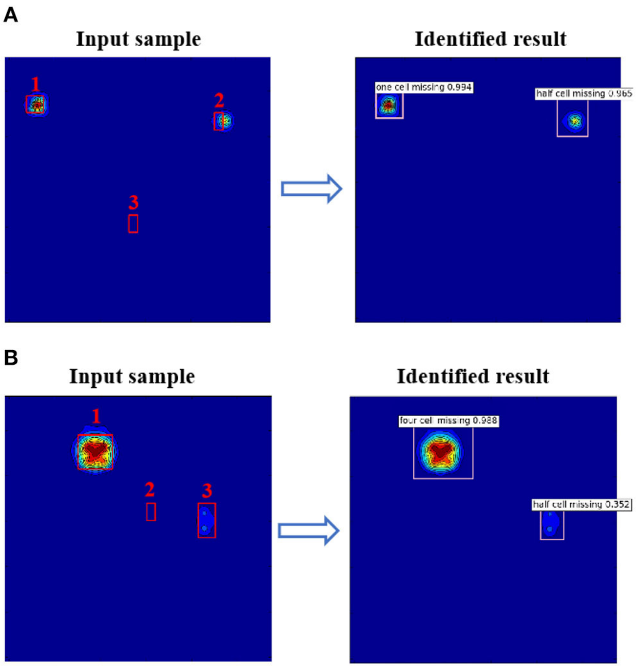

FIGURE 10 | Examples of DI-1. **(A)** Case 1 and **(B)** case 2.

OCM). When D_E is small, the identification of damage features is easily affected by other factors, such as the boundary condition or singularity caused by contact points, especially in the baseline-free damage identification process.

When the extent of the damage is small (HCM), the accuracy of damage feature identification based on DI-1 is higher than that based on DI-2, as shown in **Tables 4** and **5**. When the extent of the damage increases, the accuracy of damage feature identification based on DI-1 is smaller than that based on DI-2. From **Figure 5A**, it can be seen that the HCM feature is very obvious based on index 1. However, based on index 2, it shows that HCM tends to be covered by an influencing factor (in **Figure 5B**), such as the singularity caused by the contact nodes. Therefore, when the D_E is small, DI-1 is more effective than DI-2.

However, as the D_E increases from HCM to TCM or FCM, the accuracy based on DI-2 is better than the accuracy based on DI-1, as shown in **Tables 4** and **5**. From **Figure 5A**, when the D_E increases from HCM to TCM or FCM, the characteristics of the identified damage, such as the color gradient or area, change a little, especially for HCM, OCM, or FCM. When the trained network identifies the D_E, it is easy for the framework to identify one D_E as another D_E. But, for DI-2, it can be seen that the characteristics of the identified damage change a lot as the D_E increases from HCM to FCM. As the D_E increases, DI-2 performs better than DI-1.

According to the accuracy results in **Table 5**, it can be seen that DI-2 performs better than DI-1. Therefore, for identification of internal damage in sandwich panels, the proposed method based on DI-2 is better and more effective, as it is more successful in extracting internal damage features.

CONCLUSIONS

This paper proposed a method for identifying internal damage to sandwich panels by integrating a DL technique with a vibration-based method for internal damage in sandwich panels with a truss core. Instead of using the photographs or raw structural responses, two damage indices were used to extract the damage features and construct the dataset. According to the statistical results, the proposed method can identify the internal damage features D_L and D_E. As the D_E increases, the accuracy of identification increases. The statistical results also reveal that damage indices play a very important role in the identification process. Considering massive damage features, it is better to combine the two indices to improve their accuracy. When D_E is small, DI-1 is better than DI-2. When D_E is large, DI-2 is better than DI-1. According to the characteristics of the damage identified by the indices, we can choose suitable indices to identify as many damage features as possible.

DATA AVAILABILITY STATEMENT

The raw data supporting the conclusions of this article will be made available by the authors, without undue reservation.

AUTHOR CONTRIBUTIONS

LL: methodology, writing—original draft preparation, and funding acquisition. YW, JB, and LL: software. YW and CL: validation. LL and CL: formal analysis. LL and HS: writing—review and editing. CH: project administration. All authors contributed to the article and approved the submitted version.

FUNDING

This research was supported by the National Natural Science Foundation of China (grant nos. 11472276, 11972033, and 11332011) and the Strategic Priority Research Program of the Chinese Academy of Sciences (grant no. XDA22000000).

REFERENCES

Andrzej, K. (2014). Vibration-based spatial damage identification in honeycomb-core sandwich composite structures using wavelet analysis. *Compos. Struct.* 118, 385–391. doi: 10.1016/j.compstruct.2014.08.010

Avci, O., Abdeljaber, O., Kiranyaz, S., and Inman, D. (2017). "Structural damage detection in real-time: implementation of 1D convolutional neural networks for SHM applications," in *Structural Health Monitoring and Damage Detection, Volume 7: Proceedings of the 35th IMAC, A Conference and Exposition on Structural Dynamics.* (Garden Grove, CA), 2191–5644. doi: 10.1007/978-3-319-54109-9_6

Cha, Y. J., Choi, W., and Buyukozturk, O. (2017). Deep Learing-based crack damage detection using convolutional neural networks. *Comput-aided Civ. Inf.* 32, 361–378. doi: 10.1111/mice.12263

Chen, F. C., and Jahanshahi, M. R. (2018). NB-CNN: deep learning based crack detection using convolutional neural network and naïve bayes data fusion. *IEEE Trans. Indus. Electr.* 65, 4392–4400. doi: 10.1109/TIE.2017.2764844

Chiras, S., Mumm, D. R., Evans, A. G., Wicks, N., Hutchinson, J. W., Dharmasena, K., et al. (2002). The structural performance of near-optimized truss core panels. *Int. J. Solids Struct.* 39, 4093–4115. doi: 10.1016/S0020-7683(02)00241-X

Guo, T., Wu, L. P., Wang, C. J., and Xu, Z. L. (2020). Damage detection in a novel deep-learning framework: a robust method for feature extraction. *Struct. Health Monit.* 19, 424–442. doi: 10.1177/1475921719846051

He, Y. Z., Tian, G. Y., Pan, M. C., and Chen, D. X. (2014). Non-destructive test of low-energy impact in CFRP laminates and interior defects in honeycomb sandwich using scanning pulsed eddy current. *Compos B-Eng.* 59, 196–203. doi: 10.1016/j.compositesb.2013.12.005

Hg, A. (1969). *Analysis and Design of Structural Sandwich Panels*. Oxford: Pergamon Press.

Hu, H. W., Wang, B. T., Lee, C. H., and Su, J. S. (2006). Damage detection of surface cracks in composite laminates using modal analysis and strain energy method. *Compos. Struct.* 74, 399–405. doi: 10.1016/j.compstruct.2005.04.020

Huang, X. Y., Liu, Z. L., Zhang, X. Y., Kang, J. L., Zhang, M., and Guo, Y. L. (2020). Surface damage detection for steel wire ropes using deep learning and computer vision techniques. *Measurement* 161:107843. doi: 10.1016/j.measurement.2020.107843

Khan, A., Ko, D. K., Lim, S. C., and Kim, H. S. (2019). Structural vibration-based classification and prediction of delamination in smart composite laminates using deep learning neural network. *Compos. B-Eng.* 161, 586–594. doi: 10.1016/j.compositesb.2018.12.118

Klepka, A., Staszewski, W. J., Maio, D. D., and Scarpa, F. (2013). Impact damage detection in composite chiral sandwich panels using nonlinear vibro-acoustic modulations. *Smart Mater. Struct.* 22, 1–11. doi: 10.1088/0964-1726/22/8/084011

Kumar, M., Shenoi, R. A., and Cox, S. J. (2009). Experimental validation of modal strain energies based damage identification method for a composite sandwich beam. *Compos. Sci. Technol.* 69, 1635–1643. doi: 10.1016/j.compscitech.2009.03.019

Lai, J. (2019). Analysis on streamwise fluidelastic instability of rotated triangular tube arrays subjected to two-phase flow. *Mech. Syst. Signal Pr.* 123, 192–205. doi: 10.1016/j.ymssp.2019.01.010

Lai, J., Sun, L., and Li, P. Z. (2019b). Two-phase flow-induced instability and nonlinear dynamics of a single tube in tube bundles in the transverse direction. *Eur. J. Mech. A-Solid.* 78:10. doi: 10.1016/j.euromechsol.2019.103858

Lai, J., Sun, L., Li, P. Z., Tan, T. C., Gao, L. X., Xi, Z. D., et al. (2019a). Eigenvalue analysis on fluidelastic instability of a rotated triangular tube array considering the effects of two-phase flow. *J. Sound Vib.* 439, 194–207. doi: 10.1016/j.jsv.2018.09.060

Le, J., Lu, L. L., Wang, Y. B., Song, H. W., Xing, X. D., and Huang, C. G. (2019). Damage identification of low-density material-filled sandwich panels with truss core based on vibration properties. *Struct. Health Monit.* 18, 1711–1721. doi: 10.1177/1475921718820100

Li, B., Li, Z., Zhou, J., Ye, L., and Li, E. (2015). Damage localization in composite lattice truss core sandwich structures based on vibration characteristics. *Compos. Struct.* 126, 34–51. doi: 10.1016/j.compstruct.2015.02.046

Liu, J. Y., Zhu, X., Zhou, Z. G., Wu, L. Z., and Ma, L. (2014). Effects of thermal exposure on mechanical behavior of carbon fiber composite pyramidal truss core sandwich panel. *Compos. B-Eng.* 60, 82–90. doi: 10.1016/j.compositesb.2013.12.059

Liu, T. W., Xu, H., Ragulskis, M., Cao, M. S., and Ostachowicz, W. (2020). A data-driven damage identification framework based on transmissibility function datasets and one-dimensional convolutional neural networks: verification on a structural health monitoring benchmark structure. *Sensors* 20, 1–25. doi: 10.3390/s20041059

Lou, J., Wu, L. Z., Ma, L., Xiong, J., and Wang, B. (2014). Effects of local damage on vibration characteristics of composite pyramidal truss core sandwich structure. *Compos, B.* 62, 73–87. doi: 10.1016/j.compositesb.2014.02.012

Lu, L. L., Song, H. W., and Huang, C. G. (2017b). Experimental investigation of unbound nodes identification for metallic sandwich panels with truss core. *Compos. Struct.* 163, 248–256. doi: 10.1016/j.compstruct.2016.12.028

Lu, L. L., Song, H. W., and Huang, C. G. (2017c). Effects of random damages on dynamic behavior of metallic sandwich panel with truss core. *Compos. B-Eng.* 116, 278–290. doi: 10.1016/j.compositesb.2016.10.051

Lu, L. L., Song, H. W., Yuan, W., and Huang, C. G. (2017a). Baseline-free damage identification of metallic sandwich panels with truss core based on vibration characteristics. *Struct. Health Monit.* 16, 24–38. doi: 10.1177/1475921716660055

Pathirage, C. S. N., Li, J., Li, L., Hao, H., Liu, W. Q., and Ni, P. H. (2018). Structural damage identification based on autoencoder neural networks and deep learning. *Eng. Struct.* 172, 13–28. doi: 10.1016/j.engstruct.2018.05.109

Ren, S., He, K., Girshick, R., and Sun, J. (2015). Faster R-CNN: towards real time object detection with region proposal networks. *IEEE Trans. Pattern Anal. Machine Intelligence* 39, 1137–1149. doi: 10.1109/TPAMI.2016.2577031

Seguel, F., and Meruane, V. (2018). Damage assessment in a sandwich panel based on full-field vibration measurements. *J. Sound Vib.* 417, 1–18. doi: 10.1016/j.jsv.2017.11.048

Sikdar, S., Ostachowicz, W., and Pal, J. (2018). Damage-induced acoustic emission source identification in an advanced sandwich composite structure. *Compos. Struct.* 202, 860–866. doi: 10.1016/j.compstruct.2018.04.051

Wadley, H. N. G., Fleck, N. A., and Evans, A. G. (2003). Fabrication and structural performance of periodic cellular metal sandwich structures. *Compos. Sci. Technol.* 63, 2331–2343. doi: 10.1016/S0266-3538(03)00266-5

Yuan, W., Song, H. W., Wang, X., and Huang, C. G. (2015). Experimental investigation on thermal buckling behavior of fully-clamped truss-core sandwich panels. *AIAA J.* 53, 948–957. doi: 10.2514/1.J053246

Yuan, W., Wang, X., Song, H. W., and Huang, C. G. (2014). A theoretical analysis on the thermal buckling behavior of fully-clamped sandwich panels with truss cores. *J. Thermal Stresses* 37, 1433–1448. doi: 10.1080/01495739.2014.937263

Zhang, L., Yang, F., Zhang, Y. D., and Zhu, Y. J. (2016). "Road crack detection using deep convolutional neural network," in *IEEE International Conference on Image Processing*. (Phoenix, AZ), 3708–3712. doi: 10.1109/ICIP.2016.7533052

Zhang, Y., Sun, X. W., Loh, K. J., Su, W. S., Xue, Z. G., and Zhao, X. F. (2020). Autonomous bolt loosening detection using deep learning. *Struct. Health Monit.* 19, 105–122. doi: 10.1177/1475921719837509

Zhu, K. G., Chen, M. J., Lu, Q. H., Wang, B., and Fang, D. N. (2014). Debonding detection of honeycomb sandwich structures using frequency response functions. *J. Sound Vib.* 333, 5299–5311. doi: 10.1016/j.jsv.2014.05.023

Zhu, K. G., Qing, X. L. P., and Liu, P. (2016). Torional guided wave-based debonding detection in honeycomb sandwich beams. *Smart Mater. Struct.* 25, 1–11. doi: 10.1088/0964-1726/25/11/115048

Conflict of Interest: The authors declare that the research was conducted in the absence of any commercial or financial relationships that could be construed as a potential conflict of interest.

frontiers
in Materials

ORIGINAL RESEARCH
published: 28 September 2020
doi: 10.3389/fmats.2020.587580

Comparative Study on Mechanical Behavior of Bamboo-Concrete Connections and Wood-Concrete Connections

Zhiyuan Wang[1,2], Yang Wei[1], Junfeng Jiang[1], Kang Zhao[1] and Kaiqi Zheng[1]*

[1] College of Civil Engineering, Nanjing Forestry University, Nanjing, China, [2] School of Management Science and Engineering, Anhui University of Finance and Economics, Bengbu, China

To investigate the similarities and differences of mechanical behavior between the bamboo-concrete connections and the wood-concrete connections, thirty-six specimens were tested through push-out tests with the material type (bamboo or wood), concrete strength and dowel diameter as test parameters. In addition to the linear variable displacement transducer the digital image correlation was also used to obtain the slip distribution of the whole field of the specimens, which was conducive to the further detailed analysis of the slip distribution and a comprehensive understanding of the load-slip relationship. The results showed that the failure modes of the bamboo-concrete connections were similar to that of the wood-concrete connections, such as the concrete failure near the joint and the dowels bending in different degrees. The load-slip curves of the two kinds of connections were similar, which could be summarized as the elastic section, strengthening section and descending section. The shear stiffness and capacity of bamboo-concrete connections were higher than that of wood-concrete connections, and the shear capacity increased with the increase of dowel diameter and concrete strength. The slip distribution of the left and right sides of the specimen was basically identical. The load-transfer performance of the dowel was excellent. Finally, the prediction method of shear capacity and load-slip curve model of composite connections were proposed and verified to be effective.

Keywords: bamboo-concrete shear connections, wood-concrete shear connections, dowel-type connector, mechanical behavior, comparative study

Edited by:
Jun Wu,
Huazhong University of Science and Technology, China

Reviewed by:
Peng Lin,
Tsinghua University, China
Zhiyong Liu,
Southeast University, China

***Correspondence:**
Yang Wei
wy78@njfu.edu.cn

Specialty section:
This article was submitted to Structural Materials, a section of the journal Frontiers in Materials

Received: *26 July 2020*
Accepted: *31 August 2020*
Published: *28 September 2020*

Citation:
Wang Z, Wei Y, Jiang J, Zhao K and Zheng K (2020) Comparative Study on Mechanical Behavior of Bamboo-Concrete Connections and Wood-Concrete Connections. Front. Mater. 7:587580. doi: 10.3389/fmats.2020.587580

INTRODUCTION

The bamboo/wood-concrete composite system usually consist of a bamboo/wood part in the tensile zone, a concrete layer in the compressive zone, and a connection between bamboo/wood and concrete. Thus, the mechanical properties of each material are used in efficient ways. Bamboo/wood-concrete composite system are used in bridges and buildings (Dias et al., 2016; Sebastian et al., 2016; Shan et al., 2017). Because of the low density and renewability of bamboo/wood, bamboo/wood-concrete composite system show several advantages over reinforced concrete structures, including better efficiency in terms of strength to self-weight ratio, and better seismic and environmental friendly performance (Shan et al., 2020).

At present, many countries are short of wood resources. The wood supply in many areas is insufficient, so it is necessary to find a renewable material with excellent mechanical properties to replace wood. It is feasible to develop engineered bamboo to realize more effective utilization of bamboo (Li et al., 2019), especially in the countries where bamboo resources are abundant (Tian et al., 2019). Among them, bamboo scrimber is the most widely used engineering bamboo at present. The material performance and preparation technology of bamboo scrimber had been investigated by many researchers. Yu et al. (2017) investigated the manufacturing process and basic properties of bamboo scrimber. Wei et al. (2016, 2018, 2020a, 2020c), Chen et al. (2020c) performed tests on the mechanical properties of bamboo scrimber, including axial tension, axial compression, eccentric compression and bending. Shangguan et al. (2015), Zhong et al. (2017) studied the compressive properties and bending properties of bamboo scrimber. Xu et al. (2017), Cui et al. (2018) tested the tensile properties at elevated temperatures and thermal performance of bamboo scrimber. It could be found from the current research results that the bamboo scrimber could meet the requirements of structural materials.

However, the serviceability limit of flexural members is determined by deformation rather than strength in most cases. The bamboo flexural members have the defects of insufficient bearing capacity, low section stiffness, and insufficient spanning capacity (Chen et al., 2020a; Chen et al., 2020b; Wei et al., 2020b), which is similar to the wood flexural members. To enhance the flexural performance, the wood-concrete composite structure was proposed. For this structure, the performance of shear connections plays an important role in the composite effect of composite structure. Auclair et al. (2016) found the ductility and the performance of the wood-concrete beams could be improved by changing the concrete shell diameter and steel core diameter of connectors. Martins et al. (2016) developed a wood-concrete composite component for the floor. Three connection systems were tested. In the push-out test, the connection with dowel connectors was the best. Sebastian et al. (2016) tested the wood–concrete composite beams with different screw thread connectors. The beams with fully threaded screw connectors presented an excellent ductility, and the beams with partially threaded screw connections exhibited a good bearing capacity. Jiang et al. (2017) studied the early behavior of shear connections with screw. The results showed that the strength and stiffness of screw connections increase rapidly in the first seven days. Khorsandnia et al. (2018) studied the numerical models for the analysis of the wood-concrete composite beams with panelised reinforced concrete slabs.

Based on the reference of wood-concrete composite structure, bamboo-concrete composite (BCC) structure was proposed. Due to the obvious differences between bamboo and wood in fiber structure, manufacturing technology and mechanical properties, etc., it was not appropriate to apply the research results of wood-concrete composite structure indiscriminately to bamboo-concrete composite structure. Wei et al. (2017b, 2017c), Wang et al. (2020) had carried out the four-point bending tests and push-out test on two types of BCC structures with different connections. The results indicated that two connections showed a remarkable bearing capacity and the ductility of the perforated plate shear connections was larger. Shan et al. (2017) conducted the push-out test on six types of connections for glubam-concrete composite beams, and four kinds of connectors suitable for BCC structure are recommended. Shan et al. (2020) carried out short-term bending tests on glued laminated bamboo and concrete composite beams. Four-point bending tests were conducted on nine full-scale BCC beams with four types of connectors. All BCC beams showed excellent behavior and the 200 mm long notch connection exhibited higher bearing capacity. With the development of various engineering materials (Ding et al., 2018; Zhang et al., 2018), fiber reinforced polymer had been widely used in the reinforcement of structural members (Wei et al., 2017a; Ding et al., 2019; Zhang et al., 2020). Wei et al. (2014) presented a new fiber reinforced polymer-bamboo-concrete composite structure. The bearing capacity and section rigidity were significantly improved. The mechanical properties of the novel composite beams were intermediate between the full-composite and non-composite.

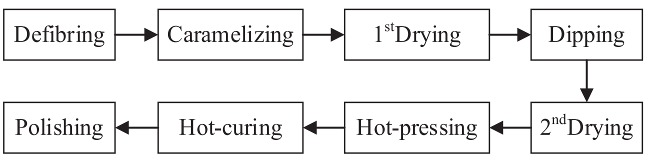

FIGURE 1 | Production of bamboo scrimber.

However, the similarities and differences of mechanical properties of bamboo-concrete and wood-concrete shear connections are rarely studied. Therefore, a series of bamboo-concrete specimens and wood-concrete specimens were tested under static push-out loading in this paper. Except for the material (bamboo or wood), other parameter the two kinds of specimens were set in the same and symmetric way. The interface slip was measured by the digital image correlation (DIC) and the linear variable displacement transducer (LVDT). The failure modes, load-slip relationship, shear stiffness, shear capacity, and slip distribution were discussed.

MATERIALS AND METHODS

Materials

Bamboo and Wood

Bamboo scrimber used in this test is made up of bamboo fibers that had been dried, impregnated, and pressed under high pressure and high temperature conditions. The key manufacturing process is shown in **Figure 1**. In this test, the impregnation rate of adhesive is about 5% of the dry weight of bamboo fibers, the average density is 1,100 kg/m^3, and the moisture content is between 6.0% and 8.0%. According to ASTM D143-09 (ASTM International, 2009), 10 tensile specimens (25 × 10 × 455 mm, TB-1 to TB-10) and 10 compressive specimens (50 × 50 × 150 mm, CB-1 to CB-10) were tested for the mechanical properties of bamboo scrimber. The test setup, stress-strain curves, and mechanical properties

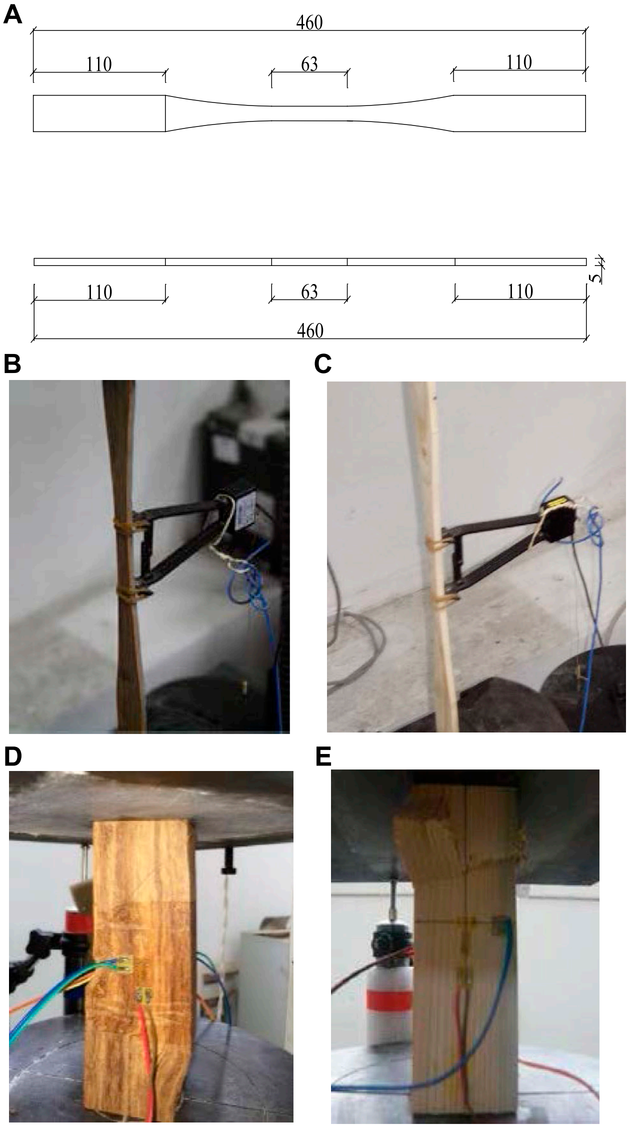

FIGURE 2 | Specimens of bamboo scrimber and wood. **(A)** Tension specimen size (units: mm). **(B)** Tension specimen of bamboo scrimber. **(C)** Tensile specimens of wood. **(D)** Compression specimen of bamboo scrimber. **(E)** Compression specimens of wood.

of the bamboo specimens are shown in **Figures 2** and **3** and **Table 1**, respectively.

The wood used in this test was made of pinus sylvestris, which is a kind of popular timber. The number, size, and test method of wood tensile specimens (TW-1 to TW-10) and compressive specimens (CW-1 to CW-10) were the same as that of the bamboo scrimber specimens. The test setup, stress-strain relationship, and mechanical properties of the wood specimens are shown in **Figures 2** and **3** and **Table 1**, respectively.

Concrete

Two kinds of concrete with different strength were used in this test. Three cylinders (φ150 × 300 mm) of C30 and C50 were tested. The average compressive strength and modulus of elasticity of C30 were 34.7 MPa and 33.3 GPa, respectively. The average compressive strength and modulus of elasticity of C50 were 58.0 MPa and 37.3 GPa, respectively.

Dowel

The dowels used in this experiment were ribbed steel bars with 8, 12, and 16 mm in diameter. Three bars of each diameter were selected for the tensile test. The average strength of dowel tensile specimens was shown in **Table 2**.

Adhesives

The adhesive used in this test was the epoxy resin adhesive, which was mainly used for the connection between dowel and bamboo (wood) hole. Its main function was to ensure the stress transfer and avoid sliding friction between them. According to the manufacturer's statement, the average tension strength, modulus of elasticity, and ultimate tensile strain of the epoxy resin adhesives were 67.7 MPa, 2.9 GPa, and 0.029, respectively.

Specimen Preparation

Eighteen bamboo-concrete connections and 18 wood-concrete connections were processed with the material type (bamboo or wood), concrete strength and dowel diameter as test parameters in this experiment. **Table 3** listed the details of these specimens. The number of specimen is based on the principle of material + concrete strength + dowel diameter, B represents bamboo, W represents wood, for example, B3008 represents BCC structure, in which the concrete strength grade is C30 and dowel diameter is 8 mm. Additionally, the number "- 1/2/3" referred to the three specimens with the same sizes in each group. As shown in **Figure 4**, the specimens consists of two concrete blocks (140 × 350 × 70 mm) and one bamboo (wood) block (140 × 350 × 70 mm). The bamboo (wood) block was located in the middle of the specimen, the concrete blocks were arranged on both sides connected. The dowel passed through the reserved hole of the bamboo (wood) block, extending 60 mm into concrete blocks both sides, respectively. The concrete is strengthened by the 8 mm diameter constructional steel bars in the direction of length, width, and height.

Push-Out Test

A 3,000 kN hydraulic actuator was used in the push-out tests. After pre-loading (510 kN load) to eliminate the influence of specimen clearance, the test was started with the loading speed of 0.2 mm/min. When the specimen approached failure, the loading speed changed to 0.5 mm/min. The details of test setup were illustrated in **Figure 4**. The interface slip between the concrete block and the bamboo block was measured by two methods. The first method was the LVDT. Four displacement meters were fixed on the concrete blocks near the interface, and the measuring rods were fixed at the same level on the bamboo block near the interface (**Figure 5**). The second method was the DIC. After the surface of the specimen was polished and cleaned, uniformly distributed spots are set up for

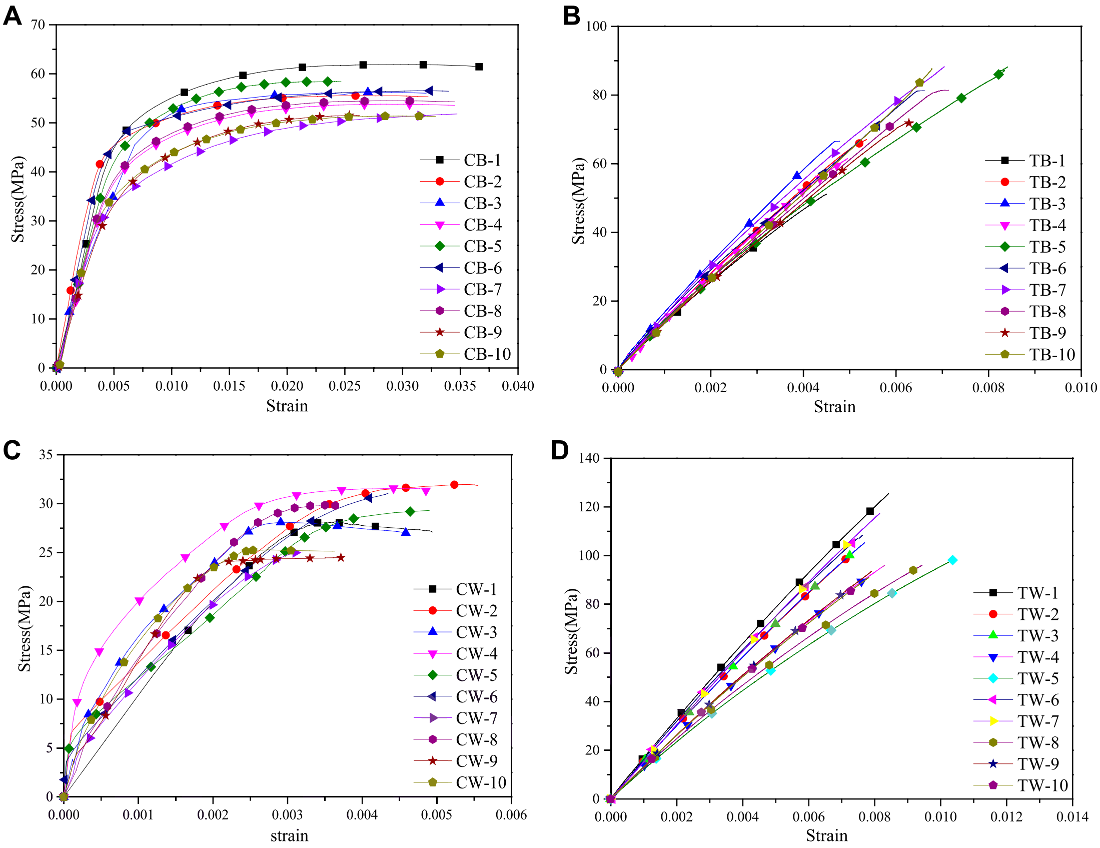

FIGURE 3 | Stress-strain curves of specimens. **(A)** Bamboo scrimber compression specimens. **(B)** Bamboo scrimber tensile specimens. **(C)** Wood compression specimens. **(D)** Wood tensile specimens.

camera recognition. After equipment calibration, two image collectors were used to continuously collect the deformation images of the specimens during the entire test process (**Figure 6**). In the test, the acquisition frequency of LVDT was the same as that of DIC, and the data was collected once every 3 s. After the pre-loading was completed, LVDT and DIC started to collect at the same time.

TEST RESULTS AND DISCUSSION

Observations and Failure Modes

Figure 7 shows the failure modes of the wood-concrete composite connections. When the load approached 70–85% ultimate capacity, the diagonal crack occurred in the concrete block near the interface. When load increased up to the ultimate

TABLE 1 | Mechanical properties of bamboo and wood.

Specimen type	Test results	Property	Average value	Standard deviation	Coefficient of variation
Bamboo	Tension test results	Ultimate tensile stress (MPa)	75.237	13.096	17.41%
		Ultimate tensile strain	0.0062	0.0012	19.96%
		MOE (GPa)	12.53	2.07	16.54%
	Compression test results	Ultimate compressive stress (MPa)	54.897	3.583	6.53%
		Ultimate compressive strain	0.032	0.005	11.56%
		MOE (GPa)	9.55	1.42	14.90%
Wood	Tension test results	Ultimate tensile stress (MPa)	102.75	11.44	10.77%
		Ultimate tensile strain	0.0083	0.0009	11.45%
		MOE (GPa)	12.33	2.02	16.38%
	Compression test results	Ultimate compressive stress (MPa)	28.5	2.7	9.2%
		Ultimate compressive strain	0.0043	0.0007	16.4%
		MOE (GPa)	8.15	0.97	11.9%

Note: MOE is modulus of elasticity.

TABLE 2 | Bearing capacity and strength of dowel tensile specimens.

Specimen type	Property	Average value	Standard deviation	Coefficient of variation
S8	Ultimate tensile stress (MPa)	618.13	21.23	3.44%
	Yield stress (MPa)	—	—	—
	MOE (GPa)	213.76	9.81	4.59%
S12	Ultimate tensile stress (MPa)	593.05	4.79	0.81%
	Yield stress (MPa)	490.00	2.13	0.44%
	MOE (GPa)	222.76	4.32	1.94%
S16	Ultimate tensile stress (MPa)	615.45	15.35	2.49%
	Yield stress (MPa)	482.26	9.69	2.01%
	MOE (GPa)	214.44	1.64	0.76%

load, there were many cracks and even spalling of the concrete surface. Subsequently, the load dropped continuously and slowly until the end of the test. When the load value dropped to about 35% ultimate capacity, the concrete blocks on both sides were destroyed along the cracks.

Figure 8 shows the failure modes of the bamboo-concrete composite connections. The cracks began to appear on concrete block near the joint under 60–80% ultimate load, and the cracks expanded around as the load increases. When load reached up to the ultimate load, the concrete near the dowels were destroyed, which caused the load value to drop rapidly. When the load value dropped to about 30% ultimate load, the concrete blocks on both sides were failed.

To sum up, the failure modes of the wood-concrete composite connections and bamboo-concrete composite connections were not significantly different, which could be defined as the moderate failure considering that the specimens had large plastic deformation after the ultimate load. After testing, the concrete slab was carefully removed, the directly interconnected fractures between the dowel holes and the dowels bending to different degrees could be found. The difference was that the wood holes were deformed while the bamboo holes were not, which could intuitively reflect the reason for the different shear stiffness and shear capacity of two kinds of specimens. Compared with wood, the higher strength of bamboo led to the different position of the inflection point of dowels.

Load-Slip Curves

As showed in **Figure 9**, the load-slip curves of the two kinds of connections were similar, which could be summarized as the elastic section, strengthening section and descending section. The load-slip curves were basically linear at the first elastic section (0–60% ultimate load). The load-slip curves were nonlinear, and the increasing rates of the interface slip were obviously accelerated at the second strengthening section (60–100% ultimate load). At the third descending section, the load dropped and the slip increased continuously until the end of the test.

Besides, it could be found that the slip values corresponding to the ultimate load of wood-concrete specimens were larger than those of bamboo-concrete specimens. After passing the ultimate load point, the curves of bamboo-concrete specimens decreased rapidly, while the curves of wood-concrete specimens decreased slowly. The slip corresponding to the ultimate load decreased with the dowel diameter increase.

To verify the reliability of the measurement results based on DIC, B5012 group, and W5012 group were selected for comparison. The load-slip curves are shown in **Figure 10**. It could be seen that the LVDT results were basically the same as the DIC results.

Shear Stiffness

According to Eurocode 5 (European Union, 2006), the shear stiffness K (**Eq. 1**) and the ductility coefficient D (**Eq. 2**) were calculated, respectively. The Ductility coefficient model is shown in **Figure 11**.

$$K = P/S \tag{1}$$

$$D = S_{\mathrm{u}} \big/ S_{\mathrm{y}} \tag{2}$$

TABLE 3 | Specimen parameters.

Specimen type	Specimen group	Dowel diameter (mm)	Strength grades of concrete	Number of specimens
Connections of bamboo-concrete	B3008	8	C30	3
	B5008	8	C50	3
	B3012	12	C30	3
	B5012	12	C50	3
	B3016	16	C30	3
	B5016	16	C50	3
Connections of wood-concrete	W3008	8	C30	3
	W5008	8	C50	3
	W3012	12	C30	3
	W5012	12	C50	3
	W3016	16	C30	3
	W5016	16	C50	3

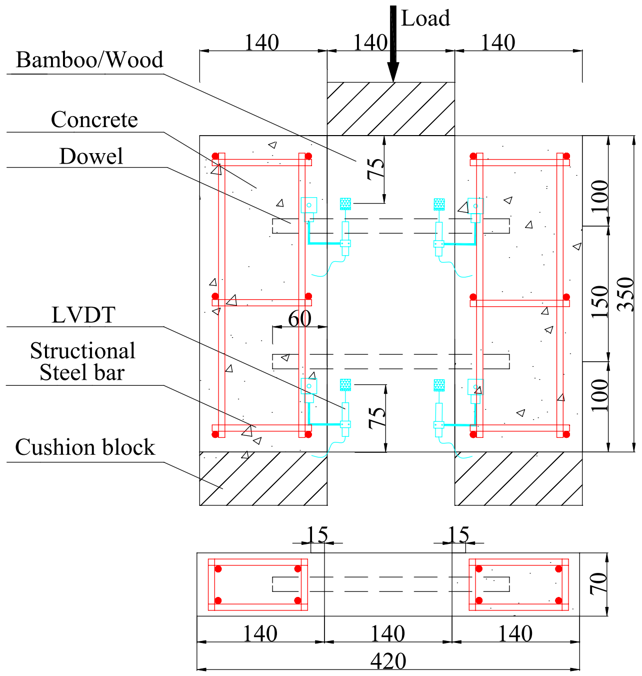

FIGURE 4 | Test setup of bamboo/wood-concrete connections.

where p is the load value, kN; P_u is the ultimate load, kN; S is the slip value, mm; S_u and S_y are the slip value corresponding the different load as showed in **Figure 11**, mm.

The results of the stiffness and ductility of all specimens are shown in **Table 4**, and the data are the average values of each group of specimens. The following findings could be obtained from the table. The values of $K_{s,0.4}$, $K_{s,0.6}$ and $K_{s,0.8}$ of all specimens showed a decreasing trend in general. The shear stiffness of bamboo-concrete connections were more than 19% higher than that of wood-concrete connections. According to the second section of this paper, the compressive strength and modulus of elasticity of bamboo are 1.93 and 1.17 times of that of wood. The different mechanical properties of two kinds of materials led to the difference of the stiffness and ductility of composite connections. The ductility of the bamboo-concrete specimens with 12 mm diameter dowels and the wood-concrete specimens with 16 mm diameter dowels was the best among all specimens. The increase of concrete strength could improve the stiffness of all specimens, but the change of concrete strength had little effect on the ductility of all specimens.

FIGURE 5 | Linear variable displacement transducer.

Shear Capacity

The average value of ultimate shear capacity of each group of specimens was showed in **Figure 12**. The ultimate capacity of bamboo-concrete specimens was up to 31% larger than that of wood-concrete specimens at most. The main reason could be considered that the higher strength of bamboo resulted in the higher shear capacity of bamboo-concrete connections. The ultimate shear capacity increased with the increase of dowel diameter and concrete strength.

Slip Distribution

The distribution of relative slip could not be obtained by LVDT, which could get only a limited number of relative slip values at the designated positions. The relative slip values between bamboo/wood and concrete at all positions of the specimen could be obtained by DIC. Base on DIC, the displacement of the whole field is shown in **Figure 13A**. Considering that the height of the specimen was 350 mm, as shown in **Figure 13B**, thirteen points (vertical spacing 25 mm) were selected along the height of the specimen on both sides of the interface. The difference value of displacement between two points in parallel position were calculated to represent the relative slip value.

The variation of slip along the specimens height on both sides of the interface was analyzed. The slip distributions of bamboo-concrete specimens under the test loads of 40, 60, 80, 100, 120, and 140 kN are shown in **Figure 14**. The slip distributions of wood-concrete specimens under the test loads of 40, 60, 80, 100, and 120 kN are shown in **Figure 15**.

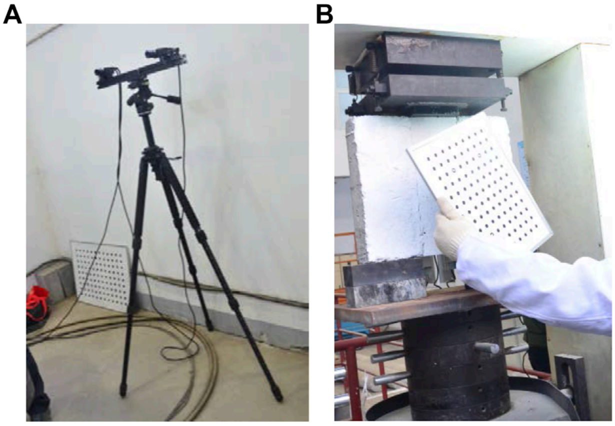

FIGURE 6 | Digital image correlation measurement. **(A)** Optical imaging system. **(B)** Calibration before collection of data.

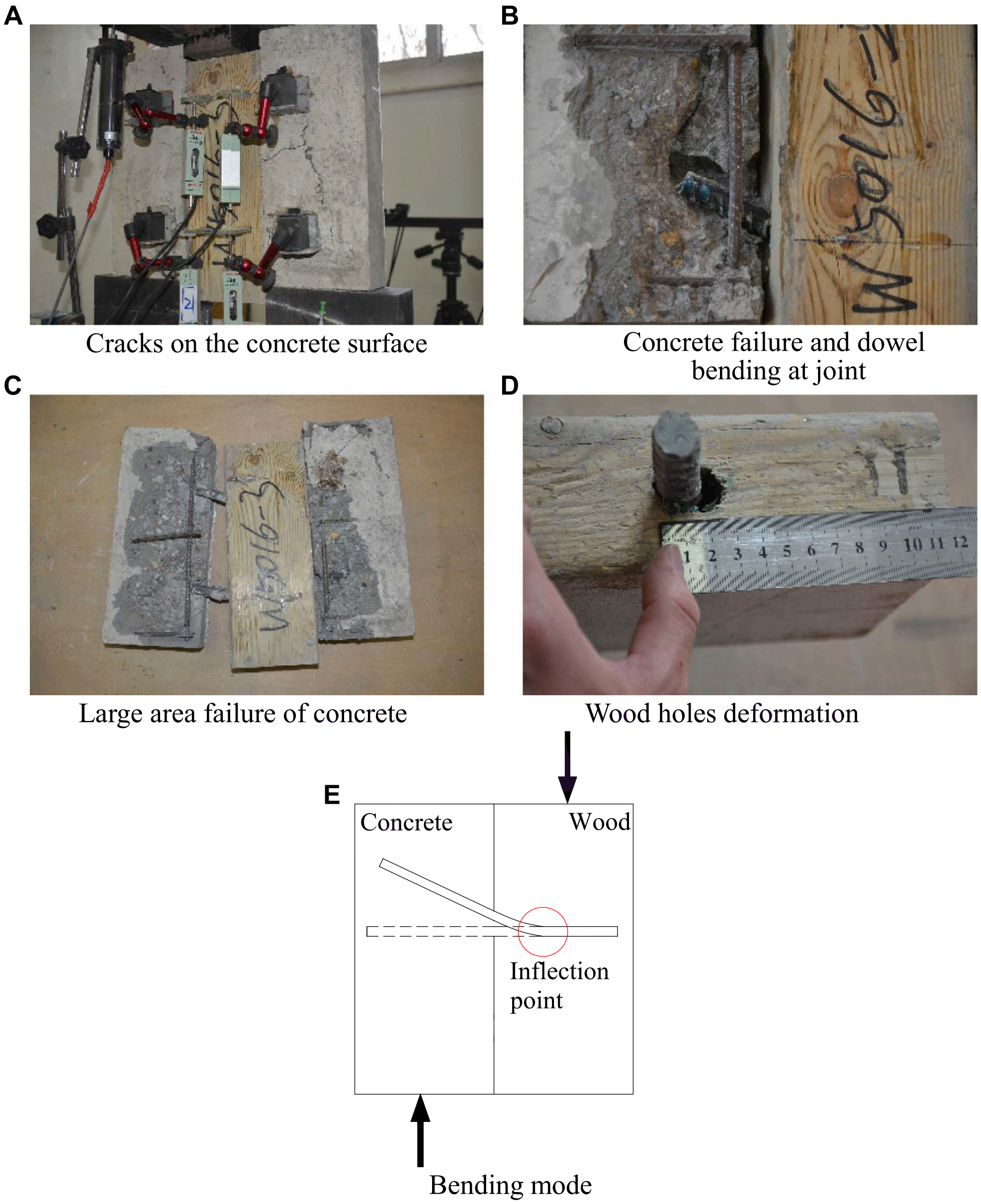

FIGURE 7 | Typical failure mode of wood-concrete connection. **(A)** Cracks on the concrete surface. **(B)** Concrete failure and dowel bending at joint. **(C)** Large area failure of concrete. **(D)** Wood holes deformation. **(E)** Bending mode.

Combined with **Figures 14** and **15**, the summary was as follows. The distribution of the slip of the wood-concrete specimens and the bamboo-concrete specimens was similar. The relative slip values of the left and right sides of the specimen were basically identical, indicating that there was no visible offset load in the testing process. The line connecting 13 points at different heights was basically a straight line, which means that the force transmission was stable without sudden change. At the later stage of the test, there was a higher increase amplitude of the slip with the same load increment, which indicated a decrease in shear stiffness of composite specimens. The slip decreased with the increase of the dowel diameter and the concrete strength grade.

THEORETICAL ANALYSIS

Shear Capacity

In reference to the calculation equation of shear capacity of the steel-concrete composite structure and wood-concrete composite structure, this paper attempted to find a suitable analytical methodologies of shear capacity of the bamboo/wood-concrete composite connections.

Ceccotti Model

Ceccotti (2002) proposed that the shear strength of the wood-concrete system should be analyzed according to three modes: the

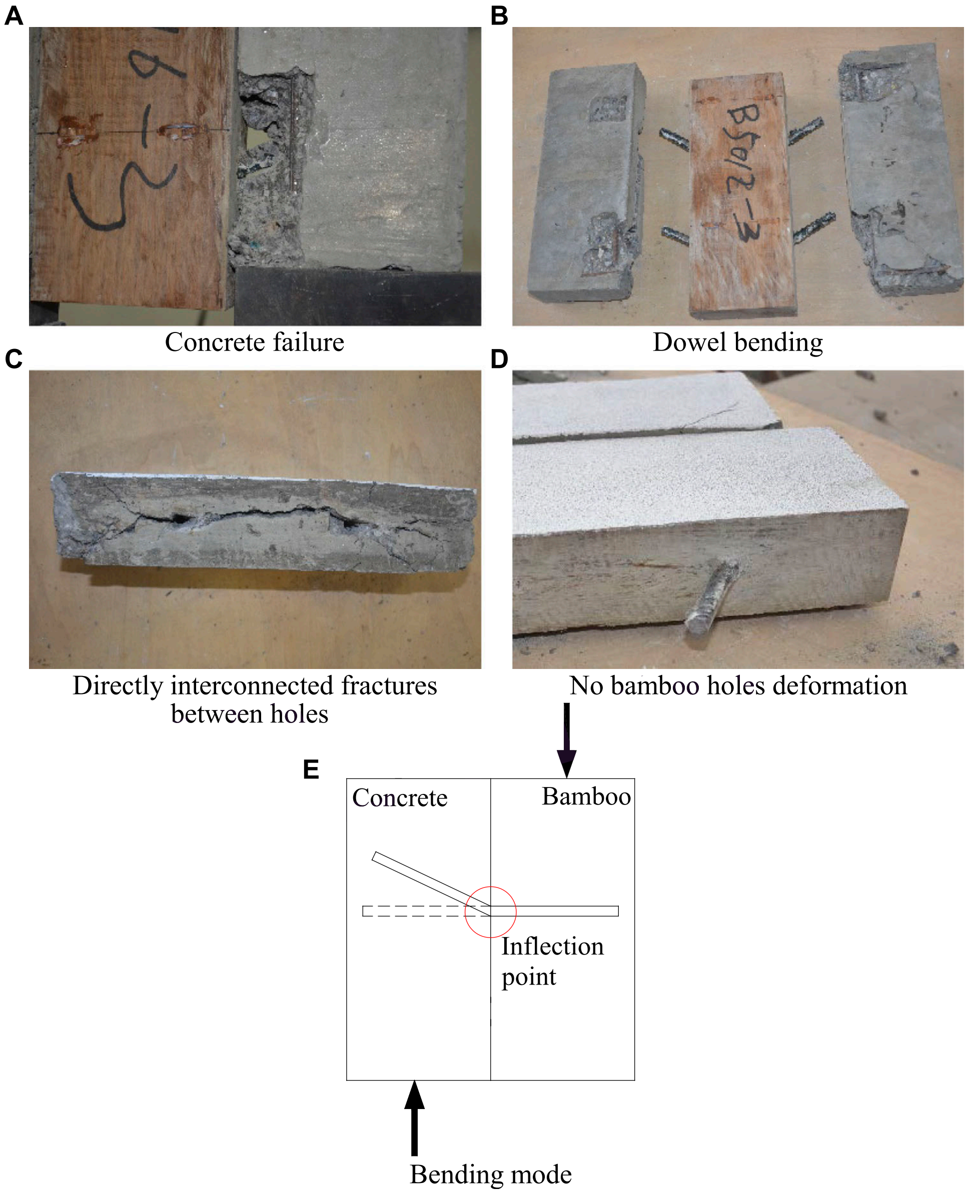

FIGURE 8 | Typical failure mode of bamboo-concrete connection. **(A)** Concrete failure. **(B)** Dowel bending. **(C)** Directly interconnected fractures between holes. **(D)** No bamboo holes deformation. **(E)** Bending mode.

failure of the timber side (**Eq. 3**), the failure of the dowel (**Eq. 4**), and the concrete side (**Eq. 5**), and the minimum of the three values should be taken as the shear capacity of the connection.

$$Q = 1.5\sqrt{2M_y f_h d} \tag{3}$$

$$Q = 0.8A_s f_u/\gamma_v \tag{4}$$

$$Q = 0.23d^2\sqrt{f_{ck}E_c/\gamma_v} \tag{5}$$

where, Q is the shear capacity of the single dowel, N; A_s is section area of the dowel, mm^2; f_u is the ultimate tensile strength of dowel, MPa; γ_v is the safety factor, generally $\gamma_v = 1.25$; d is the dowel diameter, mm; f_h is compression strength of wood parallel to the grain, MPa; f_{ck} is the compressive strength of concrete cylinder, MPa; E_c is the elastic modulus of concrete, MPa; M_y is the moment value corresponding to the formation of plastic hinges of the dowel, It could be calculated according to **Eq. 6**.

$$M_y = 0.8f_u d^3/6 \tag{6}$$

Saulius Model

Saulius et al. (2007) proposed that there were three failure modes of the wood-concrete connection: hingeless yield mode (**Eq. 7**), single hinge yield mode (**Eq. 8**), and double hinge yield mode (**Eq. 9**), as shown in **Figure 16**.

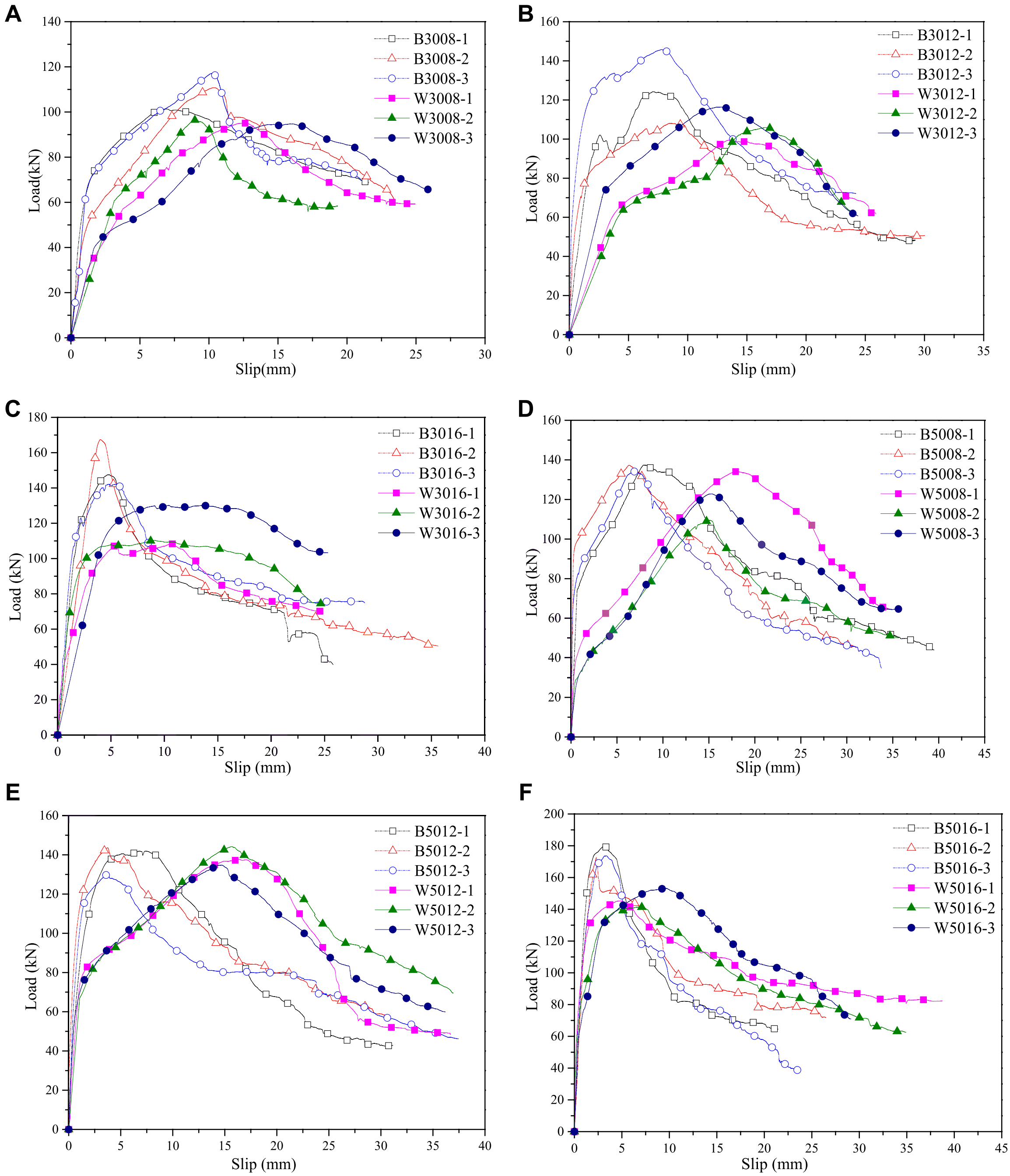

FIGURE 9 | Comparison of load-slip curves of bamboo-concrete and wood-concrete connections. **(A)** 3008, **(B)** 3012, **(C)** 3016, **(D)** 5008, **(E)** 5012, and **(F)** 5016.

1. Calculation equation of shear capacity of dowel in hingeless yield mode:

$$Q = V = f_{\mathrm{h}} \cdot d \cdot l_{\mathrm{E}} \tag{7}$$

2. Calculation equation of shear capacity of dowel in single hinge yield mode:

$$Q = V \cdot \sin\alpha = f_{\mathrm{h}} \cdot d \cdot l_{\mathrm{E}} \left(\sqrt{\left(4M_{\mathrm{y}} \cdot \sin^{2}\alpha \middle/ f_{\mathrm{h}} \cdot d \cdot l_{E}^{2} \right) + 2} - 1 \right) \tag{8}$$

3. Calculation equation of shear capacity of dowel in double hinge yield mode:

$$Q = V \cdot \sin\alpha = 2\sqrt{f_{\mathrm{h}} \cdot d \cdot M_{\mathrm{y}}} \sin\alpha \tag{9}$$

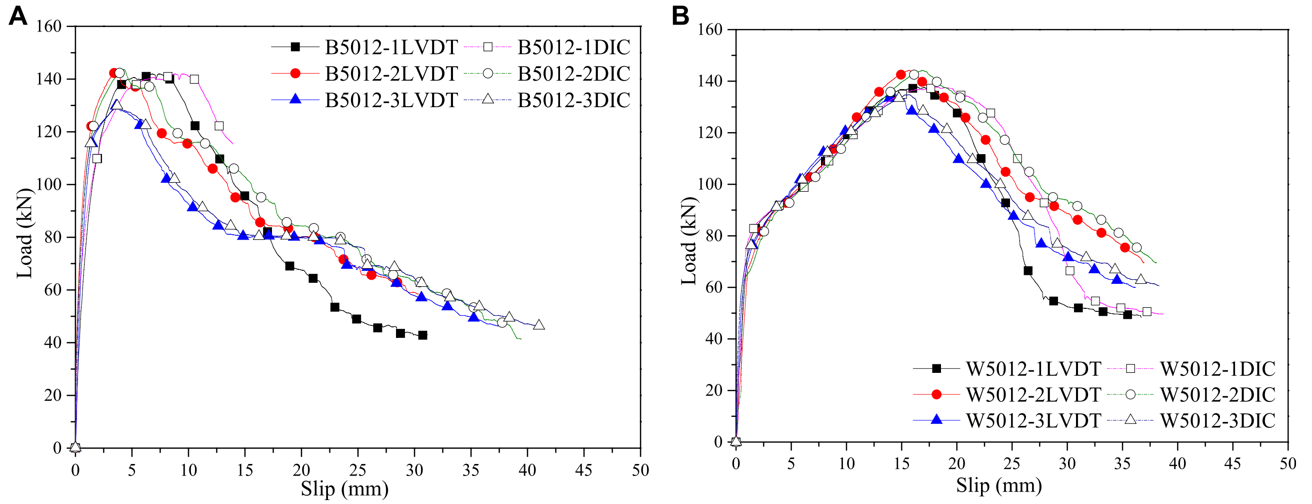

FIGURE 10 | Load-slip curves measured of connections by LVDT and DIC **(A)** B5012 and **(B)** W5012.

where, Q is the shear capacity of the single dowel, N; l_E is the length of the dowel into the wood, mm; d is the dowel diameter, mm; f_h is compression strength of wood parallel to the grain, MPa; M_y is the moment value corresponding to the dowel plastic hinge formation.

The bending angle of the dowel was small in this test. So α was larger, which was greater than 80°, sinα was approximately 1. So the shear capacity under the three yield modes could be expressed as **Eq. 10**.

$$Q = \begin{cases} f_h \cdot d \cdot l_E \ \text{(Hingeless yield mode)} \\ f_h \cdot d \cdot l_E\left(\sqrt{\left(4M_y/f_h \cdot d \cdot l_E^2\right)+2}-1\right) \\ \quad \text{(Single hinge yield mode)} \\ 2\sqrt{f_h \cdot d \cdot M_y} \ \text{(Double hinge yield mode)} \end{cases} \tag{10}$$

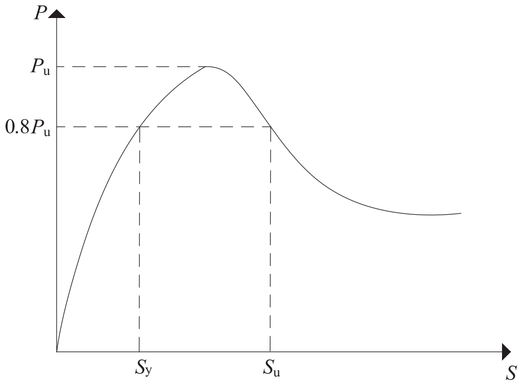

FIGURE 11 | Ductility coefficient model.

European Code

According to Eurocode 4 (European Union, 2006), the shear capacity of the steel-concrete composite system was the smaller of the two values calculated by **Eqs. 11** and **12**.

$$Q = 0.29\alpha d^2\sqrt{E_c f_{ck}}\Big/\gamma_v \tag{11}$$

$$Q = 0.8A_s f_u/\gamma_v \tag{12}$$

where, α is the influence coefficient of dowel length, when $3 \le h/d \le 4$, $a = 0.2\,[(h/d+1)] \le 1.0$, when $h/d \ge 4$, $\alpha = 1$; A_s is section area of the dowel, mm^2; f_u is the ultimate tensile strength of dowel, MPa; γ_v is the partial safety factor, generally $\gamma_v = 1.25$; d is the dowel diameter, mm; f_{ck} is the standard compressive strength of concrete cylinder, MPa; E_c is the elastic modulus of concrete, MPa.

Chinese Code

The influence of the minimum tensile strength and yield value of the dowel is further considered in the Chinese Code GB50017-2013 (Chinese Committee for Standardization, 2013). The shear capacity could be calculated by **Eq. 13**.

$$Q = 0.43A_s\sqrt{f_c E_c} \le 0.7A_s\gamma f \tag{13}$$

where, A_s is section area of the dowel, mm^2; f_c is the standard compressive strength of concrete cube, MPa; E_c is the elastic modulus of concrete, MPa; γ is the ratio of the minimum tensile strength to the yield strength of the dowel; f is the design value of dowel tensile strength, MPa.

In this test, two dowels passed through the reserved hole of the bamboo/wood block and formed four shear connectors with the concrete blocks. To divide the test load by four to get the shear capacity of a single connector. The actual shear capacity and theoretical shear capacity of all specimens were showed in **Table 5**.

It could be found from the table that increasing the dowel diameter could improve the shear capacity of the specimens according to the theoretical calculation. In contrast, the shear

TABLE 4 | Test results of bamboo/wood-concrete specimens.

Specimens type	Specimens	P_{max} (kN)	S_u (mm)	$K_{s,0.4}$ (kN/mm)	$K_{s,0.6}$ (kN/mm)	$K_{s,0.8}$ (kN/mm)	S_y (mm)	D
Bamboo-concrete connections	B3008	109.71	14.16	60.90	44.54	21.89	4.42	3.70
	B3012	126.03	12.05	148.80	91.09	53.23	2.03	6.20
	B3016	152.33	6.90	63.66	64.54	55.95	2.23	3.31
	B5008	136.29	12.26	274.84	187.23	34.82	3.52	3.79
	B5012	138.40	10.11	162.92	119.84	83.57	1.44	7.35
	B5016	175.26	6.05	140.20	125.73	103.77	1.36	4.47
Wood-concrete connections	W3008	95.45	16.77	20.96	14.87	10.67	7.37	2.24
	W3012	107.37	21.00	18.96	18.65	9.97	9.25	2.39
	W3016	116.55	20.01	49.62	42.18	35.33	2.87	7.69
	W5008	122.13	21.73	19.60	10.23	9.18	10.62	2.04
	W5012	138.88	21.83	81.46	38.36	13.82	8.12	2.71
	W5016	146.62	13.65	199.31	105.94	70.68	1.86	7.86

capacity changed little with the dowel diameter according in the test. Through preliminary analysis, the reasons for the differences could be summarized as follows.

The influence of dowel bending in the wood was considered, but the influence of concrete strength was not considered in the theoretical equation of wood-concrete connection. The influence of concrete strength was considered, but steel strength was not considered in the theoretical equation of the steel-concrete connection. In general, Saulius model was more in line with the actual failure mode of this paper. In this paper, it was suggested that the ratio (f_c/f_h) of compressive strength of concrete to that of bamboo/wood should be added as a parameter, and it was suggested to add the revised parameters α, β to modify the Saulius model.

$$Q=\begin{cases}\alpha_1\cdot\left(\dfrac{f_c}{f_h}\right)^{\beta_1}\cdot f_h\cdot d\cdot l_E\left(\sqrt{\left(4M_y/f_h\cdot d\cdot l_E^2\right)+2}-1\right)\\ \text{(Single hinge yield mode)}\\ 2\alpha_2\cdot\left(\dfrac{f_c}{f_h}\right)^{\beta_2}\cdot\sqrt{f_h\cdot d\cdot M_y}\ \text{(Double hinge yield mode)}\end{cases}\tag{14}$$

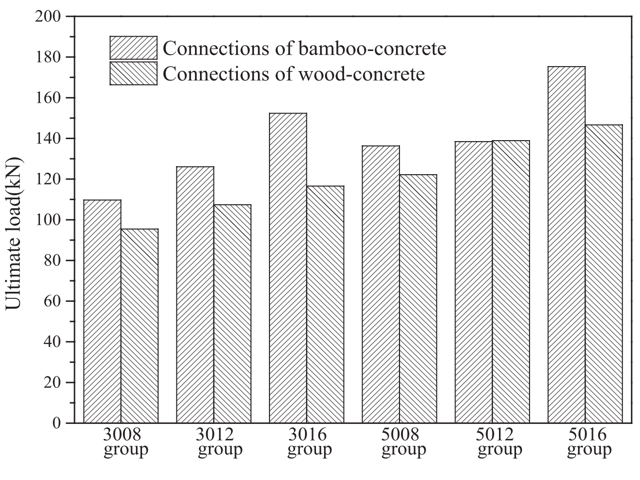

FIGURE 12 | Comparison of ultimate shear capacity.

M_y could be calculated according to the **Eq. 15**.

$$M_y = 0.8 f_u d^3/6\tag{15}$$

By using mathematical statistics method to fit the results of each specimen, it could be concluded that $\alpha_1 = 1.5$, $\beta_1 = 0.5$; $\alpha_2 = 3$, $\beta_2 = 0.4$. The revised equation was as follows.

$$Q=\begin{cases}1.5\cdot f_c^{\,0.5}\cdot f_h^{\,0.5}\cdot d\cdot l_E\left(\sqrt{\left(4M_y/f_h\cdot d\cdot l_E^2\right)+2}-1\right)\\ \text{(Single hinge yield mode)}\\ 6\cdot f_c^{\,0.4}\cdot f_h^{\,0.1}\cdot\sqrt{M_y\cdot d}\ \text{(Double hinge yield mode)}\end{cases}\tag{16}$$

where, Q is the shear capacity of the single dowel, N; f_u is the ultimate tensile strength of dowel, MPa; d is the dowel diameter, mm; l_E is the dowel length into bamboo (wood), mm; f_h is the compression strength of bamboo (wood) parallel to the grain, MPa; f_c is the standard compressive strength of concrete cube, MPa.

The shear capacity of the specimens was calculated by the above **Eq. 16** and compared with the test value. As provided in **Table 6**, there was a good correlation between the test values and the values calculated by the revised equation. The result also proved the necessity of considering the influence of concrete compressive strength in the calculation of shear capacity.

Load-Slip Curves

Dias (2012) used a three-parameter model to describe the rising segment of the load-slip curves of wood-concrete connections, as shown in **Figure 17** and **Eq. 17**. In this paper, the model was proposed to describe the upward section of the load-slip curve of the bamboo-concrete connections.

$$F/F_{max} = (c + b\cdot s)\cdot\left[1-\exp(-a\cdot s/c)\right]\tag{17}$$

where, a, b, c are the parameters, s is the slip, F is the load, F_{max} is the ultimate load. The values of a, b, and c of all specimens were fitted by mathematical software. The results were shown in **Table 7**.

After analyzing the results, it was suggested to take values of a, b, and c according to the following **Eqs. 18–20**.

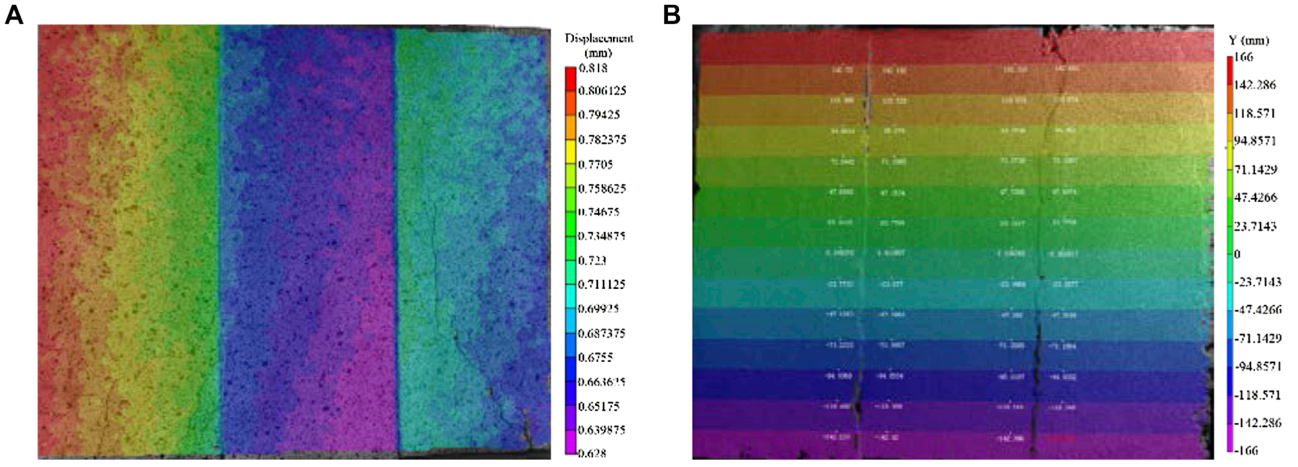

FIGURE 13 | Test results and post-processing methods based on digital image correlation. **(A)** The cloud picture of slip. **(B)** Selection of analysis points near the interface.

$$a = K_{s,0.4}/85 \tag{18}$$

$$c = K_{s,0.6}/K_{s,0.4} \tag{19}$$

$$b = (1 - c)/s_{est} \tag{20}$$

where, $K_{s,0.4}$ and $K_{s,0.6}$ are the secant slip modulus at the 40% and 60% of the ultimate shear capacity, respectively. s_{est} is the slip value corresponding to the ultimate load.

According to the above **Eqs. 18–20** the values of a, b, and c of all specimens were calculated, then the results were brought into **Eq. 17** for further calculation. It could be found that the prediction curve was more consistent with the actual test curve. Groups 3,008 and 5,012 were representatives, as shown in **Figure 18**. The predicted curves were consistent with the test curves. It was verified that this method could better express the load-slip relationship of this test. Therefore, the proposed model (**Eq. 17**) can better express the load-slip relationship of this type of bamboo/wood-concrete connection.

CONCLUSIONS

This paper reports an experimental research on the bamboo-concrete connections and the wood-concrete connections to study the similarities and differences of mechanical properties between them. The interface slip of the specimens was measured by the LVDT and the DIC. The failure mode, the load-slip relationship, the shear stiffness, the shear capacity and the slip distribution of the specimens were studied. The following conclusions could be drawn:

1. The failure modes of bamboo-concrete connections were similar to that of wood-concrete connections, which could be defined as the moderate failure considering that the specimens had large plastic deformation after the ultimate load. The concrete surface of the specimens was cracked seriously or even peeled off locally. The directly interconnected fractures between the dowel holes and the dowels bending to different degrees could be found. The difference was that the wood holes were deformed, while no bamboo holes deformation.
2. The load-slip curves of wood-concrete specimens and bamboo-concrete specimens were similar, which could be summarized as elastic section, strengthening section and descending section. The shear stiffness of bamboo-concrete connections were more than 19% higher than that of wood-concrete connections. With the increase of concrete strength, the shear stiffness of the specimen increased and the deflection of the specimen changed little. The ultimate capacity of bamboo-concrete specimens was up to 31% larger than that of wood-concrete specimens at most. The ultimate shear capacity increased with the increase of dowel diameter and concrete strength. The different strength and modulus of elasticity of two kinds of materials led to the difference of the mechanical properties of composite connections.
3. According to the data measured by DIC, it could be found that the slip distribution of the wood-concrete specimens and the bamboo-concrete specimens was similar. The relative slip values of the left and right sides of the specimen were basically identical, indicating that there was no visible offset load in the testing process. The line connecting points at different heights was basically a straight line, which means that the force transmission was stable without sudden change.
4. Revised parameters α, β and the ratio (f_c/f_h) were added to revise the Saulius model to predict the shear capacity for the bamboo (wood)-concrete connections, and the modified model could provide satisfactory calculating results. Based on Dias model, a new model was proposed to describe the rising segment of the load-slip curves of the bamboo (wood)-concrete connection, and the predicted curves were consistent with the test curves.

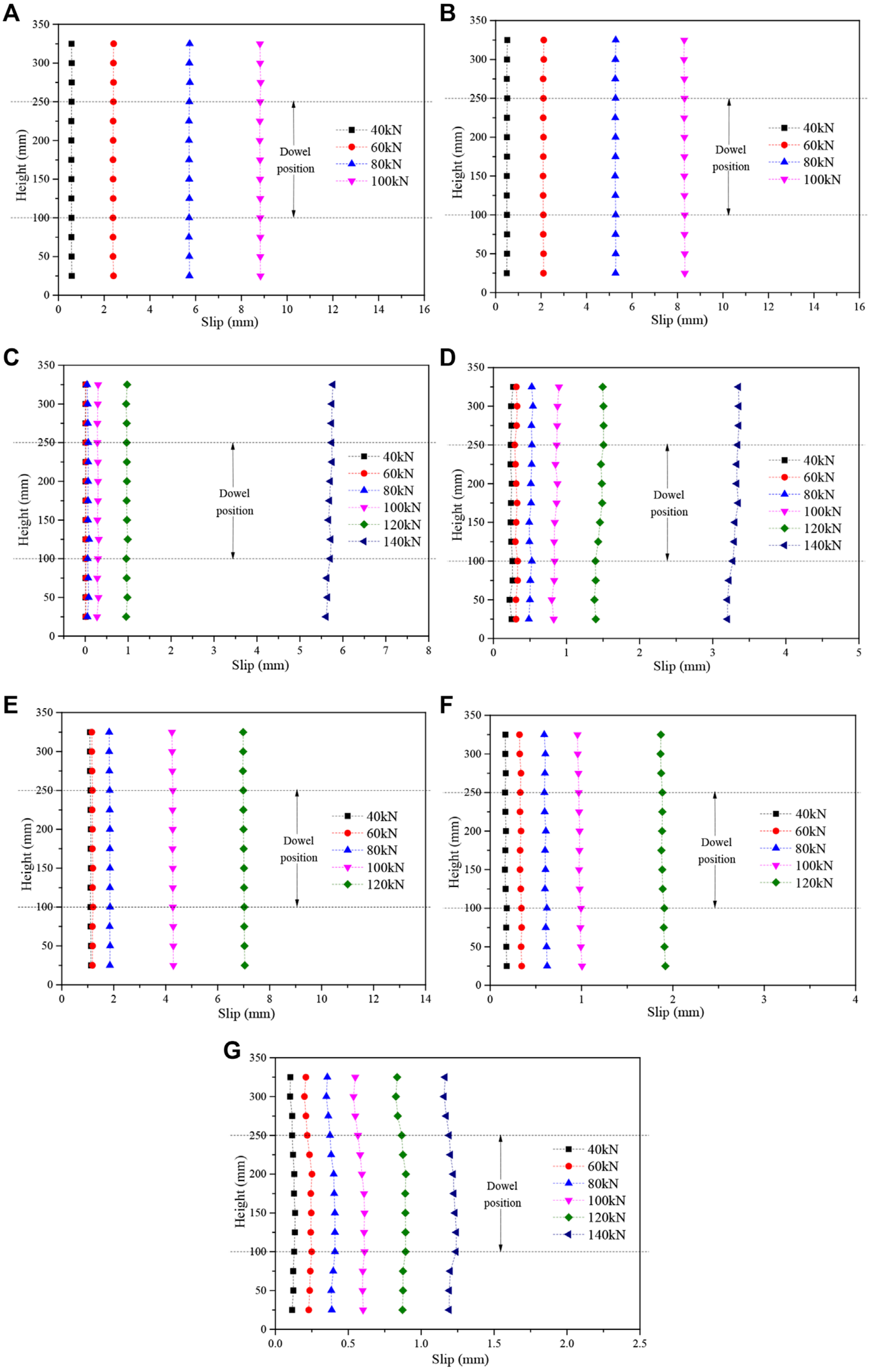

FIGURE 14 | The curves of the slip of bamboo-concrete specimens along interface height. **(A)** B3008-2 left, **(B)** B3008-2 right, **(C)** B3012-3 right, **(D)** B3016-1 right, **(E)** B5008-1 right, **(F)** B5012-3 right, **(G)** B5016-2 right.

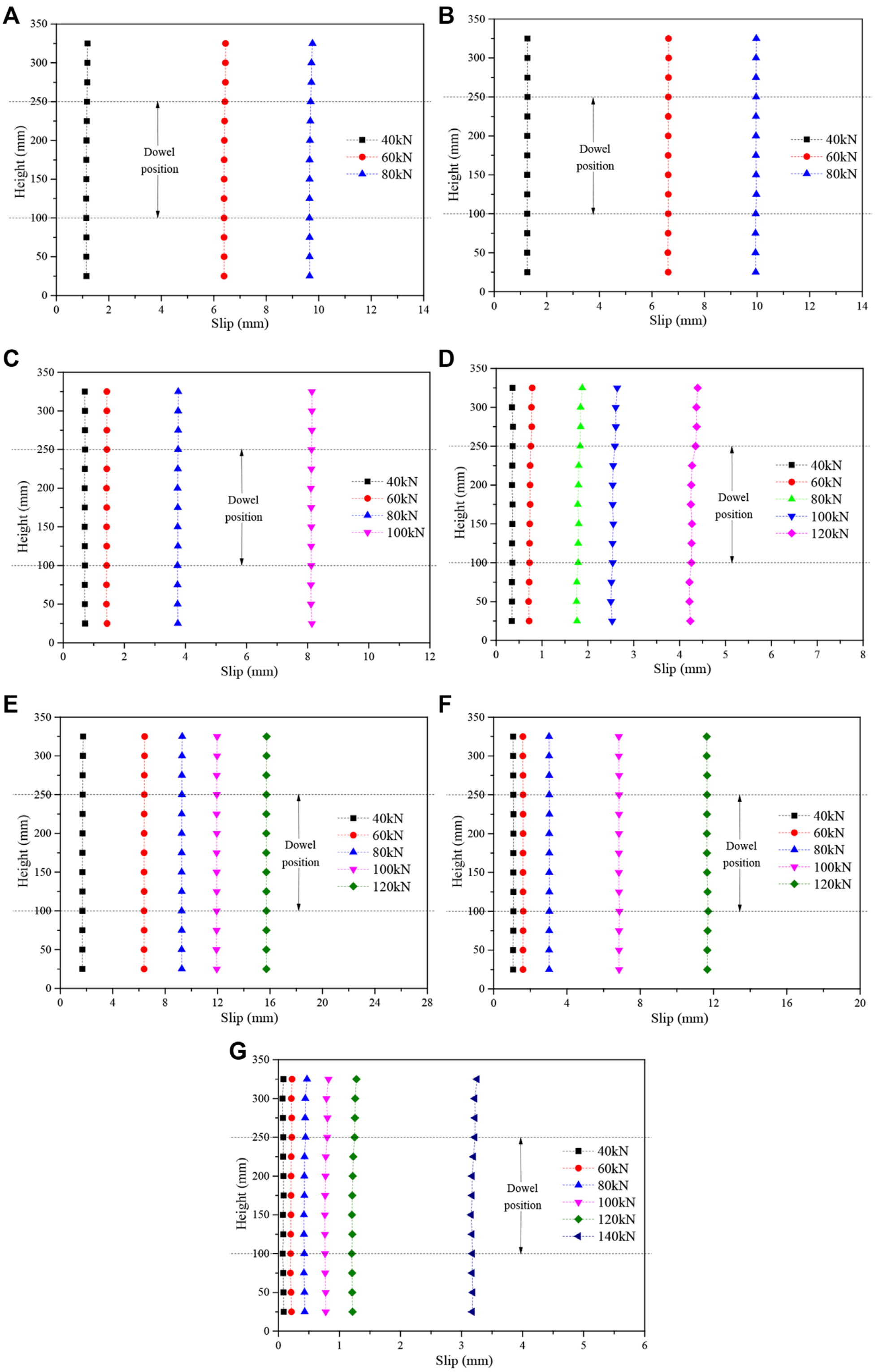

FIGURE 15 | The curves of slip of wood-concrete specimens along interface height. **(A)** W3008-3 left, **(B)** W3008-3 right, **(C)** W3012-3 right, **(D)** W3016-2 right, **(E)** W5008-3 right, **(F)** W5012-2 right, **(G)** W5016-1 right.

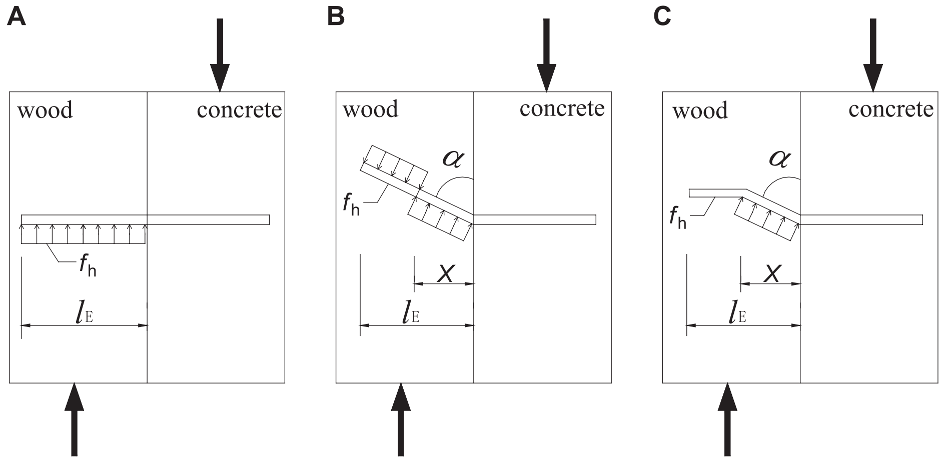

FIGURE 16 | Stress analysis of three yield modes. **(A)** Hingless yield mode, **(B)** single hinge yield mode, and **(C)** double hinge yield mode.

TABLE 5 | Comparison of shear capacity (units: kN).

Specimens	Ceccottimodel	Test value/ calculated value	Saulius model	Test value/ calculated value	Eurocode	Test value/ calculated value	Chinese standard	Test value/ calculated value
B3008	9.11	3.01	8.59	3.19	15.97	1.72	17.24	1.59
B3012	20.08	1.57	19.43	1.62	35.92	0.88	38.78	0.81
B3016	36.37	1.05	29.27	1.30	63.86	0.60	68.95	0.55
B5008	9.11	3.74	8.59	3.97	19.89	1.71	23.54	1.45
B5012	20.08	1.72	19.43	1.78	42.93	0.81	52.96	0.65
B5016	36.37	1.20	29.27	1.50	79.20	0.55	94.16	0.47
W3008	6.58	3.63	6.20	3.85	15.97	1.50	17.24	1.39
W3012	14.50	1.85	13.67	1.96	35.92	0.75	38.78	0.69
W3016	26.26	1.11	18.58	1.57	63.86	0.46	68.95	0.42
W5008	6.58	4.64	6.20	4.92	19.89	1.54	23.54	1.30
W5012	14.50	2.39	11.56	3.00	42.93	0.81	52.96	0.66
W5016	26.26	1.40	18.58	1.97	79.20	0.46	94.16	0.39

TABLE 6 | Comparison of test and calculated values of the shear capacity.

Specimens	Calculated values (kN)	Test average load (kN)	Calculated value/test value	Mean absolute error	Standard deviation	Coefficient of variation
B3008	23.50	27.43	0.86	0.14	2.20	0.08
B3012	25.97	31.51	0.82	0.18	4.12	0.14
B3016	39.13	38.08	1.03	0.03	2.39	0.06
B5008	28.86	34.07	0.85	0.15	2.28	0.07
B5012	33.57	34.60	0.97	0.03	1.40	0.04
B5016	50.57	43.82	1.15	0.15	3.00	0.07
W3008	22.02	23.90	0.92	0.08	0.81	0.03
W3012	25.53	26.84	0.95	0.05	1.60	0.06
W3016	28.25	29.14	0.97	0.03	2.12	0.07
W5008	27.04	30.53	0.89	0.11	2.65	0.09
W5012	29.59	34.72	0.85	0.15	2.38	0.07
W5016	36.52	36.66	1.00	0.00	1.05	0.03

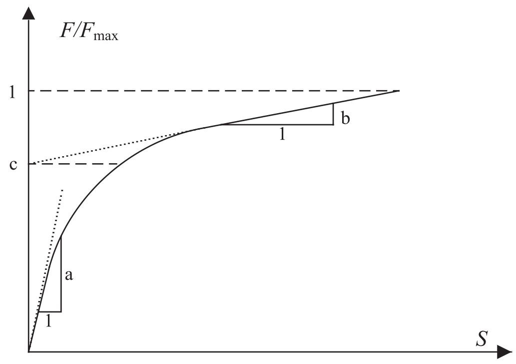

FIGURE 17 | Three-parameter model.

TABLE 7 | Results of specimen parameter.

Specimens	*a*	*b*	*C*	Specimens	*a*	*b*	*c*
B3008	0.70	0.035	0.64	W3008	0.27	0.017	0.77
B3012	1.36	0.035	0.73	W3012	0.27	0.023	0.61
B3016	0.64	0.061	0.76	W3016	0.68	0.032	0.70
B5008	1.10	0.040	0.69	W5008	0.34	0.039	0.36
B5012	1.35	0.014	0.91	W5012	0.99	0.031	0.54
B5016	1.05	0.030	0.98	W5016	1.26	0.020	0.84

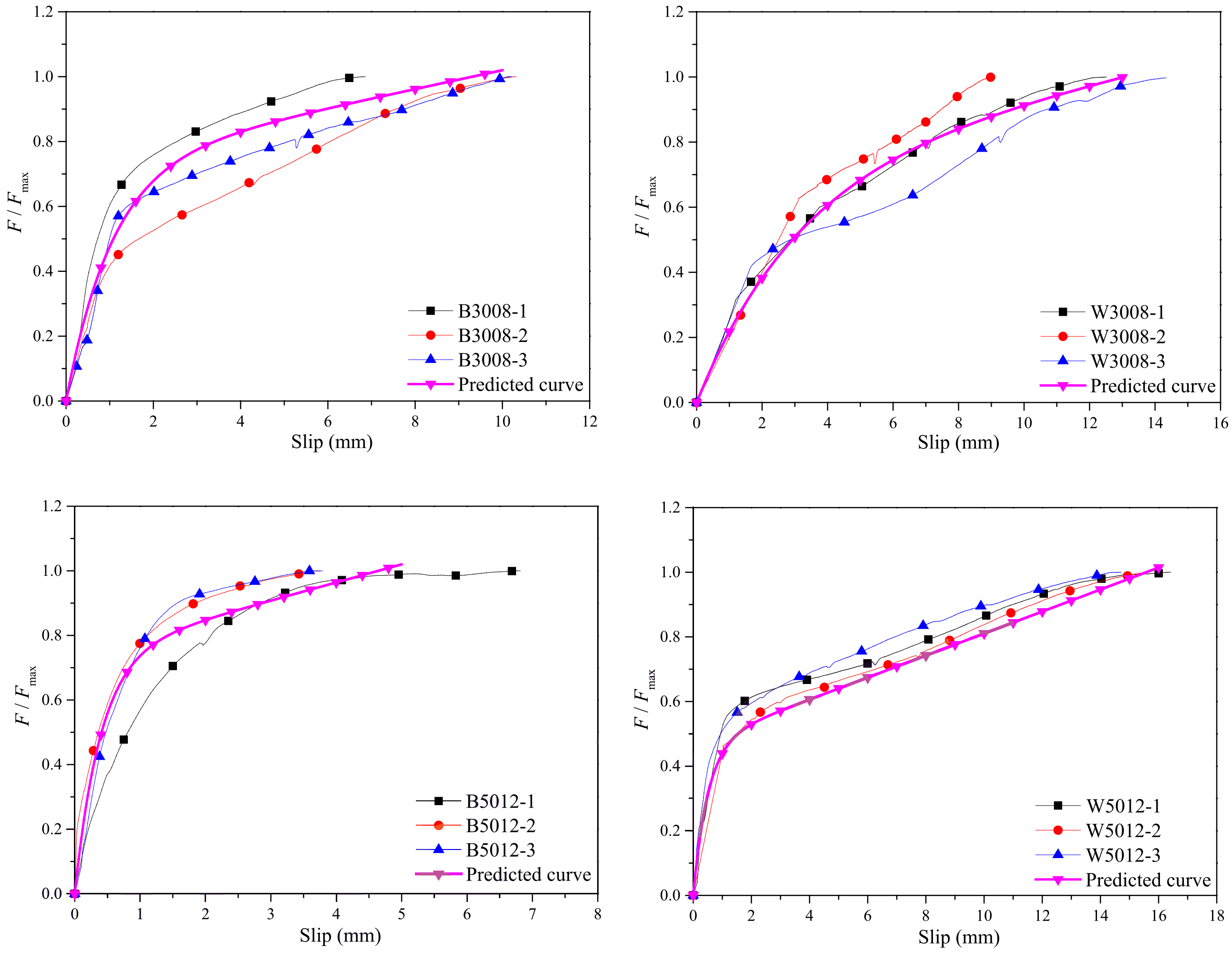

FIGURE 18 | Predicted curve and test curve. **(A)** B3008, **(B)** W3008, **(C)** B5012, **(D)** W5012.

DATA AVAILABILITY STATEMENT

All datasets generated for this study are included in the article/Supplementary Material.

AUTHOR CONTRIBUTIONS

ZW contributed to the analysis of the data and discussion of the obtained results and was a major contributor in writing the manuscript. YW contributed to the design of this analysis study. JJ and KZha contributed to the examination of all of the tests. KZhe contributed to the verification of data. All authors contributed to the article and approved the submitted version.

FUNDING

The authors acknowledge the contribution of the Natural Science Foundation of China (51778300, 51208262); the Natural Science Foundation (BK20191390), Key Research and Development Project (BE2020703) and "Qinglan Project" of Jiangsu Province, China; the "Six talent peaks project" in Jiangsu Province (JZ-017), China; the Natural Science Foundation (ACKYC20046) of Anhui University of Finance and Economics, China.

ACKNOWLEDGMENTS

The authors gratefully acknowledge Longlong Zhao, for their assistance in the experiments. The authors would further like to thank Jiawen Bai and Bo Yang.

REFERENCES

ASTM International (2009). *ASTM D143-09, standard test methods for small clear specimens of timber*. West Conshohocken, PA: ASTM International.

Auclair, S. C., Sorelli, L., and Salenikovich, A. (2016). A new composite connector for timber-concrete composite structures. *Constr. Build. Mater.* 112, 84–92. doi:10.1016/j.conbuildmat.2016.02.025

Ceccotti, A. (2002). Composite concrete-timber structures. *Prog. Struct. Eng. Mater.* 4, 264–275. doi:10.1002/pse.126

Chen, G., Wu, J., Jiang, H., Zhou, T., Li, X., and Yu, Y. (2020a). Evaluation of OSB webbed laminated bamboo lumber box-shaped joists with a circular web hole. *J. Build. Eng.* 29, 101129. doi:10.1016/j.jobe.2019.101129

Chen, G., Yu, Y., Li, X., and He, B. (2020b). Mechanical behavior of laminated bamboo lumber for structural application: an experimental investigation. *Eur. J. Wood Prod.* 78, 53–63. doi:10.1007/s00107-019-01486-9

Chen, S., Wei, Y., Hu, Y., Zhai, Z., and Wang, L. (2020c). Behavior and strength of rectangular bamboo scrimber columns with shape and slenderness effects. *Mater. Today. Commun.* 25, 101392. doi:10.1016/j.mtcomm.2020.101392

Cui, Z., Xu, M., Chen, Z., and Xiang, J. (2018). Experimental study on thermal performance of bamboo scrimber at elevated temperatures. *Constr. Build. Mater.* 182, 178–187. doi:10.1016/j.conbuildmat.2018.06.124

Dias, A., Skinner, J., Crews, K., and Tannert, T. (2016). Timber-concrete-composites increasing the use of timber in construction. *Eur. J. Wood Prod.* 74, 443–451. doi:10.1007/s00107-015-0975-0

Dias, A. M. P. G. (2012). Analysis of the nonlinear behavior of timber-concrete connections. *J. Struct. Eng.* 138, 1128–1137. doi:10.1061/(asce)st.1943-541x.0000523

Ding, L., Liu, X., Wang, X., Huang, H., and Wu, Z. (2018). Mechanical properties of pultruded basalt fiber-reinforced polymer tube under axial tension and compression. *Constr. Build. Mater.* 176, 629–637. doi:10.1016/j.conbuildmat.2018.05.036

Ding, L., Shi, J., Wang, X., Liu, Y., Jin, Y., and Wu, Z. (2019). Bond behavior between basalt fiber-reinforced polymer rebars and coral-reef-sand concrete conditioned in saline solution. *Struct. Concr.* 21, 659–672. doi:10.1002/suco.201900106

European Union (2006). *Eurocode 4, design of composite steel and concrete structures–part 1-1: general rules and rules for buildings*. Brussels, Belgium: European Union.

European Union (2006). *Eurocode 5, design of timber structures–part 1-1: general-common rules and rules for buildings*. Brussels, Belgium: European Union. EN 1995-1-1.

Chinese Committee for Standardization (2013). *G. B. 50017-2003, Code for design of steel structures*, Beijing, China: China Construction Industry Press.

Jiang, Y., Hong, W., Hu, X., Crocetti, R., Wang, L., and Sun, W. (2017). Early-age performance of lag screw shear connections for glulam-lightweight concrete composite beams. *Constr. Build. Mater.* 151, 36–42. doi:10.1016/j.conbuildmat.2017.06.063

Khorsandnia, N., Valipour, H., and Bradford, M. (2018). Deconstructable timber-concrete composite beams with panelised slabs: finite element analysis. *Constr. Build. Mater.* 163, 798–811. doi:10.1016/j.conbuildmat.2017.12.169

Li, H., Zhang, H., Qiu, Z., Su, J., Wei, D., Lorenzo, R., et al. (2019). Mechanical properties and stress strain relationship models for bamboo scrimber. *J. Renew. Mater.* 8, 13–27. doi:10.32604/jrm.2020.09341

Martins, C., Dias, A. M. P. G., Costa, R., and Santos, P. (2016). Environmentally friendly high performance timber–concrete panel. *Constr. Build. Mater.* 102, 1060–1069. doi:10.1016/j.conbuildmat.2015.07.194

Saulius, K., Audronis, K., and Balys, V. (2007). Mechanical behaviour of timber-to-concrete connections with inclined screws. *J. Civ. Eng. Manag.* 13, 201–207. doi:10.3846/13923730.2007.9636437

Sebastian, W. M., Mudie, J., Cox, G., Piazza, M., Tomasi, R., and Giongo, I. (2016). Insight into mechanics of externally indeterminate hardwood-concrete composite beams. *Constr. Build. Mater.* 102, 1029–1048. doi:10.1016/j.conbuildmat.2015.10.015

Shan, B., Wang, Z. Y., Li, T. Y., and Xiao, Y. (2020). Experimental and analytical Investigations on short-term behavior of glubam-concrete composite beams. *J. Struct. Eng.* 146, 04019217. doi:10.1061/(ASCE)ST.1943-541X.0002517

Shan, B., Xiao, Y., Zhang, W. L., and Liu, B. (2017). Mechanical behavior of connections for glubam-concrete composite beams. *Constr. Build. Mater.* 143, 158–168. doi:10.1016/j.conbuildmat.2017.03.136

Shangguan, W., Zhong, Y., Xing, X., Zhao, R., and Ren, H. (2015). Strength models of bamboo scrimber for compressive properties. *J. Wood Sci.* 61, 120–128. doi:10.1007/s10086-014-1444-9

Tian, L.-m., Kou, Y.-f., and Hao, J.-p. (2019). Axial compressive behaviour of sprayed composite mortar–original bamboo composite columns. *Constr. Build. Mater.* 215, 726–736. doi:10.1016/j.conbuildmat.2019.04.234

Wang, Z., Wei, Y., Li, N., Zhao, K., and Ding, M. (2020). Flexural behavior of bamboo–concrete composite beams with perforated steel plate connections. *J. Wood Sci.* 66, 1–20. doi:10.1186/s10086-020-1854-9

Wei, Y., Ji, X., Duan, M., and Li, G. (2017a). Flexural performance of bamboo scrimber beams strengthened with fiber-reinforced polymer. *Constr. Build. Mater.* 142, 66–82. doi:10.1016/j.conbuildmat.2017.03.054

Wei, Y., Ji, X. W., Duan, M. J., Zhao, L. L., and Li, G. F. (2018). Model for axial stress-strain relationship of bamboo scrimber. *Acta Mater. Compos. Sin.* 35, 572–579 [in Chinese, with English summary]. doi:10.13801/j.cnki.fhclxb.20170608.002

Wei, Y., Ji, X. W., Zhou, M. Q., Zhao, L. L., and Duan, M. J. (2017b). Mechanical properties of bamboo-concrete composite structures with dowel-type connections. *Trans. Chin. Soc. Agric. Eng.* 33, 65–72 [in Chinese, with English summary]. doi:10.11975/j.issn.1002-6819.2017.03.009

Wei, Y., Li, N., Wu, G., Duan, M. J., and Li, G. F. (2017c). Load-slip behavior of perforated plate connections of bamboo-concrete. *J. Southeast. Univ.* 47, 1167–1173. doi:10.3969/j.issn.1001-0505.2017.06.014

Wei, Y., Tang, S., Ji, X., Zhao, K., and Li, G. (2020a). Stress-strain behavior and model of bamboo scrimber under cyclic axial compression. *Eng. Struct.* 209, 110279, [It is English paper]. doi:10.1016/j.engstruct.2020.110279

Wei, Y., Wu, G., Li, G. F., Zhang, Q. S., and Jiang, S. X. (2014). Mechanical behavior of novel FRP-bamboo-concrete composite beams. *J. Central. South. Univ.* 45, 4384–4392 [in Chinese, with English summary. Available at: JournalArticle/5b435954c095d716a4c75fab]

Wei, Y., Yan, S., Zhao, K., Dong, F., and Li, G. (2020b). Experimental and theoretical investigation of steel-reinforced bamboo scrimber beams. *Eng. Struct.* 223, 111179. doi:10.1016/j.engstruct.2020.111179

Wei, Y., Zhao, K., Hang, C., Chen, S., and Ding, M. (2020c). Experimental study on the creep behavior of recombinant bamboo. *J. Renew. Mater*. 8, 251–273. doi:10.32604/jrm.2020.08779

Wei, Y., Zhou, M. Q., and Yuan, L. D. (2016). Mechanical performance of glulam bamboo columns under eccentric loading. *Acta Mater. Compos. Sin.* 33, 379–385 [in Chinese]. doi:10.13801/j.cnki.fhclxb.20150703.002

Xu, M., Cui, Z., Chen, Z., and Xiang, J. (2017). Experimental study on compressive and tensile properties of a bamboo scrimber at elevated temperatures. *Constr. Build. Mater.* 151, 732–741. doi:10.1016/j.conbuildmat.2017.06.128

Yu, Y., Liu, R., Huang, Y., Meng, F., and Yu, W. (2017). Preparation, physical, mechanical, and interfacial morphological properties of engineered bamboo scrimber. *Constr. Build. Mater.* 157, 1032–1039. doi:10.1016/j.conbuildmat.2017.09.185

Zhang, Y., Peng, H., and Lv, W. (2018). Shear stress transfer model for evaluating the fracture behaviour of SHCCs for RC shear strengthening. *Mag. Concr. Res.* 70, 512–517. doi:10.1680/jmacr.17.00104

Zhang, Y., Wei, Y., Bai, J., Wu, G., and Dong, Z. (2020). A novel seawater and sea sand concrete filled FRP-carbon steel composite tube column: concept and behaviour. *Compos. Struct.* 246, 112421. doi:10.1016/j.compstruct.2020.112421

Zhong, Y., Wu, G., Ren, H., and Jiang, Z. (2017). Bending properties evaluation of newly designed reinforced bamboo scrimber composite beams. *Constr. Build. Mater.* 143, 61–70. doi:10.1016/j.conbuildmat.2017.03.052

Conflict of Interest: The authors declare that the research was conducted in the absence of any commercial or financial relationships that could be construed as a potential conflict of interest

frontiers
in Materials

ORIGINAL RESEARCH
published: 28 September 2020
doi: 10.3389/fmats.2020.576806

A Deep Belief network and Least Squares Support Vector Machine Method for Quantitative Evaluation of Defects in Titanium Sheet Using Eddy Current Scan Image

Jun Bao [1,2], *Bo Ye* [1,2]*, *Xiaodong Wang* [1,2] *and Jiande Wu* [1,2]

[1] Faculty of Information Engineering and Automation, Kunming University of Science and Technology, Kunming, China, [2] Yunnan Key Laboratory of Artificial Intelligence, Kunming University of Science and Technology, Kunming, China

OPEN ACCESS

Edited by:
Jun Wu,
Huazhong University of Science and Technology, China

Reviewed by:
GuiYun Tian,
Newcastle University, United Kingdom
Pingjie Huang,
Zhejiang University, China
Wuliang Yin,
The University of Manchester, United Kingdom

Correspondence:
Bo Ye
yeripple@hotmail.com

Specialty section:
This article was submitted to Structural Materials, a section of the journal Frontiers in Materials

Received: *27 June 2020*
Accepted: *26 August 2020*
Published: *28 September 2020*

Citation:
Bao J, Ye B, Wang X and Wu J (2020) A Deep Belief network and Least Squares Support Vector Machine Method for Quantitative Evaluation of Defects in Titanium Sheet Using Eddy Current Scan Image. Front. Mater. 7:576806. doi: 10.3389/fmats.2020.576806

Titanium (Ti) is an ideal structural material whose use is gradually emerging in civil engineering. Regular defect evaluation is indispensable during the long-term use of Ti sheets, which can be performed effectively using eddy current (EC) imaging, a method of visualizing defects that is convenient for inspectors. However, as EC scan images contain abundant information and have discrepancies in terms of their quality, it is difficult to extract effective features, thus affecting the evaluation results. In this article, we propose a method that combines the EC imaging technology with a quantitative evaluation method for Ti sheet defects based on the deep belief network (DBN) and least squares support vector machine (LSSVM). A multilayer DBN is constructed to extract the effective features from EC scan images for Ti sheet defects. Based on the extracted feature vectors, a multi-objective regression model of defect dimensions is established using the LSSVM algorithm. Then, the dimensions of Ti sheet defects such as length, diameter, and depth are quantitatively evaluated by the effective features and the efficient regression model. The experimental results show that the evaluation errors for the defect lengths and depths tested are less than 3 and 5%, respectively, confirming the validity of the proposed method.

Keywords: titanium sheet, eddy current scan image, feature extraction, defect quantitative evaluation, deep belief network

INTRODUCTION

Titanium (Ti) is an ideal structural material with excellent all-round properties, such as low density, high specific strength, and excellent corrosion resistance (Cui et al., 2011). For decades, Ti was mainly used in the aerospace and defense industries (Malwina, 2016). Later, as its production increased, it was also gradually applied to other fields, such as the chemical and medical industries, and ocean and civil engineering (Gurrappa, 2003; Veiga et al., 2012; Bayrak and Yilgor Huri, 2018). In civil engineering, Ti sheets can be safely connected with ceramics, glass, and concrete because all of these materials have similar thermal expansion coefficients (Winowiecka and Adamus, 2016). As a result, the Ti sheet structures constructed are not only light and beautiful but can also be made resistant to chemical pollution, acid rain, and marine corrosion (Adamus, 2014); this construction method has been successfully applied to marine buildings and earthquake-proof constructions around the world (Adamus, 2014; Malwina, 2016). Despite the excellent all-round properties of Ti sheets, defects are inevitably produced during long-term use. In order to ascertain the remaining life of the Ti sheets, it is important to characterize the dimensions of Ti sheet defects. Therefore, a method for effectively detecting and evaluating Ti sheet defects is indispensable.

Eddy current testing (ECT) is a nondestructive testing method based on electromagnetic induction (Sophian et al., 2001), which has been widely used for detecting and evaluating defects in conductive parts of engineered structures. Compared with other nondestructive testing methods, ECT has many advantages, such as no contact, low cost, and no pollution (Fan et al., 2016). In ECT, the characterization of a material defect is considered to be an inverse problem, in which the defect dimensions are retrieved from the detected signals (Tian et al., 2005). Traditionally, the dimensions of a defect have been estimated by visual judgment of ECT detection signals by an inspector. This method usually requires highly trained personnel, and the results are usually influenced by the subjectivity of the inspector (Fan et al., 2016). Thus, some researchers have turned to machine learning methods to deal with the ECT inverse problem. In these methods, defect feature extraction mainly relies on a manual design or simple signal processing methods, such as principal component analysis (PCA) and independent component analysis (ICA) (Tian et al., 2005; Sophian et al., 2003; He et al., 2013; Daura and Tian, 2019), while the quantitative evaluation of defects mainly employs conventional machine learning methods, such as artificial neural network (ANN) and Bayesian network (Wrzuszczak and Wrzuszczak, 2005; Khan and Ramuhalli, 2008). In recent years, improved visualization methods for ECT have been developed that can accurately and intuitively reflect the shape, degree, and position of defects, while keeping the original advantages of ECT. Bodruzzaman et al. reported a neural network–based method for estimating the dimension of cracks in metal plates using eddy current (EC) scan images (Bodruzzaman and Zein-Sabatto, 2008). Diraison et al. presented an EC imager designed for defect evaluation of aeronautical lap joints, with PCA used to extract the EC image features for defect characterization (Diraison et al., 2009). He et al. investigated pulsed EC (PEC) imaging, with defect evaluation performed based on the morphological features of EC scan images (He et al., 2011). Ye et al. used a giant magnetoresistance (GMR) array to image crack defects in the inner wall of a steam generator tube and evaluated the crack depth using the amplitude of the defect area in the EC image (Ye et al., 2016). Nafiah et al. used PEC testing to obtain an EC scan image of an inclined crack, and then, three image-based features were designed to characterize the inclination and depth of the crack (Nafiah et al., 2019). With improvements in ECT scanning speed, the EC image contains more information, and there are discrepancies in image quality under different working conditions. Therefore, extracting effective features using an artificial design or simple signal processing becomes difficult, which affects the efficacy of quantitative evaluation.

To solve the above problem, deep learning seems to be a good solution. Because deep learning methods have powerful nonlinear characterization and self-learning capabilities, they are very useful for extracting essential features from high-dimensional nonlinear data (Cheng et al., 2019). In 2006, Hinton et al. discussed the deep learning theory for the first time and proposed a deep belief network (DBN) built from multiple stacked restricted Boltzmann machines (RBMs) to solve the difficulty of deep network training and optimization (Hinton et al., 2006; Hinton and Salakhutdinov, 2006). To date, deep learning has achieved good performance in many fields, such as image recognition, voice detection, and fault diagnosis (Zhang and Wu, 2013; O'Connor et al., 2013; Chen and Li, 2017; Wu et al., 2020). These valid theoretical foundations and successful applications provide new ideas for the ECT field. Currently, combining deep learning with the ECT technology is a trend in the future development of modern civil engineering material testing. Therefore, in this article, we propose a method that combines the EC scan imaging technology with a quantitative evaluation method for Ti sheet defect evaluation based on DBNs and least squares support vector machine (LSSVM). First, unsupervised self-learning was conducted on multiple RBMs layer by layer, and the trained RBMs were stacked to construct a multilayer DBN, before conducting supervised fine-tuning. Then, defect features were extracted from the EC scan images of Ti sheets using the trained DBN. Finally, based on the extracted feature vectors, a multi-objective regression model of defect dimensions was established using the LSSVM algorithm. This combination of effective features and an efficient regression model was used to perform the quantitative evaluation of Ti sheet defects. Detection and evaluation experiments were conducted on Ti sheets with different degrees of defects to confirm the validity of the proposed method. The proposed method does not require manually design features, avoiding inspector subjectivity. Furthermore, the deep learning method provides essential and concise features, leading to higher accuracy and reliability for the proposed method than for conventional methods.

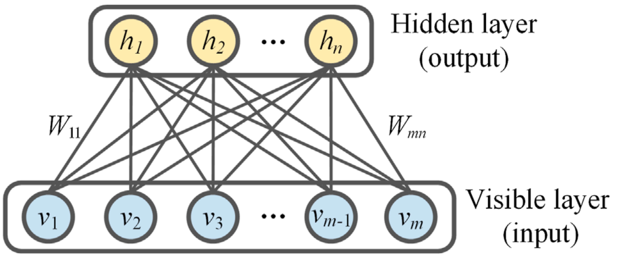

FIGURE 1 | Structure of an restricted Boltzmann machine.

The remainder of the work is arranged as follows: the DBN used for feature extraction and LSSVM used for multi-objective regression of defect dimensions are briefly introduced in **Section 2**; then, the experimental setup and materials are described in **Section 3**; in **Section 4**, the experimental results are described and discussed; and finally, conclusions and further potential work are outlined in **Section 5**.

METHOD

Restricted Boltzmann Machine

An RBM (Hinton, 2012) is a basic unit constituting the DBN and can be regarded as a neural network containing a visible layer and a hidden layer, with the number of neurons in the hidden layer usually being smaller than that in the visible layer. The main purpose of an RBM is to compress a given data set and to minimize the reconstruction error so as to obtain the effective features of the original data set. The structure of an RBM is shown in **Figure 1**.

According to **Figure 1**, combined with EC scan imaging, the visible layer represents a column vector of a rearranged EC image, while the hidden layer represents the features after dimension reduction. There is a bidirectional symmetric connection between the two layers of the RBM, with no connections within each of the layers. An RBM is an energy-based model (Zhang and Wu, 2013), with the layer-by-layer learning process following the energy function expressions:

$$E(\mathbf{v},\mathbf{h}|\theta) = -\sum_{i=1}^{m} a_i v_i - \sum_{j=1}^{n} b_j h_j - \sum_{i=1}^{m}\sum_{j=1}^{n} v_i W_{ij} h_j, \tag{1}$$

where $\theta = \{\boldsymbol{W} = (W_{\mathrm{ij}})_{m\times n}, \boldsymbol{a} = (a_{ij})_{1\times m}, \text{ and } \boldsymbol{b} = (b_i)_{1\times n}\}$ are the model parameters; v_i and a_i are the state and bias of the ith neuron in the visible layer, respectively; h_i and b_i are the state and bias of the jth neuron in the hidden layer, respectively; W_{ij} is the connection weight between the ith visible neuron and the jth hidden neuron; and m and n are the number of neurons in the visible and hidden layers, respectively.

Based on the above energy function, the joint probability distribution of the RBM over the visible and hidden neurons is defined as follows:

$$P(\mathbf{v},\mathbf{h}|\theta) = \frac{e^{-E(v,h|\theta)}}{\sum\limits_{v}\sum\limits_{h} e^{-E(v,h|\theta)}}. \tag{2}$$

Due to the structure of the RBM model (full connectivity between layers and no connectivity within layers), when the state of visible neurons is given, the activation state of each hidden neuron is conditionally independent, and vice versa (Chen and Li, 2017). Therefore, the conditional probabilities over hidden and visible neurons are given by

$$\begin{cases} P\left(h_j = 1\middle|\mathbf{v},\theta\right) = sig\left(b_j + \sum_i v_i W_{ij}\right) \\ P(v_i = 1|\mathbf{h},\theta) = sig\left(a_i + \sum_j W_{ij} h_j\right) \end{cases}, \tag{3}$$

where $sig(x)$ is a sigmoid function, which is selected as the activation function in this study.

RBM training involves adjusting the parameter θ. The training objective is to maximize the likelihood function $L(\theta|\bar{\mathbf{v}}) = P(\mathbf{v} = \bar{\mathbf{v}}|\theta)$ using the gradient descent algorithm (O'Connor et al., 2013). Suppose the input data are $\mathbf{v}^t = (v_1^t, v_2^t, \cdots, v_m^t)^T, t = 1, 2, \cdots, N$, the calculation of gradients is performed according to the following equations:

$$\begin{cases} \dfrac{\partial \ln L(\theta|\mathbf{v}^t)}{\partial W_{ij}} = P\left(h_j = 1\middle|\mathbf{v}^t\right)v_i^t - \sum_v P(\mathbf{v})P\left(h_j = 1\middle|\mathbf{v}\right)v_i, \\ \dfrac{\partial \ln L(\theta|\mathbf{v}^t)}{\partial a_i} = v_i^t - \sum_v P(\mathbf{v})v_i, \text{ and} \\ \dfrac{\partial \ln L(\theta|\mathbf{v}^t)}{\partial b_j} = P\left(h_j = 1\middle|\mathbf{v}^t\right) - \sum_v P(\mathbf{v})P\left(h_j = 1\middle|\mathbf{v}\right). \end{cases} \tag{4}$$

The calculation of $P(v)$ in **Eq 4** is very complicated. In this study, contrastive divergence (CD) (Hinton, 2002) is used to provide an approximate estimation. During training, the parameter θ is updated according to the following equations:

$$\begin{cases} W_{ij} = W_{ij} + \epsilon \dfrac{\partial \ln L(\theta|v^t)}{\partial W_{ij}} \\ a_i = a_i + \dfrac{\partial \ln L(\theta|v^t)}{\partial a_i} \\ b_j = b_j + \epsilon \dfrac{\partial \ln L(\theta|v^t)}{\partial b_j} \end{cases}, \tag{5}$$

where $\varepsilon > 0$ is the learning rate.

Deep Belief Network

A DBN is a deep network composed of multiple RBMs and is a feedforward neural network algorithm with the advantages of multiple hidden layers and fast training (Hinton et al., 2006). Due to a large number of pixels and discrepancy in quality of EC scan images, it is difficult to obtain effective defect features via self-learning using only one RBM. Therefore, in this study, a DBN containing multiple hidden layers is constructed by stacking multiple RBMs, which realize self-learning of effective features layer by layer. **Figure 2** shows a DBN comprising three stacked layers of RBMs. The training process for a DBN consists of two stages (Hinton et al., 2006): the unsupervised pretraining stage and the supervised fine-tuning stage:

(1) Pretraining uses the layer-by-layer greedy algorithm (Bengio et al., 2007) to train each RBM separately. When the training of the first layer of an RBM is completed, its output is taken as the input of the next layer of the RBM, and then, this process of transmission continues layer by layer. During the training of each layer of an RBM, the gradient is calculated according to **Eq 4** and the parameters are updated according to **Eq 5**.

(2) After pretraining, multiple RBMs are stacked, and a logic layer is added as the top layer to construct a DBN containing multiple hidden layers. The stacking of RBMs described above can be understood as initializing a deep neural network with the connection weights of multiple RBMs as an initial weight of the deep neural network. Then, the back propagation (BP) algorithm and the batch gradient descent method are used to fine-tune the network. During the training process, the error is back-propagated to each layer of the RBM from high to low, with the parameters between each layer adjusted until the maximum number of iterations is reached, to achieve the optimal DBN model

Least Squares Support Vector Machine

The LSSVM (Suykens and Vandewalle, 1999) is an improved version of the general SVM. It transforms the quadratic programming problem arising from the constraint conditions of the traditional SVM to the problem of solving linear equations, which greatly improves the solution speed (Haifeng and Dejin, 2005). In many cases, the relationship between defects and features is very complex and nonlinear, making it difficult to

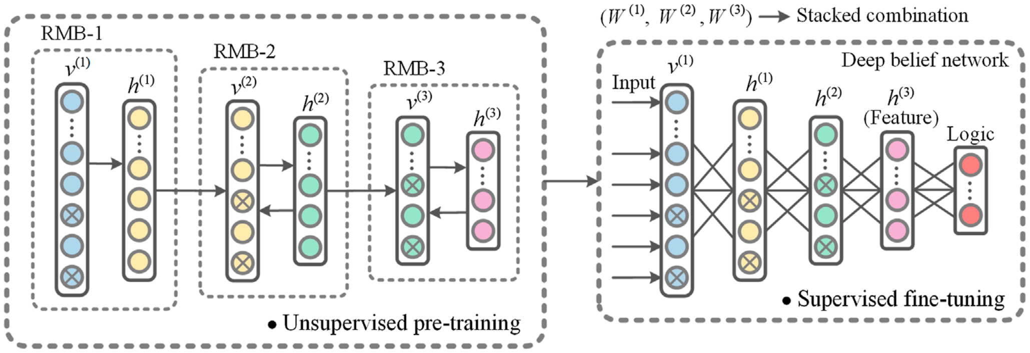

FIGURE 2 | Deep belief network structure.

build an effective mathematical model. Therefore, the LSSVM algorithm is used in this study to establish a multiple-objective regression model using the extracted features, allowing for the quantitative evaluation of defects.

For the input sample set (x_i, y_i), $i = 1, 2, \ldots, l$, x_i and y_i indicate the feature vector and defect parameters of the ith EC scan image, and l is the total number of samples. The nonlinear mapping Φ maps the features to a feature space, with the regression model expressed as

$$y = f(x) = \omega^T \Phi(x) + b. \tag{6}$$

Determining unknown parameters ω and b is equivalent to solving the following optimal problem:

$$\begin{cases} \min \frac{1}{2}\left(\|\omega\|^2 + \gamma \sum_{i=1}^{l} e_i^2\right) \\ s.t. \omega^T \Phi(x_i) + b + e_i = y_i, i = 1, 2, \cdots, l \end{cases}, \tag{7}$$

where γ is the regularization parameter controlling the penalty degree of error, ω is the weight vector, Φ is a kernel function, b is the bias, and e_i is the error variable. To solve this optimization problem, the Lagrange multiplier is introduced to construct a Lagrange function:

$$\begin{aligned} L(\omega, b, e, \alpha) = &\frac{1}{2}\left(\|\omega\|^2 + \gamma \sum_{i=1}^{l} e_i^2\right) \\ &- \sum_{i=1}^{l} \alpha_i \left(\omega^T \Phi(x_i) + b + e_i - y_i\right). \end{aligned} \tag{8}$$

According to the Karush–Kuhn–Tucker (KKT) condition for solving the nonlinear programming problem, the equation for solving ω and b is obtained as follows (Suykens and Vandewalle, 1999):

$$\begin{bmatrix} I & 0 & 0 & -Z \\ 0 & 0 & 0 & L \\ 0 & 0 & \gamma I & -I \\ Z^T & L^T & I & 0 \end{bmatrix} \begin{bmatrix} \omega \\ b \\ e \\ \alpha \end{bmatrix} = \begin{bmatrix} 0 \\ 0 \\ 0 \\ y \end{bmatrix}, \tag{9}$$

where I is an unit vector of l order, $L = [1, 1, \ldots, 1]$, $\alpha = [\alpha_1, \alpha_2, \ldots, \alpha_l]^T$, and $Z = [\Phi(x_1), \Phi(x_2), \ldots, \Phi(x_l)]$. By eliminating ω and e, **Eq 8** can be simplified as follows:

$$\begin{bmatrix} 0 & L \\ L^T & Z^T Z + \frac{1}{\gamma} I \end{bmatrix} \begin{bmatrix} b \\ \alpha \end{bmatrix} = \begin{bmatrix} 0 \\ y \end{bmatrix}, \tag{10}$$

where $Z^T Z = k(x_i, x_j)$, with k being the kernel function of LSSVM.

Since the quantitative evaluation of defects in Ti sheets has obvious nonlinear characteristics, the radial basis kernel function was chosen as k:

$$k\left(x_i, x_j\right) = \exp\left(-\frac{\|x - x_i\|}{2\delta^2}\right), \tag{11}$$

where δ^2 is the kernel parameter. Support vector coefficients α and bias b can be obtained by solving the above linear equations to determine the regression model as follows:

$$y = f(x) = \sum_{i=1}^{l} \alpha_i k(x, x_i) + b. \tag{12}$$

Quantitative Evaluation of Ti Sheet Defects Based on Deep Belief Network and Least Squares Support Vector Machine

Considering the high information content and discrepancy in quality of EC scan images, we propose a method for the quantitative evaluation of Ti sheet defects based on the DBN and LSSVM combined with EC scan imaging. This method stacks multiple RBMs to construct a DBN with multiple layers, with the deep network being trained via unsupervised self-learning and supervised fine-tuning. The trained DBN can fit nonlinear functions well, so it is used to extract the potential high-order features from EC scan images. Based on the extracted features, a multi-objective regression model of defect dimensions (length, diameter, and depth) is established using the LSSVM. The effective

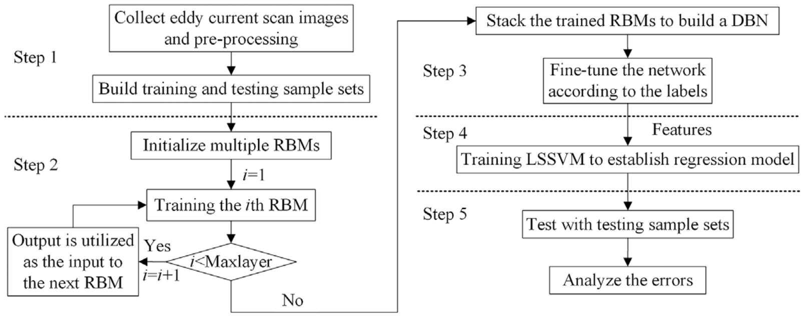

FIGURE 3 | Flowchart of the proposed method.

features and efficient regression model are then combined to achieve the quantitative evaluation of Ti sheet defects. In line with the description given above, the specific steps of the quantitative evaluation method are shown in **Figure 3**.

As shown in **Figure 3**, the main steps carried out to implement this method are as follows:

(1) EC imaging testing is performed on different Ti sheet defects to obtain EC scan images. After preprocessing (such as de-noising), the training and testing samples are constructed.
(2) Multiple RBMs are initialized, and the training samples are input into the first-layer RBM for training. After the training of the first-layer RBM is complete, its output is used as the input for the next-layer RBM, and the training is continued. This process is repeated until the training of all of the RBMs is complete.
(3) Multiple trained RBMs are stacked, and a logic layer is added to construct a DBN containing multiple hidden layers, which is then fine-tuned using the labels of the training samples.
(4) The trained DBN is used to extract features from the training samples; based on these features, a regression model of defect dimensions is established using the LSSVM algorithm.
(5) The above methods are then tested by using the DBN to extract features of the testing samples, which are input into the LSSVM model to obtain quantitative evaluation results. Finally, error analysis is conducted on the results.

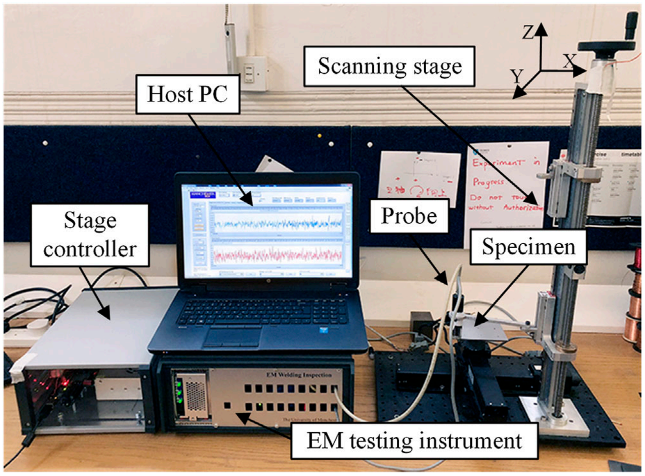

FIGURE 4 | Experimental detection system.

EXPERIMENTAL SETUP AND MATERIALS

The entire detection system used in this study is shown in **Figure 4**, consisting of a programmable scanning stage, a stage controller, an EC probe, a host PC, and an electromagnetic (EM) instrument. The EM instrument was developed by the Sensing, Imaging, and Signal Processing Group at the School of Electrical and Electronic Engineering at the University of Manchester (Yin and Peyton, 2006; Yin et al., 2011). The EM instrument can operate at frequencies of 5–200 kHz and can perform digital demodulation at a rate of 100 k/s (Yin et al., 2019).

The probe used in the above system is a transmitter–receiver (T-R)–type probe composed of two coils: one for excitation and the other for pickup. A schematic of the T-R probe is shown in **Figure 5**. Compared with absolute probes with a single coil, T-R probes have a higher gain, have a wider frequency range, and are unaffected by thermal drift (Cao et al., 2018). In addition, the spatial resolution of T-R probes along a scan line is almost twice as high as that of absolute probes with the same coil size. These characteristics make the T-R probes more suitable for imaging applications (Cheng et al., 2017). Although the T-R probes have good performance, their detection effect is also affected by coil

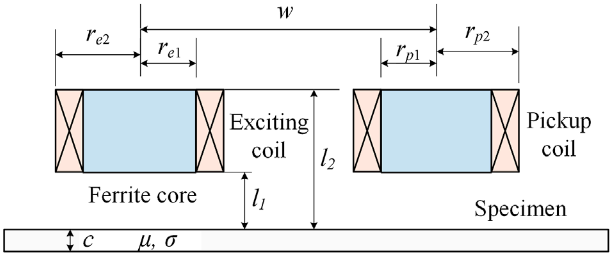

FIGURE 5 | Structure of eddy current probe.

TABLE 1 | Probe parameters.

Probe parameter	Value
Excitation coil outer/inner radius (r_{e1}/r_{e2})	0.75 mm/1.25 mm
Pickup coil outer/inner radius (r_{p1}/r_{p2})	0.75 mm/1.50 mm
Height of coil (l_2–l_1)	3.00 mm
Lift-off (L_1)	0.50 mm
Gap of two coils (w)	3.50 mm
Excitation/pickup coil turns (N_1/N_2)	160/200

parameters such as coil radius, coil gap, and lift-off of the probe. The parameters of T-R probes should be selected as needed.

The larger the coil, the lower the working frequency required for maximum sensitivity; however, it also results in a reduction in spatial resolution (Xu et al., 2018). Considering the dimensions of the smallest defect in the specimen used in this study, the inner radius of the coils was chosen to be 0.75 mm. The outer radius of the coils is related to coil turns to ensure sufficient signal strength. After coil processing, the outer radius of transmitter and receiver coils was 1.25 and 1.50 mm, respectively. In addition, the sensitivity decreases and the lift-off resistance increases with the increase in coil gap (Ona et al., 2019). After testing, the receiving coil voltage was greatest at the smallest coil gap of 2.75 mm and almost zero when the coil gap was greater than 10.00 mm. Following consideration of the balance of sensitivity and lift-off resistance, a median value of 3.50 mm was taken as the coil gap. With a decided coil gap, the voltage variation in the receiver coil will be maximized at a certain lift-off. For the above coil gap, the voltage variation achieves its maximum at a lift-off of 0.50 mm. According to the above analysis, the parameters of the T-R probe used in this study are determined and listed in **Table 1**.

In order to simulate defects of different types and degrees, two representative types of defects were selected for processing in two Ti specimens. As shown in **Figure 6**, cracks and holes were machined in two 3.0-mm-thick Ti (TA2) sheets via electrical discharge machining, respectively. Each specimen contained nine defects of different dimensions. From **Figure 6A**, the width of all cracks was 1.0 mm, while the length of each row was 4.0, 8.0, and 12.0 mm, respectively, and the depth of each column was 0.5, 1.5, and 2.5 mm, respectively; from **Figure 6B**, the hole diameter of each row was 1.0, 2.0, and 3.0 mm, respectively, and the depth of each column was 0.5, 1.5, and 2.5 mm, respectively. The numbers and parameters of defects are listed in **Table 2**.

The T-R probe used in this study is a directional sensor, and the detection mainly relies on the coupling of coils and eddy current, which are predominant in the middle part of two coils. During the scanning process, to facilitate the description, the direction of the connection line between the two coil centers is

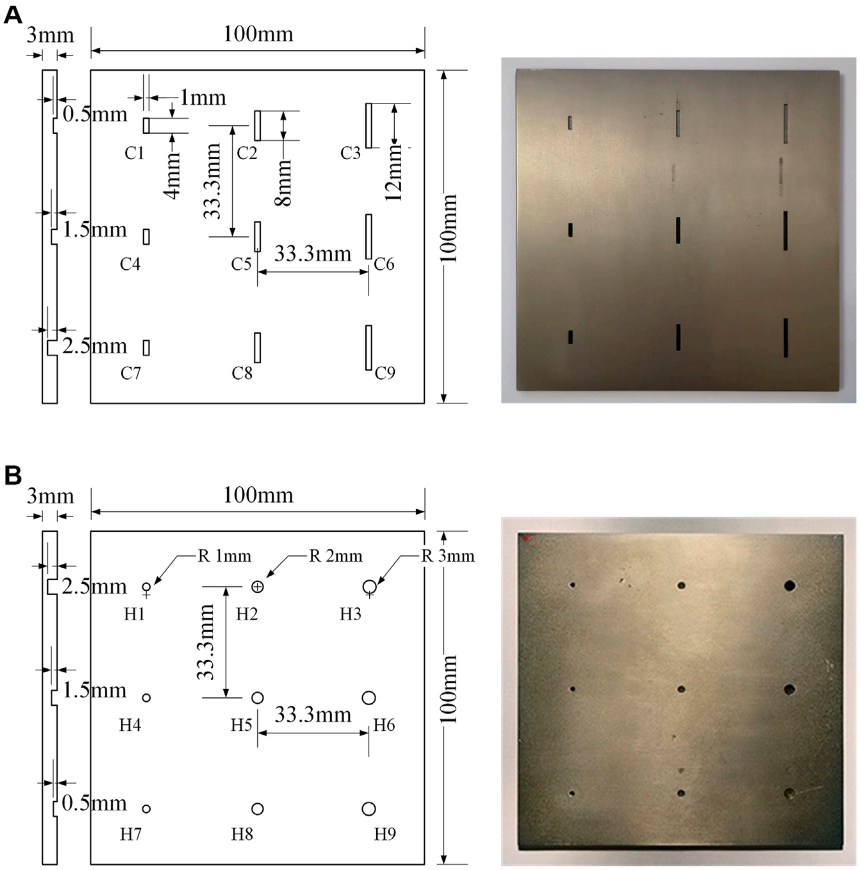

FIGURE 6 | Machined specimen: **(A)** specimen #1; **(B)** specimen #2.

TABLE 2 | Parameters of defects.

Crack no	Length (mm)	Width (mm)	Depth (mm)	Hole no	Diameter (mm)	Depth (mm)
C1/C2/C3	4.0/8.0/12.0	1.0	0.5	H1/H2/H3	1.0/2.0/3.0	2.5
C4/C5/C6	4.0/8.0/12.0	1.0	1.5	H4/H5/H6	1.0/2.0/3.0	1.5
C7/C8/C9	4.0/8.0/12.0	1.0	2.5	H7/H8/H9	1.0/2.0/3.0	0.5

defined as the probe direction, as shown in **Figure 7A**. When the transmitter coil of the T-R probe approaches a defect, the EC is cut off by the defect, as shown in **Figure 7B**. The severed EC is concentrated at the edge of the crack, and the EC density in the middle part of the two coils is stronger than that in the other areas. If the probe direction is along the scan direction, the concentrated EC in the middle of the two coils is propitious to strengthen the coupling between the transmitter and receiver coils. If the probe direction is perpendicular to the scan direction, as shown in **Figure 7C**, the T-R probe is under completely different operation conditions. The receiver coil is away from the area where the EC is concentrated. Thus, the mutual coupling between the transmitter and receiver coils was significantly reduced under the influence of eddy current, and the sensitivity of the receiver coil, which is in the perpendicular direction, decreases significantly.

According to the above discussion, the scan mode used in the experiments is shown in **Figure 8**. Better performance of scan detection can be obtained if the scan direction is along the probe direction, which makes the voltage variation in the receiver coil to be greater when the T-R probe moves to a defect. In this way, defects in the EC scan image will also be better represented. From **Figure 8**, during the experimental measurement, the scan stage was driven by the stage controller to move the probe to scan the specimen: the steps in the X and Y directions were 0.40 and 1.25 mm, respectively, and the scanning points for each defect were arranged in a 40 × 20 grid (covering a 15.60-mm area × 23.75-mm area).

During the scanning process, the EM instrument provided a sine voltage output to the excitation coil of the T-R probe, thereby generating an alternating magnetic field over the specimen. The induced EC generates a magnetic field opposite to the original magnetic field, and the pickup coil receives the resultant magnetic flux. The resultant magnetic flux varies in the presence of a defect, thus changing the induced voltage in the pickup coil. Then, the pickup coil voltage was sampled by the analog-to-digital converter (ADC) in the EM instrument. At the same time, two quadrature reference signals with the same frequency as excitation were generated in the processor of the EM instrument. The two reference signals were input into the digital phase-sensitive detection (PSD) module together with the sampling signal. The real and imaginary parts of the sampling signal were obtained by mixing and integrating the sampling signal and each reference signal. Finally, the real and the imaginary parts of the signals were transmitted to the host PC via an Ethernet interface.

In addition, the working frequency of ECT determines the skin depth and detection accuracy. Generally, the lower the working frequency, the greater the skin depth, but the smaller the detection precision. The selection of working frequency depends on the thickness and electromagnetic characteristics of the measured material. The expression of the standard skin depth δ is given as follows:

$$\delta = 1 \Big/ \sqrt{\pi f \mu_0 \mu_r \sigma}, \tag{13}$$

where f is the working frequency; σ and μ_r are the conductivity and relative permeability of the measured material, respectively; and μ_0 is the permeability of free space.

In the experiment, the thickness of the Ti (TA2) specimen is 3.0 mm, the conductivity is 1.8 MS/m, and the relative permeability is 1. The standard skin depth was selected as 0.7 times the thickness of the specimen to prevent EC from appearing on the other side of the specimen and to ensure the depth and accuracy of the detection. According to **Eq 13**, the working frequency used for the EM instrument in the experiment carried out in this study was 30 kHz.

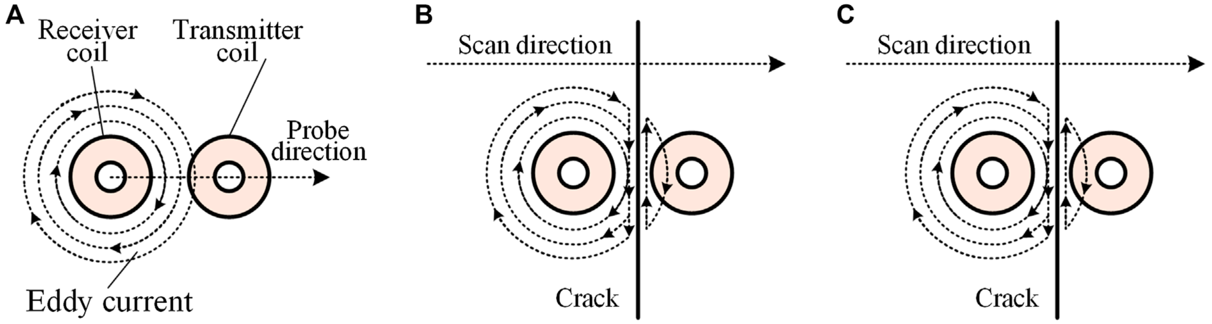

FIGURE 7 | Influence of T-R probe direction: **(A)** probe direction definition; **(B)** probe direction is along the scan direction; **(C)** probe direction is perpendicular to the scan direction.

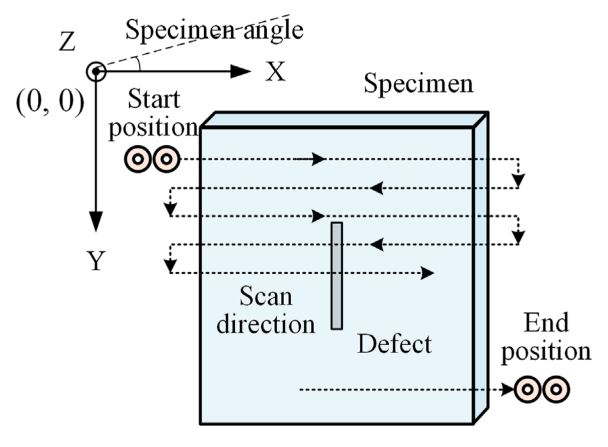

FIGURE 8 | Scan mode.

EXPERIMENTAL RESULTS

A defect in a Ti sheet causes a change in the voltage of the pickup coil. However, for different materials, the sensitivity of the real and imaginary parts of the voltage differs. In order to determine the more sensitive signal components, we first carried out a line scanning along the vertical direction of three defects. Defects with the minimum length and different depths were selected as examples (C1, C4, and C7 defects in specimen #1) and referenced to Ti sheets without defects; the differences in the pickup coil voltages are shown in **Figure 9**.

From **Figures 9A–C**, it can be seen that the real and imaginary parts of the coil voltage difference reach the peak value at the defect center and that the trend of the change is opposite to this. However, the peak-to-peak value of the real part is much larger than that of the imaginary part. As shown in **Figure 9D**, the peak-to-peak value of the real part is on average five times greater than that of the imaginary part. From this, it can be concluded that the real part of the peak-to-peak value is more sensitive at detecting defects in Ti sheets. According to the preliminary testing mentioned above, visualization of defects can be improved by using the difference in the real part because the stronger signals are not as easily drowned out by environmental noise.

The scan mode described in **Figure 8** was adopted to scan the different defects in the two specimens. However, in actual detection, differences in manual operations will result in discrepancies in the quality of the scan images. Such situations were simulated by scanning each defect at different angles and from different start positions to provide experimental samples for subsequent evaluation, where the angle refers to the angle between the specimen and the scan direction, from 0 to 25° with an interval of 5°, and the *X* and *Y* axis coordinates of the start position change in the range of −2 to 2 mm with an interval of 2 mm. With six angles and nine start position combinations, each scan was repeated five times. In total, 270 samples were obtained for each defect: 200 samples of each defect were randomly selected as the training data, and the remaining 70 samples

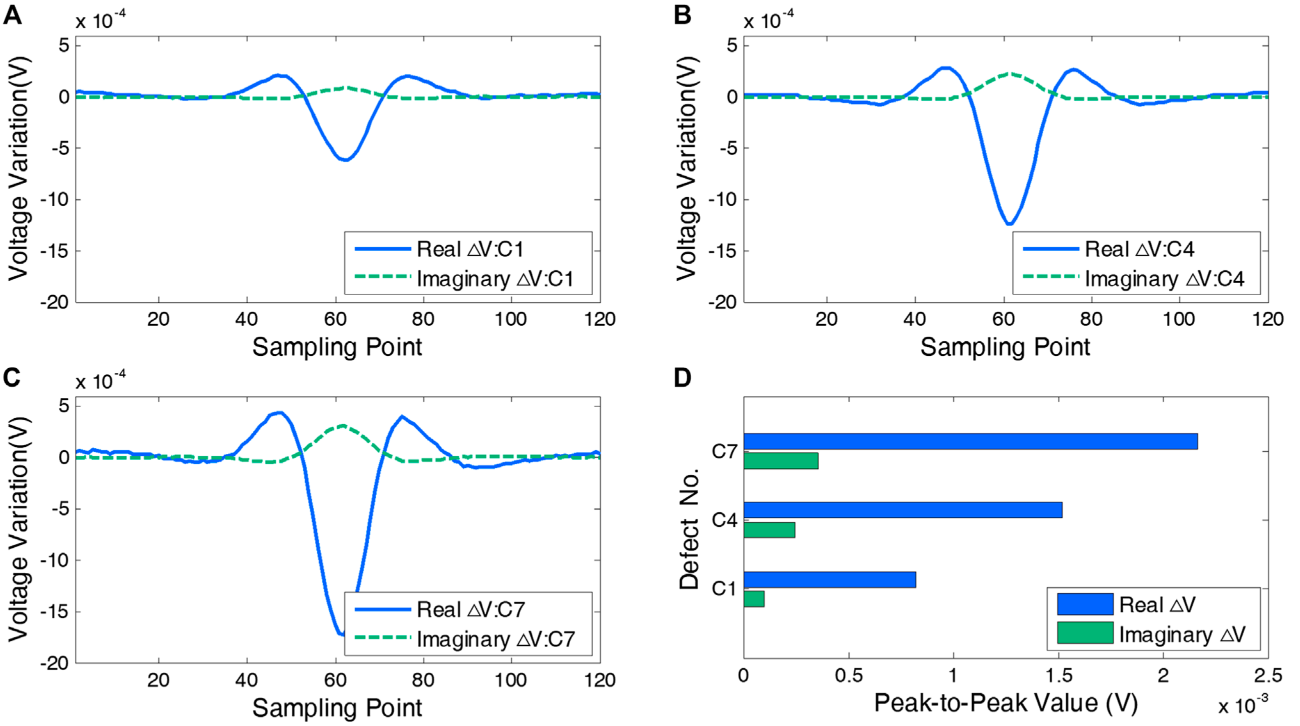

FIGURE 9 | Signal strength comparison: **(A)** real and imaginary parts of voltage difference for C1 notch; **(B)** real and imaginary parts of voltage difference for C4 notch; **(C)** real and imaginary parts of voltage difference for C7 notch; **(D)** comparison of peak-to-peak values.

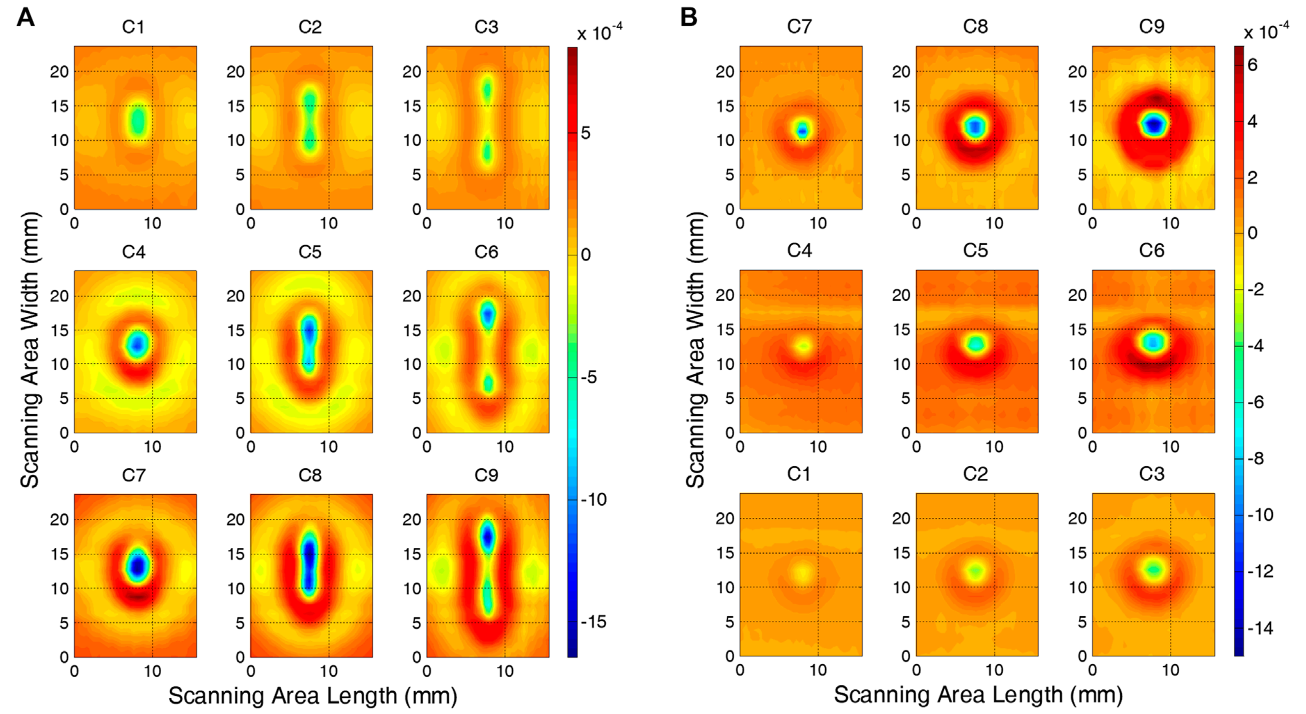

FIGURE 10 | Imaging effect: **(A)** specimen #1 (crack defects); **(B)** specimen #2 (hole defects).

were used as the testing data. Finally, for each specimen, the total number of training samples was 1,800 and the number of testing samples was 630. After the above scan process was completed, taking the scanning image with the start position of (0,0) and scanning angle of 0° as an example, the imaging effect of the two specimens is shown in **Figure 10**.

Figures 10A,B show the nine crack defects and nine hole defects in specimens #1 and #2, respectively. In **Figures 10A,B**, each panel represents the imaging effect of the defect of the corresponding number, allowing the shape and depth of defects to be intuitively assessed in EC scan images. For the defects with the same shape, the defect regions in EC scan images had relatively similar contours. For the defects with the same depth, the defect regions in EC scan images had similar pixel value distribution, and as the defect depth increases, the color value of the defect region in EC scan image gradually decreases.

Before the experiments of feature extraction and quantitative evaluation, how the parameters in the DBN and LSSVM affect the performance of the proposed method was first discussed and analyzed. The network structure is the most important factor for the DBN and is related to the number of hidden neurons and the

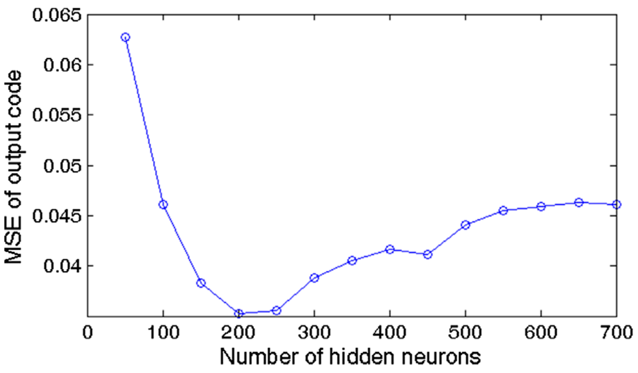

FIGURE 11 | Mean square error (MSE) curves of different numbers of hidden neurons.

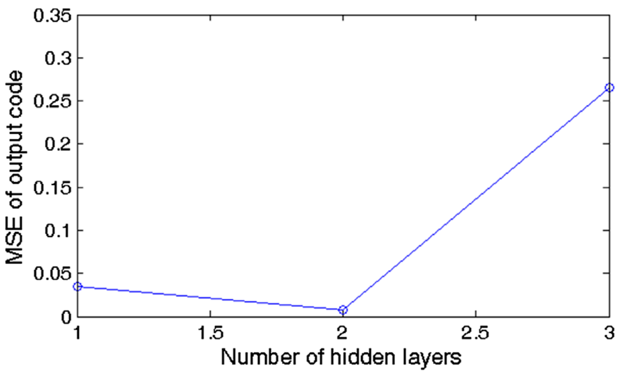

FIGURE 12 | Mean square error curves of different numbers of hidden layers.

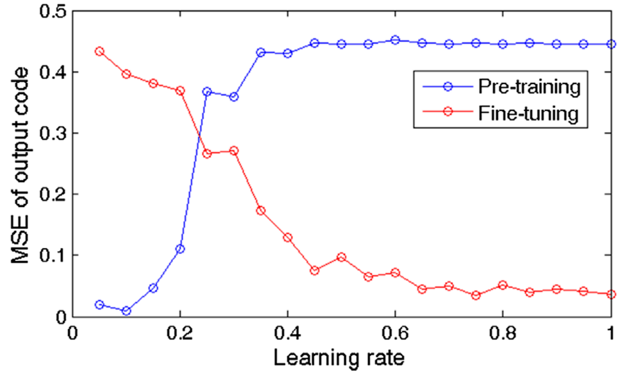

FIGURE 13 | MSE curves of different numbers of learning rate.

TABLE 3 | Parameters of deep belief network model.

Parameter	Value
Network structure	800/200/50/9
Activation function	Sigmoid
Learning rate (pretraining/fine-tuning)	0.10/1.00
Momentum factor	0.50
Batch size	100
Epoch number (pretraining/fine-tuning)	350/150

number of layers. Since each RBM in the DBN is independently trained, taking the first RBM to construct a DBN as an example, an experiment was conducted to determine the appropriate number of hidden neurons. The input layer and the output layer were set to 800 and nine neurons, respectively, representing the input data dimension and the binary-coded defect type. The hidden neurons were set to 50–700 at a step of 50. The mean square error (MSE) between output code and actual code is used to evaluate feature characterization ability of the DBN. The mean results of two specimens are shown in **Figure 11**. It is noted that the feature characterization results seem to be satisfactory when the number of neurons in the hidden layer is less than 1/4th that in the previous layer.

Based on the analysis above, the number of hidden layers in the DBN was set to 1–3, and their network structure was 800/200/9, 800/200/50/9, and 800/200/50/12/9, respectively. An experiment was conducted to analyze the influence of the number of hidden layers on the deep learning structure. The results for each experimental condition are shown in **Figure 12**. It is noted that the results seem to be best when the number of hidden layers is 2.

Learning rate plays an important role in the DBN to determine whether and when the objective function converges to the minimum; momentum factor determines the direction and efficiency of gradient descent. So, a suitable learning rate and momentum factor could not only improve the learning ability but also enhance the computing efficiency. Taking all of the above results together, further experiments of the learning rate and momentum factor were conducted. In the experiments, the learning rate was set to 0.05–1.00 in the pretraining and fine-tuning stages; when one stage was analyzed, the learning rate of the other stage remained unchanged, which was 1.00; the momentum factor was set to 0.05–1.00 in pretraining and fine-tuning stages. The results of the experiments above are shown in **Figures 13** and **14**, respectively.

From **Figure 13**, in the pretraining stage, the MSE increases with the increase in the learning rate, and the MSE becomes stable gradually after the learning rate is greater than 0.35. In addition, the MSE achieves its minimum of 0.01 at a learning rate of 0.10. In the fine-tuning stage, the MSE decreases with the increase in the learning rate. As the learning rate varies from 0.70 to 1.00, the MSE clearly decreases, with a result of 0.037–0.049, and the MSE shows little variation when the learning rate continues to increase. From **Figure 14**, when the momentum factor was taken as an intermediate value, the MSE is the smallest, and the MSE achieves its minimum of 0.021 at a momentum factor of 0.50.

After the above analysis and preliminary experiment, the DBN used in this experiment was set to contain two hidden layers, and the outputs of the last hidden layer were the extracted features. Detailed parameters of the DBN are listed in **Table 3**.

In LSSVM algorithm, the regularization parameter and kernel parameter directly affect the learning and generalization ability. Besides, there is no necessary relationship between the

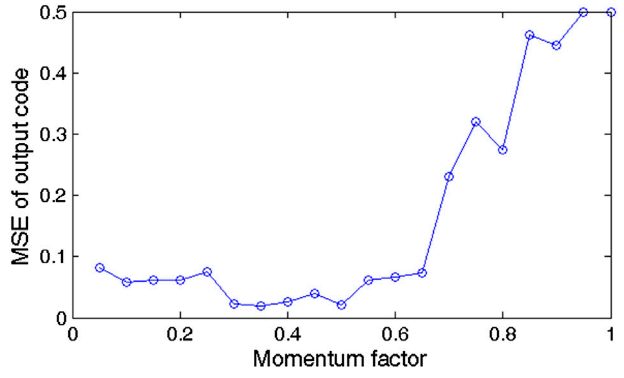

FIGURE 14 | MSE curves of different numbers of momentum factor.

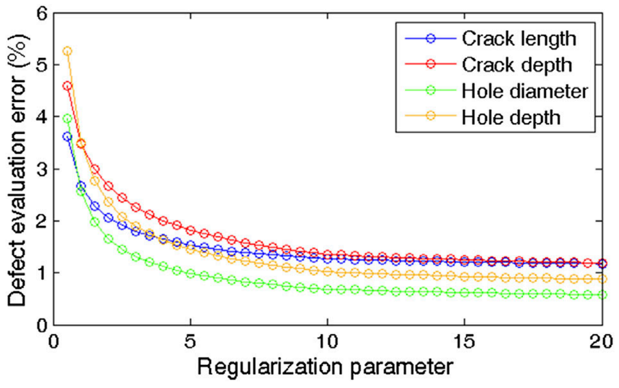

FIGURE 15 | Defect evaluation results of different regularization parameters.

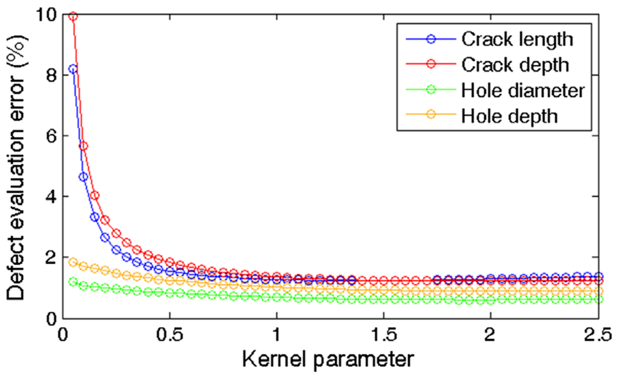

FIGURE 16 | Defect evaluation results of different kernel parameters.

regularization parameter and kernel parameter. Thus, they can be analyzed and discussed independently. A DBN model with the parameters in **Table 3** was trained by training samples. The trained DBN model was used to extract features from the training and testing samples. The features from the training samples were used to establish the LSSVM regression model, and the features from the testing samples were used to analyze how the parameters affect the LSSVM. The regularization parameter was set to 0.1–20.0, and the kernel parameter was set to 0.05–2.50. According to the above parameter settings, the relative errors of defect evaluation by using the LSSVM are shown in **Figures 15** and **16**.

From **Figure 15**, the relative error of defect evaluation decreases with the increase in the regularization parameter. For both crack and hole defects, the relative error decreases obviously in the range of the regularization parameter from 0.5 to 12.0, and the relative error shows little variation when the regularization parameter continues to increase. From **Figure 16**, the variation in relative error with the kernel parameter is similar to the above description of the regularization parameter. The relative error shows little variation when the kernel parameter is greater than 1.00 and achieves its minimum at a kernel parameter of 1.50. So, we determine that the regularization parameter and kernel parameter of the LSSVM are 10.0 and 1.50, respectively.

After the above preliminary experiments, we analyzed the effects of parameters in the DBN and LSSVM on the performance of the proposed method and determined the optimal parameters. Next, the feature extraction and defect quantitative evaluation experiments were carried out. A

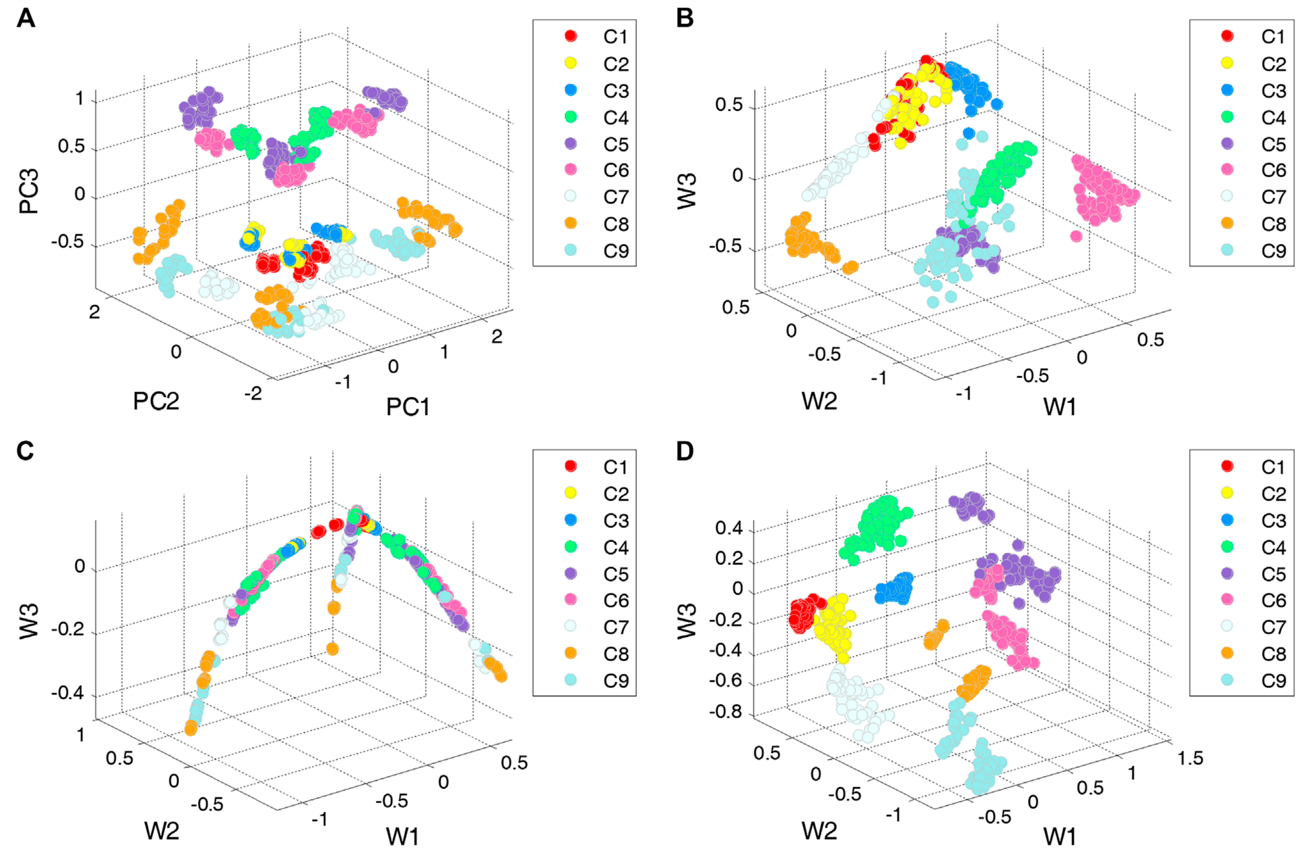

FIGURE 17 | Comparison of feature extraction effects: **(A)** PCA; **(B)** ANN; **(C)** RBM; **(D)** DBN.

TABLE 4 | Relative error of the defect evaluation of deep belief network–least squares support vector machine.

Defect parameter of specimen #1	**Relative error of the corresponding defect (%)**									
	C1	**C2**	**C3**	**C4**	**C5**	**C6**	**C7**	**C8**	**C9**	**Mean**
Crack length	4.020	1.844	0.477	1.434	0.086	0.510	2.242	0.047	0.439	1.233
Crack depth	2.931	2.609	2.236	0.355	0.579	0.479	0.873	0.717	0.322	1.233
Defect parameter of specimen #2	**Relative error of the corresponding defec (%)**									
	H1	**H2**	**H3**	**H4**	**H5**	**H6**	**H7**	**H8**	**H9**	**Mean**
Hole diameter	0.657	0.722	0.986	0.997	0.257	0.407	1.058	0.180	0.305	0.619
Hole depth	1.987	2.067	2.551	0.212	0.355	0.283	0.296	0.306	0.219	0.920

trained DBN model was used to extract features from the EC scan images in the testing samples. In addition, in this experiment, PCA, ANN, and single-layer RBM were used for comparison, where the number of neurons in each layer of the ANN was set to 800/200/50/9 and the structure of the RBM was set to 800/50, with the other parameters being the same as those in the DBN. To visualize the distribution of features, the obtained features were mapped to 3D feature vectors, taking specimen #1 as an example, and the results are shown in **Figure 17**.

From **Figure 17**, it can be seen that the defect features extracted by PCA were relatively mixed, which shows that this method has difficulty in processing high-dimensional nonlinear data. The features of the same defect extracted by the ANN were obviously clustered, but for different defects, there were some overlaps of between-class features. The features extracted by the RBM formed a curve-like distribution, also with some overlaps of between-class features when there were too many defect types. The performance of the DBN model was better than that of the other models; this is mainly because the unsupervised self-learning of the DBN (based on its deep structure) is conducive to characterizing the essential and concise high-order features, while the supervised learning of the DBN improves the clustering of inner-class feature sets. Therefore, the features extracted by the DBN are more suitable for the quantitative evaluation of defects.

The extracted features from EC scan images of two specimens were input into the previously established LSSVM regression model to quantitatively evaluate the Ti sheet defects. This experiment involved performing a multi-objective regression task to evaluate the lengths and depths of the crack defects, and the diameters and depths of the hole defects. **Table 4** shows the relative errors of the estimation results.

As shown in **Table 4**, the relative errors of estimation of crack length were between 0.047 and 4.020%, and those of crack depth were between 0.322 and 2.931%; the relative errors of estimation of hole diameter were between 0.180 and 0.997%, and those of the hole depth were between 0.212 and 2.551%. Overall, larger deviations were observed in the estimation of smaller degrees of defects (smaller in length/diameter and depth), and the mean relative errors of the above estimations were 1.233, 1.233, 0.619, and 0.920%, respectively; all errors are very small and within a reasonable range. Then, the above method was compared with other methods. In the comparison experiments, the four types of features (PCA, ANN, RBM, and DBN) described in **Figure 17** were used, and two regression methods, multiple linear regression (MLR) and LSSVM, were used to reconstruct the defect dimensions. **Table 5** shows the mean relative errors of the evaluation results for a total of eight groups of comparison experiments.

As shown in **Table 5**, in terms of the features used in these methods, the performance of the methods using PCA or ANN features is similar. Compared with the above features, the

TABLE 5 | Mean relative error of the defect evaluation of the comparison methods.

Comparison method	**Defect parameter relative error (%)**			
	Crack length	**Crack depth**	**Hole diameter**	**Hole depth**
PCA–MLR	20.006	16.871	13.515	20.776
ANN–MLR	12.423	9.358	7.984	17.779
RBM–MLR	23.091	9.69	6.540	23.649
DBN–MLR	5.477	10.522	3.302	8.561
PCA–LSSVM	3.041	3.893	0.959	1.376
ANN–LSSVM	2.543	2.884	1.008	1.560
RBM–LSSVM	18.164	3.707	1.637	16.991
DBN–LSSVM	1.233	1.233	0.619	0.920

PCA, principal component analysis; MLR, multiple linear regression; ANN, artificial neural network; RBM, restricted Boltzmann machines; DBN, deep belief network; LSSVM, least squares support vector machine.

TABLE 6 | Repeatability of the evaluation methods.

Comparison method	**Defect parameter standard deviation (mm)**			
	Crack length	**Crack depth**	**Hole diameter**	**Hole depth**
PCA–MLR	1.274	0.334	0.195	0.212
ANN–MLR	0.900	0.201	0.199	0.276
RBM–MLR	0.917	0.178	0.148	0.145
DBN–MLR	0.556	0.195	0.097	0.131
PCA–LSSVM	0.218	0.054	0.010	0.009
ANN–LSSVM	0.285	0.045	0.013	0.013
RBM–LSSVM	1.009	0.047	0.054	0.154
DBN–LSSVM	0.116	0.018	0.010	0.009

PCA, principal component analysis; MLR, multiple linear regression; ANN, artificial neural network; RBM, restricted Boltzmann machines; DBN, deep belief network; LSSVM, least squares support vector machine.

performance of RBM features is relatively weak, which indicates that the single-layer RBM is difficult to approximate high-order functions and extract effective features. In addition, the DBN feature has the best performance, and the errors of reconstructed defect dimensions are the smallest, no matter which regression algorithm was used. In terms of the regression algorithm used in these methods, the LSSVM is much better than MLR, and the average error is one order of magnitude smaller, which indicates that the LSSVM is more suitable for dealing with the nonlinear relationship between high-dimensional features and defect dimensions.

These results were further analyzed to evaluate the repeatability of the proposed method. The experiments were repeated under identical conditions, with the standard deviation used to evaluate the repeatability of the proposed method, and the results are shown in **Table 6**.

As shown in **Table 5**, the standard deviations of the experimental results for the DBN–LSSVM method ranged from 0.009 to 0.116 mm for the different defect parameters. These values are far below those of other comparison methods, demonstrating that the results of the proposed method do not readily fluctuate and show better repeatability. All in all, the above experiments prove the validity of the proposed method from the two aspects of accuracy and repeatability. The proposed method can be applied to perform effective detection and quantitative evaluation of Ti sheet defects, providing a novel way of combining deep learning with the EC scan imaging technology.

CONCLUSION

This study proposed a method for quantitatively evaluating Ti sheet defects based on the DBN and LSSVM combined with the EC scan imaging technology. The proposed method utilizes a trained DBN to extract effective features from the EC scan images of Ti sheet defects. Then, based on the extracted feature vectors, the LSSVM algorithm was used to establish a multi-objective regression model of the dimensions of the Ti sheet defects. The combination of effective features and an efficient regression model was used to perform the quantitative evaluation of Ti sheet defects. The main conclusions of this study are as follows:

(1) For defects in Ti materials, the strength of the real part of the detection signal is on average five times greater than that of the imaginary part. Therefore, the real part of the signal is not easily drowned out by environmental noise and can therefore achieve better imaging results. Furthermore, it is also better suited to the quantitative evaluation of defects based on features extracted from EC scan images.
(2) The proposed method does not require manually designed features, thus avoiding the problem of the subjectivity of the inspector. In addition, compared with feature extraction by conventional methods, the proposed method stacks multiple RBMs and combines unsupervised and supervised learning, giving it a stronger ability to characterize features.
(3) The proposed method utilizes the LSSVM algorithm to transform the complex ill-posed ECT inverse problem to a simple problem of solving linear equations. The final experimental results showed that the maximum relative error and standard deviation of the defect evaluation were less than 4.1% and 0.12 mm, respectively, and the proposed method yielded a higher accuracy and repeatability than the other conventional methods tested.

In addition, due to limitations in our capacity to process the specimen, the defects studied in this research were all regular, ideal defects. However, defects often have more complex shapes in actual situations. We hope that future work will be able to extend the proposed method to investigate more complex defects. Second, the method should not be limited to the detection of Ti sheets in civil engineering but can also be extended to other ECT applications, such as reinspection and quality monitoring in the manufacturing of various metal sheets. In industrial production, with the accumulation of EC image data, the training samples will be enriched and the generalization capability of the proposed method will be further improved. We hope that future work will also focus on how to extend the proposed method to more ECT applications.

DATA AVAILABILITY STATEMENT

The raw data supporting the conclusions of this article will be made available by the authors, without undue reservation.

AUTHOR CONTRIBUTIONS

JB proposed the idea and wrote the original manuscript. BY designed the experiments and the titanium sheet specimen. JB and BY analyzed the data. XW and JW guided the research and were tasked with the critical revisions of the manuscript.

FUNDING

This work was supported in part by the National Natural Science Foundation of China under Grant 51465024 and in part by the Applied Basic Research Programs of Science and Technology Commission Foundation of Yunnan Province under Grant 2019FB081.

ACKNOWLEDGMENTS

The authors would like to acknowledge Wuliang Yin (School of Electrical and Electronic Engineering, University of Manchester, United Kingdom) for his help and the experimental instrument provided.

REFERENCES

Adamus, J. (2014). Applications of titanium sheets in modern building construction. *Adv. Magn. Reson.* 1020, 9–14. doi:10.4028/www.scientific.net/AMR.1020.9

Bayrak, E., and Yilgor Huri, P. (2018). Engineering musculoskeletal tissue interfaces. *Front. Mater.* 5. doi:10.3389/fmats.2018.00024

Bengio, Y., Lamblin, P., Popovici, D., and Larochelle, H. (2007). "Greedy layer-wise training of deep networks," in Proceedings of the Advances in neural information processing systems.

Bodruzzaman, M., and Zein-Sabatto, S. (2008). "Estimation of micro-crack lengths using eddy current c-scan images and neural-wavelet transform," in Proceedings of the IEEE SoutheastCon. doi:10.1109/SECON.2008.4494355

Cao, B.-H., Li, C., Fan, M.-B., Ye, B., and Tian, G.-Y. (2018). Analytical model of tilted driver-pickup coils for eddy current nondestructive evaluation. *Chin. Phys. B* 27, 030301. doi:10.1088/1674-1056/27/3/030301

Chen, Z., and Li, W. (2017). Multisensor feature fusion for bearing fault diagnosis using sparse autoencoder and deep belief network. *IEEE Trans. Instrum. Meas.* 66, 1693–1702. doi:10.1109/TIM.2017.2669947

Cheng, J., Qiu, J., Ji, H., Wang, E., Takagi, T., and Uchimoto, T. (2017). Application of low frequency ect method in noncontact detection and visualization of CFRP material. *Compos. B. Eng.* 110, 141–152. doi:10.1016/j.compositesb.2016.11.018

Cheng, Y., Zhu, H., Wu, J., and Shao, X. (2019). Machine health monitoring using adaptive kernel spectral clustering and deep long short-term memory recurrent neural networks. *IEEE Trans. Ind. Inf.* 15, 987–997. doi:10.1109/TII.2018.2866549

Cui, C., Hu, B., Zhao, L., and Liu, S. (2011). Titanium alloy production technology, market prospects and industry development. *Mater. Des.* 32, 1684–1691. doi:10.1016/j.matdes.2010.09.011

Daura, L. U., and Tian, G. Y. (2019). Wireless power transfer based non-destructive evaluation of cracks in aluminum material. *IEEE Sensor. J.* 19, 10529–10536. doi:10.1109/JSEN.2019.2930738

Diraison, Y. L., Joubert, P.-Y., and Placko, D. (2009). Characterization of subsurface defects in aeronautical riveted lap-joints using multi-frequency eddy current imaging. *NDT E Int.* 42, 133–140. doi:10.1016/j.ndteint.2008.10.005

Fan, M., Wang, Q., Cao, B., Ye, B., Sunny, A., and Tian, G. (2016). Frequency optimization for enhancement of surface defect classification using the eddy current technique. *Sensors* 16, 649. doi:10.3390/s16050649

Gurrappa, I. (2003). Characterization of titanium alloy ti-6al-4v for chemical, marine and industrial applications. *Mater. Char.* 51, 131–39. doi:10.1016/j.matchar.2003.10.006

Haifeng, W., and Dejin, H. (2005). "Comparison of svm and ls-svm for regression." in Proceedings of the 2005 international conference on neural networks and brain. doi:10.1109/ICNNB.2005.1614615

He, Y., Pan, M., Luo, F., Chen, D., and Hu, X. (2013). Support vector machine and optimised feature extraction in integrated eddy current instrument. *Measurement* 46, 764–774. doi:10.1016/j.measurement.2012.09.014

He, Y., Pan, M., Luo, F., and Tian, G. (2011). Pulsed eddy current imaging and frequency spectrum analysis for hidden defect nondestructive testing and evaluation. *NDT E Int.* 44, 344–352. doi:10.1016/j.ndteint.2011.01.009

Hinton, G. E. (2012). "A practical guide to training restricted Boltzmann machines," in *Neural networks: tricks of the trade*. New York, NY: Springer. 599–619.

Hinton, G. E., Osindero, S., and Teh, Y. W. (2006). A fast learning algorithm for deep belief nets. *Neural Comput.* 18, 1527–1554. doi:10.1162/neco.2006.18.7.1527

Hinton, G. E., and Salakhutdinov, R. R. (2006). Reducing the dimensionality of data with neural networks. *Science* 313, 504. doi:10.1126/science.1127647

Hinton, G. E. (2002). Training products of experts by minimizing contrastive divergence. *Neural Comput.* 14, 1771–1800. doi:10.1162/089976602760128018

Khan, T., and Ramuhalli, P. (2008). A recursive bayesian estimation method for solving electromagnetic nondestructive evaluation inverse problems. *IEEE Trans. Magn.* 44, 1845–1855. doi:10.1109/TMAG.2008.921842

Malwina, T. M. (2016). Application of titanium properties in civil engineering and architecture. *Key Eng. Mater.* 687, 220–227, Trans Tech Publ.

Nafiah, F., Sophian, A., Khan, M. R., Abdul Hamid, S. B., and Zainal Abidin, I. M. (2019). Image-based feature extraction technique for inclined crack quantification using pulsed eddy current. *Chin. J. Mech. Eng.* 32, 26. doi:10.1186/s10033-019-0341-y

O'Connor, P., Neil, D., Liu, S.-C., Delbruck, T., and Pfeiffer, M. (2013). Real-time classification and sensor fusion with a spiking deep belief network. *Front. Neurosci.* 7, 178. doi:10.3389/fnins.2013.00178

Ona, D. I., Tian, G. Y., Sutthaweekul, R., and Naqvi, S. M. (2019). Design and optimisation of mutual inductance based pulsed eddy current probe. *Measurement* 144, 402–409. doi:10.1016/j.measurement.2019.04.091

Sophian, A., Tian, G. Y., Taylor, D., and Rudlin, J. (2001). Electromagnetic and eddy current ndt: a review. *Insight* 43, 302–306.

Sophian, A., Tian, G. Y., Taylor, D., and Rudlin, J. (2003). A feature extraction technique based on principal component analysis for pulsed eddy current ndt. *NDT E Int.* 36, 37–41. doi:10.1016/S0963-8695(02)00069-5.

Suykens, J. A. K., and Vandewalle, J. (1999). Least squares support vector machine classifiers. *Neural Process. Lett.* 9, 293–300. doi:10.1023/A:1018628609742

Tian, G. Y., and Sophian, A. (2005). Defect classification using a new feature for pulsed eddy current sensors. *NDT E Int.* 38, 77–82. doi:10.1016/j.ndteint.2004.06.001

Tian, G. Y., Sophian, A., Rudlin, J., and Taylor, D. (2005). Wavelet-based pca defect classification and quantification for pulsed eddy current ndt. *IEE Proc. Sci. Meas. Technol.* 152, 141–148. doi:10.1049/ip-smt:20045011

Veiga, C., Davim, J. P., and Loureiro, A. J. R. (2012). Properties and applications of titanium alloys: a brief review. *Rev. Adv. Mater. Sci.* 32, 133–148.

Winowiecka, J., and Adamus, K. (2016). The assessment of mechanical properties of titanium sheets applied to building elevations and roofs. *Kemi* (687, 250–257), Trans Tech Publ 250–257. doi:10.4028/www.scientific.net/kem.687.250

Wrzuszczak, M., and Wrzuszczak, J. (2005). Eddy current flaw detection with neural network applications. *Measurement* 38, 132–136. doi:10.1016/j.measurement.2005.04.004

Wu, J., Hu, K., Cheng, Y., Zhu, H., Shao, X., and Wang, Y. (2020). Data-driven remaining useful life prediction via multiple sensor signals and deep long short-term memory neural network. *ISA (Instrum. Soc. Am.) Trans.* 97, 241–250. doi:10.1016/j.isatra.2019.07.004

Xu, H., Salas Avila, J. R., Wu, F., Roy, M. J., Xie, Y., Zhou, F., et al. (2018). Imaging x70 weld cross-section using electromagnetic testing. *NDT E Int.* 98, 155–160. doi:10.1016/j.ndteint.2018.05.006

Ye, C., Huang, Y., Udpa, L., and Udpa, S. S. (2016). Novel rotating current probe with gmr array sensors for steam generate tube inspection. *IEEE Sensor. J.* 16, 4995–5002. doi:10.1109/JSEN.2016.2556221

Yin, L., Ye, B., Zhang, Z., Tao, Y., Xu, H., Salas Avila, J. R., et al. (2019). A novel feature extraction method of eddy current testing for defect detection based on machine learning. *NDT E Int.* 107, 102108. doi:10.1016/j.ndteint.2019.04.005

Yin, W., Chen, G., Chen, L., and Wang, B. (2011). The design of a digital magnetic induction tomography (mit) system for metallic object imaging based on half cycle demodulation. *IEEE Sensor. J.* 11, 2233–2240. doi:10.1109/JSEN.2011.2128866

Yin, W., and Peyton, A. J. (2006). A planar emt system for the detection of faults on thin metallic plates. *Meas. Sci. Technol.* 17, 2130–2135. doi:10.1088/0957-0233/17/8/011

Zhang, X., and Wu, J. (2013). Deep belief networks based voice activity detection. *IEEE Trans. Audio Speech Lang. Process.* 21, 697–710. doi:10.1109/TASL.2012.2229986

Conflict of Interest: The authors declare that the research was conducted in the absence of any commercial or financial relationships that could be construed as a potential conflict of interest.

frontiers in Materials

ORIGINAL RESEARCH
published: 27 October 2020
doi: 10.3389/fmats.2020.00298

Identification of Grout Sleeve Joint Defect in Prefabricated Structures Using Deep Learning

Hesheng Tang[1]*, *Yajuan Xie*[1], *Taotao Zhao*[1] *and Songtao Xue*[1,2]

[1] Department of Disaster Mitigation for Structures, Tongji University, Shanghai, China, [2] Department of Architecture, Tohoku Institute of Technology, Sendai, Japan

A grout sleeve connection is a typical kind of joint in prefabricated structures. However, for construction and manufacturing reasons, defects in this kind of joint are usually inevitable. The joint quality of a prefabricated structure has a significant influence on its overall performance and can lead to structural failure. Due to the complexity of various types of materials used in grout sleeve connections, traditional non-destructive testing methods, such as Acoustic Emission (AE), Ultrasonic Testing (UT), Guided Wave Testing (GW), are facing great challenges. The recent development of deep learning technology provides a new opportunity to solve this problem. Deep learning can learn the inherent rules and abstract hierarchies of sample data, and it has a powerful ability to extract the intrinsic features of training data in complex classification tasks. This paper illustrates a deep learning framework for the identification of joint defects in prefabricated structures. In this method, defect features are extracted from the acceleration time history response of a prefabricated structure using a convolutional neural network. The proposed method is validated by vibration experiments on a half-scaled, two-floor prefabricated frame structure with column rebars spliced by different defective grout sleeves.

Keywords: prefabricated structure, grout sleeve, convolutional neural network, deep learning, defect identification

Edited by:
Wen Deng,
Missouri University of Science and Technology, United States

Reviewed by:
Sattar Dorafshan,
University of North Dakota, United States
Xiaolong Xia,
Missouri University of Science and Technology, United States

Correspondence:
Hesheng Tang
thstj@tongji.edu.cn

Specialty section:
This article was submitted to Structural Materials, a section of the journal Frontiers in Materials

Received: *22 June 2020*
Accepted: *10 August 2020*
Published: *27 October 2020*

Citation:
Tang H, Xie Y, Zhao T and Xue S (2020) Identification of Grout Sleeve Joint Defect in Prefabricated Structures Using Deep Learning. Front. Mater. 7:298. doi: 10.3389/fmats.2020.00298

INTRODUCTION

In recent years, prefabricated structures have been widely used in construction, and grout sleeves are the most widely used connection type in these structures. Usually, the special grout used in these connections has good fluidity, early and high strength, and micro-expansion. However, most of these sleeves have complicated internal structures and complicated construction procedures, and this often leads to joint defects during the construction process. The underfilling of sleeve grouting is one of the typical defects that are seen in these connections. Such defects will seriously affect the mechanical properties of the joints and eventually affect the bearing capacity and seismic performance of the overall structure (Zhu et al., 2019). Conveniently and effectively detecting the fullness of sleeve grouting has always been a difficult problem in prefabricated concrete buildings. The ultrasonic wave method (Feng et al., 2020), the impact-echo method (Chou, 2019), the X-ray CT method (Zelelew et al., 2013; Gao et al., 2017), the damped vibration method (Zhu et al., 2018), the X-ray method (du Plessis and Boshoff, 2019), and the embedded wire-drawing method (Gao et al., 2019) are relatively mature detection technologies, but they are expensive and labor intensive, which means they are not conducive to the full detection of sleeve grouting. Because such defects are typically local, traditional global-based non-destructive dynamic testing methods also face great challenges when used with complex structures, because these technologies are unable to obtain effective local feature information from global dynamical data (Yoon et al., 2010). Moreover, with the increasing complexity of these connections, the influences of the different parts will increase, which will lead to these methods being unable to effectively extract feature information.

As a subset of machine learning in artificial intelligence (AI), deep learning involves networks that are capable of learning without supervision from original data. Deep learning technology has the potential to provide a new identification method in a case such as this because it can autonomously learn highly abstract features from original data.

Deep learning has enabled many practical applications of machine learning, and by extension the overall field of AI. An increasing number of researchers have tried to apply deep learning to identification problems in the field of civil engineering. LeCun et al. (1989) developed the first deep convolutional neural network (DCNN) to realize handwritten postcode identification (LeNet-5), using back propagation (BP), a supervised training algorithm. Cha et al. (2017) proposed a crack detection method for concrete structures based on a convolutional neural network (CNN) that used crack photographs taken under different conditions (such as different photo sizes, light sources, and shadows) for testing. Dorafshan et al. (2018) compared the performance of commonly used edge detectors and DCNNs in crack detection in concrete structures and proposed a method combining a DCNN and edge detectors that can reduce residual noise. Xu et al. (2019) proposed a fast region-CNN (R-CNN) method for identifying and locating multiple types of seismic damage to damaged reinforced concrete columns from images. The image data sets were established through on-site imaging, and these were expanded using a data-enhancement method. Based on fast R-CNN, Beckman et al. (2019) proposed a method for detecting concrete layer damage and studied the influence of the distance between the specimen and the sensor on the recognition accuracy. Chen et al. (2019) built a four-camera vision system that can obtain visual information about targets, including static objects and a dynamic concrete-filled steel tube specimen. Tang et al. (2019) presented a dynamic real-time detection method for examining surface deformation and full-field strain in recycled aggregate concrete-filled steel tubular columns. Mathematical models were proposed that combined the four-ocular visual coordinates and point-cloud matching.

Abdeljaber et al. (2018) presented an enhanced CNN-based approach which only needs two measurement sets for structural damage detection. Dorafshan and Azari (2020) proposed one-dimensional CNN which can successfully detect the subsurface defects of cement overlay bridge using impact echo data. Li et al. (2018) proposed a damage- identification method for bridges based on a CNN. The acceleration time-history responses from nine measuring points in a simply supported beam were used as input data to train and test the CNN, and the effects of different excitation sizes and different noise environments on the CNN identification results were analyzed. Xie et al. (2018) proposed a bridge damage-identification method based on a stacked noise-reduction autoencoder. The damage features of the bridge's acceleration response were extracted using multiple autoencoders, and the softmax function was used to identify bridge damage. Zhao (2019) proposed a blade damage-recognition method based on CNN, selecting a residual neural network (ResNet) as the basic model structure, and combined a batch gradient descent algorithm with CNN to improve learning efficiency. Lin et al. (2017) proposed a damage-recognition method based on CNN that automatically extracts features from time-domain response data from the structure. A numerical test of a simply supported Euler–Bernoulli beam was designed, and the CNN was trained and tested using the response time history of the beam under different working conditions. Abdeljaber et al. (2017) developed a structural-damage-recognition system based on a one-dimensional CNN that integrated feature extraction and classification into a complete learning module, thereby realizing vibration-based damage detection and real-time damage location.

Pathirage et al. (2018) proposed a deep learning network based on autoencoders that can identify structural damage through vibration responses. The natural frequency, vibration mode, and other vibration characteristics were taken as inputs, and structural damage was the output. Lee et al. (2018) compared DNNs with different hidden layers, activation functions, and optimization algorithms, and tested the performance of different combinations. Khodabandehlou et al. (2019) established an 11-layer, two-dimensional CNN that can extract features from the acceleration response time history of a structure, making it possible to classify bridge damage using acceleration measurements. Duan et al. (2019) proposed a bridge damage detection method based on CNN. The acceleration response time history and Fourier spectrum were compared as a training data set for the CNN. Gulgec et al. (2019) trained and compared 50 CNNs with different learning rates, convolutional layers, and fully connected layers, and finally proposed a CNN approach for structural damage detection and localization. Wang et al. (2019) proposed a dual-path network composed of a ResNet and a densely connected convolutional network. A spatial time-frequency data set was established using multi-dimensional vibration signals, and different railway events were classified by monitoring data that contained environmental noise. Kim and Sim (2019) proposed a framework composed of a fast R-CNN and a region-suggestion network based on deep learning that can automatically extract peaks in frequency-domain pattern recognition. Tang et al. (2020) presented an overview of recognition and localization methods for vision-based fruit-picking robots. Yu et al. (2019) proposed a deep CNN-based method for the identification of damages in buildings. The proposed method can automatically extract high-level features from raw signals in time domain, and the performance of the method is verified by a five-level benchmark building. Avci et al. (2020) introduced the recent applications of deep learning methods which is used in vibration-based structural damage detection in the area of civil structures.

Convolutional neural networks have been widely recognized as powerful tools to deal with problems such as image identification. Identification methods based on image processing need to collect response images as input data. While it is usually difficult to collect images of defects in an actual prefabricated structure, acceleration response data can be obtained from such a structure relatively easily. However, effectively utilizing this sensing data for structural response modeling to identify defects remains a challenge.

In this paper, we propose an approach for sleeve joint defect identification in prefabricated frame structures using a CNN with a customized architecture. The proposed method is verified by dynamic tests of a half-scaled, two-floor prefabricated concrete frame structure. Structural acceleration response sensing data are taken as input samples. The existence of defects, and their location and degree, are identified, and the accuracy is evaluated using a confusion matrix (Thongkam et al., 2008).

MATERIALS AND METHODS

Grout Sleeve Connection

For prefabricated concrete structures, grout sleeves are the most widely used rebar connection type. As shown in **Figure 1**, a full grouting sleeve connection mainly includes three parts: a sleeve, ribbed steel bar, and grout. In this paper, the material used for the sleeve was nodular cast iron and the ribbed steel bar was made from steel with a standard value of yield strength of 400 MPa and a modulus of elasticity of 200 GPa. The rebar diameter was 12 mm. According to the Technical Specification for Precast Concrete Structures, the outer and inner diameters of the sleeve were set as 44 and 34 mm, respectively, and the length was set as 250 mm (China Institute of Building Standard Design and Research, 2014). The grout was made from cement as the basic material, and this was mixed with fine aggregate, a concrete admixture, and other materials. After stirring with water, this mixture had good fluidity, early and high strength, and micro-expansion.

To form the joints, two steel bars were inserted into the sleeve, one from each end. The upper and lower longitudinal ribs extended into the sleeve by 120 and 110 mm, respectively. The special grout was then poured in via the grouting hole and flowed out from the overflow slurry hole until the sleeve was filled. In this situation, the hardened grout grips both the steel bar and the sleeve, and due to its micro-expansion and high strength characteristics, the positive force between the sleeve and the steel bar is strengthened (Zheng et al., 2015).

The construction of a full grouting sleeve is very complicated, and during the construction process, sleeve defects, such as grout leakage, eccentricity of the steel bars, incomplete fill of grout, and peeling of the grout from the connecting members are usually inevitable. Grout sleeve bond failure is a typical but undesirable failure mode in grout sleeve joints. Grout sleeve defects will seriously affect the mechanical properties of the joint, becoming

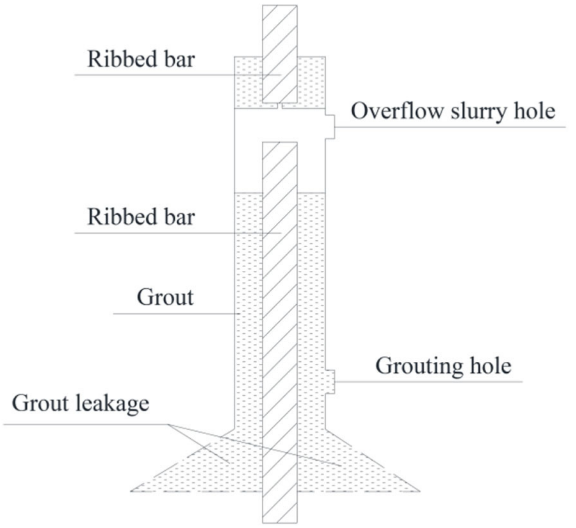

FIGURE 2 | Incomplete fill of grout sleeve defect caused in on-site construction.

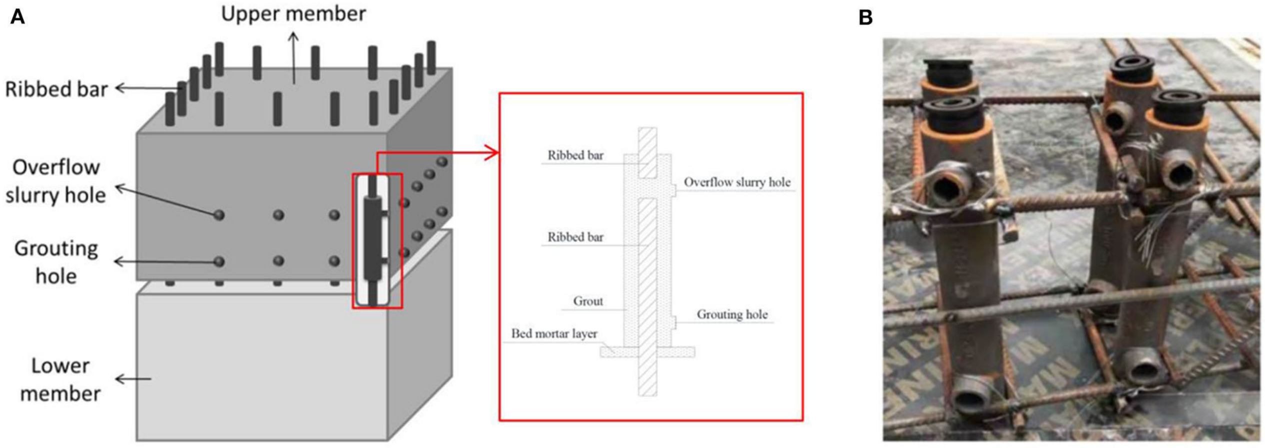

FIGURE 1 | Full grouting sleeve connection. **(A)** Schematic diagram. **(B)** Physical diagram.

a potential risk to the structure. **Figure 2** shows an incomplete fill of grout sleeve defect caused in on-site construction, and it is the most common defect type in actual engineering.

CNN-Based Defect Identification Method

This study presents a defect identification method for prefabricated concrete structures based on a deep convolutional neural network. This network can directly extract defect features from the dynamic response of the fabricated concrete structure. An overview of the proposed method is shown in **Figure 3** and is described briefly as follows: (1) An experiment is conducted to obtain acceleration response data for the fabricated concrete structure; (2) the collected dynamic response data are preprocessed, data sets (training, validation and test sets) are established, and the samples are labeled; (3) a deep CNN, as shown in **Figure 4**, is trained on the training data set; (4) the loss of validation during the training process was calculated for each epoch to test whether it is over fitting; (5) the test set is

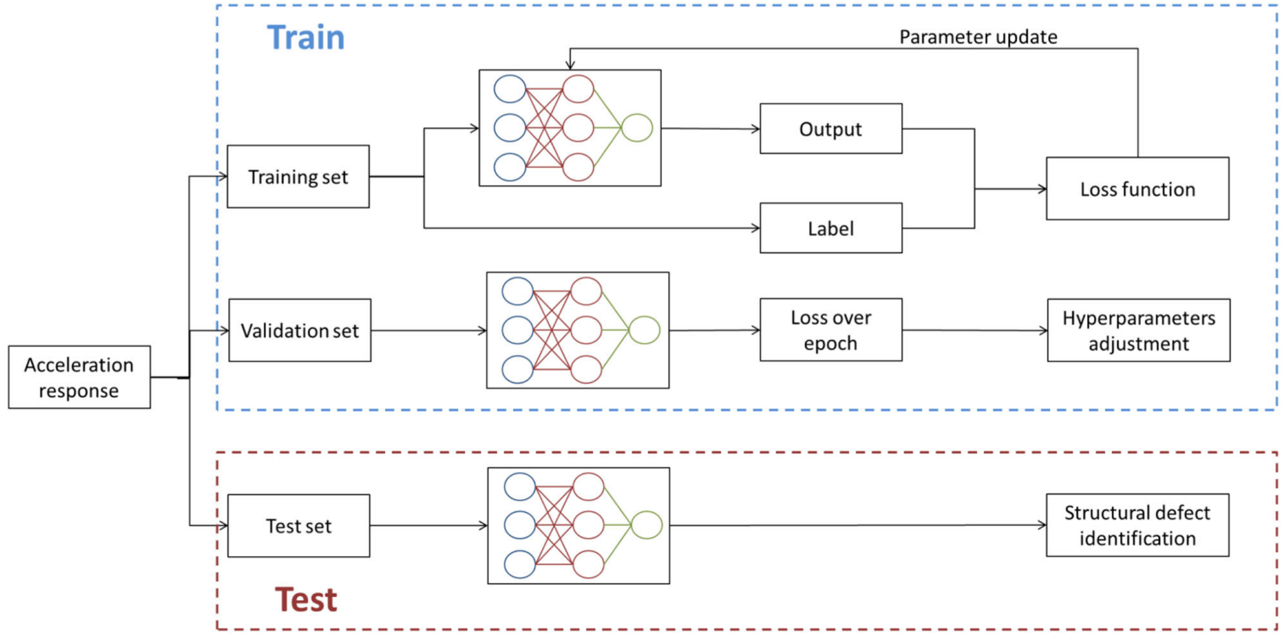

FIGURE 3 | The process of structural defect identification based on a CNN. Here, defect probability represents that the output was mapped into a probability distribution in the range [0, 1] through the Softmax function.

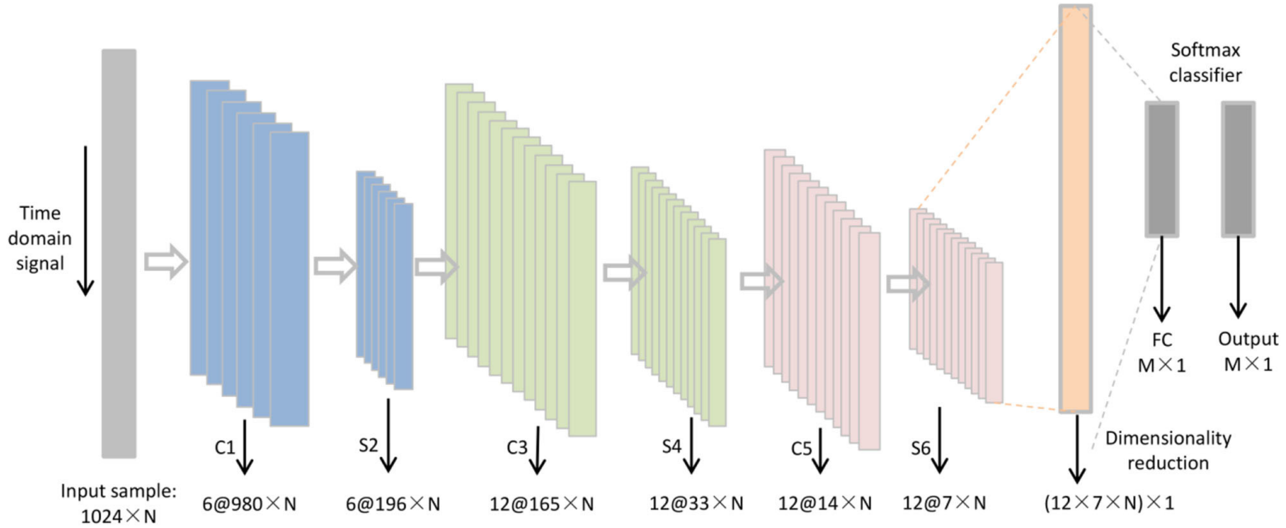

FIGURE 4 | Basic framework of the CNN. Here, C represents a convolution layer, S represents a pooling layer, FC represents the fully connected layer, N represents the number of nodes in the input sample, and M represents the number of nodes in the output.

used to verify the feasibility and accuracy of the CNN; (6) Defect location and degree were identified.

The deep learning network is established based on LeNet-5 (LeCun et al., 1989), a CNN that is famous for its simple structure and high efficiency. The Matlab toolkit DeepLearnToolbox was employed to establish the proposed CNN architecture. DeepLearnToolbox is the most widely used deep learning toolkit in Matlab, and the CNN in this toolkit was built by Rasmus Berg Palm on the basis of LeNet-5. In a recognition test of the Modified National Institute of Standards and Technology database, an error rate of 1.22% was obtained. The proposed deep CNN basic framework is shown in **Figure 4**. It can be seen that the CNN consisted of an input layer, three alternating convolutional and pooling layers, a fully connected layer, and an output layer. The components of the CNN and the selection of the activation function and optimization algorithm are described in the next sections.

Convolution Layer

The convolution layer is the core of the CNN, and its purpose is to use a convolution kernel to extract signal features. Generally, convolution is a mathematical operation on two real variable functions. The convolution expression of functions x and w can be calculated as

$$s(t) = \int x(a) \times w(t-a)da \tag{1}$$

The discrete form of this convolution operation can be defined as

$$s(t) = (x * w)(t) = \sum x(a)w(t-a) \tag{2}$$

In general, the first parameter in the convolution operation is called the input, the second parameter is called the convolution kernel, and the output is called a feature map. According to the convolution expression, each element in the output is obtained by the weighted addition of the elements of the corresponding block in the input, and the weight value is determined by the convolution kernel. The convolution kernel therefore plays the role of filtering or feature extraction in the convolution. Convolutional layers have powerful feature-learning capabilities. In general, deep networks can continuously and iteratively extract higher-level features from the features of the underlying network.

Activation Function

Generally, a convolutional layer is followed by a non-linear activation function. The activation function maps the linear input data into non-linear features through its own non-linear features, and the features obtained in the convolutional layer are filtered. Common non-linear functions in convolutional neural networks include the sigmoid, tanh, softsign, and ReLU functions (Zhou and Mi, 2017). Generally, the performance of the ReLU function is considered best. In this study, the defect identification accuracies obtained using tanh and ReLU functions with different learning rates of 0.005, 0.01, 0.02, and 0.05 were compared using experimentally obtained sensing acceleration response data. The results are shown in **Table 1**, and these show that the identification accuracy of the tanh function in this example is significantly better than that of the ReLU function. Therefore, the tanh function was selected as the activation function of the convolutional layer in the CNN. An expression for the tanh function is shown in Equation (3).

$$y = \frac{e^x - e^{-x}}{e^x + e^{-x}} \tag{3}$$

TABLE 1 | Identification accuracy for tanh and ReLU activation functions with different learning rates.

Learning rate	0.005	0.01	0.02	0.05
tanh	76.11%	97.31%	94.08%	88.74%
ReLU	60.59%	70.97%	70.54%	64.40%

Pooling Layer

Pooling is mainly used to filter redundant features and reduce the number of parameters, avoiding over-fitting. There are two common pooling operations: maximum pooling and average pooling. Maximum pooling takes the maximum value of each pooling window and average pooling takes the average value of each pooling window. In this work, the average pooling method was used. The average pooling operation is shown in **Figure 5**.

Fully Connected Layer and Softmax Classifier

The fully connected layer is connected to all the activations in the previous layer. In this work, all the elements in the feature map of pooling layer S6 were processed into an M-dimensional column vector, multiplied by weighting coefficients, and added with corresponding offsets. The softmax function was then used to calculate the final output of the CNN. The softmax function can be expressed as

$$S_i = \frac{e^{V_i}}{\sum_{i=1}^{C} e^{V_i}} \tag{4}$$

where S_i is the probability that the current input is the i-th category, e is Euler's number, V_i is the i-th output of the previous

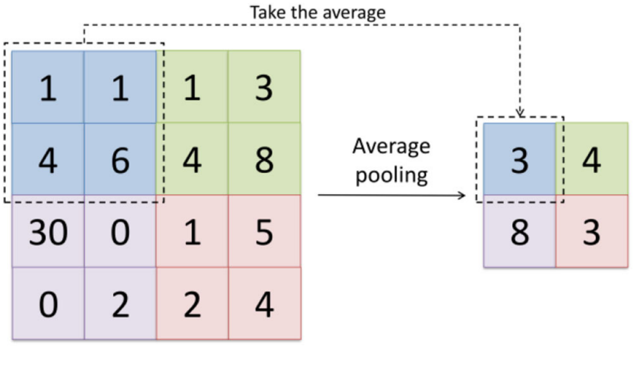

FIGURE 5 | The average pooling operation.

output unit, and C is the total number of categories. As shown in Equation (4), the softmax classifier maps the output of the previous output unit to the interval (0, 1), and this represents the relative probabilities of different categories so that the input samples can be classified according to their probability.

Batch Gradient Descent Algorithm

In the calculation process of the backpropagation algorithm, the parameters in the CNN need to be optimized to minimize the cost function to obtain an optimal solution. In this work, a cross-entropy cost function was used. The cross-entropy cost function can be expressed as

$$E = -\frac{1}{N}\left(y^{(i)} \times \ln(o^{(i)}) + (1 - y^{(i)}) \times \ln(1 - o^{(i)})\right) \qquad (5)$$

where E represents the cost function value, N represents the total number of samples, $y^{(i)}$ represents the true output (label) of the i-th sample, and $o^{(i)}$ represents the predicted output of the i-th sample. The small-batch gradient descent algorithm was used as the optimization algorithm. As shown in **Table 1**, in this example, the identification accuracy is better when the learning rate is 0.01, so the learning rate was set as 0.01 in the batch gradient descent algorithm.

Experimental Verification

To verify the accuracy and feasibility of the proposed deep learning method, dynamic excitation tests were carried out on a prefabricated half-scaled, two-floor concrete frame with different defective columns.

Experimental Model

A half-scaled, two-floor prefabricated concrete frame structure was constructed. This mainly comprised four parts: precast columns, precast beams, precast foundation beams, and a poured concrete slab. The beams and columns were made from concrete, the standard value of compressive strength of concrete cube

FIGURE 7 | The grouting process.

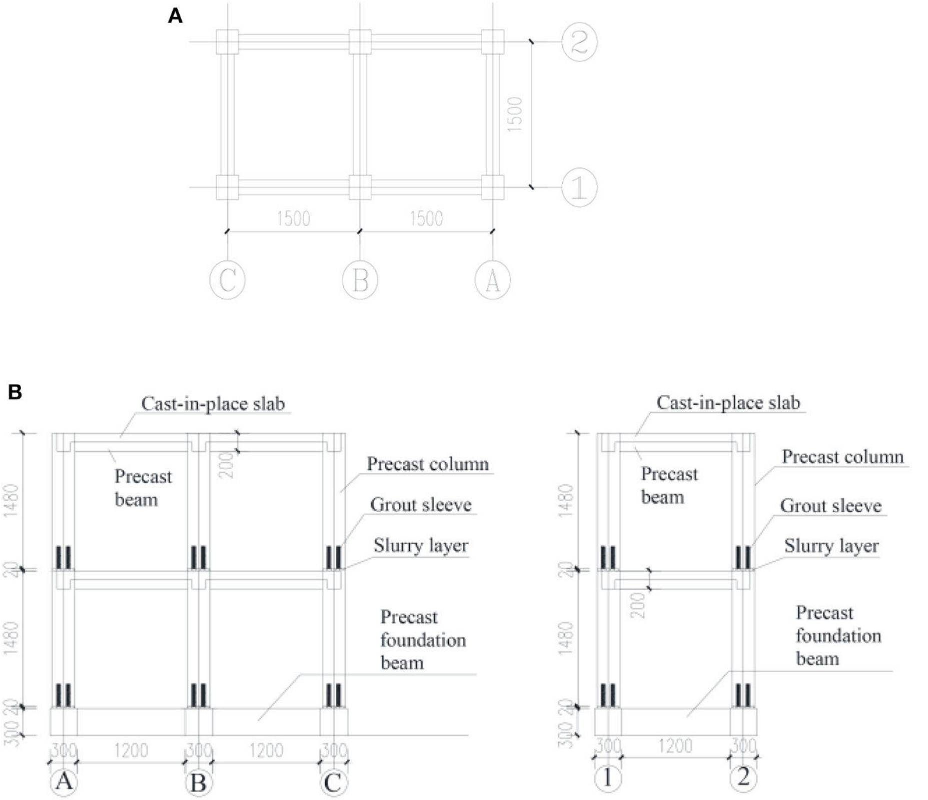

FIGURE 6 | Plan and elevation views of the frame model. **(A)** Plan view of the column net of the frame model. **(B)** The A–C and 1–2 elevation views of the frame model.

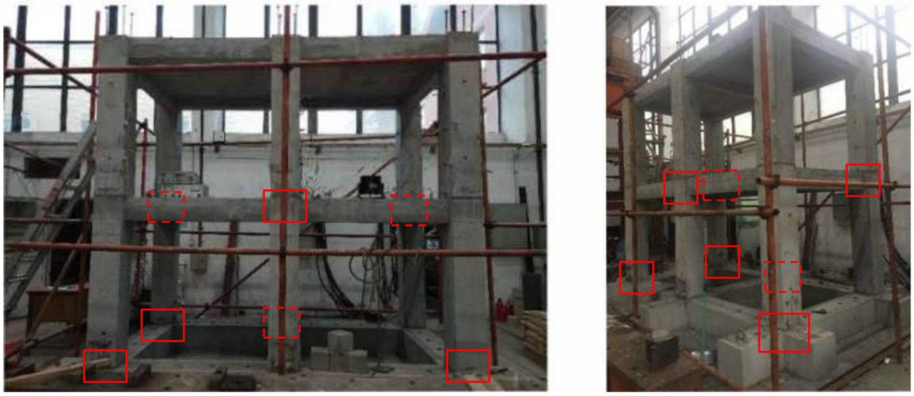

FIGURE 8 | Frame structure model after assembly. Red rectangles represent locations of defects (the dashed lines indicate that they are shaded).

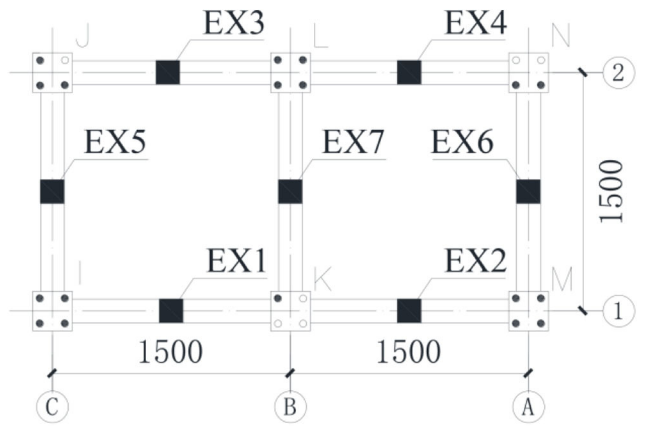

FIGURE 9 | Defect setting of the second floor and excitation point arrangement. Solid dots represent grouting sleeves and hollow dots represent ungrouted sleeves. EX represents the excitation point location.

TABLE 2 | Working conditions.

Working condition	Excitation point	Non-defective column number	Defective column number (ungrouted sleeve number)
1	EX1 (JZ 1–2)	1	2 (3)
2	EX2 (JZ 3–2)	3	4 (1)
3	EX3 (JZ 5–4)	5	6 (2)
4	EX4 (JZ 5–6)	5	4 (1)
5	EX5 (JZ 1–4)	1	2 (3)
6	EX6 (JZ 5–2)	5	2 (3)
7	EX7 (JZ 3–6)	4	6 (2)

is 30 N/mm. Longitudinal reinforcements and stirrups were made from hot-rolled ribbed bars with a standard value of yield strength of 400 MPa and a modulus of elasticity of 200 GPa. The full grouting sleeve connection method was used to splice the internal reinforcements in the foundation beams and columns. A plan of the column net in this experimental model is shown in **Figure 6A**, and elevation views are shown in **Figure 6B**. Total 48 grouting connections were used in this frame structure model. The grouting process is shown in **Figure 7**.

In this test, precast beam and column members were manufactured by professional prefabricated assembly member manufacturing plants, and they were assembled in the laboratory of Tongji University after curing. The frame structure model after assembly is shown in **Figure 8**.

Defect Setting

In these experiments, defects in grout sleeve joints are introduced through incomplete grouting. To avoid structural damage to or collapse of the structure, the defects were arranged in the precast columns of the second floor instead of the first floor. As shown in **Figure 9**, for comparative analysis, defects were set only on one of the columns on either side of a particular beam. Excitation points were arranged across the span of the beams. Thus, for the same excitation, both defective column vibration responses and non-defective column vibration responses could be obtained.

As shown in **Table 2**, there were seven working conditions corresponding to seven excitation points. Taking working condition 5 as an example, 14 measuring points were arranged for each working condition. The locations and numbers of excitation points and measuring points are shown in **Figure 10**.

RESULTS AND DISCUSSION

Data Collection

Excitation was applied by vibration exciters, and acceleration sensors were arranged at the measuring points to collect acceleration responses. The excitation force was 200 N and the acquisition frequency was 1,024 Hz. Each excitation point is excited once, and the duration of excitation is 60 s.

According to the acceleration time-history curve analysis, the amplitude at each measuring point in each working condition was different. For the stability of the convolutional neural network during the training process, a normalization layer is added to the proposed network (Dorafshan and Azari, 2020). The amplitudes of the acceleration time-histories are normalized as

$$y_i = \frac{x_i}{\max\limits_{i=1,2,\cdots,N}(|x_i|)} \tag{6}$$

where x represents the original acceleration time history, y represents the acceleration time history after the amplitude is normalized, and i is the index of each measuring point.

The acceleration time history from each measuring point was taken as the input sample. For each working condition, 14 acceleration time histories were obtained. As shown in **Figure 11**, the 60 × 1,024 signals of each measuring point were divided into 5,000 parts. Each part includes 1,024 signals and adjacent parts have an overlap of 1,012 signals. The first seven acceleration time histories were collected from the columns and beams without defects and constituted the non-defective sample; the last seven acceleration time histories were collected from the defective columns and beams and constituted the defective sample. That is, there are in total 5,000 non-defective samples and 5,000 defect samples for each working condition, and each sample contains 7 × 1,024 acceleration signals. Sixty percentange of the total samples were randomly selected as the training set, 20% of the samples were selected randomly as validation set, with the remaining 20% constituting the test set.

The number of training set samples generated in this experiment was relatively small. The batch size was therefore set to five to ensure that there were a sufficient number of samples for training; the epoch number was set to 20. The number of iterations can be calculated as

$$IN = EN \times \frac{TS}{BS} \tag{7}$$

where IN represents the number of iterations, EN represents epoch number, TS represents the training set size, and BS represents the batch size.

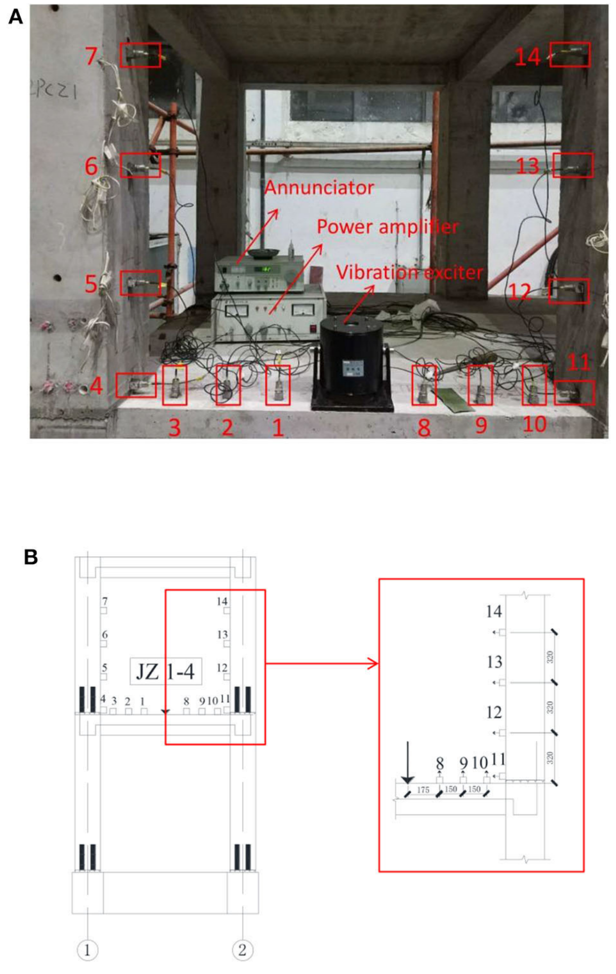

FIGURE 10 | Arrangement of the excitation points and measuring points. **(A)** Physical diagram. **(B)** Schematic diagram.

Defect Location Identification

The defects and their locations were identified for the samples in each working condition. The samples were labeled with a vector consisting of eight elements. The first seven elements represent the probability that a defect is located at each of the seven corresponding measurement points. The eighth element represents the probability that the sample is a non-defective sample. In this experiment, a defect was set at measuring point 4, so the label of the defective sample was [0, 0, 0, 1, 0, 0, 0, 0]; the label of the non-defective sample was [0, 0, 0, 0, 0, 0, 0, 1]. Thus, the sample is identified as a defective sample when the fourth element in the sample output vector is > 0.95, the sample is identified as a non-defective sample when the eighth element in a sample output vector is >0.95, and the identification is invalid when no element in a sample output vector is > 0.95. Based on the above label setting, the detailed parameters for each layer in the CNN are shown in **Table 3**.

As shown in **Figure 12**, during the training process, the loss function in the CNN gradually decreased with an increasing number of iterations and converged to a stable level for each working condition. As shown in **Figure 13**, the loss of validation during the training process was calculated for each epoch to test whether it is over fitting, and the training stopped in the 20th epoch (the loss of validation was not changed significantly). The identification accuracies for each working condition during the training process of the CNN are shown in **Figure 14**. It can be seen that during the CNN training process, the identification accuracy rate of samples in the seven working conditions continuously increased with the growth of the epochs, and finally stabilized at 100%. The four longitudinal working conditions (conditions 1–4) converged faster than the three lateral working conditions (conditions 5–7).

For each working condition, 2,000 test samples were sequentially input into the trained convolutional neural network. The test results showed that the identification accuracies of the seven test sets were all 100%. This means that the proposed method can successfully identify defects and their locations.

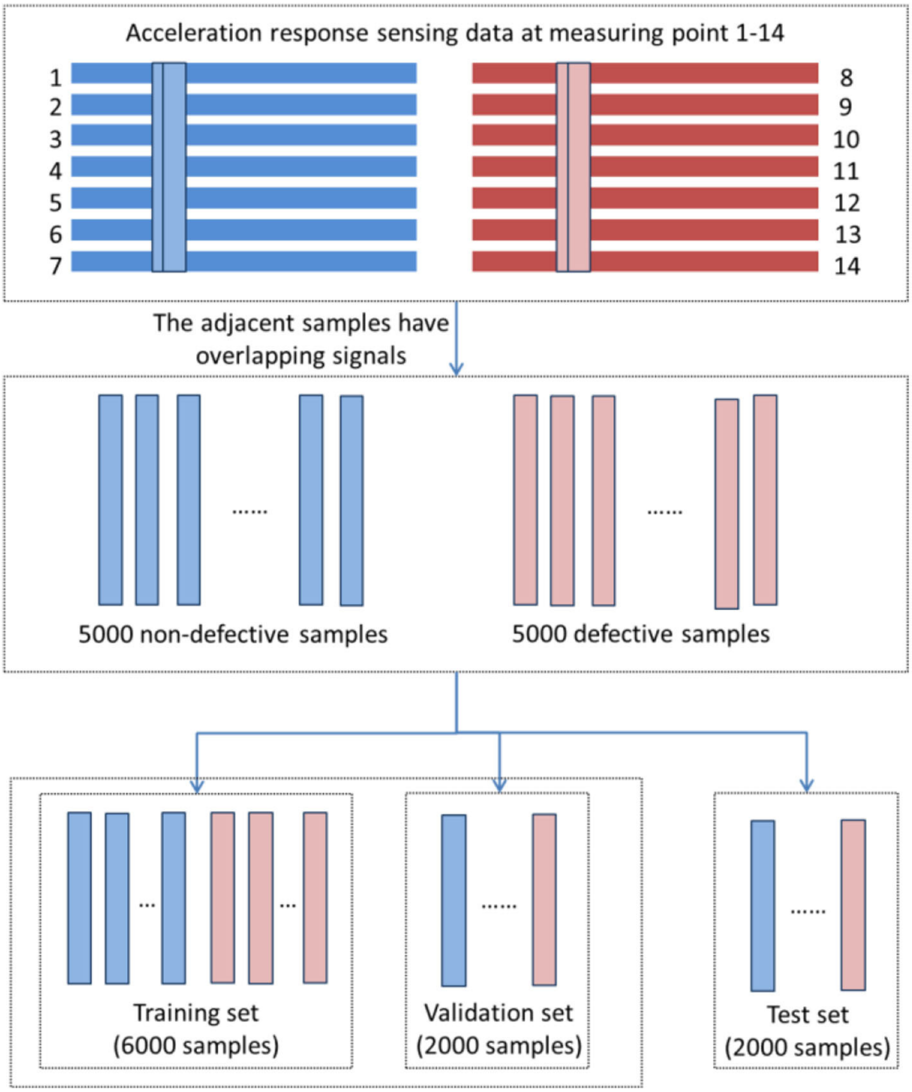

FIGURE 11 | The creation of datasets.

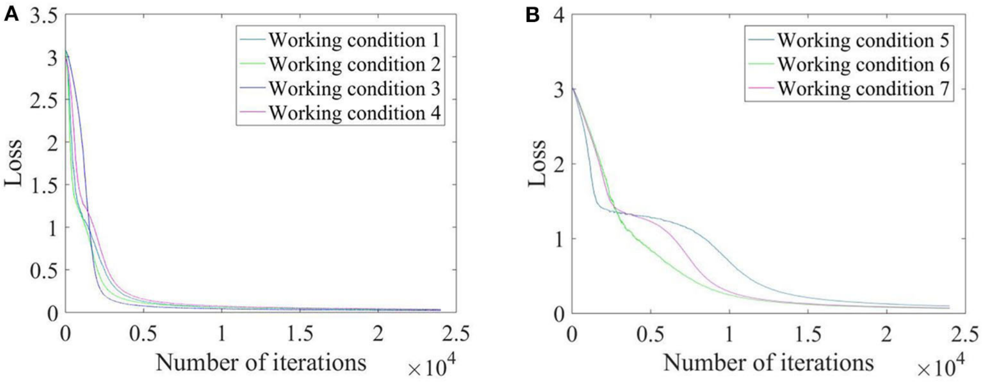

FIGURE 12 | The loss functions for each working condition during the CNN training process. **(A)** Working conditions 1–4. **(B)** Working conditions 5–7.

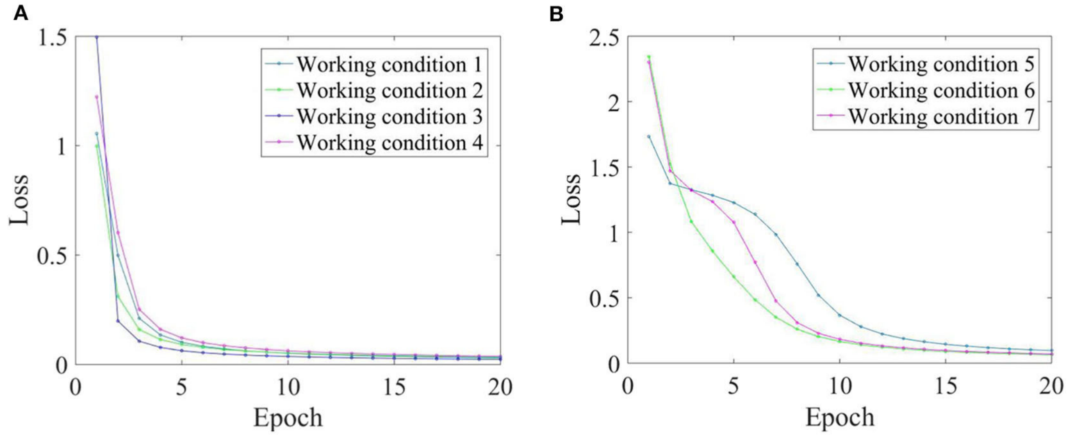

FIGURE 13 | Losses of validation for each working condition during the CNN training process. **(A)** Working conditions 1–4. **(B)** Working conditions 5–7.

TABLE 3 | Detailed parameters of each layer in the CNN.

Number	Type	Kernel num.	Kernel size	Stride	Input	Output
C1	Convo.	45	6	1	1,024 × 7	6@980 × 7
S2	Pooling	5	None	1	6@980 × 7	6@196 × 7
C3	Convo.	32	12	1	6@196 × 7	12@165 × 7
S4	Pooling	5	None	1	12@165 × 7	12@33 × 7
C5	Convo.	20	12	1	12@33 × 7	12@ 14 × 7
S6	Pooling	2	None	1	12@14 × 7	12@7 × 7
FC	FC	None	None	None	12@7 × 7	8 × 1

Defect Degree Identification

For defect degree identification, the precast defective columns of working conditions 5, 6, and 7 have covered the defect degrees of 25, 75, and 50% with the same boundary conditions in the test. So these three working conditions (5, 6, and 7) were taken as this section's research object. There were in total 15,000 samples, 60% of these were randomly selected as the training set, 20% of the samples were selected as validation set, with the remaining 20% constituting the test set. The batch size was set to five, and the epoch number was set to 20.

The sample labels were vectors consisting of three elements. The first element represents the defect degree being 25%, the second element represents the defect degree being 50%, and the third element represents the defect degree being 75%. For example, a sample label with 25% defect degree would be [1, 0, 0].

To realize the identification of the defect degree, the difference between the sample output vector and the sample label vector is calculated using the Euclidean distance (Schnitzer et al., 2012). The Euclidean distance ρ between two points $(x_1, x_2, \ldots, x_n)$ and $(y_1, y_2, \ldots, y_n)$ in n-dimensional space can be calculated from

$$\rho = \sqrt{(x_1 - y_1)^2 + (x_2 - y_2)^2 + \cdots + (x_n - y_n)^2} \qquad (8)$$

A confusion matrix is used to measure the classification and prediction ability of the model (Thongkam et al., 2008). The identification result of a sample can be one of four types, as shown in **Table 4**: true positive (TP), false positive (FP), false negative (FN), and true negative (TN). The precision ratio (p) and recall ratio (r) of the confusion matrix can be calculated from

$$p = \frac{TP}{TP + FP} \qquad (9)$$

$$r = \frac{TP}{TP + FN} \qquad (10)$$

During the training process, the losses of train and validation are shown in **Figure 15**. Three samples (from three working conditions) were randomly selected from the test set. The Euclidean distances between the output vectors and the sample labels are shown in **Table 5**. Test samples were sequentially input into the trained convolutional neural network, and the confusion matrix of the identification results is shown in **Table 6**. This table shows that both the precision ratio and the recall rate for each sample type were 100%. The evaluation target of precision ratio is the prediction results, the number of positive samples among the samples whose prediction is positive. The precision ratio is 100%, indicating that the prediction results of all samples with different defect degrees are positive. The evaluation target of recall ratio is the original samples, the number of positive examples that are predicted correctly. The recall ratio is 100%, indicating that all

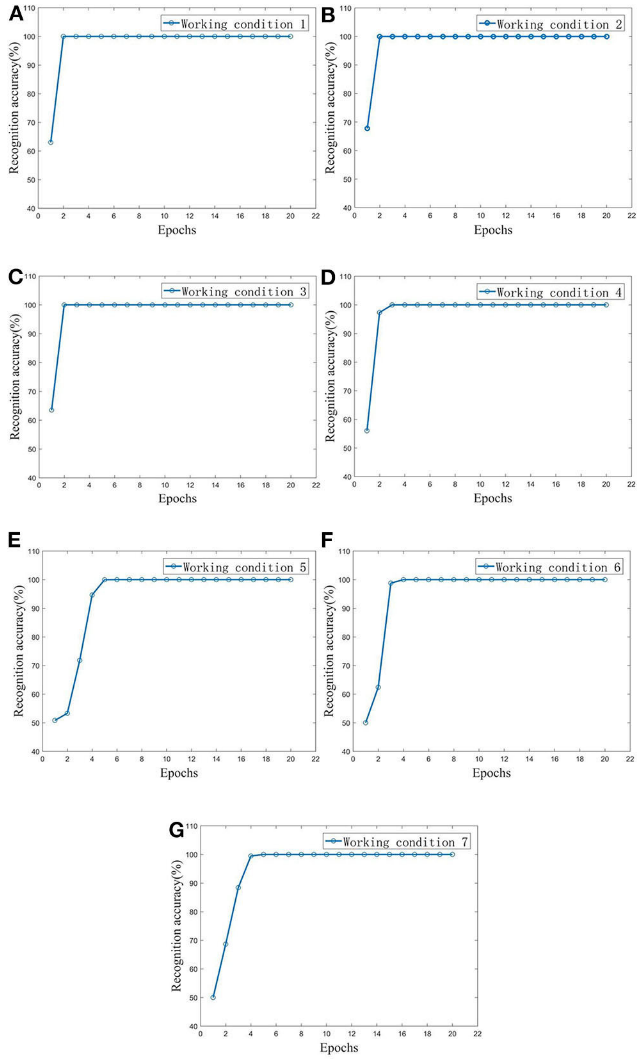

FIGURE 14 | The identification accuracies of seven working conditions during the CNN training process. **(A)** Working condition 1. **(B**) Working condition 2. **(C)** Working condition 3. **(D)** Working condition 4. **(E)** Working condition 5. **(F)** Working condition 6. **(G)** Working condition 7.

TABLE 4 | Confusion matrix.

Confusion Matrix		**True value**	
		Positive	**Negative**
Predicted value	Positive	TP	FP
	Negative	FN	TN

TABLE 5 | Euclidean distances between the output vectors and the sample labels.

Working condition	**Output vector**	**Label vector**	**Euclidean distance**	**Identification result**
5	[0.98, 0.02, 0]	[1, 0, 0]	0.03	25% defect
		[0, 1, 0]	1.38	
		[0, 0, 1]	1.40	
6	[0, 0.02, 0.98]	[1, 0, 0]	1.40	75% defect
		[0, 1, 0]	1.38	
		[0, 0, 1]	0.03	
7	[0.02, 0.97, 0.01]	[1, 0, 0]	1.37	50% defect
		[0, 1, 0]	0.04	
		[0, 0, 1]	1.38	

TABLE 6 | Confusion matrix of the identification results.

Confusion matrix	**Defect degree**	**True defect**			**Precision ratio**
		25%	**50%**	**75%**	
Identification result	25%	1,000	0	0	100%
	50%	0	1,000	0	100%
	75%	0	0	1,000	100%
Recall ratio		100%	100%	100%	–

the samples with different defect degrees have been predicted correctly. **Table 6** shows that the CNN is stable and has good identification performance for structural defect identification in a prefabricated frame. There was no significant difference between the recall rate and the accuracy rate, indicating that the CNN does not show bias toward different defect types.

CONCLUSIONS

This paper presented a deep-CNN-based method for identification of sleeve joint defects in prefabricated concrete frame structures. The proposed method uses LeNet-5 as the basic framework and refers to the CNN in the DeepLearnToolbox. Non-destructive dynamic tests on a half-scaled, two-floor prefabricated concrete frame structure were carried out. The CNN was trained using only the collected sensing acceleration responses to extract features for sleeve joint defect identification. In the experiment, there were seven working conditions due to the different defect degrees and boundary conditions. For each working condition, 5,000 non-defective samples and 5,000 defective samples were collected, and 60% of these were selected randomly as the training set, 20% of these were selected as validation set, while the remaining 20% were used to test the CNN. The defects and their locations were identified using the CNN, and the identification accuracy was 100% in each working condition. The Euclidean distances between the output vectors and the label vectors were calculated to determine the defect identification result, and a confusion matrix was used to judge the identification accuracy. Defects with different degrees were identified in lateral working conditions 5, 6, and 7. The results showed that both the precision ratio and the recall rate were 100%, and the proposed method did not show bias toward different defect degrees. Overall, the proposed method was found to be very effective in joint defect identification in prefabricated concrete frame structures in the experimental situation examined in this paper.

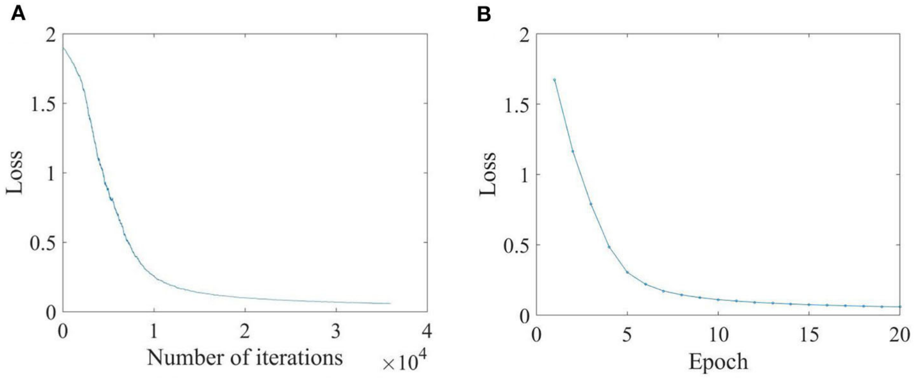

FIGURE 15 | The train and validation losses during the CNN training process. **(A)** Train losses over iterations. **(B)** Validation losses over epochs.

DATA AVAILABILITY STATEMENT

The raw data supporting the conclusions of this article will be made available by the authors, without undue reservation. Raw data are provided in the **Supplementary Material**.

AUTHOR CONTRIBUTIONS

HT, TZ, YX, and SX: methodology. TZ: software. HT and SX: supervision. YX: validation and writing—original draft. HT, YX, and SX: writing—review and editing. All authors read and agreed to the published version of the article.

FUNDING

This research was funded by the Ministry of Science and Technology of China (grant number SLDRCE19-B-02) and the National Key R&D Program of China (grant numbers 2017YFC0703600 and 2016YFC0701800).

SUPPLEMENTARY MATERIAL

The Supplementary Material for this article can be found online at: https://www.frontiersin.org/articles/10.3389/fmats.2020.00298/full#supplementary-material

REFERENCES

Abdeljaber, O., Avci, O., Kiranyaz, M. S., Boashash, B., Sodano, H., and Inman, D. J. (2018). 1-D CNNs for structural damage detection: Verification on a structural health monitoring benchmark data. *Neurocomputing* 275, 1308–1317. doi: 10.1016/j.neucom.2017.09.069

Abdeljaber, O., Avci, O., Kiranyaz, S., Gabbouj, M., and Inman, D. J. (2017). Real-time vibration-based structural damage detection using one-dimensional convolutional neural networks. *J. Sound Vib.* 388, 154–170. doi: 10.1016/j.jsv.2016.10.043

Avci, O., Abdeljaber, O., Kiranyaz, S., Hussein, M. F., Gabbouj, M., and Inman, D. J. (2020). A review of vibration-based damage detection in civil structures: from traditional methods to machine learning and deep learning applications. *arXiv:2004.04373*. doi: 10.1016/j.ymssp.2020.107077

Beckman, G. H., Polyzois, D., and Cha, Y. J. (2019). Deep learning-based automatic volumetric damage quantification using depth camera. *Autom. Constr.* 99, 114–124. doi: 10.1016/j.autcon.2018.12.006

Cha, Y. J., Choi, W., and Büyüköztürk, O. (2017). Deep learning-based crack damage detection using convolutional neural networks. *Comp.-Aided Civil Inf. Eng.* 32, 361–378. doi: 10.1111/mice.12263

Chen, M., Tang, Y., Zou, X., Huang, K., Li, L., and He, Y. (2019). High-accuracy multi-camera reconstruction enhanced by adaptive point cloud correction algorithm. *Opt. Lasers Eng.* 122, 170–183. doi: 10.1016/j.optlaseng.2019.06.011

China Institute of Building Standard Design and Research (2014). *JGJ 1-2014. Technical Specification for Precast Concrete Structures.* Beijing: China Construction Industry Press.

Chou, H. C. (2019). Concrete object anomaly detection using a non-destructive automatic oscillating impact-echo device. *Appl. Sci.* 9:904. doi: 10.3390/APP9050904

Dorafshan, S., and Azari, H. (2020). Evaluation of bridge decks with overlays using impact echo, a deep learning approach. *Automat. Constr.* 113:103133. doi: 10.1016/j.autcon.2020.103133

Dorafshan, S., Thomas, R. J., and Maguire, M. (2018). Comparison of deep convolutional neural networks and edge detectors for image-based crack detection in concrete. *Constr. Build. Mater.* 186, 1031–1045. doi: 10.1016/j.conbuildmat.2018.08.011

du Plessis, A., and Boshoff, W. P. (2019). A review of X-ray computed tomography of concrete and asphalt construction materials. *Constr. Build. Mater.* 199, 637–651. doi: 10.1016/J.CONBUILDMAT.2018.12.049

Duan, Y., Chen, Q., and Zhang, H. (2019). CNN-based damage identification method of tied-arch bridge using spatial-spectral information. *Smart Struct. Syst.* 23, 507–520. doi: 10.12989/SSS.2019.23.5.507

Feng, K., Zhao, Q., and Qiu, Y. (2020). Damage imaging in mesoscale concrete modeling based on the ultrasonic time-reversal technique. *Acta Mech. Solida Sin.* 33, 61–70. doi: 10.1007/s10338-019-00153-z

Gao, R., Li, X., Liu, H., Xu, Q., Wang, Z., and Zhang, F. (2019). Experimental study on detecting sleeve grouting defect depth by embedded non-contact steel wire drawing hole-forming method. *Constr. Technol.* 48, 17–19. doi: 10.7672/sgjs2019090017

Gao, R., Li, X., and Zhang, F. (2017). Testing test of sleeve grouting compactness based on X-ray industrial CT technology. *Nondestruct. Test.* 39, 6–11. doi: 10.11973/wsjc201704002

Gulgec, N. S., Takáč, M., and Pakzad, S. N. (2019). Convolutional neural network approach for robust structural damage detection and localization. *J. Comput. Civ. Eng.* 33:04019005. doi: 10.1061/(ASCE)CP.1943-5487.0000820

Khodabandehlou, H., Pekcan, G., and Fadali, M. S. (2019). Vibration-based structural condition assessment using convolution neural networks. *Struct. Control Health Monit.* 26:e2308. doi: 10.1002/STC.2308

Kim, H., and Sim, S. H. (2019). Automated peak picking using region-based convolutional neural network for operational modal analysis. *Struct. Control Health Monit.* 26:e2436. doi: 10.1002/stc.2436

LeCun, Y., Boser, B., Denker, J. S., Henderson, D., Howard, R. E., and Hubbard, W., et al. (1989). Backpropagation applied to handwritten zip code recognition. *Neural Computation* 1, 541–551. doi: 10.1162/neco.1989.1.4.541

Lee, S., Ha, J., and Zokhirova, M. (2018). Background information of deep learning for structural engineering. *Arch. Comput. Methods Eng.* 25, 121–129. doi: 10.1007/s11831-017-9237-0

Li, X., Lin, Y., and Ma, H. (2018). Research on the application of bridge damage identification method based on convolutional neural network. *J. Qinghai Univ.* 2, 41–46. doi: 10.13901/j.cnki.qhwxxbzk.2018.02.007

Lin, Y., Nie, Z., and Ma, H. (2017). Structural damage detection with automatic feature-extraction through deep learning. *Comp.-Aided Civil Inf. Eng.* 32, 1025–1046. doi: 10.1111/mice.12313

Pathirage, C. S., Li, J., and Li, L. (2018). Structural damage identification based on autoencoder neural networks and deep learning. *Eng. Struct.* 172, 13–28. doi: 10.1016/J.ENGSTRUCT.2018.05.109

Schnitzer, D., Flexer, A., Schedl, M., and Widmer, G. (2012). Local and global scaling reduce hubs in space. *J. Mach. Learn. Res.* 13, 2871–2902. doi: 10.1051/cocv/2012004

Tang, Y., Chen, M., Wang, C., Luo, L., Li, L., and Zou, X. (2020). Recognition and localization methods for vision-based fruit picking robots: a review. *Front. Plant Sci.* 11:510. doi: 10.3389/fpls.2020.00510

Tang, Y., Li, L., Wang, C., Chen, M., Feng, W., Zou, X., et al. (2019). Real-time detection of surface deformation and strain in recycled aggregate concrete-filled steel tubular columns via four-ocular vision. *Robot. Comput. Integr. Manuf.* 59, 36–46. doi: 10.1016/j.rcim.2019.03.001

Thongkam, J., Xu, G., and Zhang, Y. (2008). "AdaBoost algorithm with random forests for predicting breast cancer survivability," in *2008 IEEE International Joint Conference on Neural Networks* (IEEE World Congress on Computational Intelligence), 3062–3069. doi: 10.1109/IJCNN.2008.4634231

Wang, Z., Zheng, H., and Li, L. (2019). Practical multi-class event classification approach for distributed vibration sensing using deep dual path network. *Opt. Express* 27, 23682–23692. doi: 10.1364/OE.27.023682

Xie, X., Shan, D., and Zhou, X. (2018). Bridge damage identification method based on stacked denoising autoencoders. *Railw. Construct.* 58, 1–5. doi: 10.3969/j.issn.1003–1995.2018.05.01

Xu, Y., Wei, S., Bao, Y., and Li, H. (2019). Automatic seismic damage identification of reinforced concrete columns from images by a region-based deep convolutional neural network. *Struct. Control Health Monit.* 26, 1–22. doi: 10.1002/stc.2313

Yoon, M. K., Heider, D., Gillespie, J. W., Ratcliffe, C. P., and Crane, R. M. (2010). Local damage detection with the global fitting method using operating deflection shape data. *J. Nondestruct. Eval.* 29, 25–37. doi: 10.1007/s10921-010-0062-8

Yu, Y., Wang, C., Gu, X., and Li, J. (2019). A novel deep learning-based method for damage identification of smart building structures. *Struct. Health Monitor.* 18, 143–163. doi: 10.1177/1475921718804132

Zelelew, H. M., Almuntashri, A., Agaian, S., and Papagiannakis,. A. T. (2013). An improved image processing technique for asphalt concrete X-ray CT images. *Road Mater. Pavement Des.* 14, 341–359. doi: 10.1080/14680629.2013.794370

Zhao, Y. (2019). *Research on Blade Damage Identification Method Based on Convolutional Neural Network*. Tianjin: School of Aeronautical Engineering, Civil Aviation University of China. doi: 10.27627/d.cnki.gzmhy.2019.000074

Zheng, Y., Guo, Z., and Cao, J. (2015). Constraint mechanism and constraint stress distribution of new grout sleeve. *J. Harbin Inst. Tech.* 47, 106–111. doi: 10.11918/j.issn.0367-6234.2015.12.019

Zhou, C., and Mi, H. (2017). A comparative study on the performance of three kinds of activation functions in deep learning. *J. Beijing Institute Electron. Technol.* 4, 27–32. doi: 10.3969/j.issn.1672-464X.2017.04.005

Zhu, W., Gao, Z., and Huang, S. (2018). Research on testing technology of grouting plumpness of sleeve based on vibration amplitude of sensors method. *Constr. Qual.* 36, 7–10. doi: 10.3969/j.issn.1671-3702.2018.11.003

Zhu, W., Xu, J., Zhang, H., Han, W., and Cai, Y. (2019). Common quality defects and repair methods of precast concrete members. *Concrete* 5, 115–118. doi: 10.3969/j.issn.1002-3550.2019.05.028

Conflict of Interest: The authors declare that the research was conducted in the absence of any commercial or financial relationships that could be construed as a potential conflict of interest.

frontiers
in Materials

ORIGINAL RESEARCH
published: 16 November 2020
doi: 10.3389/fmats.2020.576918

Fusion and Visualization of Bridge Deck Nondestructive Evaluation Data via Machine Learning

Sara Mohamadi[1], *David Lattanzi*[1]* *and Hoda Azari*[2]

[1]*Department of Civil, Environmental, and Infrastructure Engineering, George Mason University, Fairfax, VA, United States,*
[2]*Turner-Fairbank Highway Research Center, McLean, VA, United States*

To maintain infrastructure safety and integrity, nondestructive evaluation (NDE) technologies are often used for detection of subsurface defects and for holistic condition assessment of structures. While the rapid advances in data collection and the diversity of available sensing technologies provide new opportunities, the ability to efficiently process data and combine heterogeneous data sources to make robust decisions remains a challenge. Heterogeneous NDE measurements often conflict with one another and methods to visualize integrated results are usually developed ad hoc. In this work, a framework is presented to support fusion of multiple NDE techniques in order to improve both detection and quantification accuracy while also improving the visualization of NDE results. For data sources with waveform representations, the discrete wavelet transform (DWT) is used to extract salient features and facilitate fusion with scalar-valued NDE measurements. The description of a signal in terms of its salient features using a wavelet transform allows for capturing the significance of the original data, while suppressing measurement noise. The complete set of measurements is then fused using nonparametric machine learning so as to relax the need for Bayesian assumptions regarding statistical distributions. A novel visualization schema based on classifier confidence intervals is then employed to support holistic visualization and decision making. To validate the capabilities of the proposed methodology, an experimental prototype system was created and tested from NDE measurements of laboratory-scale bridge decks at Turner-Fairbank highway research center (TFHRC). The laboratory decks exhibit various types of artificial defects and several non-destructive tests were previously carried out by research center technicians to characterize the existing damages. The results suggest that the chosen feature extraction process, in this case the DWT, plays a critical role in classifier performance. The experimental evaluation also indicates a need for nonlinear machine learning algorithms for optimal fusion performance. In particular, support vector machines provided the most robust and consistent data fusion and defect detection capabilities. Overall, data fusion combinations are shown to provide more accurate and consistent detection results when compared to single NDE detection approaches, particularly for the detection of subsurface delamination.

Keywords: data fusion, nondestructive Evaluation, visualization, machine learning, support vector machine, feature extraction, wavelet transform

Edited by:
Juncai Xu,
Case Western Reserve University,
United States

Reviewed by:
Nenad Gucunski,
Rutgers, The State University of New Jersey, United States
Jinyoung Kim,
Ajou University, South Korea
Hung Manh La,
University of Nevada, Reno,
United States

Correspondence:
David Lattanzi
dlattanz@gmu.edu

Specialty section:
This article was submitted to Structural Materials, a section of the journal Frontiers in Materials

Received: *27 June 2020*
Accepted: *19 October 2020*
Published: *16 November 2020*

Citation:
Mohamadi S, Lattanzi D and Azari H (2020) Fusion and Visualization of Bridge Deck Nondestructive Evaluation Data via Machine Learning. Front. Mater. 7:576918. doi: 10.3389/fmats.2020.576918

INTRODUCTION

To preserve infrastructure safety and integrity, reliable and effective damage detection techniques need to be established. Increasingly, nondestructive evaluation (NDE) technologies are used for the detection of surface and subsurface defects, evaluation of the extent of defects, and as a critical aspect of holistic asset management. A key challenge with NDE is that the accuracy of the data from a single source is dependent on operator training and environmental conditions that can add considerable uncertainty to defect detection and quantification (McCann and Forde 2001). From a practical standpoint, this measurement uncertainty has inhibited the adoption of NDE across many application domains.

To reduce measurement uncertainty, researchers have explored the concept of using multiple NDE methods in conjunction with data fusion algorithms. Recent advances in sensing and data analytics have led to the adoption of data fusion in fields such as computer vision and image analysis (Chen et al., 2017), transportation systems (Faouzi, Leung, and Kurian 2011; Faouzi and Klein 2016), biometrics (Haghighat, Abdel-Mottaleb, and Alhalabi 2016), and structural health monitoring (Sun et al., 2016; Wu and Jahanshahi, 2018; Ramos et al., 2015; Chen et al., 2017; Habib et al., 2016; Kralovec and Schagerl, 2020). In these cases, the use of data fusion was shown to provide a better interpretation of observed information by decreasing the measurement uncertainty present in individual source data (Faouzi and Klein, 2016).

Data fusion encompasses a vast array of analytical methods ranging from Bayesian probabilistic approaches, Dempster–Shafer (DS) evidence approaches, fuzzy reasoning, and machine learning (Wu and Jahanshahi, 2018; Khan and Anwar, 2019). These methods have been used for damage identification, quantification, and system response estimates (Hall and Llinas, 2001; Chair and Varshney, 1986; Liu et al., 1999; Vanik et al., 2000). For example, a recursive Bayesian framework was used to update the parameters of a crack growth model, as well as the probability distribution of the crack size and crack growth rate (Rabiei and Modarres, 2013), and a neural network and fuzzy inference were combined to evaluate the structural condition of a cable bridge (Sun et al., 2016).

Data fusion can generally be carried out at various “levels” of data processing ranging from combinations of raw data to a fusion of individual operational decisions (Steinberg and Bowman, 2017). *Data-level* fusion refers to combining raw data directly and it is possible only if the sensors measure the same physical quantities. On the other hand, if the survey observations are heterogeneous, then the data must be fused at the *feature-level* or *decision-level*. For *feature-level* fusion, a vector of data descriptors is extracted from the raw measurements of individual NDE results and the features are then combined together into a single concatenated descriptor vector (Chen and Jen, 2000). This combined vector can be further processed through machine learning techniques based on neural networks or clustering algorithms (Kittler 1975; Sun et al., 2016). Once features are fused through machine learning, the resulting output reflects the correlations in data content and reduces the uncertainty of results. *Decision-level* fusion is the blending of operational decisions derived from individual data streams considered in isolation. Decision-level fusion naturally leads to loss of performance, but this type of fusion represents a feasible fusion approach when fusion at lower levels is not practical or advisable.

Frequently applied fusion methods in structural health monitoring include: Bayesian probabilistic approaches including techniques such as Kalman filtering (Vanik et al., 2000; Rabiei and Modarres, 2013; Ramos et al., 2015), Dempster–Shafer (DS) evidential reasoning (Wu, 2004; Huang et al., 2014), and machine learning algorithms such as artificial neural networks (ANN) (Chen and Jahanshahi, 2018; Jiang et al., 2011) or support vector machines (SVM) (Zhou et al., 2015). SHM applications tend to focus on the fusion of time-series sensor data, such as from accelerometers, to reduce measurement and state-estimation uncertainty.

In this work, the application of machine learning driven data fusion to the NDE assessment of concrete bridge decks is considered. Bridge deck deterioration plays a critical role in highway asset management due to the costs and traffic disruptions associated with deck repair and replacement. While pattern analysis and machine learning have been studied for use with individual concrete NDE methods, they have not been considered as a basis for data fusion. Furthermore, how the results of NDE data fusion can be intuitively visualized and assessed holistically by engineers remains an under-studied problem.

The primary contributions of this work are:

- A wavelet-based approach to extracting statistically relevant features from NDE waveforms
- A non-parametric machine learning approach to the fusion of NDE data features
- A novel visualization schema for representing the fused results and measurement uncertainty

In order to best illustrate the benefits of NDE fusion, the machine learning models developed in this work were trained and evaluated for the detection of single defect classes (binary classification). As such, they do not provide defect diagnosis across a range of observed defects. Such considerations may lead to different conclusions regarding fusion efficacy and are an avenue for future work.

The remainder of this paper is structured as follows. First, the overall methodological framework is presented. This is followed by an experimental case study to illustrate the behavior and performance of the approach, based on laboratory scale data collected at the Turner-Fairbank Highway Research Center (TFHRC). The NDE data for this case study was captured in a manner that mimicked the NDE systems available onboard an inspection robot developed at TFHRC, illustrating a potential practical application for the proposed framework. The following NDE methods were considered (see *Experimental Validation* for more details): ultrasonic surface waves (USW), impact echo (IE),

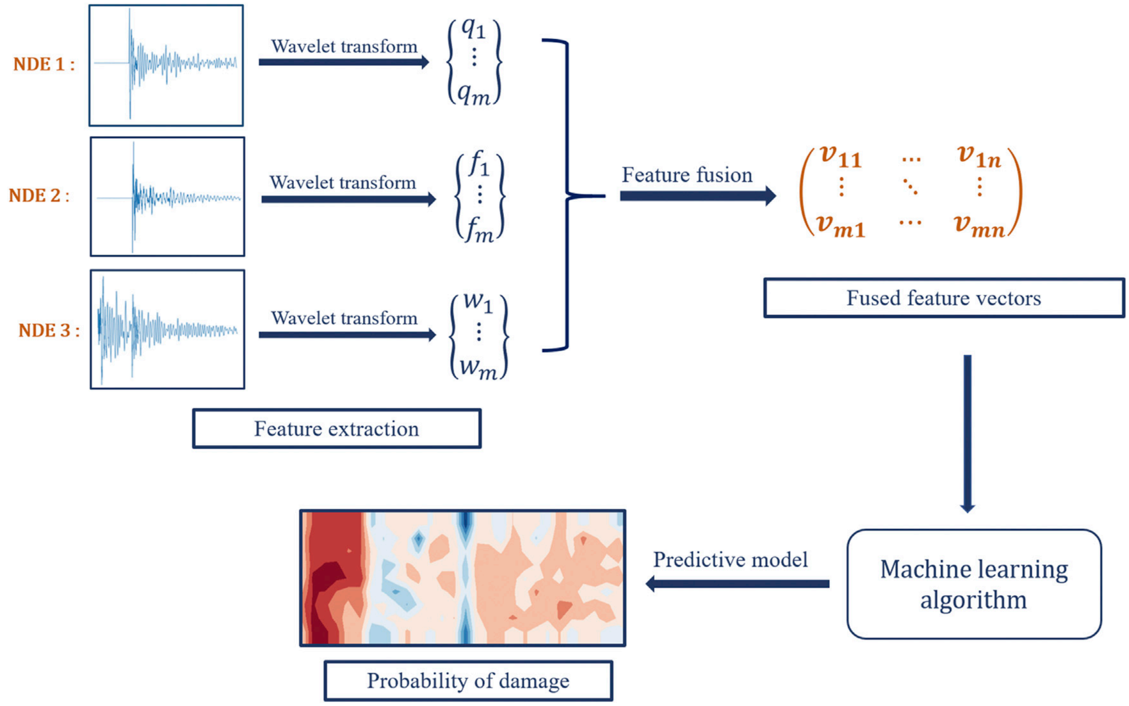

FIGURE 1 | Schematic overview of the proposed methodology for multiple NDE feature fusion.

ground penetrating radar (GPR), electrical resistivity (ER), ultrasonic tomography (UT), half-cell potential (HCP), infrared thermography (IRT), and impulse response (IR). The paper concludes with a discussion of outstanding research efforts that must be considered prior to practical implementation.

METHODOLOGY

The primary focus of this study was on the development of a feature-level fusion approach (**Figure 1**). A decision-level fusion approach was also developed for comparative purposes and is discussed in Decision Fusion. First, data from multiple NDE sources are preprocessed for spatial registration and salient numerical features are extracted from each NDE data source. Feature extraction is achieved through the discrete wavelet transform (DWT). Once extracted, features are combined into a concatenated feature (descriptor) vector**.** This feature vector then serves as input to a supervised machine learning classifier trained to detect subsurface defects in the concrete specimen. For model training, features extracted from test data were manually labeled to generate a ground truth. Once the machine learning model assesses the likelihood of a defect at each location along a bridge deck, the probability of occurrence of damage across the deck is visualized as a red-blue heatmap.

Data Preprocessing

Data preprocessing encompasses a range of tasks such as data cleaning, data transformation, and feature extraction (Nantasenamat et al., 2009). In this work, the emphasis for data preprocessing is on making heterogeneous NDE datasets spatially compatible followed by feature extraction. Even for robotic multi-NDE systems, discrepancies in the location of measurements is inevitable. To accommodate, measurements are linearly interpolated onto a consistent 2D grid spacing. Incomplete data is also an inevitable problem in handling most real-world data sources, and is interpolated as well.

Some NDE techniques provide scalar valued measurements at each test point (e.g., HCP or ER) while others produce a waveform result (e.g., IE or GPR). This data heterogeneity necessitates fusion at either the feature or decision-level. To fuse at the feature-level, numerical feature must first be extracted from waveform measurements. These descriptors are then concatenated with scalar response data (**Figure 2**).

Waveform Feature Extraction

Feature extraction refers to the process of extracting statistically salient numerical descriptors from the original data. In most conventional approaches to NDE data analysis, feature extraction has focused on reducing an NDE waveform measurement to a single scalar-valued representation. For data fusion, such approaches dramatically reduce the amount of relevant information. The wavelet transform is a time-frequency analysis technique that is commonly used for advanced signal processing (Daubechies, 1992). It was developed as an alternative to the short time Fourier (Mallat 1989; Nouri Shirazi et al., 2014) to overcome problems related to the simultaneous representation of frequency and time resolution properties. Compared to a

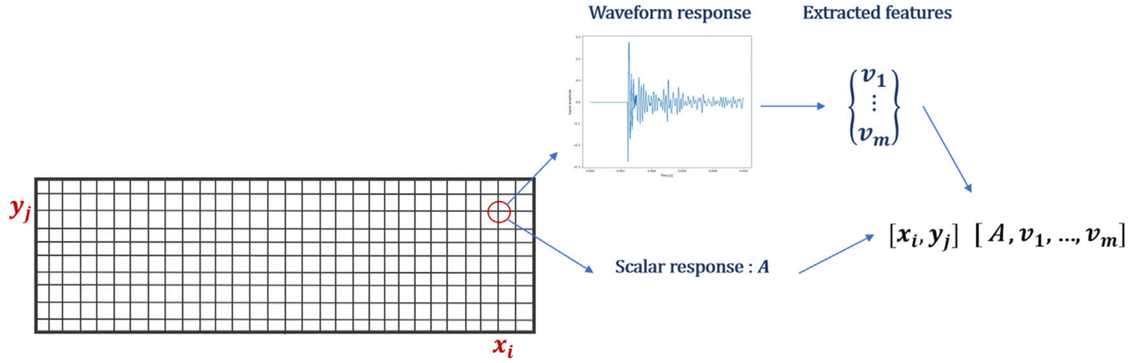

FIGURE 2 | Combining scalar and waveform responses of interpolated data.

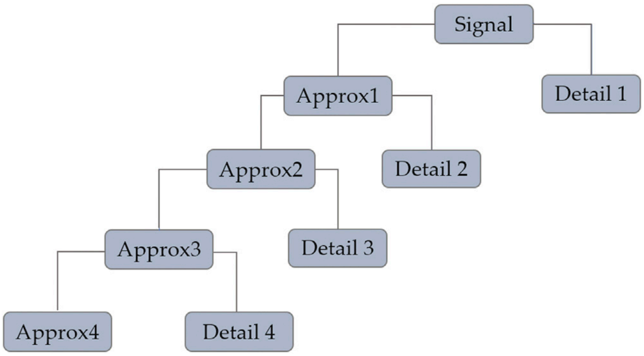

FIGURE 3 | Schematic discrete wavelet transforms for the four-level Symlet wavelet decomposition used in this work.

traditional Fourier analysis, a wavelet transformation has the ability to simultaneously reproduce temporal and scale data, making it better suited for analyzing signals that are periodic, transient (or non-stationary), and noisy. As a result, wavelet transforms are increasingly employed in numerous applications for feature extraction (Epinat et al., 2001; Ghazali et al., 2007; Luk et al., 2008; Al Ghayab et al., 2019). In particular, wavelet transforms have recently seen use in SHM and NDE analysis, for instance in the assessment of acoustic IE measurements of concrete slabs (Saadat et al., 2004; Khatam et al., 2007; Yeh and Liu, 2008; Hou et al., 2015).

Wavelets can be considered as a family of functions constructed from translations and dilations of a single function called the "mother wavelet" (t) (Mallat, 2009). They are defined by the following equation:

$$\Psi_{a,b}(t) = \frac{1}{\sqrt{|a|}}\Psi\left(\frac{t-b}{a}\right) \qquad a, b \in R,\ a \neq 0 \tag{1}$$

The parameter a is the scale, and it measures the degree of compression. The parameter b is the translation parameter that determines the time location of the wavelet and t is time (Debnath and Shah, 2014). For a signal (t), the transformed wavelet representation of the signal, W_s, at scale a, position b is defined as an inner product:

$$W_s(b, a) = \int_{-\infty}^{\infty} s(t)\frac{1}{\sqrt{|a|}}\Psi\left(\frac{t-b}{a}\right)dt \tag{2}$$

The wavelet transform can be implemented in either a continuous or discrete form. The widely used DWT is employed in this study. DWT is an adaptive decomposition which decomposes a signal with high- and low-pass filters and increases the frequency resolution in lower frequency bands (Zhang et al., 2018a). The DWT decomposes a signal onto a set of bases that correspond to different time and frequency scales or resolutions (**Figure 3**). At the first stage of decomposition, the initial signal is decomposed into approximation and detail coefficients. The first level approximation coefficients are further decomposed into second-level approximation and detail coefficients, and the process is repeated, resulting in levels of approximation and detail that capture both frequency and time domain information about a signal (Zhang et al., 2016). The approximations are the high-scale, low-frequency components of the signal, while the details are low-scale, high frequency. This wavelet decomposition also suppresses signal noise, effectively serving to denoise the signals prior to data fusion.

In this work, a fourth order variant of the Daubechies wavelet, known as the Symlet wavelet, is used in conjunction with the DWT. This particular wavelet feature extraction approach was first developed in (Zhang et al., 2016) for the analysis of IE data. In this study, this wavelet extraction approach is applied to both IE and GPR signals. Both IE and GPR signals are considered transient in nature with nonstationary noise characteristics, indicating that they are well suited for wavelet representation (Zhang et al., 2018b). Based on prior studies and empirical analysis by the authors, a four-level decomposition is adopted for both IE and GPR signals and decomposition, as illustrated in **Figure 4**. After decomposition and reconstruction of sub-signals, four features are extracted from each wavelet basis. The root mean square (i.e., average power of signal), standard deviation (i.e., Second spectral moment), kurtosis (i.e., Third spectral moment) and

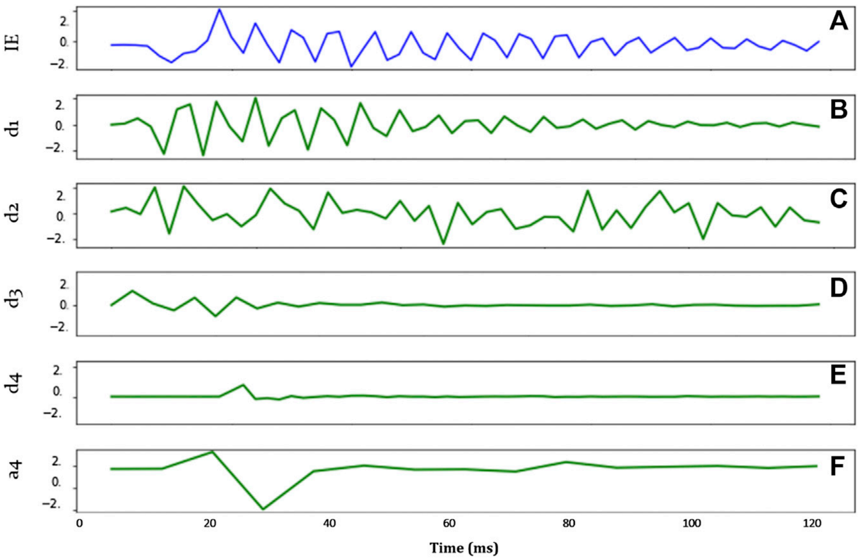

FIGURE 4 | A) Original IE signal; **(B–E)** reconstructed detail coefficients at level 1 **(B)**, level 2 **(C)**, level 3**(D)**, level 4**(E)**; **(F)** reconstructed approximation coefficients at level 4.

skewness (i.e., Fourth spectral moment). Overall, this results in 20 features for each original measurement signal. These features extracted from IE and GPR signals are later combined into a vector as an input to a given statistical model. The functions for feature calculation are defined as follows:

Let x_n, n = 1, 2, . . ., N be the time domain signals and $[p_i, f_i]$, i = 1, 2, . . ., M be its corresponding spectrum, where p_i and f_i are the amplitude and the frequency at *i*th frequency bin, respectively.

$$Total\ Power\ :\ TP = \sum_{i=1}^{M} p_i,$$

$$Centroid :\ M_1 = \sum_{i=1}^{M} p_i.f_i \Big/ TP \tag{3}$$

$$Root\ Mean\ Square = \sqrt{1\Big/M \sum_{i=1}^{M} p_i^2} \tag{4}$$

$$Standard\ Deviation :\ M_2 = \sqrt{\sum_{i=1}^{M} (f_i - M_1)^2.p_i \Big/ TP} \tag{5}$$

$$Skewness :\ M_3 = \frac{\sum_{i=1}^{M} (f_i - M_1)^3.p_i}{M_2^3.TP} \tag{6}$$

$$Kurtosis\ :\ M_4 = \frac{\sum_{i=1}^{M} (f_i - M_1)^4.p_i}{M_2^4.TP} \tag{7}$$

Data Interpolation

In a multi-NDE assessment scenario, the goal is to capture measurements at identical locations across an assessment area. However, the practicalities of NDE mean that it is typically not possible to achieve this goal. For instance, in the experimental study of this work, NDE measurement spacing was not consistent across NDE techniques and there were intermittent missing measurements. Prior to data fusion, NDE values must be interpolated onto a consistent grid spacing. In the example shown in **Figure 5**, the grid spacings of measurements NDE 1 and NDE 2 are different. Features from NDE 2 are measured at grid points x0, x, and x1, resulting in measurements u0, u, and u1. Features extracted from NDE 1 are only measured at grid points x0 and x1 (measurements f0 and f1). The features f at location x are linearly interpolated via first order polynomial. The relationship between spatially distributed NDE measurements is not well-defined, and more complex interpolation approaches could prove more suitable. This is one potential avenue for future study.

Data Fusion

As discussed previously, feature and decision-level fusion are considered in this study because the heterogeneity of bridge deck NDE data prohibits the use of data level fusion. In general, the "higher up" in the fusion ontology from data to decision-level, the greater the loss of information. As such, it is generally advisable to fuse data at the lowest possible level, motivating the focus on feature-level fusion in this work.

The general concept is to take the concatenated set of wavelet features extracted from each NDE measurement (*Waveform Feature Extraction*) at each location and use the combined vector of features as the inputs into a statistical model that associates the vector with a statistical assessment of material condition. Here this statistical model takes the form of a statistical classification problem, one that classifies a feature vector as being a member of either a "detected defect" or "sound concrete" assessment class. Multiclass classifications are also possible,

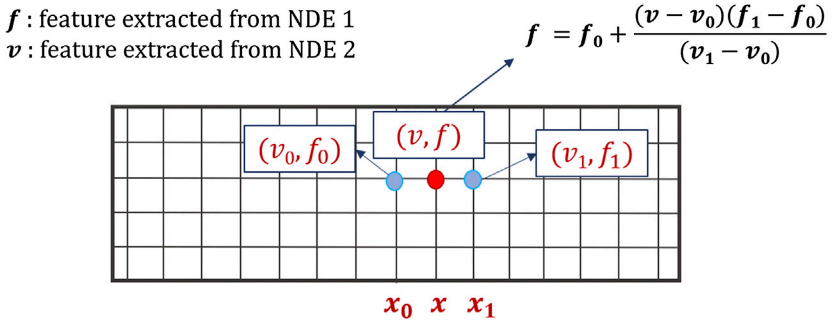

FIGURE 5 | Linear interpolation of NDE data.

though they were not extensively studied here due to limited data availability (see *Experimental Validation* for more details). Ultimately, the end result is that the raw data from each NDE source is effectively fused together to provide an enhanced assessment.

There are a broad range of classification algorithms that can be used such purposes. Generally, they can be divided into parametric and nonparametric methods. Parametric techniques make assumptions about the underlying statistical distribution or the measurement uncertainty of observations in order to enable inference. Implicitly, such techniques often require statistical stationarity, as well as consistent and quantifiable measurement uncertainty. The alternative are nonparametric fusion methods. Nonparametric methods relax assumptions regarding underlying statistical distributions and instead construct a model of measurement states from sets of existing data (Tsiliki and Kossida, 2011). Such approaches have the advantage of being applicable to highly complex and nonlinear statistical problems. Machine learning approaches have become the dominant paradigm for nonparametric data fusion, with ANN and SVM as the most widely used approaches. ANN have the advantage of being more flexible with respect to data input and can be highly tuned for optimization to a specific problem domain. SVM have fewer user parameters (hyperparameters), making them more suitable for rapid prototyping and problems with less data available for model training (Dong et al., 2009). Given the limited size of the available data sets for prototyping, the focus here is on the use of SVM. The behavior of several other methods are presented as well for comparative purposes. These methods included: logistic regression, decision tree-based models and ANN. The weighted decision-level fusion is also studied and is briefly discussed (Lu and Michaels, 2009; Heideklang and Shokouhi, 2013).

Conventional machine learning performance metrics are used to assess data fusion capabilities, including confusion matrices, ROC curves and F1 scores (Fawcett, 2006). While classifiers typically produce a discrete classification, statistical probabilities are used for class separation. This statistical probability provides a more nuanced representation of classifier performance, and can be used for holistic assessment and visualization purposes (see Holistic Visualization for details).

Feature Fusion - SVM

SVM are a group of algorithms that were originally designed for binary classification, and gained popularity due to promising performance in a wide range of applications (Cortes and Vapnik, 1995; Cristianini and Shawe-Taylor, 2000; Ruiz and Lopez-de-Teruel, 2001). SVMs attempt to discriminate between classes of data by finding the optimal high-dimensional hyperplanes that bisect the data, and then combining these hyperplane bi-sections to enable more complex reasoning. The original data points from an input feature vector are projected by a kernel function into a higher dimension feature space (**Figure 6**). In this space, SVM tends to find the hyperplane that separates the data with the largest margin. The method places class-separating hyperplanes in the original or transformed feature space, and the new sample is labeled with the class label that maximizes the decision function—the distance between support vectors (Boser et al., 1992; Vapnik, 2000).

The SVM is especially suited for scenarios with smaller sample sizes, as is the case for many NDE assessment scenarios (Luts et al., 2012). In contrast to other algorithms, SVM tends to use all available features, even if they are not of real statistical importance, and therefore requires more care regarding cleaning and preprocessing of the input data.

SVM Standardization

Standardization (i.e., feature scaling) refers to the process of rescaling the values of the input variables so that they share a common scale, in order to reduce classifier biasing. Standardization is an important step for SVM classifiers. For instance, many elements used in the RBF kernel of Support Vector Machines assume that all features are centered around 0 and have variance in the same order. If a feature has a variance that is orders of magnitude larger than others, it can potentially dominate the objective function and make the estimator unable to learn from other features. Data standardization also can speed up training time of SVM by starting the training process for each feature within the same scale (Kotsiantis et al., 2006). Here, features are standardized by removing the mean and scaling to a unit variance. The standard score of a sample x is calculated as:

$$Z = \frac{(x - u)}{s} \tag{8}$$

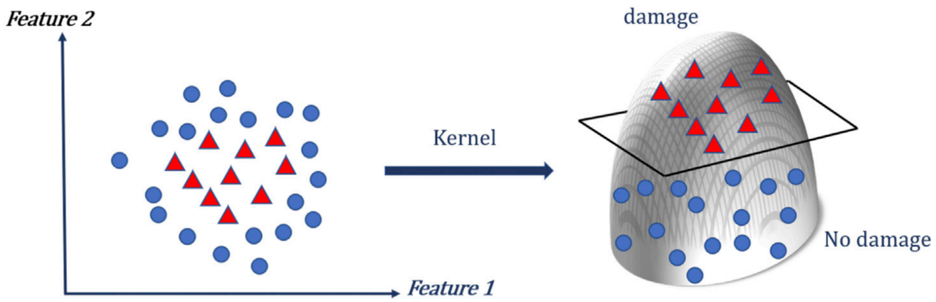

FIGURE 6 | Support Vector Machine illustration of projection of 2D data into a higher dimension through kernel function projection.

where u is the mean of the training samples and s is the standard deviation of the training samples (Shanker et al., 1996). Centering and scaling happen independently on each feature by computing the relevant statistics from samples in the training set. These scaling parameters are then applied to the test data.

Hyperparameter Identification

Prior to model training and fitting, the model hyperparameters must be optimized (Wang et al., 2010). Good model selection is the key to getting good performance from any machine learning algorithm. Also, if the hyperparameters are not selected appropriately, an SVM may take an unduly long time to train (Nalepa et al., 2018). The SVM model contains two main parameters that must be optimized: the kernel function used for dimensional reprojection, and the regularization parameter (c). SVM algorithms can use different types of kernel functions such as linear, polynomial, sigmoid, and radial basis functions (RBF). The regularization parameter (c) is used to prevent overfitting. In this study, a hyperparameter search (grid search) is performed across combinations of different kernel functions and regularization parameters. The performance of the selected hyperparameters and resulting trained model is then measured on a dedicated evaluation set that was not used during formal model selection and training. Different combinations of hyperparameters are compared against each other based on model predictive performance. For the experimental data set discussed in *Experimental Validation*, a combination of the Radial Based Function and regularization parameter, *c*, equal to unity showed the best performance among all combinations.

Other Considered Classifiers

To provide a point of comparison with SVM data fusion, logistic regression, decision trees, and ANN are presented and evaluated here as well. Logistic regression is a simple, parametric machine learning algorithm which assumes a linear mapping function between input data and output classification, and has been used extensively in the data fusion literature (Pigeon et al., 2000; Sohn and Lee, 2003). Generally, this function is a linear combination of the input variables. The benefit of the algorithm is that it does not require as much training data as methods such as methods such as SVM and ANN, however it is constrained to the specified logistic functional form, which may or may not be sufficiently accurate. As will be shown in *Experimental Validation*, since logistic regression is only suitable for linear problems, its performance was strongly biased to one of the technique's results and did not provide a true fusion of information for NDE data.

Tree-based learning models such as the Decision tree (DT) classifier are nonparametric algorithms that first select the best feature for an initial separation of the data (root node) using the concept of information gain ratio. It then builds subtrees and nodes in a recursive manner that splits the data into classes based on an evaluation of each feature in an input vector (Demirbas, 1989). Decision trees generally work better for larger datasets and are prone to overfitting.

An ANN employs a complex network of nonlinear response functions, with the value of each function in the network weighted based on an optimized fitting to training data (Zhang et al., 2017). The input "layer" of the network can range from combinations of raw data to a set of extracted data features to a numerical representation of a set of decisions. The output can be a layer of the same size and type as the input, or smaller. Increasing the complexity of an ANN architecture allows for more nonlinear and sophisticated representations and fusions and is the basis for modern deep learning strategies. However, such increases in complexity typically require even larger increases in the amount of training data used to find network weights. Similarly, SVM outperformed the ANN in the preliminary analysis. The reason is that unlike ANNs, the computational complexity of SVMs does not depend on the dimensionality of the input space. ANNs use empirical risk minimization, while SVMs use structural risk minimization. The reason that SVMs often outperform ANNs in practice, particularly for smaller data sets, is that SVMs are less prone to overfitting (Olson and Dursun, 2008). In recent years, deep learning–based approaches have become popular across research fields due to their ability to automatically learn meaningful feature representations from the raw data (Hinton et al., 2006; Najafabadi et al., 2015). However for smaller dataset sizes, such as those in this study, deep learning algorithms do not perform well and become prone to overfitting (Brownlee, 2017).

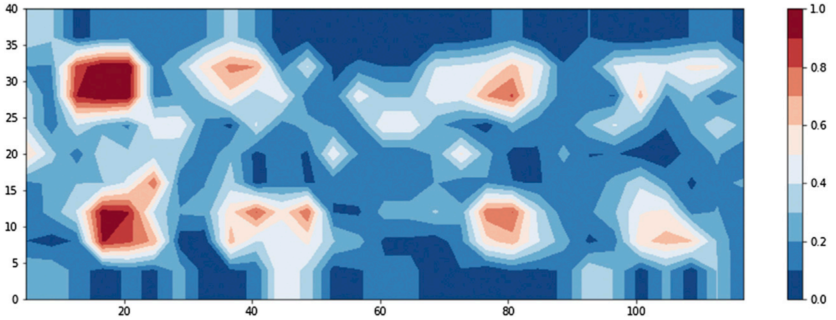

FIGURE 7 | Heat map showing confidence of defect prediction.

Decision Fusion

Decision-level fusion combines information after each sensor source has been independently processed to make a preliminary determination of the existence of damage. Such fusions are valuable when an effective workflow for using a single data source in decision making already exists. Decision-level fusion then allows those existing workflows to be integrated and combined. As a point of comparison, the weighted decision combination algorithm (Hall and Llinas, 2001) was used in this study.

Weighted decision making assumes that each individual assessment has its own weight with respect to accuracy or validity. These weights can be assumed equal for simplicity, however usually the decision from a data source with less precision and confidence is assigned a smaller weight contribution prior to the fusion. For classification tasks, the selection of appropriate thresholds is needed to assign the predicted damage pattern. This method therefore requires a priori assumptions regarding statistical distributions or the uncertainty of any given measurement.

It should be noted that many data fusion techniques can be used for decision-level fusion as easily as they can for feature or data-level fusions. What differs across these levels is the simplicity of the inputs to the algorithms, with data-level fusion requiring the largest and most complex inputs and decision-level requiring the simplest, with correlated requirements for the size of the data necessary for training and testing. Feature-level stands as a flexible compromise between the two extremes.

Holistic Visualization

The developed approach to visualization stemmed from a series of interviews the authors performed with NDE end-users, as well as recent advances in data visualization (Rangwala et al., 2009; Choo et al., 2012). Rather than present the discrete output classification of the machine learner at each measurement location, the model's statistical confidence in its prediction is presented (**Figure 7**). To accomplish this, the aggregated detection results across the deck slab are shown as a contour heat map, as is common practice. But rather than indicate a discretized detection, what is shown is in fact the machine learning model's classification confidence at each location, represented by a probability score ranging from 0.0 (confident in no defect) to 1.0 (confident in a detected defect). Once the probability of a defect's existence is estimated by the fusion algorithm for each measurement grid location, the grids with the same probability value range are then connected through polygonization. Further polygons are filled with varying shades of color corresponding to their probability score (**Figure 8**). The heat map uses a two color diverging heat map scale, with varying shades of blue if no defect is more likely, and varying shades of red for a likely detected defect (Moreland, 2009). Lighter color intensity indicates lower model confidence, with a white midpoint suggesting no confidence in an assessment. The resulting heatmap provides end users with a data product that is familiar to them while presenting nuanced information in an intuitive and comprehensible format. Moreover, the confidence thresholds can potentially be tuned and controlled by the end user, as several interview participants requested.

EXPERIMENTAL VALIDATION

This section presents an experimental study designed to illustrate the potential capabilities of a machine-learning approach to data fusion. Prior to this study, researchers at Turner-Fairbank Highway Research Center (TFHRC) constructed a series of laboratory-scale bridge decks and performed a set of NDE assessments on those decks. Overall, eight NDE techniques were used to collect synchronous data from the specimens. Four of these NDE measurements simulate measurements from the Federal Highway Administration (FHWA) Robotics-Assisted Bridge Inspection Tool (RABIT), a robot designed to perform synchronous multi-NDE assessments of bridge decks (Gucunski et al., 2017; La et al., 2017; Gibb et al., 2018; Ahmed et al., 2020). The other four are commonly used techniques for bridge deck NDE.

The data from these NDE assessments was used to prototype and test the data fusion algorithms discussed in *Methodology*. The performance of the data fusion algorithm was tested for two different types of defects and NDE methods. The first set of tests focused on deck corrosion detection, while the second sets of tests explored algorithm performance for sub-surface delamination detection.

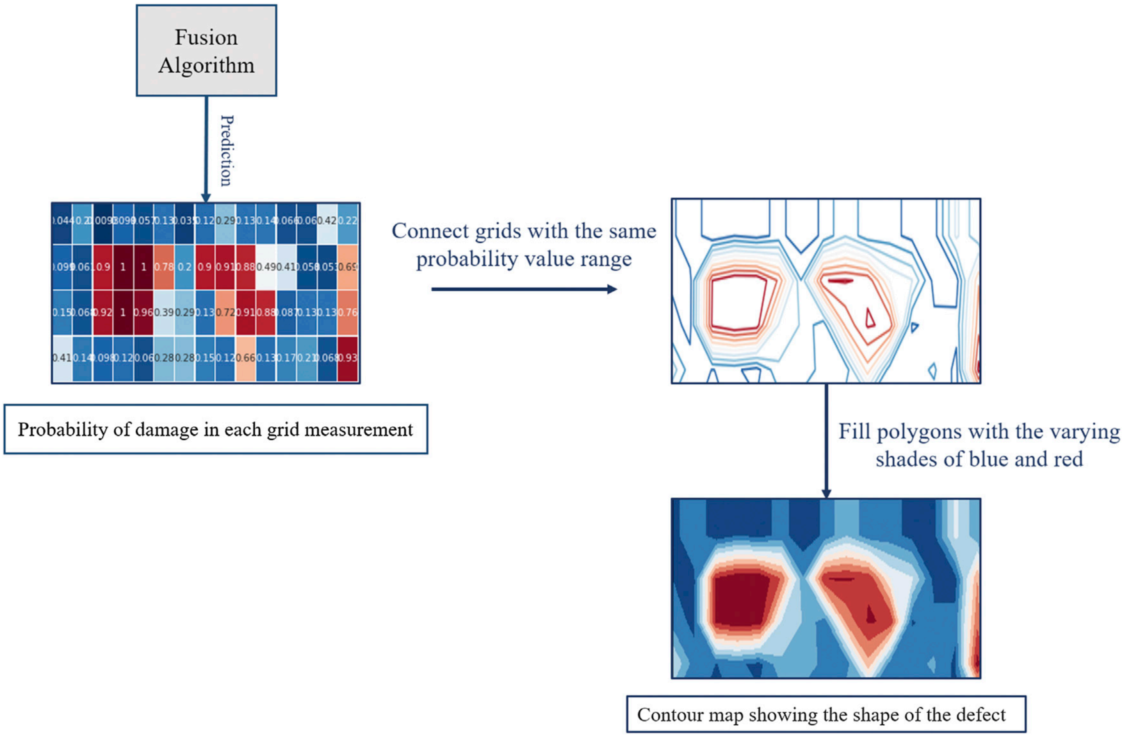

FIGURE 8 | Flowchart of the process for generating fusion confidence visualizations.

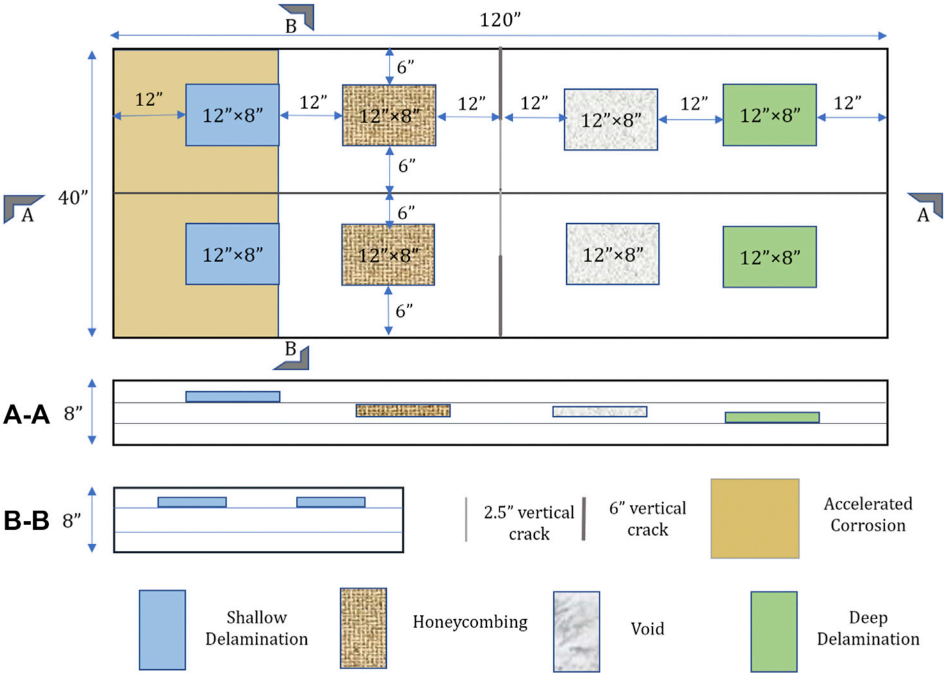

FIGURE 9 | Laboratory-scale bridge deck specimen design. Section **(A-A)** shows the location for each defect type with respect to slab depth. Section **(B-B)** shows defect placement for shallow delaminations. The placement of other defects in the cross-section is similar, accounting for variations in depth.

TABLE 1 | Details of NDE measurements used for data fusion.

Method	Measurement spacing	Number of samples prior to interpolation
IE	4 inches - data was not collected at centerline vertical crack	2,016
GPR (A-scan)	9 longitudinal scan lines at 4 inch spacing–GPR was set to 36 scans/foot	2,898
HCP	4 inches	2,088
ER	4 inches	2,088

TABLE 2 | Comparison of fusion algorithm performance for corrosion detection.

Fusion Algorithm	Accuracy	Precision	Recall	F1-score
SVM	0.96	0.92	0.91	0.91
ANN	0.95	0.92	0.89	0.90
Decision tree	0.91	0.89	0.89	0.89
Logistic regression	0.89	0.82	0.82	0.82

It is important to note that these experiments were all performed under idealized laboratory conditions. While the test specimens and data are representative of real-world scenarios, environmental conditions and the practicalities of full-scale field assessments will inevitably degrade algorithm behavior. Still, the results of these experiments illustrate the potential benefits of data fusion and serve as motivation for larger-scale testing under field conditions.

Nondestructive Evaluation Data Generation

Researchers at TFHRC constructed eight geometrically identical concrete decks with a series of controlled subsurface defects (**Figure 9**). These defects included deep and shallow delamination, honeycombing, voids and vertical cracks and accelerated corrosion. The 12 × 8 inch artificial delaminations were built using plexiglass and plastic gutter guards. Two plexiglass sheets with a thickness of 0.093 inches were cut to size, and two layers of plastic gutter guard were placed between the sheets to create an air gap, then the edges were sealed with duct tape. This artificial delamination was used to simulate shallow and deep delaminations at the top and bottom rebar levels. The artificial honeycombing was simulated with a bag of loose aggregates. For each honeycomb defect, 12 lbs of aggregate were placed into mesh bags and the edges were stitched with wire. The mesh bags were then placed in wood molds and secured to the rebar cage. The 23 × 8 × 2 inch voids were simulated with Styrofoam boards, Corrugated plastic sheets with a height of either 6 inches or 2.5 inches, a thickness of 0.16 inch, and a length of 10 inches were used to simulate vertical cracks within the concrete structure. Then the RC decks were then constructed using normal-weight concrete mix with a water-to-cement ratio of 0.37.

After the RC decks were fully cured, prior to data collection, accelerated corrosion was employed to create a corrosive environment with elevated chloride content in the concrete and active corrosion in the pre-corroded rebar. Different levels and uneven distribution of chloride content were introduced by a sponge saturated with NaCl solution. The reader should consult (Meng et al., 2020) for more details on deck construction and the development of the corrosive environment. Of the eight specimens, four also had an overlay. After construction of the test specimens, 8 NDE techniques were used to collect synchronous data from the specimens. Employed technologies included ultrasonic surface waves (USW), IE, GPR, ER (RABIT-based techniques), ultrasonic tomography (UT), HCP, infrared thermography (IRT) and impulse response (IR).

Of all eight NDE techniques, HCP, ER and GPR A-scan data were used in this research for corrosion detection: HCP for detection of corrosion activity, ER for detection of corrosive environment, and GPR for condition assessment. Previous nondestructive testing (NDT) applications on RC decks have demonstrated that ER and GPR can detect corrosive environments in concrete (elevated chloride content in this study), and HCP can detect active corrosion in the reinforcement (Gucunski et al., 2011; Gucunski et al., 2012). For delamination detection, GPR, IE and ER were used for condition assessment. For each specimen, nine gridlines were established with a spacing of 4 inches in the transverse direction, and 29 gridlines with a spacing of 4 inches were set in the longitudinal direction. For all techniques, data was collected on a specific grid spacing across the deck surface, though that spacing varied based on the specific NDE method used. ER, HCP and IE data were collected at grid points, and GPR A-scans were collected along each gridlines. The GPR was set to 36 scan/foot, resulting 322 scans along the longitudinal direction. As discussed in *Data Interpolation*, the data from each NDE method was linearly interpolated to generate approximate measurements on a consistent grid spacing. The specifics of the data set are shown in **Table 1**.

Data Fusion for Corrosion Detection

There are various electrochemical and physical methods for the detection of corrosion in concrete and the advantages and disadvantages of each respective method is well-explained in the literature (Alonso et al., 1988). The study concludes that there is no optimal method, and usually a combination of several techniques is used. For this study, three different NDE methods were chosen for corrosion detection: HCP, GPR, and ER. The HCP technique is a generally accepted method for identifying active corrosion in reinforced concrete bridge decks. The method is supported by an American Society for Testing Materials C876–09 standard (ASTM C876–09, 1999) with well-defined thresholds distinguishing actively corroded

TABLE 3 | Comparison of weighted decision combination with various weight order in corrosion detection.

Techniques	HCP > GPR > ER	GPR > ER > HCP	GPR > HCP > ER	SVM
Overall accuracy (%)	94.0	88.5	85.65	96.0

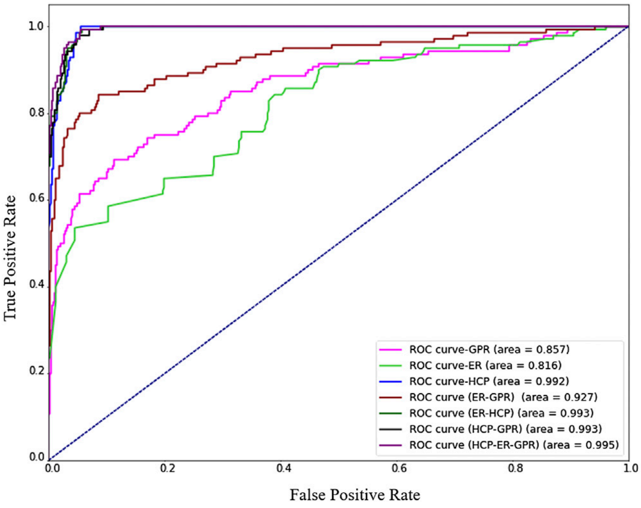

FIGURE 10 | Receiver Operating Characteristic curve of Support Vector Machine for corrosion detection.

and non-corroded areas. GPR data has been shown to correlate reasonably well with HCP data on bridge decks (Martino et al., 2014). ER probes are also frequently used in corrosion monitoring systems in various industrial fields, especially in the Petro-chemical industry (Legat, 2007). In previous study (Legat et al., 2004) it was shown that measurements with ER probes are efficient for measuring the corrosion of steel in concrete.

The HCP and ER data sources provided scalar values (voltage and resistivity value respectively) at each measurement location, whereas the GPR data was a waveform. Wavelet features were extracted from the GPR signal (including mean power of reconstructed waveform and second, third, and fourth spectral moment of spectrum of reconstructed waveform from each wavelet basis, see *Waveform Feature Extraction*) and combined with the scalar-valued HCP and ER data for model training and testing. All the values were standardized and hyperparameters were identified prior to training, as discussed in *Methodology*. Classifiers were then trained using 70% of the data and tested on the remaining 30%. Using the training dataset, the classifier automatically determines an optimal decision boundary, a hypersurface that partitions data into defect and no defect classes. The classifier then classifies all the points on one side of the decision boundary as belonging to one class and all those on the other side as belonging to the other class. Unfortunately, direct interpretation of this hypersurface is challenging, and is a significant downside to machine learning driven analysis.

Corrosion Detection: Results and Discussion

Once the scalar values from ER and HCP data sources and extracted features from GPR waveform are combined into a concatenated vector, this vector is then an input to a statistical model. In this study, as explained in Feature fusion - SVM (*Other Considered Classifiers*), ANN, decision tree, and logistic regression algorithms are considered to provide a point of comparison to SVM fusion. The performance of all mentioned algorithms are shown in **Table 2**. The results of this comparative analysis show that the SVM and ANN fusion algorithms produced relatively similar results. Accuracy for the decision tree model was slightly degraded, mostly due to a loss of precision. The logistic regression approach yielded by far the worst results, indicating that the statistical relationships between NDE measurements and corrosion are sufficiently nonlinear in nature to warrant more sophisticated machine learning approaches. Given the comparably performance of the SVM and ANN classifiers, the SVM approach is preferable due to the fewer hyperparameters and reduced risk of model overfitting.

Decision Fusion for Corrosion Detection

As a point of comparison, a decision-level fusion approach was also developed. This approach combined the independent detection assessments of various different NDE methods, weighting them based on their statistical significance, a technique referred to as a Weighted-Sum Model (Hall and Llinas, 2001). Each NDE technique was used to generate an independent decision based on its own features and an SVM classifier, with a binary declaration of either “corrosion” or “no corrosion.” The weight of each decision was then determined. Several metrics for weighting were considered, including false positive rate, probability of detection (recall), and precision (Lu and Michaels, 2009). Using precision as the criterion, the order of weights was GPR > HCP > ER. Considering recall, the order of weights changed to HCP > GPR > ER. For the false positive rate, the resulting weight order was GPR > HCP > ER. The resulting weighted decisions were then combined and compared against the SVM classifier (**Table 3**). As is shown, the accuracy never reached the level of feature-level fusion via SVM. Similar results were found for decision fusion of delamination defects.

SVM Fusion Analysis

Once SVM was identified as the preferred machine learning method for corrosion detection, a more in-depth analysis of SVM model behavior was performed. In addition to a fusion of all the techniques, different fusion combinations were studied. The goal was to understand the effect of adding an NDE data source to fusion models and identify the best combination of

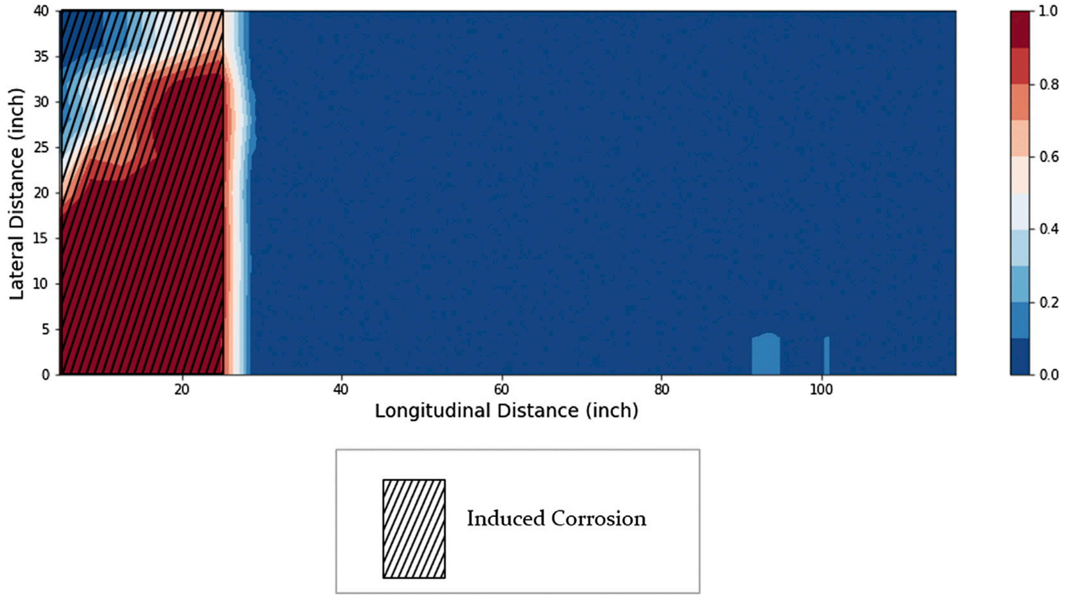

FIGURE 11 | Fusion heat map based on Support Vector Machine indicating existence of corrosion in slab.

techniques for deck assessment. The following data fusion combinations were tested: ER + HCP, ER + GPR, HCP + GPR, and ER + HCP + GPR. SVM classifiers were also constructed for each NDE type separately. For scalar-valued HCP and ER data a linear function was fit to the data, whereas for the waveform GPR data, wavelet-based features were fit to an SVM model with a RBF function, similar to the model used for the fused case.

Some of these algorithms didn't increase the corrosion detection accuracy in compare with individual techniques, also their underperformance in comparison with SVM was more for delamination detection.

The resulting Receiver-Operator-Characteristic (ROC) curves from each fusion combination for corrosion detection is shown in **Figure 10**. The area under a ROC curve is an effective measure of the sensitivity of a classifier to variations in classification thresholds, with a larger area indicating a more robust classifier. What can clearly be seen is that HCP on its own is a highly effective method of quantifying corrosion, whereas ER and GPR perform relatively poorly in isolation. In fact, GPR actually serves to *degrade* classifier accuracy when fused with HCP data. This behavior is due to the nature of laboratory conditions for the HCP measurements that were idealized, and may not be representative of performance under field conditions. After the RC decks were fully cured, accelerated corrosion was employed with elevated chloride content in the concrete and active corrosion in the pre-corroded rebar. This caused corrosion to occur much faster compared to natural conditions (Meng et al., 2020). This type of accelerated corrosion is ideal for HCP measurements and led to high detection accuracy for HCP (Yuan et al., 2007). Such a result reflects the potential for model biasing that can occur in machine learning. The fusion of all three data sources is slightly better than for HCP or HCP + ER, but these differences are statistically negligible. The most notable result is that the fusion of ER + GPR is measurably better than either measurement on its own, and highlights the value of statistical data fusion.

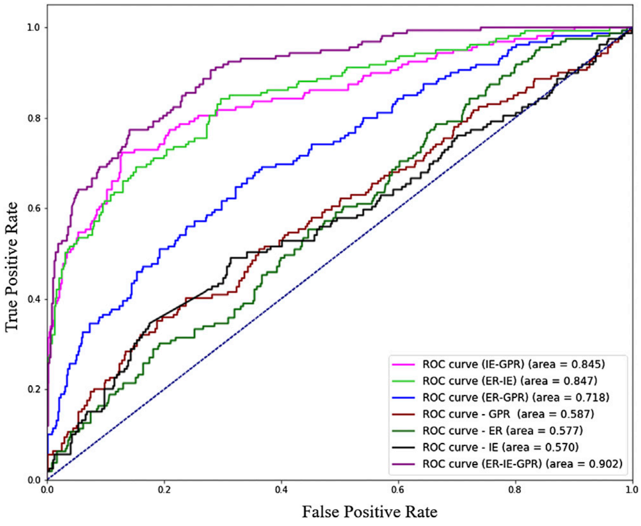

FIGURE 12 | Receiver Operating Characteristic curve of Support Vector Machine classifiers for delamination detection.

A visualization heat map for the complete fusion (HCP + ER + GPR) is shown in **Figure 11**. An analysis of the visualization shows that the certainty of corrosion was degraded near the upper left corner of the slab. Again, the reasons for this loss in detection certainty are likely due to experimental testing conditions.

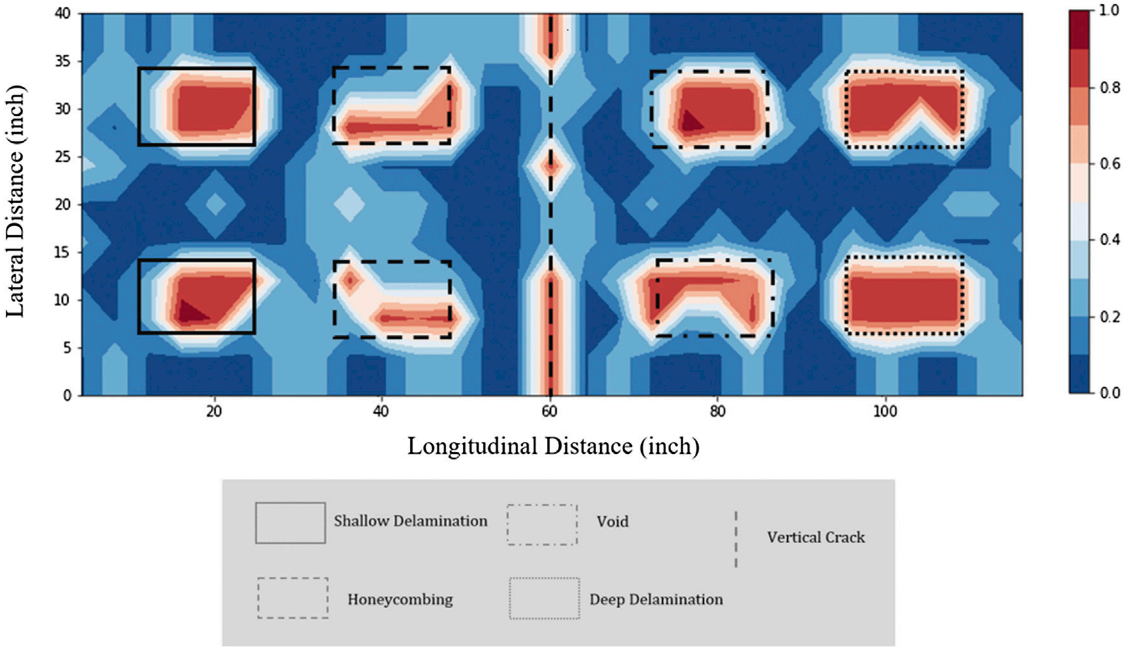

FIGURE 13 | Support Vector Machine fusion heat map indicating the existence and extents of delamination and cracking.

Data Fusion for Delamination and Crack Detection

To evaluate the impact of data fusion for detecting subsurface delamination and cracks, three NDE methods were considered: GPR, ER and IE. Similar to the procedure for corrosion detection, data from these techniques were combined into a unified dataset. Like GPR, IE produces a waveform signal at each grid location, and wavelet features were extracted from IE and GPR (*Waveform Feature Extraction*). Once salient features were extracted using wavelet transform, a series of classifiers were prototyped. As with the corrosion tests, the SVM classifier produced the most accurate and robust classifications. Results for the ANN, decision tree, and logistic regression classifiers, as well as the decision-level fusions were similar to the corrosion tests and are not reported here.

Delamination Detection: Results and Discussion

The resulting ROC curves for SVM classifiers for delamination and crack detection are shown in **Figure 12**, and the resulting heat map is shown in **Figure 13**. For this set of tests, no single NDE method dominated classifier performance and single-source NDE assessments were consistently poor performers. In all cases, fusions produced substantially improved assessments, and the complete data fusion was substantially better than any other combination. These results not only show that the fusion algorithm significantly improve delamination detection capabilities on their own, but the fusion of any combination of techniques results in a substantial improvement in detection accuracy compared individual techniques. This was most notable for IE data. For example, IE + GPR fusion improved detection accuracy by +50% compared to IE and GPR detection. These results show the most dramatic improvements from data fusion observed in this study and should be the focus of future data fusion efforts.

The results for the ER data warrant additional discussion. ER measurements are not designed to explicitly detect delaminations in concrete, but rather the associated rebar corrosion, and the artificial delaminations of this test were not corroded to simulate this relationship. Yet adding ER data to the fusion of IR and GPR had a measurable beneficial impact on detection accuracy and served to reduce measurement uncertainty across the slab. An analysis of the results indicates that this benefit is not isolated to the corroded left-hand portion of the slab or any particular type of defect within the slab. While not conclusive, the authors believe that this result may be related to how the artificial defects are installed within the test slabs and may not be representative of field conditions. Further investigation is warranted and highlights the need for physics-driven understanding of machine learning analysis.

While not shown here for clarity, an initial series of tests utilized scalar-valued measurements extracted from the IE waveform results, as was done in (Hsiao et al., 2008). Single-source classifications were comparable between waveform and scalar valued NDE data. The benefits of data fusion without the complete waveform response were negligible. What this suggests is that components of an NDE signal that are not relevant for single-source assessments can be of high value for a data fusion scenario.

The behavior of the fused SVM classifier is more clearly seen in the heatmap visualization of **Figure 12**. The upper and lower part of the crack in the middle of the slab was detected while the middle part was not detected because of the shallower crack depth

(2” vs. 6”). While not every defect was perfectly identified, a large portion of each of the eight defects was classified as a delamination by the SVM. The worst performance was seen for the honeycombing defect, where a smaller portion of the defect was detected. The other six defects were more clearly detected. For a holistic assessment, this kind of visualization goes beyond defect detection and illustrates both the extents of a defect and NDE detection confidence in an intuitive context that is familiar to engineers and inspectors.

CONCLUSION AND FUTURE WORK

In this work, a methodology to process and fuse multiple NDE data sources for bridge deck defect detection is developed. This approach leverages a wavelet transform (DWT) to extract numerical features from waveform NDE responses. Using the DWT provides consistent feature extraction that is well suited to signals that are periodic, transient (or non-stationary), and noisy. In conjunction with scalar-valued NDE measurements, these data sources are used as input in a machine learning classifier to provide a feature-level data fusion of NDE measurements. Support vector machine methods showed demonstrably better detection accuracy than other machine learning algorithms, most noticeably when compared to linear classification methods that more closely mirror conventional assessment methods. The benefits of data fusion were most significant for the detection of delaminations and cracks, while the results from the corrosion analysis were likely biased by how HCP data was collected in the laboratory and may not be representative of realistic field performance. Overall, the findings of this study show that data fusion has a measurable and positive impact on defect detection performance for both corrosion assessment and generalized defect detection. The visualization approach developed in this study is capable of intuitively representing the classifiers detection confidence—a key criterion for inspectors and engineers managed as part of this study—and provides a more nuanced representation of NDE assessments that help to quantify the geometric extents of a defect. As stated before, the laboratory conditions for the test data likely overestimate classifier accuracy under field conditions, but they do reflect the relative benefits of data fusion over single-source NDE assessments. It is also important to emphasize that the data fusion processes developed in this work do not allow direct insight into the capabilities of any single NDE method to detect defects such as delaminations. Creating fusion approaches that provide such insights is a compelling avenue for future work.

This study was part of an on-going research program and various part of the presented methodology are being considered for further improvement. The goal of this study was to fundamentally explore fusion viability, leveraging NDE data relevant to the FHWA RABIT inspection system. While the results show the promise of data fusion, there are many unanswered questions. For instance, this study only considered a small subset of possible data fusion combinations and defect classes, and the results showed that data fusion was more beneficial for delamination detection than corrosion. This suggests the need for additional studies that consider a broader range of NDE methods and defect types, and that the benefits of fusion for any given scenario cannot be easily generalized to other scenarios. However, the framework and evaluative methodology presented here are generalizable enough to be effective for a diverse range of experimental scenarios. As stated earlier, the statistical learning models developed here are not capable of distinguishing between defect classes, a simplification that aided illustration of the impact of NDE fusion. Future work could include expanding the work to include defect diagnosis, rather than detection, for instance the distinction between shallow and deep defects for a given data fusion. Based on these initial findings, additional studies on the wavelet decomposition-based feature extraction methods are warranted as well. There is also a need to evaluate these approaches under realistic field conditions. Lastly, the probability score of damage in the structural component can be modeled as stochastic process and tracked over time and using time series modeling their future states can be predicted. Tracking the fused data for prognostic purposes would be highly beneficial to engineers and managers attempting to do portfolio-level asset management.

DATA AVAILABILITY STATEMENT

The data analyzed in this study is subject to the following licenses/restrictions: Datasets are property of Federal Highway Administration. Requests to access these datasets should be directed to hoda.azari@dot.gov.

ETHICS STATEMENT

Ethical review and approval was not required for the study on human participants in accordance with the local legislation and institutional requirements. Written informed consent for participation was not required for this study in accordance with the national legislation and the institutional requirements.

AUTHOR CONTRIBUTIONS

SM developed the algorithms, performed the experiments, and generated the first draft of the paper. DL and HA oversaw the research program and provided guidance. DL and HA provided major revisions and comments on the manuscript.

FUNDING

Portions of this work were supported by grants from the Federal Highway Administration (TO#693JJ318F000190) and the Office of Naval Research (No. N00014-18-1-2014). Any opinions, findings, and conclusions or recommendations expressed in this material are those of the authors and do not necessarily reflect the views of the Office of Naval Research or the Federal Highway Administration.

ACKNOWLEDGMENTS

The authors would like to thank Sattar Dorafshan and Russell Kok for their help in accessing and working with the experimental data sets used in this paper.

REFERENCES

Ahmed, H., La, H. M., and Gucunski, N. (2020). Review of non-destructive civil infrastructure evaluation for bridges: state-of-the-art robotic platforms, sensors and algorithms. *Sensors* 20 (14), 3954. doi:10.3390/s20143954

Al Ghayab, H. R., Li, Y., Siuly, S., and Abdulla, S. (2019). A feature extraction technique based on tunable Q-factor wavelet transform for brain signal classification. *J. Neurosci. Methods* 312, 43–52. doi:10.1016/j.jneumeth.2018.11.014

Alonso, C., Andrade, C., and González, J. A. (1988). Relation between resistivity and corrosion rate of reinforcements in carbonated mortar made with several cement types. *Cement Concr. Res.* 18 (5), 687–698. doi:10.1016/0008-8846(88)90091-9

ASTM C876-09 (1999). *Standard test method for half cell potentials of reinforcing steel in concrete*. West Conshohocken, PA: ASTM

Boser, B. E., Guyon, I. M., and Vapnik, V. N. (1992). "A training algorithm for optimal margin classifiers," in *Proceedings of the fifth annual ACM Workshop on computational learning theory*, Pittsburgh, PA: Association for Computing Machinery, 144–152.

Brownlee, J. (2017). *Deep learning with Python: develop deep learning models on theano and TensorFlow using keras*. Vermont VIC, Australia: Machine Learning Mastery.

Chair, Z., and Varshney, P. K.. (1986). Optimal data fusion in multiple sensor detection systems. *IEEE Trans. Aero. Electron. Syst.* AES-22 (1), 98–101. doi:10.1109/taes.1986.310699

Chen, F.-C., and Jahanshahi, M. R.. (2018). NB-CNN: deep learning-based crack detection using convolutional neural network and naïve bayes data fusion. *IEEE Trans. Ind. Electron.* 65 (5), 4392–4400. doi:10.1109/tie.2017.2764844

Chen, F.-C., Jahanshahi, M. R., Wu, R.-T., and Joffe, C. (2017). A texture-based video processing methodology using bayesian data fusion for autonomous crack detection on metallic surfaces. *Comput. Aided Civ. Infrastruct. Eng.* 32 (4), 271–287. doi:10.1111/mice.12256

Chen, S.-L., and Jen, Y. W. (2000). Data fusion neural network for Tool condition monitoring in CNC milling machining. *Int. J. Mach. Tool Manufact.* 40 (3), 381–400. doi:10.1016/s0890-6955(99)00066-8

Choo, J., Li, F., Joo, K., and Park, H. (2012). "A visual analytics approach for protein disorder prediction," in *Expanding the Frontiers of Visual Analytics and Visualization*. Editors J. Dill, R. Earnshaw, D. Kasik, J. Vince and P. C. Wong (London: Springer London).

Cortes, C., and Vapnik, V. (1995). Support-vector networks. *Mach. Learn.* 20 (3), 273–297. doi:10.1023/a:1022627411411

Cristianini, N., and Shawe-Taylor, J. (2000). *An introduction to support vector machines and other kernel-based learning methods. cambridge core*. Cambridge, UK: Cambridge University Press.

Daubechies, I. (1992). "Ten lectures on wavelets," in *CBMS-NSF regional conference series in applied mathematics*. Philadelphia, PA: Society for Industrial and Applied Mathematics.

Debnath, L., and Shah, F. A. (2014). *Wavelet transforms and their applications*. Berlin, Germany: Springer.

Demirbas, K. (1989). Distributed sensor data fusion with binary decision trees. *IEEE Trans. Aero. Electron. Syst.* 25 (5), 643–649. doi:10.1109/7.42081

Dong, J., Zhuang, D., Huang, Y., and Fu, J. (2009). Advances in multi-sensor data fusion: algorithms and applications. *Sensors* 9 (10), 7771–7784. doi:10.3390/s91007771

Epinat, V., Stein, A., de Jong, S. M., and Bouma, J. (2001). A wavelet characterization of high-resolution NDVI patterns for precision agriculture. *Int. J. Appl. Earth Obs. Geoinf.* 3 (2), 121–132. doi:10.1016/s0303-2434(01)85003-0

Faouzi, N.-E. E., Leung, H., and Kurian, A. (2011). Data fusion in intelligent transportation systems: progress and challenges - a survey. *Inf. Fusion* 12 (1), 4–10. doi:10.1016/j.inffus.2010.06.001

Faouzi, N.-E. E., and Klein, L. A. (2016). Data fusion for ITS: techniques and research needs. *Transp. Res. Proc.* 15, 495–512. doi:10.1016/j.trpro.2016.06.042

Fawcett, T. (2006). An introduction to ROC analysis. *Pattern Recogn. Lett.* 27 (8), 861–874. doi:10.1016/j.patrec.2005.10.010

Ghazali, K. H., Mansor, M. F., Mustafa, M. M., and Hussain, A. (2007). "Feature extraction technique using discrete wavelet transform for image classification," in 2007 5th Student Conference on Research and Development, Selangor, Malaysia, December12–11, 2007, (IEEE), 1–4.

Gibb, S., La, H. M., Le, T., Nguyen, L., Schmid, R., and Pham, H. (2018). Nondestructive evaluation sensor fusion with autonomous robotic system for civil infrastructure inspection. *J. Field Robot.* 35 (6), 988–1004. doi:10.1002/rob.21791

Gucunski, N., Basily, B., Kim, J., Yi, J., Duong, T., Dinh, K., et al. (2017). RABIT: implementation, performance validation and integration with other robotic platforms for improved management of bridge decks. *Int. J. Intell Robot Appl.* 1 (3), 271–286. doi:10.1007/s41315-017-0027-5

Gucunski, N., Imani, A., Romero, F., Nazarian, S., Yuan, D., Herbert, W., et al. (2012). *Nondestructive testing to identify concrete bridge deck deterioration*. Washington, D.C.: Transportation Research Board.

Gucunski, N., Romero, F., Kruschwitz, S., Feldmann, R., and Parvardeh, H. (2011). *Comprehensive bridge deck deterioration mapping of nine bridges by nondestructive evaluation technologies*. Ames, IA: Iowa Department of Transportation.

Habib, C., Makhoul, A., Darazi, R., and Salim, C. (2016). Self-adaptive data collection and fusion for health monitoring based on body sensor networks. *IEEE Trans. Ind. Inf.* 12 (6), 2342–2352. doi:10.1109/tii.2016.2575800

Haghighat, M., Abdel-Mottaleb, M., and Alhalabi, W. (2016). Discriminant correlation analysis: real-time feature level fusion for multimodal biometric recognition. *IEEE Trans. Inf. Forensics Secur.* 11 (9), 1984–1996. doi:10.1109/tifs.2016.2569061

Hall, D., and Llinas, J. (2001). *Multisensor data fusion*. Cleveland, OH: CRC Press.

Heideklang, R., and Shokouhi, P. (2013). "Application of data fusion in nondestructive testing (NDT)," in Proceedings of the 16th international Conference on information fusion, Istanbul, Turkey, July 9–12, 2013, (IEEE), 835–841.

Hinton, G. E., Osindero, S., and Teh, Y.-W. (2006). A fast learning algorithm for deep belief nets. *Neural Comput.* 18 (7), 1527–1554. doi:10.1162/neco.2006.18.7.1527

Hou, J., Jankowski, Ł., and Ou, J. (2015). Frequency-domain substructure isolation for local damage identification. *Adv. Struct. Eng.* 18 (1), 137–153. doi:10.1260/1369-4332.18.1.137

Hsiao, C., Cheng, C.-C., Liou, T., and Juang, Y. (2008). Detecting flaws in concrete blocks using the impact-echo method. *NDT E Int.* 41 (2), 98–107. doi:10.1016/j.ndteint.2007.08.008

Huang, J., Liu, W., and Sun, X. (2014). A pavement crack detection method combining 2D with 3D information based on dempster-shafer theory. *Comput. Aided Civ. Infrastruct. Eng.* 29 (4), 299–313. doi:10.1111/mice.12041

Jiang, S.-F., Zhang, C.-M., and Zhang, S. (2011). Two-stage structural damage detection using fuzzy neural networks and data fusion techniques. *Expert Syst. Appl.* 38 (1), 511–519. doi:10.1016/j.eswa.2010.06.093

Khan, M. N., and Anwar, S. (2019). Time-domain data fusion using weighted evidence and dempster-shafer combination rule: application in object classification. *Sensors* 19 (23), 5187. doi:10.3390/s19235187

Khatam, H., Golafshani, A. A., Beheshti-Aval, S. B., and Noori, M. (2007). Harmonic class loading for damage identification in beams using wavelet analysis. *Struct. Health Monit.* 6 (1), 67–80. doi:10.1177/1475921707072064

Kittler, J. (1975). Mathematical methods of feature selection in pattern recognition. *Int. J. Man Mach. Stud.* 7, 609–637. doi:10.1016/S0020-7373(75)80023-X

Kotsiantis, S. B., Zaharakis, I. D., and Pintelas, P. E. (2006). Machine learning: a review of classification and combining techniques. *Artif. Intell. Rev.* 26 (3), 159–190. doi:10.1007/s10462-007-9052-3

Kralovec, C., and Schagerl, M. (2020). Review of structural health monitoring methods regarding a multi-sensor approach for damage assessment of metal and composite structures. *Sensors* 20 (3), 826. doi:10.3390/s20030826

La, H. M., Gucunski, N., Dana, K., and Kee, S.-H. (2017). Development of an autonomous bridge deck inspection robotic system. *J. Field Robot.* 34 (8), 1489–1504. doi:10.1002/rob.21725

Legat, A., Leban, M., and Bajt, Ž. (2004). Corrosion processes of steel in concrete characterized by means of electrochemical noise. *Electrochim. Acta* 49 (17), 2741–2751. doi:10.1016/j.electacta.2004.01.036

Legat, A. (2007). Monitoring of steel corrosion in concrete by electrode arrays and electrical resistance probes. *Electrochim. Acta* 52 (27), 7590–7598. doi:10.1016/j.electacta.2007.06.060

Liu, Z., Tsukada, K., Hanasaki, K., and Kurisu, M. (1999). Two-dimensional eddy current signal enhancement via multifrequency data fusion. *Res. Nondestr. Eval.* 11 (3), 165–177. doi:10.1080/09349849908968154

Lu, Y., and Michaels, J. E. (2009). Feature extraction and sensor fusion for ultrasonic structural health monitoring under changing environmental conditions. *IEEE Sensor. J.* 9 (11), 1462–1471. doi:10.1109/JSEN.2009.2019339

Luk, B. L., Jiang, Z. D., Liu, L. K. P., and Tong, F. (2008). "Impact acoustic non-destructive evaluation in noisy environment based on wavelet packet decomposition," in Proceedings of the international conference on mechanical engineering and mechanics 2007, Wuxi, China, November 5–7, 2007, 4.

Luts, J., Molenberghs, G., Verbeke, G., Van Huffel, S., and Suykens, J. A. K. (2012). A mixed effects least squares support vector machine model for classification of longitudinal data. *Comput. Stat. Data Anal.* 56 (3), 611–628. doi:10.1016/j.csda.2011.09.008

Mallat, S. G. (1989). A theory for multiresolution signal decomposition: the wavelet representation. *IEEE Trans. Pattern Anal. Mach. Intell.* 11 (7), 674–693. doi:10.1109/34.192463

Mallat, S. (2009). *A wavelet tour of signal processing: the sparse way*. 3rd Edn. Cambridge, MA: Academic Press.

Martino, N., Birken, R., Maser, K., and Wang, M. (2014). *Developing a deterioration threshold model for the assessment of concrete bridge decks using ground penetrating radar*. Washington, D.C.: Transportation Research Board.

McCann, D. M., and Forde, M. C. (2001). Review of NDT methods in the assessment of concrete and masonry structures. *NDT E Int.* 34 (2), 71–84. doi:10.1016/s0963-8695(00)00032-3

Meng, D., Lin, S., and Azari, H. (2020). Nondestructive corrosion evaluation of reinforced concrete bridge decks with overlays: an experimental study. *J. Test. Eval.* 48 (1), 20180388. doi:10.1520/jte20180388

Moreland, K. (2009). "Diverging color maps for scientific visualization," in Advances in visual computing 5th International Symposium. *Lecture notes in computer science*. Las Vegas, NV, November 30–December 2, 2009, (Berlin, Heidelberg: Springer), 92–103.

Najafabadi, M. M., Villanustre, F., Khoshgoftaar, T. M., Naeem, S., Randall, W., and Muharemagic, E. (2015). Deep learning applications and challenges in big data analytics. *Journal of Big Data* 2 (1), 1. doi:10.1186/s40537-014-0007-7

Nalepa, J., Kawulok, M., and Dudzik, W. (2018). "Tuning and evolving support vector machine models," in International Conference on man-machine interactions. *Advances in intelligent systems and computing*. (Cham, Switzerland: Springer International Publishing), 5, 418–428.

Nantasenamat, C., Isarankura-Na-Ayudhya, C., Naenna, T., and Prachayasittikul, V. (2009). A practical overview of quantitative structure-activity relationship. *EXCLI J.* 8, 74–88. doi:10.17877/DE290R-690

Nouri Shirazi, M. R., Mollamahmoudi, H., and Seyedpoor, S. M. (2014). Structural damage identification using an adaptive multi-stage optimization method based on a modified particle swarm algorithm. *J. Optim. Theor. Appl.* 160 (3), 1009–1019. doi:10.1007/s10957-013-0316-6

Olson, D. L., and Dursun, D. (2008). *Advanced data mining techniques*. Berlin, Germany: Springer Science & Business Media.

Pigeon, S., Druyts, P., and Verlinde, P. (2000). Applying logistic regression to the fusion of the NIST'99 1-speaker submissions. *Digit. Signal Process.* 10 (1), 237–248. doi:10.1006/dspr.1999.0358

Rabiei, M., and Modarres, M. (2013). A recursive bayesian framework for structural health management using online monitoring and periodic inspections. *Reliab. Eng. Syst. Saf.* 112, 154–164. doi:10.1016/j.ress.2012.11.020

Ramos, L. F., Miranda, T., Mishra, M., Fernandes, F. M., and Manning, E. (2015). A bayesian approach for NDT data fusion: the saint torcato church case study. *Eng. Struct.* 84, 120–129. doi:10.1016/j.engstruct.2014.11.015

Rangwala, H., Kauffman, C., and Karypis, G. (2009). A kernel framework for protein residue annotation. *BMC Bioinf.* 10, 439. doi:10.1186/1471-2105-10-439

Ruiz, A., and Lopez-de-Teruel, P. E. (2001). Nonlinear kernel-based statistical pattern analysis. *IEEE Trans. Neural Network.* 12 (1), 16–32. doi:10.1109/72.896793

Saadat, S., Noori, M. N., Buckner, G. D., Furukawa, T., and Suzuki, Y. (2004). Structural health monitoring and damage detection using an intelligent parameter varying (IPV) technique. *Int. J. Non Lin. Mech.* 39 (10), 1687–1697. doi:10.1016/j.ijnonlinmec.2004.03.001

Shanker, M., Hu, M. Y., and Hung, M. S. (1996). Effect of data standardization on neural network training. *Omega* 24 (4), 385–397. doi:10.1016/0305-0483(96)00010-2

Sohn, S. Y., and Lee, S. H. (2003). Data fusion, ensemble and clustering to improve the classification accuracy for the severity of road traffic accidents in korea. *Saf. Sci.* 41 (1), 1–14. doi:10.1016/s0925-7535(01)00032-7

Steinberg, A. N., Bowman, C. L., and White, F. E. (2017). "Revisions to the JDL data fusion model," in *Handbook of multisensor data fusion*. Editors M.IILiggins, D. Hall, and J. Llinas (Boca Raton, FL: CRC Press).

Sun, D., Lee, V. C. S., and Lu, Y. (2016). "An intelligent data fusion framework for structural health monitoring," in 2016 IEEE 11th Conference on Industrial Electronics and Applications (ICIEA), Hefei, China, June 5–7, 2016, (IEEE), 49–54.

Tsiliki, G., and Kossida, S. (2011). Fusion methodologies for biomedical data. *Journal of Proteomics* 74 (12), 2774–2785. doi:10.1016/j.jprot.2011.07.001

Vanik, M. W., Beck, J. L., and Au, S. K. (2000). Bayesian probabilistic approach to structural health monitoring. *J. Eng. Mech.* 126 (7), 738–745. doi:10.1061/(asce)0733-9399(2000)126:7(738)

Vapnik, V. (2000). *The nature of statistical learning theory. Information science and statistics*. 2nd ed.. New York: Springer-Verlag.

Wang, T., Huang, H., Tian, S., and Xu, J. (2010). Feature selection for SVM via optimization of kernel polarization with Gaussian ARD kernels. *Expert Syst. Appl.* 37 (9), 6663–6668. doi:10.1016/j.eswa.2010.03.054

Wu, H. (2004). *Sensor data fusion for context -aware computing using dempster -shafer theory*. Pittsburgh, PA: Carnegie Mellon University.

Wu, R.-T., and Jahanshahi, M. R. (2018). Data fusion approaches for structural health monitoring and system identification: past, present, and future. *Struct. Health Monit.* 19 (6). doi:10.1177/1475921718798769

Yeh, P.-L., and Liu, P.-L. (2008). Application of the wavelet transform and the enhanced fourier spectrum in the impact echo test. *NDT E Int.* 41 (5), 382–394. doi:10.1016/j.ndteint.2008.01.002

Yuan, Y., Ji, Y., and Shah, S. P. (2007). Comparison of two accelerated corrosion techniques for concrete structures. *ACI Struct. J; Farmington Hills* 104 (3), 344–347. doi:10.14359/18624

Zhang, A., Wang, K. C. P., Li, B., Yang, E., Dai, X., and Peng, Y., et al. (2017). Automated Pixel-Level Pavement Crack Detection on 3D Asphalt Surfaces Using a Deep-Learning Network. *Comput.-Aided Civ. Infrastructure Eng.* 32 (10), 805–819. doi:10.1111/mice.12297

Zhang, G., Li, C., Zhou, H., and Wagner, T. (2018a). Punching process monitoring using wavelet transform based feature extraction and semi-supervised clustering. *Proc. Manufac.* 26, 1204–1212. doi:10.1016/j.promfg.2018.07.156

Zhang, J.-K., Yan, W., and Cui, D.-M. (2016). Concrete condition assessment using impact-echo method and extreme learning machines. *Sensors* 16 (4), 447. doi:10.3390/s16040447

Zhang, X., Nilot, E., Feng, X., Ren, Q., and Zhang, Z. (2018b). IMF-slices for GPR data processing using variational mode decomposition method. *Rem. Sens.* 10 (3), 476. doi:10.3390/rs10030476

Zhou, Q., Zhou, H., Zhou, Q., Yang, F., Luo, L., and Li, T. (2015). Structural damage detection based on posteriori probability support vector machine and dempster-shafer evidence theory. *Appl. Soft Comput.* 36 (C), 368–374. doi:10.1016/j.asoc.2015.06.057

Conflict of Interest: The authors declare that the research was conducted in the absence of any commercial or financial relationships that could be construed as a potential conflict of interest.

frontiers in Materials

ORIGINAL RESEARCH
published: 30 November 2020
doi: 10.3389/fmats.2020.568870

Adapting Artificial Intelligence to Improve In Situ Concrete Compressive Strength Estimations in Rebound Hammer Tests

Yu Ren Wang, Yen Ling Lu and Dai Lun Chiang*

Department of Civil Engineering, Natioanl Kaohsiung University of Science and Technology, Kaohsiung, Taiwan

Compressive strength is probably one the most crucial properties of concrete material. For existing structures, core samples are drilled and tested to obtain the concrete compressive strength. Many times, taking core samples is not feasible, and as a result, nondestructive methods to examine the concrete are required. The rebound hammer test is one of the most popular methods to estimate concrete compressive strength without causing damage to the existing structure. The test is inexpensive and can be easily conducted compared to other nondestructive testing methods. Also, concrete compressive strength estimations can be obtained almost instantly. However, previous results have shown that concrete compressive strength estimations obtained from rebound hammer tests are not very accurate. As a result, this research attempts to apply artificial intelligence prediction models to estimate concrete compressive strength using data from *in situ* rebound hammer tests. The results show that artificial intelligence methods can effectively improve *in situ* concrete compressive strength estimations in rebound hammer tests.

Keywords: artificial intelligence, non-destructive test, concrete strength, rebound hammer test, artificial neural networks, support vector machines, adaptive network-based fuzzy inference systems

Edited by:
Juncai Xu,
Case Western Reserve University,
United States

Reviewed by:
Mahdi Shariati,
University of Malaya, Malaysia
Lucio Nobile,
University of Bologna, Italy
Harsha Vardhan,
National Institute of Technology,
Karnataka, India

****Correspondence:***
Yu-Ren Wang
yrwang@nkust.edu.tw

Specialty section:
This article was submitted to
Structural Materials,
a section of the journal
Frontiers in Materials

Received: *02 June 2020*
Accepted: *30 September 2020*
Published: *30 November 2020*

Citation:
Wang YR, Lu YL, Chiang DL (2020)
Adapting Artificial Intelligence to
Improve In Situ Concrete Compressive
Strength Estimations in Rebound
Hammer Tests.
Front. Mater. 7:568870.
doi: 10.3389/fmats.2020.568870

INTRODUCTION

Concrete is a man-made composite material, consisting mainly of aggregate, water, and cement. Because it is relatively cheap and provides high compressive strength, concrete is one of the most commonly used materials in the construction industry. It is extensively used in buildings, bridges, roads, and many other structures. To ensure the safety of the structures, the quality of the concrete material, especially the concrete strength, is of great concern to the construction industry. One of the most popular ways to assess the performance of concrete is to measure its compressive strength. Compressive strength is one of the most important criteria used to examine whether a given concrete mixture will fulfill its design requirements. Compressive strength is typically measured by breaking cylinder concrete samples in a compressor machine. These specimens are randomly sampled from different ready-mixed concrete batches delivered to the construction site. Nevertheless, for existing structures, it is necessary to drill core samples in order to obtain concrete compressive strength in the field. Taking core samples causes certain damage to existing structures, and sometimes, it is not feasible to take core samples (for example, when you cannot obtain the owner's consent). Under such circumstances, alternative testing methods, such as nondestructive tests, are desirable for assessing concrete compressive strength. Among the nondestructive concrete compressive strength tests, rebound hammer (RH) and ultrasonic pulse velocity (UPV) tests are commonly seen in the industry.

The major benefits of RH and UPV tests are their abilities to examine the condition of a concrete structure without causing damage (Shariati et al., 2011).

In the RH test, a spring-loaded steel hammer is pushed against the surface of the concrete. When released, the hammer impacts the concrete with a predetermined amount of energy. The hardness of the concrete affects the extent of the elastic mass rebound. This rebound distance is measured and used to estimate the concrete strength (ASTM C805 / C805M – 18, 2020). In the UPV test, first, the propagation velocity of longitudinal stress wave pulses through concrete is measured. Then, the compressive strength of the concrete is estimated using the measured UPV. The UPV test is conducted by transmitting ultrasonic pulses through the test specimen, and then, the time taken by the pulse to pass through the concrete is measured. Higher velocities indicate good quality and continuity of the material, and lower velocities may indicate cracks or voids in the concrete (ASTM C597 – 16, 2020). Compared to other nondestructive methods, RH tests are cheaper (in terms of test equipment), faster, and easier to conduct (Hamidian et al., 2012). In addition, RH tests are adopted in the American Society for Testing and Materials (ASTM 805) (ASTM C597 – 16, 2020) and Chinese National Standards (CNS 10732) as an alternative way to assess concrete compressive strength. Therefore, this research utilizes RH tests to estimate concrete compressive strength.

Typically, the rebound distance measured is used to estimate concrete compressive strength either using the conversion table or equations provided by the manufacturer. Nevertheless, despite its convenience, compressive strength estimations from RH tests are not very accurate, and an average of more than 20% mean absolute percentage error (MAPE) is reported (Huang et al., 2011). In light of this, this research attempts to further examine the relationship between RH measurements and actual compressive strength.

Previous research has attempted different approaches to investigate the relationship between RH measurements and actual compressive strength. To achieve this goal, many researchers adopt linear and nonlinear statistical regressions to improve the concrete compressive strength estimation in the RH test (Hajjeh, 2012; Rojas-Henao et al., 2012; El Mir and Nehme, 2017; Xu and Li, 2018; Kocáb et al., 2019). In addition, some researchers have successfully adopted nontraditional statistical methods, such as artificial neural networks (ANNs), to improve concrete compressive strength estimations in RH tests (Yılmaz and Yuksek, 2008; Iphar, 2012; Asteris and Mokos, 2019). Nevertheless, most research uses new cube or cylinder samples produced in the laboratory. As a result, there might be some limitations when applying these research findings to *in situ* RH tests. In light of this, this research intends to investigate the relationships between RH measures and actual compressive strength for existing structures. *In situ* RH tests and core sampling are conducted on a large residential complex building. Both traditional (linear/nonliner regression) and nontraditional (artificial intelligence or AI) statistical analyses are conducted to develop concrete compressive strength prediction models. The research results show that, by introducing the AI methods into the RH tests, concrete compressive strength estimations can be improved for *in situ* test objects. It should be noted that the emphasis of this research is on examining the relationships between *in situ* RH measurements and concrete strength; therefore, the nature of the RH test itself is not discussed in this research.

LITERATURE REVIEW

By adopting AI methods, this research intends to investigate the relationships between *in situ* RH test measurements and actual concrete compressive strengths. First, previous research related to RH tests and concrete compressive strength estimation are reviewed. Then, literature related to AI methods are reviewed.

Rebound Hammer Test

When destructive test measures are not feasible, nondestructive testing methods have been adopted as an alternative to examine the properties of construction materials. Over the years, successful results have been obtained by researchers using nondestructive methods to estimate material properties (Kumar et al., 2019). For concrete material, the RH test is often chosen as an alternative nondestructive testing method to estimate compressive strength. RH test standards have been established in different countries and regions, such as ASTM 805 in the United States (ASTM C805 / C805M – 18, 2020), BS 1881: part 202 in the United Kingdom (British Standards Institution (BSI), 1986), EN 12504-2 in Europe (European Normalization Committee (En), 2012), and CNS 10732 in Taiwan The National Standards of the Republic of China, 1986. The RH test is easy to conduct, and the test results can be obtained almost instantly. RH measurements can be used to estimate concrete compressive strength either using a conversion table or a conversion equation provided by the instrument manufacturer. However, these concrete compressive strength estimations are not very accurate when using RH test measurements (Huang et al., 2011). Some researchers have attempted to improve concrete compressive strength estimations by introducing factors other than RH value, such as water:cement ratio, age, and types of admixture (Atoyebi et al., 2019). Others have attempted different prediction methods to better correlate the RH value with actual compressive strength. Among them, traditional statistical regressions are the most popular methods adopted by the researchers (Hajjeh, 2012; Rojas-Henao et al., 2012; El Mir and Nehme, 2017; Xu and Li, 2018; Kocáb et al., 2019). In recent years, nontraditional statistical regression methods, such as ANNs, are reported to have better compressive strength estimations when compared to traditional regression methods (Yılmaz and Yuksek, 2008; Iphar, 2012; Asteris and Mokos, 2020). In addition to traditional regression methods and ANNs, this research also adopts alternative AI methods, support vector regression, and adaptive network-based fuzzy inference systems (ANFIS) to develop concrete compressive prediction models. These methods are introduced in the next section.

Artificial Intelligence Methods

Some previous RH estimation research adopts traditional statistical methods to correlate RH measurements and

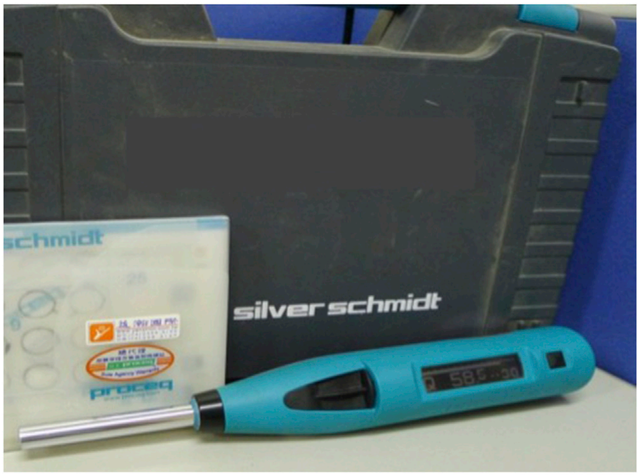
[redacted]

FIGURE 1 | Silver schmidt type N-PC rebound hammer.

concrete compressive strength. However, the results have not been satisfactory so far (Qasrawi, 2000; Szilágyi et al., 2011; Brencich et al., 2013; Breysse and Martínez-Fernández, 2014). This research attempts to use AI methods to investigate the relationship between RH measurements and concrete compressive strength. As an application of AI, machine learning algorithms use sample data to develop (or train) mathematical models. Learning from sample data allows the model to make predictions without being explicitly programmed (Bishop, 2006). For this research, RH experiments are conducted to obtain sample data for machine learning prediction models. Among the various machine learning techniques for regression, ANNs, support vector machines (SVMs), and ANFIS are chosen to develop the prediction models. For this research, these techniques are chosen because ANNs, SVMs, and ANFIS are reported to have been successfully applied in many different areas, such as finance, engineering, medicine, and manufacturing. The model prediction results from these AI techniques also outperformed traditional statistical regression methods (Shirsath and Singh, 2010; Balabin and Lomakina, 2011; Yilmaz and Kaynar, 2011; Rezaeianzadeh et al., 2014).

Based on the literature, this research adapts AI regression methods to improve concrete compressive strength estimation for *in situ* RH tests. The RH test and AI regression methods are briefly introduced in the next section.

METHODOLOGY

RH tests are popular nondestructive tests to measure the surface hardness and penetration resistance of concrete. RH test measurements can be related to the elastic properties or strength of the test object. In the RH tests, the hammer is first pressed against the concrete surface (small, nonstructural beams in this research). Next, the spring-loaded hammer mass strikes with a defined energy, and then the rebound is measured. The rebound value measured is known as the rebound number. By referring to the conversion table or equation provided by the manufacturer, the concrete compressive strength can then be estimated using the rebound number. For digital RH, the compressive strength can be automatically calculated (Information on, 2012). The RH gives an indication of the test object's surface hardness. When using RH to examine concrete compressive strength, a lower rebound value is obtained for low strength and stiffness concrete due to more energy absorption (Brencich et al., 2013).

For this research, the research team first conducted RH tests on nonstructural beams in the basement of a large residential complex. After the RH tests, core samples were carefully drilled and then tested in the laboratory to obtain the actual compressive strength. Due to the destructive nature of the core drilling process, *in situ* RH test data are difficult to collect. In order to get more reliable concrete strength estimations, data from a total of 100 samples are collected. A digital RH (Silver Schmidt Type N-PC) is used for this research as shown in **Figure 1**. The digital hammer offers intuitive, menu-guided operation; electronic data processing; automatic correction for testing positions; and test data storage (Information on, 2012). This instrument is chosen because its accuracy and repeatability are improved compared to traditional concrete test hammers. The collected data are then used to develop and validate the AI regression models.

ANNs are machine learning methods that are inspired by the biological neural systems in the brain. An ANN consists of interconnected nodes (artificial neurons), and these nodes can receive, process, and transmit signals to artificial neurons connected to them. Each artificial neuron has weighted inputs, one transfer function, and one output. Although a single neuron can perform certain simple tasks, the real computation power comes from the interconnecting neurons. Typically, these interconnected neurons are aggregated into the input layer, the hidden layer(s), and the output layer. Signals are received by the input layer and then transmitted through the hidden layer(s) and output layer. Such systems are able to learn from examples without being programmed with task-specific rules (Zupan and Gasteiger, 1991; Gurney, 2014). A typical three-layer neural network is shown in **Figure 2** with one input layer, one hidden layer, and one output layer.

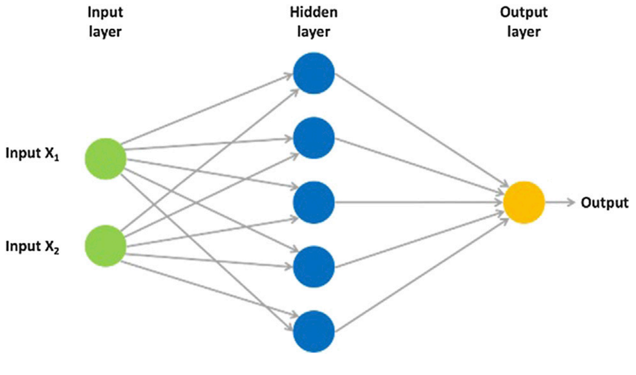

FIGURE 2 | Three-layer ANNs.

In the hidden layer, the neurons receive activation signals from the neurons in the input layer. The activation signal entering each neuron is the weighted sum of all the signals from the input layer. This weighted sum of all signals (also known as activation signal) is shown in **Eq. 1**. In **Eq. 1**, x_j is the activation signal that neuron j in the hidden layer receives; I_i is ith neuron in the input layer, and W_{ij} is the weight of the connection between neuron j in the hidden layer and the input layer neuron I_i. After receiving the activation signals, the neuron generates an output through a predetermined activation function. One of the most common activation functions is the sigmoid function, illustrated in **Eq. 2**. In **Eq. 2**, x_j is the input for neuron j in the hidden layer and h_j is the output of neuron j. Sigmoid functions transform input values into output values between 0 and 1.

$$x_j = \sum_i I_i W_{ij} \tag{1}$$

$$h_j = f\left(x_j\right) = \frac{1}{1 + e^{-x_j}} \tag{2}$$

$$y_k = \sum_j h_j W_{jk} \tag{3}$$

The outputs of the hidden layer neurons are then transmitted to the output layer. As shown in **Eq. 3**, h_j is the output of neuron j and W_{jk} is the weight of the connection between neurons j and k. y_k is the activation signal received by the output layer neuron k, the weighted sum of inputs to the output layer neuron k. In the output layer, the activation function transforms the received activation signals and generates the outputs of the neural networks. As illustrated in **Eq. 4**, o_k is the output of the neural network model after sigmoid function transformation. For supervised neural networks, the model error, $E(W)$, is then calculated by comparing the desired (or actual) value d_k and the model output o_k as calculated in **Eq. 5**.

$$o_k = f\left(y_k\right) = \frac{1}{1 + e^{-y_k}} \tag{4}$$

$$E(W) = \frac{1}{2}\sum_k \left(d_k - o_k\right)^2 \tag{5}$$

In neural network model development, the error function, $E(W)$, is minimized to find the best fit model. One of the most popular techniques to minimize he error is the back-propagation (BP) algorithm. In the BP algorithm, the errors obtained at the output layers are propagated backward to the hidden layer and then to the input layer. During the BP process, the connecting weights between all the neurons in the networks are updated. With the updated weights, the network output is recalculated. The error obtained from the updated neural network is back-propagated to update the weights again. This process is repeated to minimize the error until the best fit model is found.

ANNs have been successfully applied in many research fields to make predictions. Some researchers have successfully adapted ANNs to predict concrete compressive strength using input variables such as age, Portland cement, water, sand, crushed stone, high range water-reducing agent, and fly ash (Topçu and Sarıdemir, 2008). This research also utilizes ANNs to develop the concrete strength prediction model.

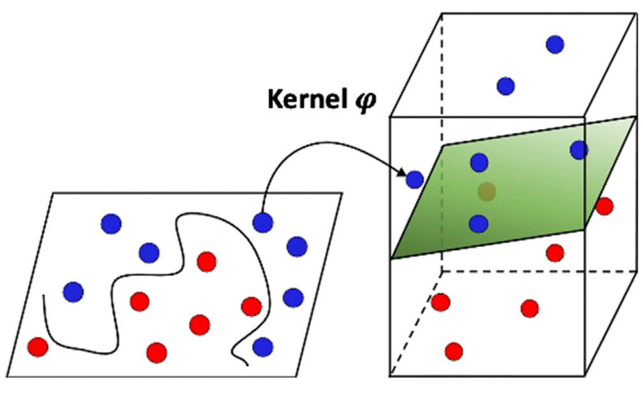

FIGURE 3 | SVM higher dimension mapping.

SVMs, first purposed by Vapnik (2013), are supervised machine learning methods based on statistical learning theory. As shown in **Figure 3**, SVMs first conduct nonlinear mapping of sample data into the higher dimensional feature space, and then the sample data can be classified using a linear model. The Φ indicates the transformation function for the nonlinear mapping.

SVMs were first developed for classification; Drucker et al. further proposed using the concepts for regression (Drucker et al., 1997), also known as support vector regression. The support vector regression concepts are briefly described below (Smola and Schölkopf, 2004).

For a given data set, $D = \{(x_i, d_i)\}_i^n$, x_i is the input vector, d_i is the desired (target) value, and n is the size of the data set. With the nonlinear mapping (Φ) of the input vector, the nonlinear regression in the lower dimensional space can then be represented by the linear regression in the higher dimensional feature space as shown in **Eq. 6**.

$$f(x) = \omega\Phi(x) + b, \tag{6}$$

where ω is the weight vector, Φ is the higher dimensional feature space, and b is the bias.

The main concepts of the support vector regression are to minimize the structural risks. By minimizing the risk penalty function, ω and b can be obtained as shown below (Smola and Schölkopf, 2004):

$$R_{SVR}(C) = C \times \frac{1}{n}\sum_{i-1}^{n} L\varepsilon\left(d_i, y_i\right) + \frac{1}{2}\|\omega\|^2, \tag{7}$$

where

$$L\varepsilon = \begin{cases} \left|d - y\right| - \varepsilon & if\left|d - y\right| \geq \varepsilon \\ 0 & \text{otherwise} \end{cases}, \tag{8}$$

where $C \times 1/n\sum_{i-1}^{n} L\varepsilon(d_i, y_i)$ is the estimated risk based on $L\varepsilon$ (ε -insensitive loss function) in **Eq. 7**, y_i is the target, $1/2\|\omega\|^2$ is the penalty item for estimating the structural risk, and C is the penalty constant.

By introducing the slack variables ξ and ξ^*, ω and b can be estimated. Then, the new objective function is shown as.

Minimize

$$R_{SVMs}\left(\omega, \xi^{(*)}\right) = C \times \frac{1}{n}\sum_{i-1}^{n}\left(\xi_i + \xi_i^*\right) + \frac{1}{2}\|\omega\|^2 \tag{9}$$

Subject to

$$\begin{aligned} d_i - \omega\varphi(x_i) - b_i &\le \varepsilon + \xi_i \\ \omega\varphi(x_i) + b_i - d_i &\le \varepsilon + \xi_i^* \end{aligned} \qquad \xi^{(*)} \ge 0 \tag{10}$$

The Lagrange multipliers, a_i and $a_i{}^*$, can then be incorporated, and the SVM decision function becomes

$$f\left(x, a_i, a_i^*\right) = \sum_{i=1}^{n}\left(a_i - a_i^*\right)K\left(x, x_i\right) + b \tag{11}$$

Next, the Lagrange multipliers, a_i and $a_i{}^*$, are adopted in the penalty objective function as shown below:

Maximize

$$\begin{aligned} R\left(a_i, a_i^*\right) = \sum_{i=1}^{n} d_i\left(a_i - a_i^*\right) - \varepsilon\left(a_i + a_i^*\right) - \frac{1}{2}\sum_{i=1}^{n}\sum_{j=1}^{n}\left(a_i - a_i^*\right) \\ \times\left(a_j - a_j^*\right)K\left(x, x_i\right) \end{aligned} \tag{12}$$

Subject to

$$\sum_{i=1}^{n}\left(a_i - a_i^*\right) = 0, \quad \begin{aligned} 0 \le a_i \le C \quad & i = 1, 2, \ldots, n \\ 0 \le a_i^* \le C \quad & i = 1, 2, \ldots, n \end{aligned} \tag{13}$$

The kernel function, K (x_i, x_j), is the inner product of x_i and x_j in the corresponding feature spaces $\psi(x_i)$ and $\psi(x_j)$, $K(x_i, x_j) = \varphi(x_i) * \varphi(x_j)$.

Compared to ANNs, which are sometimes criticized as black box approximations, the support vector regression can be theoretically analyzed using computational learning theory (Smola and Schölkopf, 2004; Anguita et al., 2010). Several research results have shown that SVMs are able to provide better prediction results when comparing to ANNs (Kim, 2003; Huang et al., 2005). As a result, this research uses support vector regression as one of the AI prediction techniques in the model development.

ANFIS is a kind of ANN that is based on the Takagi–Sugeno fuzzy inference system (Jang, 1993). It is a hybrid intelligent system that integrates the human-like reasoning style of fuzzy systems and the learning structure of neural networks. Fuzzy if–then rules are incorporated into the inference system so that the system can learn to approximate nonlinear functions from sample data. ANFIS is based on the first-order Sugeno fuzzy model proposed by Takagi and Sugeno. Considering two input variables (x and y) and one output variable (z), with the Sugeno fuzzy model, ANFIS incorporates the learning algorithms in the ANNs to determine the parameters in the premise and consequent parts of the fuzzy rules (Abraham, 2005). The structure of the ANFIS model with two input variables (x and y) and one output variable (z) is shown in **Figure 4**.

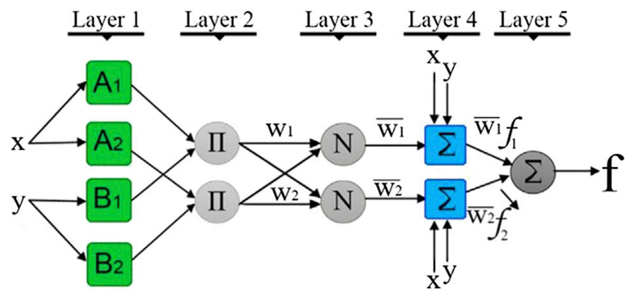

FIGURE 4 | ANFIS model.

The functions of each layer in this ANFIS structure are introduced below (Abdulshahed et al., 2015):

Layer 1 is the input layer, which is intended for input fuzzification. In this layer, input variables are mapped into the fuzzy sets. Each node represents an adaptive node with node function.

$$O_{1,i} = \mu_{A_i}(x) \quad \text{for } i = 1, 2 \tag{14}$$

$$or\ O_{1,i} = \mu_{B_i}(y) \quad for\ i = 1, 2 \tag{15}$$

x and y are the inputs for node i; $O_{1,i}$ is the membership degree for fuzzy set A (membership functions A1, A2) or fuzzy set B (membership functions B1, B2). The typical bell-shaped membership function in this layer can be expressed as

$$\mu_A(x) = \frac{1}{1 + \left|\frac{x - c_i}{a_i}\right|^{2b_i}} \tag{16}$$

In **Eq. 16**, a, b, and c are the parameters for membership function $u(x)$. These parameters determine the shape of the membership function and are referred to as premise parameters.

Layer 2 is the rule layer, which calculates the product of all the incoming signals to the nodes. Each node in this layer is a fixed node, and the output of this layer is the product of all the incoming signals or obtained from min (AND) in the fuzzy sets. Each node represents the firing strength of the rule. It can be calculated as

$$O_{2,i} = \mathrm{wi} = \mu_{A_i}(x)\mu_{B_i}(y) \quad for\ i = 1, 2 \tag{17}$$

$$or\ O_{2,i} = w_i = \min\left(\mu_{A_i}(x), \mu_{B_i}(y)\right) \quad for\ i = 1, 2 \tag{18}$$

Layer three is the normalization layer, which normalizes the firing strength of each node. Each node in this layer is also a fixed node, and the output is referred to as the normalized firing strength of that node. The output of the ith node is obtained by calculating the ratio of the ith rule’|’s firing strength to the sum of all rules’ firing strengths. It can be calculated as

$$O_{3,i} = \overline{w} = \frac{w_i}{w_1 + w_2} \quad for\ i = 1, 2 \tag{19}$$

Layer 4 is the inference layer, which is intended for defuzzification. Each node in this layer is an adaptive node. It takes the outputs from layer 3 and then multiplies them by the consequent parameters. It can be calculated as

$$O_{4,i} = \overline{w}_i f_i = \overline{w}_i \left(p_i x + q_i y + r_i\right) \tag{20}$$

In **Eq. 20**, $\overline{w_i}$ is the normalized firing strength from layer 3 and $\{p_i, q_i, r_i\}$ are the relevant consequent parameters for that node.

Layer 5 is the output layer, which calculates the overall output. There is only one fixed node in this layer. It calculates the overall output as the summation of all incoming signals and can be expressed as

$$O_{5,i} = \sum_i \overline{w}_i f_i = \frac{\sum_i w_i f_i}{\sum_i w_i} \tag{21}$$

In the ANFIS structure, the premise parameters are typically nonlinear, and consequent parameters are normally linear. This makes the parameter optimization process very complicated. Jang (Jang, 1993) proposes a hybrid learning algorithm to solve this problem. It involves a forward and backward process. In the forward pass, the premise parameters are first fixed, and the algorithm uses the least-squares method to identify the consequent parameters in Layer 4. After comparing the model output and desired output and obtaining the errors, the errors are propagated backward to the first layer, and the premise parameters are updated by the gradient descent method in the backward pass. This forward/backward process is repeated many times until the errors fall within the tolerance level. Since its introduction, ANFIS has been adopted to develop prediction models in many different research disciplines and is able to produce good prediction results (Vural et al., 2009; Boyacioglu and Avci, 2010; Abdulshahed et al., 2015).

Based on the related research, this research attempts to adopt three AI techniques (ANNs, SVMs, and ANFIS) to further investigate the relationship between *in situ* RH measurements and actual concrete compressive strength.

DATA COLLECTION

The researchers collaborated with a government-certified material testing laboratory and the Chinese Professional Civil Engineer Association for data collection. The RH tests were conducted on nonstructural beams in the basement of a large residential complex as shown in **Figure 5**. For consistency, all test hammer measurements were taken by the same personnel. The specifications in ASTM 805 and CNS 10732 for RH tests were carefully followed. After the RH tests, core samples were taken in order to obtain the actual compressive strength. To limit the structural damage due to coring, test locations were carefully chosen by the professional engineers. The design drawings were carefully reviewed to avoid rebar in the test areas. Before the test was conducted, test locations were examined again to avoid heavily textured or soft surfaces or surfaces with loose mortar. The digital RH was held firmly so that the plunger is perpendicular to the test surface. Ten readings were taken for each test area, and all the distances between impact points are greater than 25 mm. After each impact, the impression made on the surface was examined to see if the impact crushed or broke through a near-surface air void. If so, the reading was disregarded, and another reading was taken.

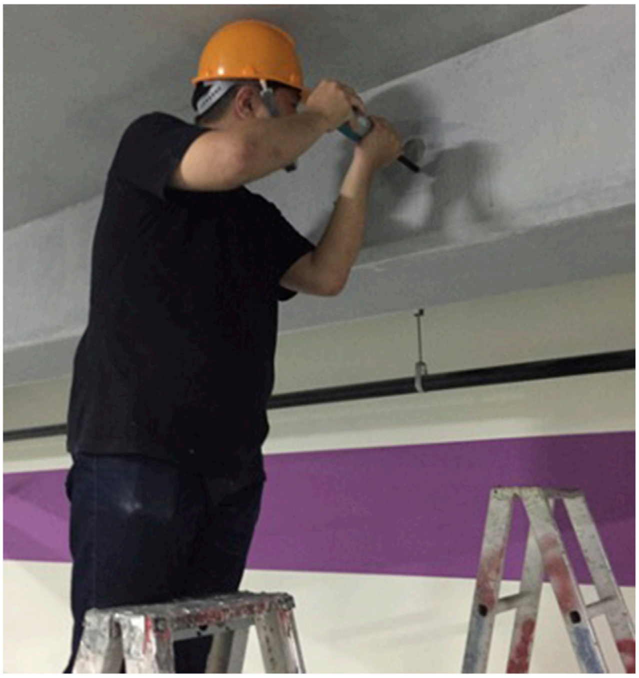

FIGURE 5 | *In situ* rebound hammer test.

To obtain the actual compressive strength, core samples were also taken at the same location and then brought back to the laboratory for destructive compression tests. Design drawings were carefully reviewed, and professional engineers were consulted when determining the test locations (mostly within the middle third section of the beam). To avoid damage to the rebar, rebar detectors were employed to confirm the locations of rebar before drilling took place. In addition, the void was filled with low-shrinkage concrete right after the drilling. All of the core drillings were conducted by the same professional team from a local material testing laboratory. All the core samples were taken and prepared per the CNS 1238 A3051 (method of test for obtaining and testing drilled core samples of concrete) specifications. After cores were drilled, the surface water was wiped off, and the sample was stored in a nonabsorbent container. Before the compression tests, the ends of the core specimens were sawed so that they were flat and perpendicular to the longitudinal axis. The size of the test specimens is 7.5 Φ × 10 cm.

The basement is mainly intended for parking, and the building construction was approaching the completion stage when the tests were conducted. A total of 100 small beams were chosen for the RH tests, and these beams are have the same dimensions (50 cm in width and 70 cm in depth). For each beam, a total of 10 RH measurements were taken at one location. The Silver Schmidt N-Type electronic RH was used to conduct the tests. Core samples were taken at the same locations after the RH tests as shown in **Figure 6**. RH tests, core sample collection, and compression tests were conducted during a period of 4 weeks. These drilled core samples were taken back to the laboratory and carefully cured after the drill. To obtain the compressive strength, destructive compression tests were conducted using the HT-8391

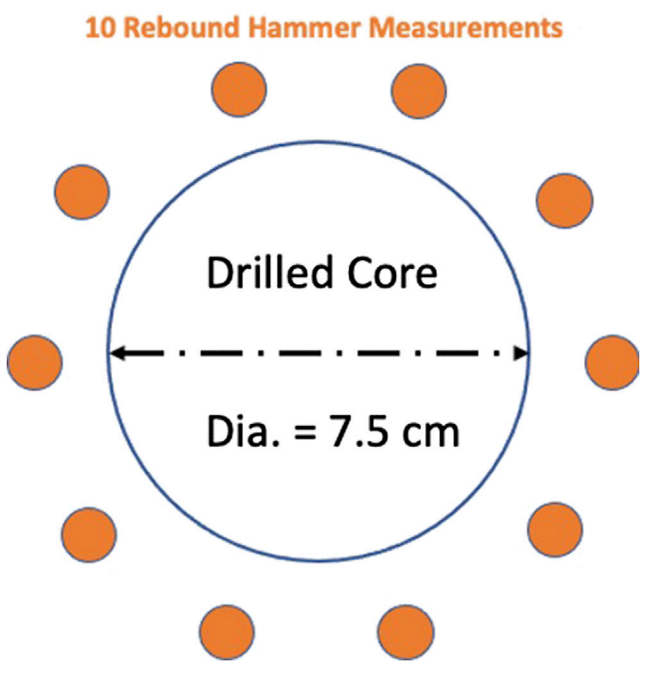

FIGURE 6 | Rebound hammer and core sample location.

200-ton concrete compression test machine. The data collected were used to develop and test the ANN, SVM, and ANFIS prediction models.

It should be noted that, before conducting the experiments, the research team were requested to sign a confidential agreement by the facility owner. As a result, only limited information regarding the research results can be revealed to the public. The descriptive statistics of RH tests and core sample compressive strength tests are shown in **Table 1**.

MODEL DEVELOPMENT AND VALIDATION

A total of 100 RH test sample data were collected for this research analysis. The data are used to develop and validate the regression and artificial intelligence (ANNs, SVMs, and ANFIS) prediction models. Among the 100 samples, 80 of them are randomly chosen as the training data set, and the remaining 20 samples are assigned as the testing data set. For consistency, all the prediction models use the same 80 randomly selected samples to develop the models, and the same 20 samples are used to validate the models.

TABLE 1 | Rebound hammer and core sample test results summary.

Test Results	Max	Min	Average	Stdev.
Rebound Value (*n* = 100 × 10)	64	30	55.7	5.24
Actual Compressive Strength (kgf/cm^2) (*n* = 100)	673	158	486.3	98.18

Some researchers have incorporated additional factors (such as water:cement ratio, aggregate size, and age) as input variables in their prediction models. Nevertheless, it is difficult (sometimes not feasible) to obtain these properties for existing structures. Therefore, this research only used RH measurements as the model inputs. For each test location, a total of 10 rebound measurements were taken as shown in **Figure 6**. These measurements were first recorded in the test hammer, and then the averages and standard deviations were calculated. All models proposed by this research have two input variables (average and standard deviation of the RH measurements) and one output variable (actual concrete compressive strength). As for the measure of model prediction accuracy, this research uses MAPE to compare prediction accuracies between the proposed models. MAPEs are widely used measures in examining the prediction accuracies for AI models (Nurcahyo and Nhita, 2014; Priya and Iqbal, 2015; Ramasamy et al., 2015). The MAPE is calculated using the following equation:

$$MAPE = \frac{1}{n}\sum_{i=1}^{n}\left|\frac{A_i - P_i}{A_i}\right| \tag{22}$$

where A_i is actual compressive strength, P_i is model output, and n is the total number of data.

In addition to MAPE, root mean square error (RMSE) is also calculated as an alternative prediction measurement for models. Compared to MAPE, RMSE emphasizes large errors as shown in the following equation:

$$RMSE = \sqrt{\frac{1}{n}\sum_{i=1}^{n}(A_i - P_i)^2} \tag{23}$$

Also, the variance accounted for (VAF) between the actual (desired) value and model prediction (output) is also calculated using the following equation (Kumar et al., 2013):

$$VAF = \left(1 - \frac{var(A - P)}{Var(A)}\right) \times 100\% \tag{24}$$

If the output values all equal the desired values, the MAPE and RMSE equal 0; the VAF equals 100%.

Regression Models

First, scatterplots of the collected data are plotted and examined for possible relationships between the average RH measurements and actual compressive strength. Next, simple linear and nonlinear regressions are conducted to see if simple regression models can yield good prediction results. The randomly chosen 80 training data are used to develop the linear and nonlinear regression models as shown in **Figures 7**, **8**.

The linear regression function obtained is

$$y = 6.3826\,x + 144.6 \tag{25}$$

For the linear regression model, the MAPE obtained from the training data is 17.88% and the RMSE is 90.81 kgf/cm^2.

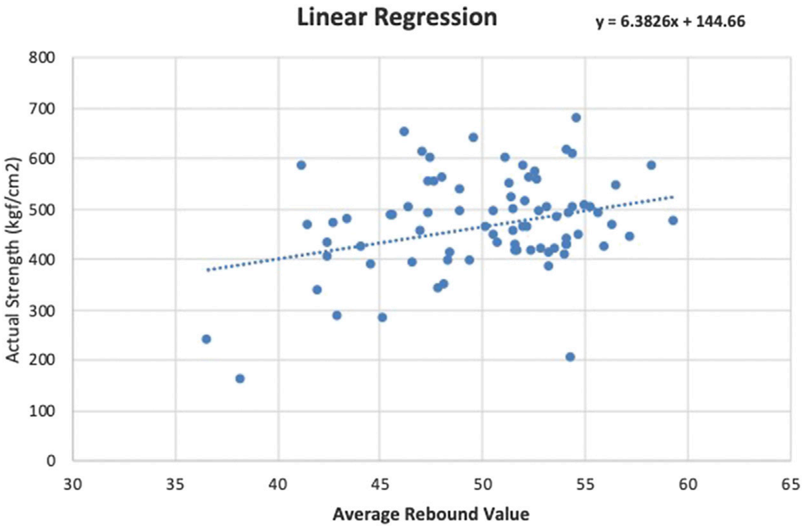

FIGURE 7 | Linear regression scatterplot.

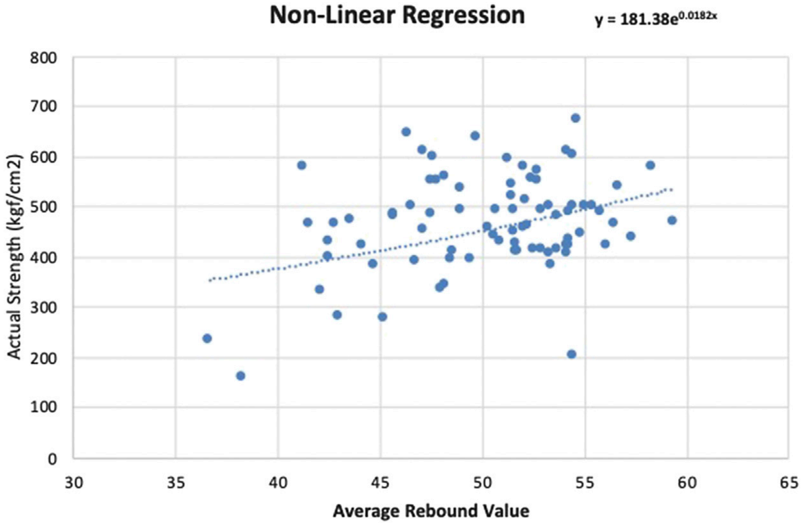

FIGURE 8 | Nonlinear regression scatterplot.

The nonlinear regression function obtained is:

$$y = 181.38\, e^{0.0182\, x} \tag{26}$$

For the nonlinear regression model, the MAPE obtained from the training data is 16.62% and the RMSE is 92.4 kgf/cm^2.

After obtaining the regression equations, the remaining 20 testing data are used to validate the regression models. The average rebound values from the testing data set are input into the equations to obtain concrete compressive strength predictions. The prediction results are then compared with the actual compressive strength obtained from the core sample destructive compression tests. The MAPE, VAF, and RMSE calculated for the linear regression model are 15.67%, −21.58%, and 103.07 kgf/cm^2, respectively. For the nonlinear regression models, the MAPE, VAF, and RMSE obtained are 16.75%, −19.13%, and 110.79 kgf/cm^2, respectively.

The prediction results show that both the linear and nonlinear regression models have MAPEs over 15%. Similar results are observed from other research indicating that traditional linear and nonlinear regression methods might not yield good prediction results (Wei, 2012; Mishra et al., 2019). In order to improve the prediction accuracy, this research proposes alternative prediction models based on AI methods (ANNs, SVMs, and ANFIS).

TABLE 2 | ANNs model setup.

Model Parameter	Settings	
Exemplars	Training Dataset	80
	Cross-Validation	10[a]
	Testing Dataset	20
Hidden Layers	One and two	
Transfer Functions	TanhAxon, SigmoidAxon, LinearAxon	
Learning Rule	Levenberg Marqua, Momentum	
Maximum Epochs	Starting from 500	

[a] *These 10 samples are randomly chosen from the 80 training samples.*

Artificial Neural Networks Models

This research uses NeuroSolutions 7.0 to develop the BP network (BPN) model for concrete compressive strength estimations. During the ANN model development process, parameters such as number of hidden layers, number of neurons in each layer, type of transfer functions, and learning rules are explored to obtain better prediction models. For this research, ANN models with both one and two hidden layers are developed. Different numbers of neurons in each layer, transfer functions, and learning rules are also investigated. In other words, trial and error is implemented to obtain better model parameter setup. Please refer to **Table 2** for ANN model parameter setup details.

There are 80 samples in the training data set (including 10 cross-validation samples) and 20 samples in the testing data set. In order to find the best ANN prediction model, the ANN parameters are explored through the trial and error process. After several trials, it was found that better results (lower training errors) are obtained when using the “TanhAxon” transfer function and “Levenberg-Marquardt” (LM) learning rule. The TanhAxon transfer function applies a bias and tanh function to each neuron in the layer. This squashes the range of each neuron in the layer to between −1 and 1. The LM algorithm is a standard technique for nonlinear least-squares problems and can be thought of as a combination of steepest descent and the Gauss-Newton method.

The best training results obtained from the one-hidden-layer network is from a 2 to 5-1 (two inputs, five process elements in the hidden layer, and one output) ANN model. The MAPE and RMSE obtained are 16.82% and 101.21, respectively, from the training data set. This model is validated with the 20 samples using the testing data set. The MAPE, VAF, and RMSE obtained from the one-hidden-layer ANN model are 14.77%, −33.88%, and 92.67, respectively, when validating with the testing data.

ANN models with two hidden layers are also developed using the same training data set. Various parameter settings are explored in order to obtain lower training errors. The best training results obtained from the two-hidden-layer network is from a 2-5 to 5-1 (two inputs, five process elements in the first and second hidden layers, and one output) ANN model. The corresponding MAPE and RMSE obtained from the training data are 11.9% and 85.36, respectively, which are lower than the one-hidden-layer model. The training and validation errors for this ANN model are shown in **Figure 9**.

Next, the two-hidden-layer model is validated with the 20 samples from the testing data set. The MAPE, VAF, and RMSE obtained from the testing data are 12.37%, −30.68%, and 88.45, respectively, which are also lower than the one-hidden-layer model. The desired values (actual compressive strength) and model outputs are presented in a scatterplot as shown in **Figure 10**. If the model output equals the desired value, it should fall on the red line. In **Figure 11**, the line chart of the desired and model output compressive strengths is also plotted. To get a better understanding of the individual errors between the desired values and model outputs, a residual histogram of the testing samples is presented in **Figure 12**.

From the above, it can be observed that, most of the time, the predicted values (model outputs) are smaller than the desired values. It indicates that this ANN model tends to underestimate.

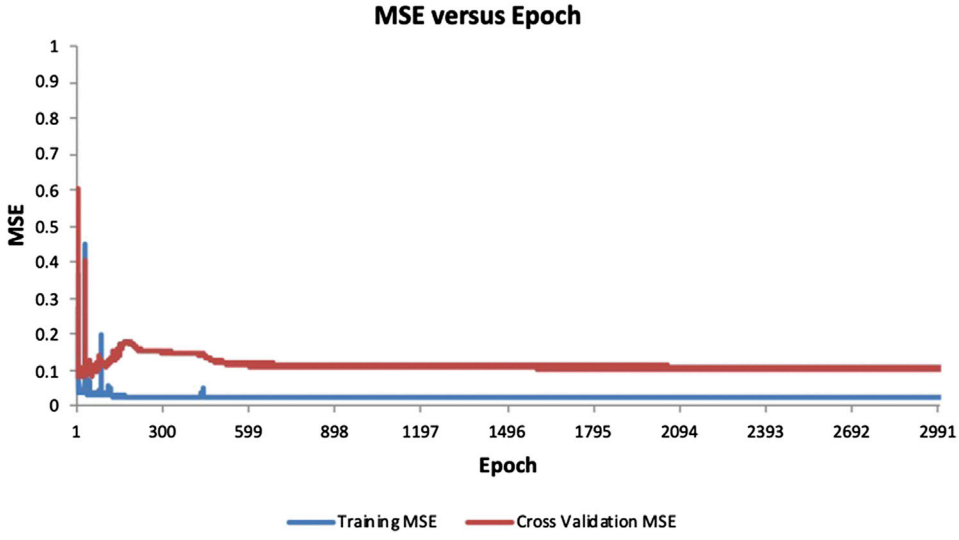

FIGURE 9 | ANN model (2-5-5–1) training and validation error.

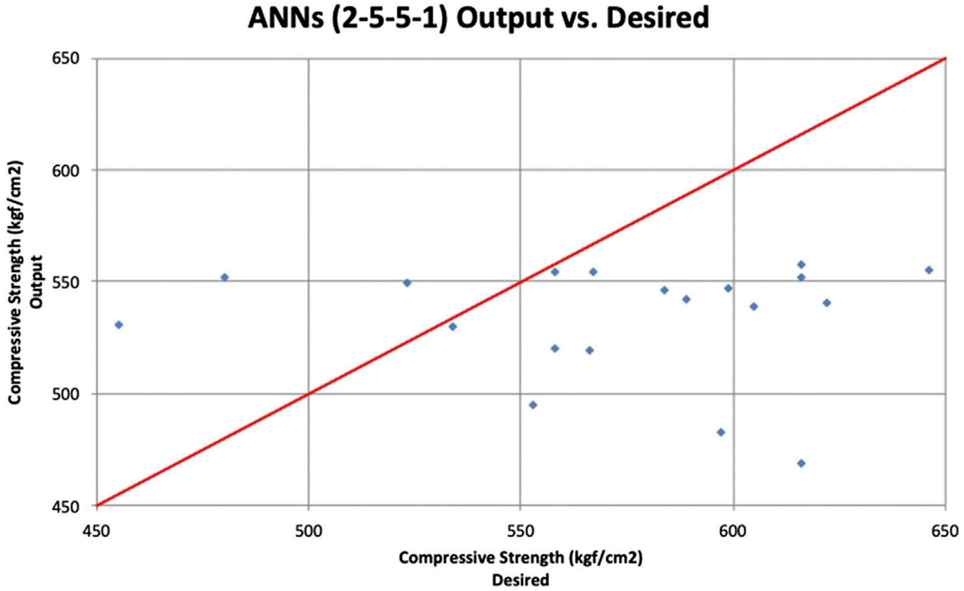

FIGURE 10 | ANN model (2-5-5–1) scatterplot.

In addition, there are 10 samples with residuals over 50 kgf/cm^2, which might contribute to the low prediction accuracy. The training and testing results of ANN models with one and two hidden layers are summarized in **Table 3**.

Support Vector Regression Models

This research uses the least squares SVM (LSSVM) in the Matlab R2018a to develop the support vector regression model. The same 80 training data used in ANN model development are used to develop the LSSVM regression model.

For the SVM regression models, there are typically four types of kernel functions: linear, polynomial, sigmoid, and radial basis function (RBF) kernels. Among them, RBF is favorable for its capability of dealing with nonlinearity and high-dimensional computation and effectiveness in reducing complexity for inputs by adjusting C and γ (Hsu et al., 2003), where C is the cost of the soft-margin SVM loss function and gamma is the free parameter of the RBF. For this research, support vector regression parameters are obtained from the trial and error process. Different C and γ values are investigated to obtain the best SVM model with the training data set as shown in **Table 4**.

From **Table 4**, the best training MAPE obtained for the SVM model is 15.13%, and the corresponding C and γ values are 2 and 5,000, respectively.

Next, this model is validated with the 20 samples from the testing data set. The desired values (actual compressive strength)

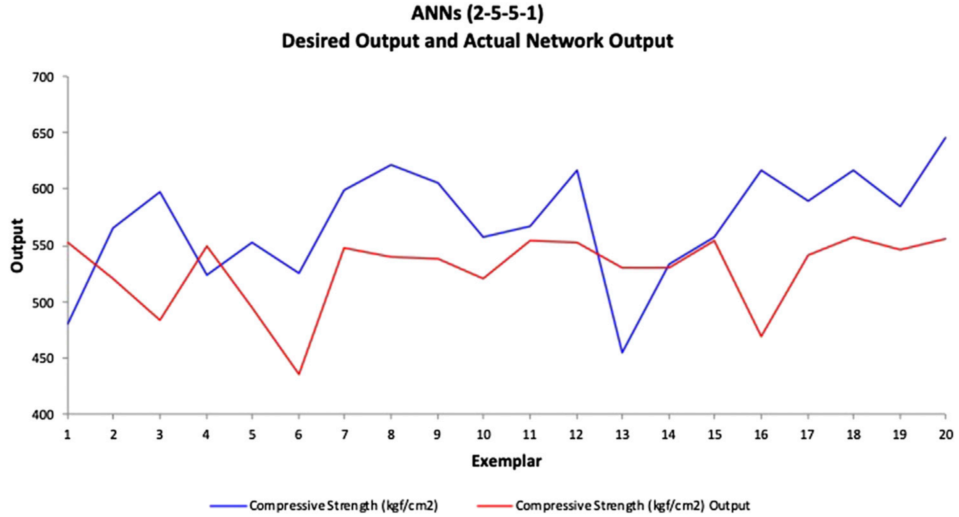

FIGURE 11 | ANN model (2-5-5–1) line chart.

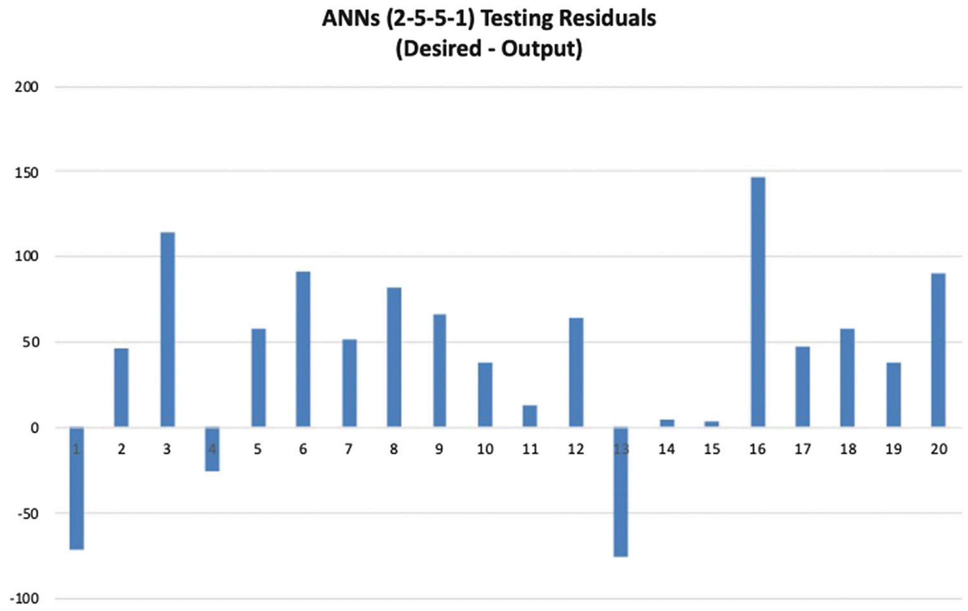

FIGURE 12 | ANN model (2-5-5–1) residual histogram.

and support vector regression model outputs are presented in a scatterplot as shown in **Figure 13**. The red line indicates 100% accuracy prediction. The MAPE, VAF, and RMSE obtained for this support regression model are 16.08%, 6.05%, and 99.05, respectively. The line chart of the desired and model output compressive strengths is provided in **Figure 14**. The residual histogram of the testing samples is presented in **Figure 15**. The results show that the support vector regression model is not as accurate compared to the ANN model.

Adaptive Network-Based Fuzzy Inference Models

The ANFIS model is developed in the Matlab 2018a environment. The same 80 training samples used in ANN and SVM model development are also used to develop the ANFIS model. When developing the ANFIS models, the researchers can choose different numbers and types of membership functions. The researchers developed three different sets of models (models with three, five, and eight membership functions). For each membership function setting in Matlab 2018, there are eight different types to choose from: triangular (trimf), trapezoidal (trapmf), generalized bell-shaped (gbell), Gaussian (gauss1), Gaussian combination (gauss2), pi-shaped (pimf), difference between two sigmoidal (dsigmf), and product of two sigmoidal membership functions (psigmf). Each of them is tried in the ANFIS model development to find the best prediction results.

TABLE 3 | ANNs model results.

ANNs Model Type	**Training**		**Testing**	
	MAPE	**RMSE**	**MAPE**	**RMSE**
2-5-1	16.82%	101.21	14.77%	92.67
2-5-5-1	11.9%	85.36	12.37%	88.45

In the model setup, the tolerance level is set as 0, and the training is set to repeat 1,000, 2,000, and 3,000 times. The training error diagram for the model with three sigmoid membership functions (dsigmf) is shown in **Figure 16**.

ANFIS models with three, five, and eight membership functions are developed using different types of membership functions. The models that yield the best training results are summarized in **Table 5**. For models with three membership functions ([3, 3]), the best MAPE, 10.45%, is obtained with the sigmoid membership functions (dsigmf). For models with five membership functions ([5, 5]), the best MAPE, 10.10%, is obtained with the trapezoidal membership functions (trapmf). For models with eight membership functions ([8, 8]), the best MAPE, 9.11%, is obtained with the trapmf membership function.

After the best training model ([8, 8]), trapmf membership function) is identified, the remaining 20 testing samples (unseen data to the model) are used to obtain the concrete compressive strength predictions. The desired values (actual compressive strength) and support vector regression model outputs are presented in a scatterplot as shown in **Figure 17**. The line chart of the desired and ANFIS model output is provided in **Figure 18**. The residual histogram of the testing samples is presented in **Figure 19**. The MAPE, VAF, and RMSE obtained are 10.01%, −58.58%, and 62.46, respectively.

TABLE 4 | SVM parameter settings and training error.

***C* value**	**γ value**	**Training MAPE**	***C* value**	**γ value**	**Training MAPE**
2	1,000	15.24%	2	1,000	15.24%
4	1,000	15.54%	2	1,500	15.20%
8	1,000	15.60%	2	2,000	15.18%
16	1,000	15.72%	2	3,000	15.15%
32	1,000	16.05%	**2**	**5,000**	**15.13%**
64	1,000	16.40%	2	7,000	16.11%
128	1,000	16.40%	2	10,000	16.14%

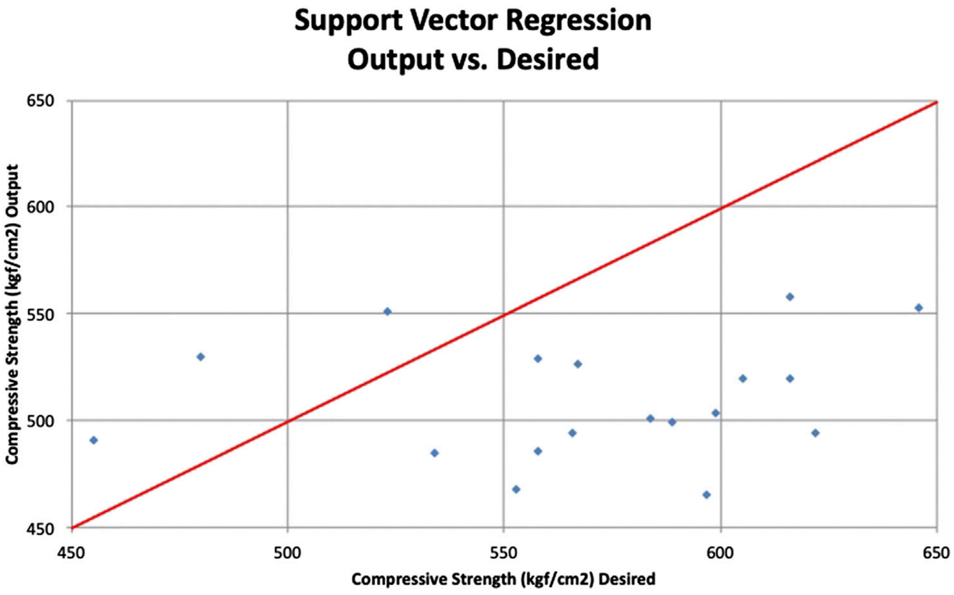

FIGURE 13 | Support vector regression model scatterplot

The prediction results show that MAPEs in both training and testing data sets obtained from the three AI-based models are better than the 20% MAPE observed from previous research. Among them, the ANFIS model yields the best prediction accuracy with both the lowest training MAPE (9.11%) and testing MAPE (10.01%).

In order to examine the reliability of the prediction results, K-fold cross-validation is used to test the ANFIS model. In K-fold cross-validation, part of the available data is used to develop the model, and a different part of the data is used to test it. The K-fold cross-validation is also known as leave-one-out cross-validation (Hastie et al., 2009). For this research, the data are split into five equal-sized parts. Each of the five parts has 20 samples, and there are 100 samples in total. Four parts are first chosen to develop the prediction model, and the fifth part is used to calculate the prediction error. Then, another four parts are chosen to develop the model, and the remaining part is used to test the model. This process is repeated five times until all of the five parts are used to test the prediction model. The MAPE average and standard deviation of the five-fold cross-validation are 9.90% and 2.28%, respectively. The RMSE average and standard deviation of the five-fold cross-validation are 58.67 and 8.93, respectively. This result shows

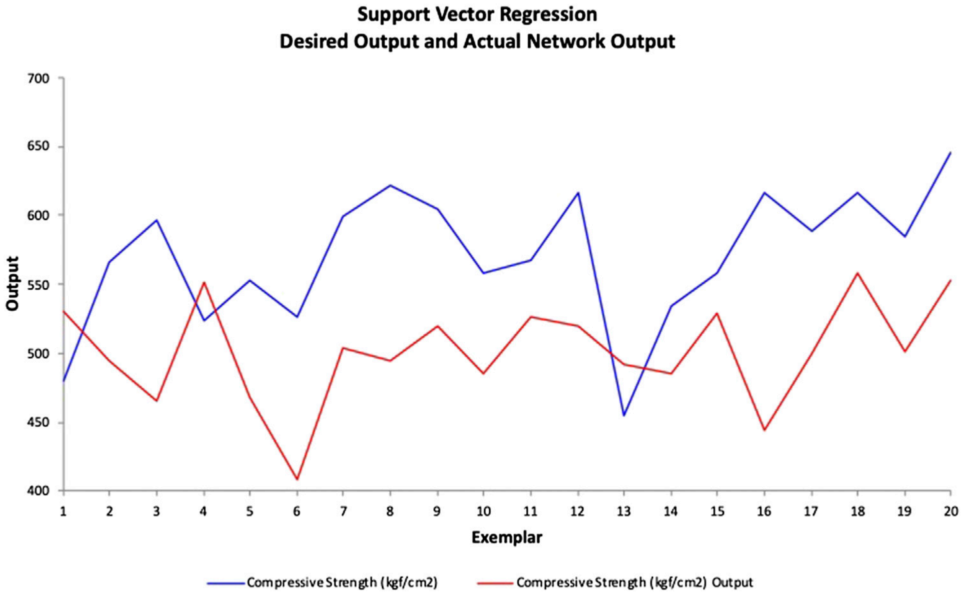

FIGURE 14 | Support vector regression model line chart.

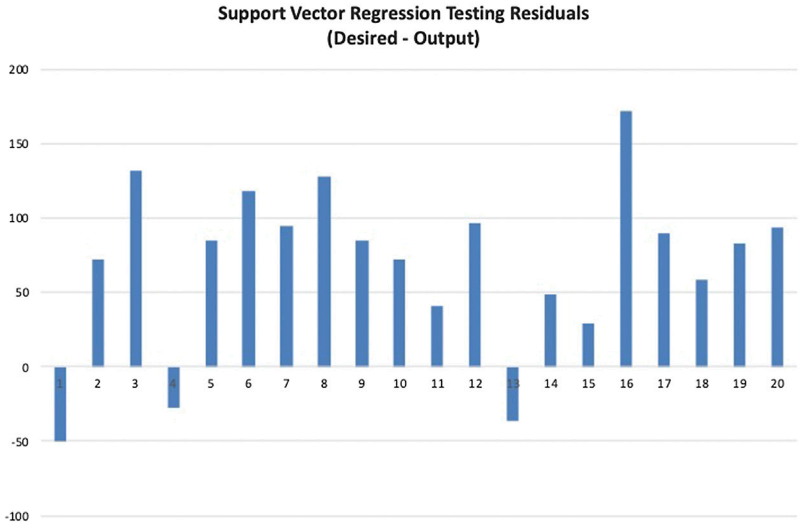

FIGURE 15 | Support vector regression model residual histogram.

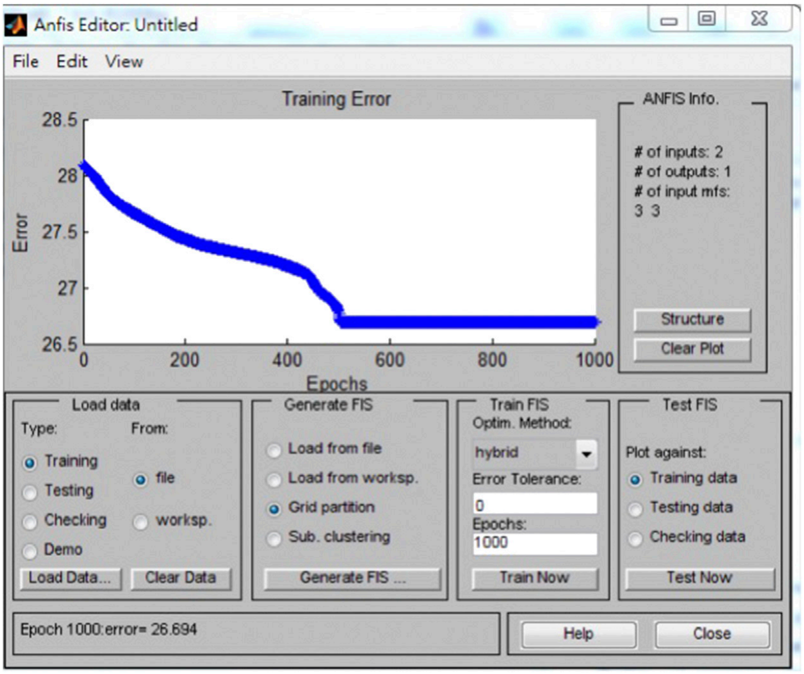

ANFIS Info.

# of inputs: 2
# of outputs: 1
# of input mfs:
3 3

Load data

Type:
● Training
○ Testing
○ Checking
○ Demo

From:
● file
○ worksp.

Generate FIS

○ Load from file
○ Load from worksp.
● Grid partition
○ Sub. clustering

Train FIS

Optim. Method: hybrid
Error Tolerance: 0
Epochs: 1000

Test FIS

Plot against:
● Training data
○ Testing data
○ Checking data

Epoch 1000:error= 26.694

FIGURE 16 | ANFIS model training error.

that, with different combinations of training and testing data, the ANFIS models are able to yield consistent prediction accuracies.

In summary, this research collected a total of 100 *in situ* RH and core sampling test data to develop concrete compressive estimation models. Among them, 80 samples were randomly selected to train the models, and the remaining 20 samples were

TABLE 5 | ANFIS model training results.

ANFIS Model	Transfer Function Type	Training MAPE	Training RMSE
[3 3]	Dsigmf	10.45%	64.43
[5 5]	Trapmf	10.10%	64.16
[8 8]	Trapmf	9.11%	57.48

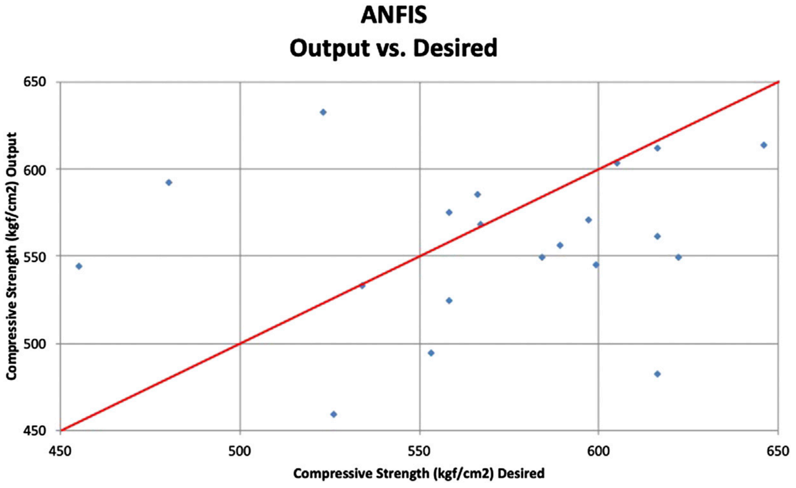

FIGURE 17 | ANFIS model scatterplot

used for model validation. First, linear and nonlinear regression models were developed and tested. The compressive strength prediction accuracies (measured by MAPE) obtained from the linear and nonlinear regression models are 15.66 and 16.75%, respectively, which do not show significant improvement from previous research. Subsequently, AI-based models (ANNs, SVMs, and ANFIS) were developed and validated using the same training and testing data sets. For each model, various model parameters were explored in order to achieve lower training error and higher prediction accuracy. Among these models, the ANFIS model yielded the best training and testing results with the lowest training and testing MAPEs of 9.11 and 10.01%, respectively. The model development and validation results from this research effort are summarized in **Table 6**. From **Table 6**, it can be observed that both ANN and ANFIS models are able to generate better prediction accuracies when compared to traditional linear and nonlinear regression models. Similar to Wei's research results (Wei, 2012), the ANFIS model can produce the lowest prediction errors when using the RH measurement to measure concrete compressive strength.

CONCLUSIONS AND RECOMMENDATIONS

To further investigate the relationship between *in situ* RH test measurements and actual concrete compressive strength, this research adopts AI techniques to develop concrete compressive strength prediction models. A total of 100 test data are collected

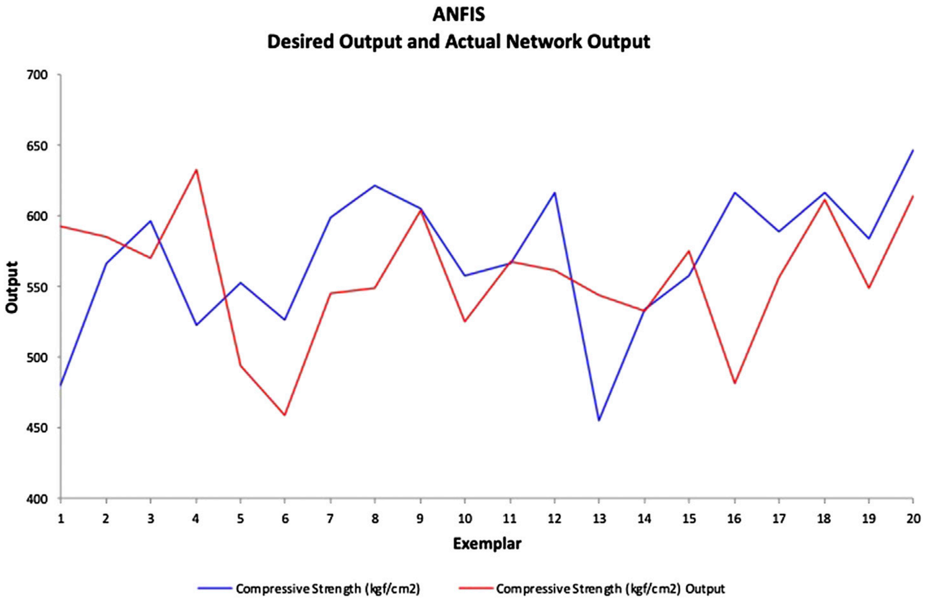

FIGURE 18 | ANFIS model line chart.

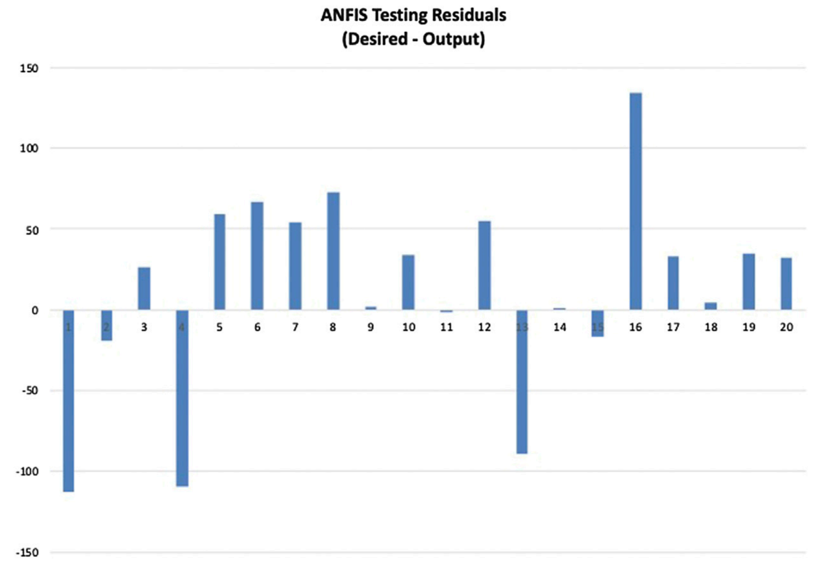

FIGURE 19 | ANFIS model residual histogram.

TABLE 6 | Summary of model validation result.

Model Type	Model Setup	Testing MAPE	Testing RMSE
Regression	linear	15.67%	103.07
	Non-linear	16.75%	110.79
ANNs	2-5–5-1	12.37%	88.45
SVMs	$C = 2$, $\gamma = 5{,}000$	16.08%	99.05
ANFIS	[8 8], Trapmf	10.01%	62.46

from a large residential complex building. The data collected are used to develop and validate traditional regression models as well as AI-based models (ANN, SVM, and ANFIS models). For traditional regression models, the MAPEs calculated for the linear and nonlinear models are 15.66 and 16.75%, respectively. For the ANN model, the best prediction results are obtained from a two-hidden-layer network (2-5–5-1), and the MAPE obtained is 12.37%. For the support vector regression model, the best MAPE obtained is 16.08%. The corresponding parameters for the best support vector regression model are $C = 2$ and $\gamma = 5{,}000$. For this research, the ANFIS model yields the best prediction accuracy with an MAPE of 10.01% when the model is validated using the testing data. This result is obtained from the ANFIS model with eight membership functions for the two input variables ([8, 8]), and the membership function type is trapmf. K-fold cross-validation is also conducted, and the results show that the ANFIS model have consistent prediction errors when validated with different data. The research results show that AI techniques can be used to develop concrete compressive strength prediction models using *in situ* RH test measurements. The prediction accuracies are better when comparing to previous research results.

It should be noted that the RH test measurements are highly related to the near surface of the test object. Therefore, it is recommended that the RH tests can be combined with other nondestructive test methods (such as UPV tests) to improve concrete compressive strength estimations. Research results have shown that the SonReb (UPV + RH test) method (Rilem Report TC43-CND, 1993) might improve concrete strength estimations in NDT tests (Nobile, 2015; Rashid and Waqas, 2017; Pereira and Romão, 2018). For this research, the results are obtained from the 100-sample data collected. In order to improve reliability, it is suggested that more sample data could be collected for model development and validation.

DATA AVAILABILITY STATEMENT

The datasets presented in this article are not readily available because confidential agreements are signed before the authors are allowed to conduct the experiments. Requests to access the datasets should be directed to yrwang@nkust.edu.tw.

ETHICS STATEMENT

Written informed consent was obtained from the individual(s) for the publication of any potentially identifiable images or data included in this article.

AUTHOR CONTRIBUTIONS

Y-RW conceived the presented idea, supervised the experiments and analysis. Y-LL and D-LC conducted the experiment, developed the models and analyzed the data. Y-RW took the lead in writing the manuscript with help from Y-LL and D-LC.

ACKNOWLEDGMENTS

This material is based upon work supported by the Ministry of Science and Technology, TAIWAN under grant no. MOST 103-2221-E-151-053.

REFERENCES

Abdulshahed, A. M., Longstaff, A. P., and Fletcher, S. (2015). The application of ANFIS prediction models for thermal error compensation on CNC machine tools. *Appl. Soft Comput.* 27, 158–168. doi:10.1016/j.asoc.2014.11.012

Abraham, A. (2005). Adaptation of fuzzy inference system using neural learning. *Stud. Fuzziness Soft Comput.* 181, 53–83. doi:10.1007/11339366_3

Anguita, D., Ghio, A., Greco, N., Oneto, L., and Ridella, S. (2010). "Model selection for support vector machines: advantages and disadvantages of the machine learning theory,"in The 2010 international joint conference on neural networks (IJCNN), Barcelona, Spain, July 18–23, 2010 (IEEE), 1–8.

Asteris, P. G., and Mokos, V. G. (2019). Concrete compressive strength using artificial neural networks. *Neural Comput. Applc.* 32, 11807–11826. doi:10.1007/s00521-019-04663-2

ASTM C597–16 (2020). Standard test for pulse velocity through concrete. Available at: http://web.archive.org/web/20190904130233/https://www.astm.org/Standards/C597.htm.

ASTM C805/C805M (2020). Standard test method for rebound number of hardened concrete. Available at: http://web.archive.org/web/20190502123317/https://www.astm.org/Standards/C805.htm.

Atoyebi, O. D., Ayanrinde, O. P., and Oluwafemi, J. (2019). Reliability comparison of schmidt rebound hammer as a non-destructive test with compressive strength tests for different concrete mix. *J. Phys. Conf.* 1378 (3), 032096. doi:10.1088/1742-6596/1378/3/032096

Balabin, R. M., and Lomakina, E. I. (2011). Support vector machine regression (SVR/LS-SVM)-an alternative to neural networks (ANN) for analytical chemistry? Comparison of nonlinear methods on near infrared (NIR) spectroscopy data. *Analyst* 136 (8), 1703–1712. doi:10.1039/c0an00387e

Bishop, C. M. (2006). *Pattern recognition and machine learning*. Berlin, Germany: Springer.

Boyacioglu, M. A., and Avci, D. (2010). An adaptive network-based fuzzy inference system (ANFIS) for the prediction of stock market return: the case of the Istanbul stock exchange, *Expert Syst. Appl.* 37 (12), 7908–7912. doi:10.1016/j.eswa.2010.04.045

Brencich, A., Cassini, G., Pera, D., and Riotto, G. (2013). Calibration and reliability of the rebound (Schmidt) hammer test. *Civil Eng. Arch.* 1 (3), 66–78. doi:10.13189/cea.2013.010303

Breysse, D., and Martínez-Fernández, J. L. (2014). Assessing concrete strength with rebound hammer: review of key issues and ideas for more reliable conclusions. *Mater. Struct.* 47 (9), 1589–1604. doi:10.1617/s11527-013-0139-9

British Standards Institution (BSI) (1986). *Testing concrete - Part 202: Recommendations for surface hardness testing by rebound hammer*. BS 1881-202

Drucker, H., Burges, C. C., Kaufman, L., Smola, A. J., and Vapnik, V. (1997). "Support vector regression machines," in *Advances in neural information processing systems*. M. Mozer, M. Jordan, and T. Petsche (Cambridge, MA: MIT Press), 155–161.

El Mir, A., and Nehme, S. G. (2017). Repeatability of the rebound surface hardness of concrete with alteration of concrete parameters. *Construct. Build. Mater.* 131, 317–326. doi:10.1016/j.conbuildmat.2016.11.085

European Normalization Committee (En) (2012). *Testing concrete in structures - Part 2: non-destructive testing - determination of rebound number*. EN 12504-2: 2012

Gurney, K. (2014). *An introduction to neural networks*. Boca Raton, FL: CRC press.

Hajjeh, H. R. (2012). Correlation between destructive and non-destructive strengths of concrete cubes using regression analysis. *Contemp. Eng. Sci.* 5 (10), 493–509.

Hamidian, M., Shariati, A., Khanouki, M. A., Sinaei, H., Toghroli, A., and Nouri, K. (2012). Application of Schmidt rebound hammer and ultrasonic pulse velocity techniques for structural health monitoring. *Sci. Res. Essays* 7 (21), 1997–2001. doi:10.5897/SRE11.1387

Hastie, T., Tibshirani, R., and Friedman, J. (2009). *The elements of statistical learning: data mining, inference, and prediction*. Berlin, Germany: Springer Science & Business Media.

Hsu, C. W., Chang, C. C., and Lin, C. J. (2003). *A practical guide to support vector classification*. Tech. Rep. Department of Computer Science, National Taiwan University.

Huang, W. L., Chang, C. Y., Chen, W. C., and We, C. N. (2011). Using ANNs to improve prediction accuracy for rebound hammers. *Taiwan Highway Engineering* 37 (2), 2–18.

Huang, W., Nakamori, Y., and Wang, S.-Y. (2005). Forecasting stock market movement direction with support vector machine. *Comput. Oper. Res.*, ; 32(10), p 2513–2522. doi:10.1016/j.cor.2004.03.016

Information on The Constructor (2012a). Rebound hammer test on concrete - principle, procedure, advantages & disadvantages. Availabe at: http://web.archive.org/web/20200221015718/https://theconstructor.org/concrete/rebound-hammer-test-concrete-ndt/2837/.

Information on Gilson Company Inc. (2012b). Silver schmidt PC concrete test hammer. Availabe at: http://web.archive.org/web/20200221015938/https://www.globalgilson.com/silver-schmidt-pc-concrete-test-hammer-type-n

Iphar, M. (2012). ANN and ANFIS performance prediction models for hydraulic impact hammers. *Tunn. Undergr. Space Technol.* 27 (1), 23–29. doi:10.1016/j.tust.2011.06.004

Jang, J.-S. R. (1993). ANFIS: adaptive-network-based fuzzy inference system. *IEEE Trans. Syst. Man. Cybern.* 23 (3), 665–685. doi:10.1109/21.256541

Kim, K. J. (2003). Financial time series forecasting using support vector machines. *Neurocomputing* 55 (1-2), 307–319. doi:10.1016/s0925-2312(03)00372-2

Kocáb, D., Misák, P., and Cikrle, P. (2019). Characteristic curve and its use in determining the compressive strength of concrete by the rebound hammer test. *Materials* 12 (17), 2705. doi:10.3390/ma12172705

Kumar, B. R., Vardhan, H., Govindaraj, M., and Vijay, G. S. (2013). Regression analysis and ANN models to predict rock properties from sound levels produced during drilling. *Int. J. Rock Mech. Min. Sci.* 58, 61–72. doi:10.1016/j.ijrmms.2012.10.002

Kumar, C. V., Vardhan, H., and Murthy, C. S. (2019). Multiple regression model for prediction of rock properties using acoustic frequency during core drilling operations. *Geomechanics and Geoengineering* 15, 1–16. doi:10.1080/17486025.2019.1641631

Mishra, M., Bhatia, A. S., and Maity, D. (2019). A comparative study of regression, neural network and neuro-fuzzy inference system for determining the compressive strength of brick–mortar masonry by fusing nondestructive testing data. *Eng. Comput*. doi:10.1007/s00366-019-00810-4

Nobile, L. (2015). Prediction of concrete compressive strength by combined non-destructive methods. *Meccanica* 50 (2), 411–417. doi:10.1007/s11012-014-9881-5

Nurcahyo, S., and Nhita, F. (2014). "Rainfall prediction in kemayoran jakarta using hybrid genetic algorithm (ga) and partially connected feedforward neural network (pcfnn)," 2nd International Conference on Information and Communication Technology (ICoICT). Bandung, Indonesia, May 28–30, 2014, 166–171.

Pereira, N., and Romão, X. (2018). Assessing concrete strength variability in existing structures based on the results of NDTs. *Construct. Build. Mater.* 173, 786–800. doi:10.1016/j.conbuildmat.2018.04.055

Priya, S. S., and Iqbal, M. H. (2015). Solar radiation prediction using artificial neural network. *Int. J. Comput. Appl.* 116 (16), p 28–31. doi:10.5120/20422-2722

Qasrawi, H. Y. (2000). Concrete strength by combined nondestructive methods simply and reliably predicted. *Cement Concr. Res.* 30 (5), 739–746. doi:10.1016/s0008-8846(00)00226-x

Ramasamy, P., Chandel, S. S., and Yadav, A. K. (2015). Wind speed prediction in the mountainous region of India using an artificial neural network model. *Renew. Energy* 80, 338–347. doi:10.1016/j.renene.2015.02.034

Rashid, K., and Waqas, R. (2017). Compressive strength evaluation by non-destructive techniques: an automated approach in construction industry. *J.Build. Eng.* 12, 147–154. doi:10.1016/j.jobe.2017.05.010

Rezaeianzadeh, M., Tabari, H., Arabi Yazdi, A., Isik, S., and Kalin, L. (2014). Flood flow forecasting using ANN, ANFIS and regression models. *Neural Comput. Appl.* 25 (1), 25–37. doi:10.1007/s00521-013-1443-6

RILEM Recommendation. (1993). Draft recommendation for in situ concrete strength determination by combined non-destructive methods. *Mater. Struct*, 26, 43–49.

Rojas-Henao, L., Fernández-Gómez, J., and López-Agüí, J. C (2012). Rebound hammer, pulse velocity, and core tests in self-consolidating concrete. *ACI Mater. J.* 109 (2), 235–243. doi:10.14359/51683710

Shariati, M., Ramli-Sulong, N. H., Kh, M. M. A., Shafigh, P., and Sinaei, H. (2011). Assessing the strength of reinforced concrete structures through ultrasonic pulse velocity and schmidt rebound hammer tests. *Sci. Res. Essays* 6 (1), 213–220. doi:10.5897/SRE10.879

Shirsath, P. B., and Singh, A. K. (2010). A comparative study of daily pan evaporation estimation using ANN, regression and climate based models. *Water Resour. Manag.* 24 (8), 1571–1581. doi:10.1007/s11269-009-9514-2

Smola, A. J., and Schölkopf, B. (2004). A tutorial on support vector regression. *Stat. Comput.* 14 (3), 199–222. doi:10.1023/b:stco.0000035301.49549.88

Szilágyi, K., Borosnyói, A., and Zsigovics, I. (2011). Rebound surface hardness of concrete: introduction of an empirical constitutive model. *Construct. Build. Mater.* 25 (5), 2480–2487. doi:10.1016/j.conbuildmat.2010.11.070

The National Standards of the Republic of China (1986). *Chinese National Standards (CNS). Methods of test for rebound number of Hardened Concrete*. CNS 10732-1984, Taiwan: CNS

Topçu, İ. B., and Sarıdemir, M. (2008). Prediction of compressive strength of concrete containing fly ash using artificial neural networks and fuzzy logic. *Comput. Mater. Sci.* 41 (3), 305–311. doi:10.1016/j.commatsci.2007.04.009

Vapnik, V. (2013). *The nature of statistical learning theory*. Berlin, Germany: Springer science & business media.

Vural, Y., Ingham, D. B., and Pourkashanian, M. (2009). Performance prediction of a proton exchange membrane fuel cell using the ANFIS model. *Int. J. Hydrogen Energy* 34 (22), 9181–9187. doi:10.1016/j.ijhydene.2009.08.096

Wei, S. H. (2012). Application of the adaptive neuro-fuzzy inference system model in predicting the concrete compressive strength from the silverschmidt hammer. Master thesis. Kaohsiung (Taiwan): National Kaohsiung University of Applied Sciences

Xu, T., and Li, J. (2018). Assessing the spatial variability of the concrete by the rebound hammer test and compression test of drilled cores. *Construct. Build. Mater.* 188, 820–832. doi:10.1016/j.conbuildmat.2018.08.138

Yılmaz, I., and Yuksek, A. G. (2008). An example of artificial neural network (ANN) application for indirect estimation of rock parameters. *Rock Mech. Rock Eng.* 41 (5), 781–795. doi:10.1007/s00603-007-0138-7

Yilmaz, I., and Kaynar, O. (2011). Multiple regression, ANN (RBF, MLP) and ANFIS models for prediction of swell potential of clayey soils. *Expert Systems with Applications* 38 (5), 5958–5966. doi:10.1016/j.eswa.2010.11.027

Zupan, J., and Gasteiger, J. (1991). Neural networks: a new method for solving chemical problems or just a passing phase?. *Anal. Chim. Acta* 248 (1), 1–30. doi:10.1016/s0003-2670(00)80865-x

Conflict of Interest: The authors declare that the research was conducted in the absence of any commercial or financial relationships that could be construed as a potential conflict of interest.

frontiers in Materials

ORIGINAL RESEARCH
published: 22 December 2020
doi: 10.3389/fmats.2020.587738

A Positioning Method of Temperature Sensors for Monitoring Dam Global Thermal Field

***Haoyang Peng*[1], *Peng Lin*[1]*, *Yunfei Xiang*[1], *WenQi Chen*[2], *Shaowu Zhou*[3], *Ning Yang*[3] and *Yu Qiao*[3]**

[1]Department of Hydraulic Engineering, Tsinghua University, Beijing, China, [2]Institute for Network Sciences and Cyberspace, Tsinghua University, Beijing, China, [3]China Three Gorges Corporation, Beijing, China

During the concrete pouring process of a dam construction, timely and accurate temperature monitoring is of great significance to reveal the thermal distribution characteristics and evolution process, and control concrete cracking. In this study, a positioning method of temperature sensors (PMTS) in a concrete dam is developed to determine the arrangement of temperature sensors quantitatively. The proposed positioning method is related to the restructured thermal field based on the natural neighbor interpolation algorithm, and the cross-validation. Based on the method, thermometers, distributed optical fibers and infrared thermal imagers are optimally installed in a super-high arch dam for real-time measurement of concrete temperature. The results show that the PMTS is reasonable and reliable for obtaining the dam global thermal field. The on-site temperature monitoring data indicate that the time and space temperature distribution law of the restructured thermal field is consistent with the actual situation of the super-high arch dam. In addition, the cons and pros, and improvement of the PMTS are further discussed. The proposed PMTS is a valuable method to monitor the global thermal field of concrete dams.

Keywords: positioning method of temperature sensors, global thermal field, cross-validation, restructured thermal field, concrete dam

Edited by:
Juncai Xu,
Case Western Reserve University,
United States

Reviewed by:
Junfeng Guan,
North China University of Water Conservancy and Electric Power,
China
Hongyuan Liu,
University of Tasmania, Australia

****Correspondence:***
Peng Lin
celinpe@tsinghua.edu.cn

Specialty section:
This article was submitted to Structural Materials,
a section of the journal
Frontiers in Materials

Received: *27 July 2020*
Accepted: *24 November 2020*
Published: *22 December 2020*

Citation:
Peng H, Lin P, Xiang Y, Chen W, Zhou S, Yang N and Qiao Y (2020) A Positioning Method of Temperature Sensors for Monitoring Dam Global Thermal Field.
Front. Mater. 7:587738.
doi: 10.3389/fmats.2020.587738

INTRODUCTION

Concrete dams usually have a large pouring size during construction. Due to the large amount of heat released by cement hydration, the concrete temperature rises sharply. As concrete age increases, the concrete temperature would decrease because of the ambient temperature influence. Different concrete areas have temperature differences during the process of temperature change. Under certain constraints, a remarkable thermal stress could be generated (Lin et al. 2014). Since mass concrete usually contains few steel bars, the thermal stress is almost entirely borne by the concrete. Concrete is a fragile material, and the tensile strength is generally 1/10 of the compressive strength. The ultimate tensile deformation during short-term loading is only $(0.6\text{–}1) \times 10^{-4}$, and $(1.2\text{–}2) \times 10^{-4}$ during the long-term loading (Zhu 1999). Therefore, if a larger tensile stress is generated due to the temperature change, a greater impact on the crack resistance of the concrete would be inevitable (Jaafar et al. 2007; Lin et al. 2015; Schackow et al. 2016; Lin et al. 2018; Lin et al. 2019). In order to effectively control the temperature change process of mass concrete and reduce the risk of concrete cracking, timely and accurate temperature monitoring is of great significance during a concrete dam construction

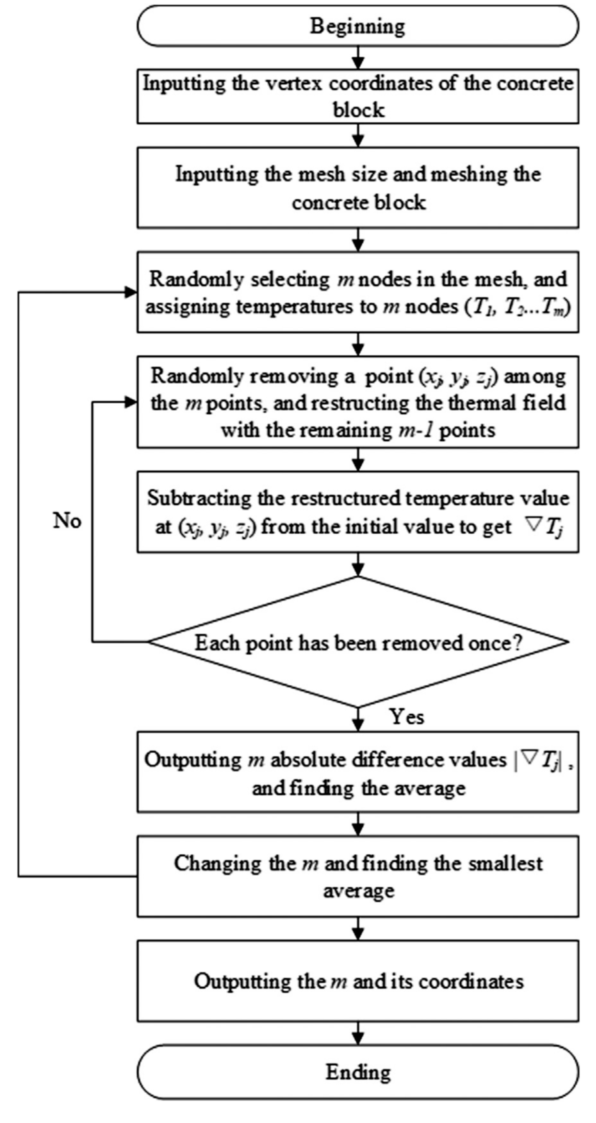

FIGURE 1 | The flow chart of the PMTS.

(Lin et al. 2012; Peng et al. 2019). Generally, with the pouring of dam concrete, a number of temperature sensors are synchronously buried to obtain the real-time temperature.

At present, there are mainly three types of concrete temperature sensors:

1) thermometers for point temperature measurement inside concrete. In concrete dams, the most commonly used temperature sensors are thermometers. In order to verify the cooling effect and observe the long-term temperature change, 440 resistance thermometers are installed in the concrete during the Hoover Dam construction (Fan et al. 2016). Most of these thermometers are placed on two symmetrical cross-sections about 30 m away from the central cross-section. Almost all thermometers are placed 15 m–23 m away from the galleries. About 70 resistance thermometers installed at a depth of some centimeters from the external surface in the Alto Lindoso dam are used to monitor the temperature of air, water and concrete (Mata et al. 2014). There are 26 thermometers installed in the La Baells double curvature arch dam. The water temperature is measured by means of five water thermometers installed at the upstream surface of the dam. The concrete temperature is measured by means of 21 concrete thermometers at midpoints between dam surfaces (Santillán et al. 2014; Santillan et al. 2015). The Tichy Haf arch dam is equipped with 12 thermometers for temperature monitoring. The thermometers are usually located at 4 m–5 m away from the upstream or downstream surface, or in the middle of the concrete blocks (Belmokre et al. 2019). In buttress No.13 of the SefidRud concrete buttress dam, the approximate location of the thermometers are near the upstream and downstream surface to monitor the concrete temperature (Mirzabozorg et al. 2019).

2) distributed optical fibers for line temperature measurement inside concrete. In recent years, due to the development of the optical fiber sensing technology, optical fibers have also been adopted in concrete dams for line temperature monitoring. In the Baise Hydropower Station, the temperature-sensing optical fibers

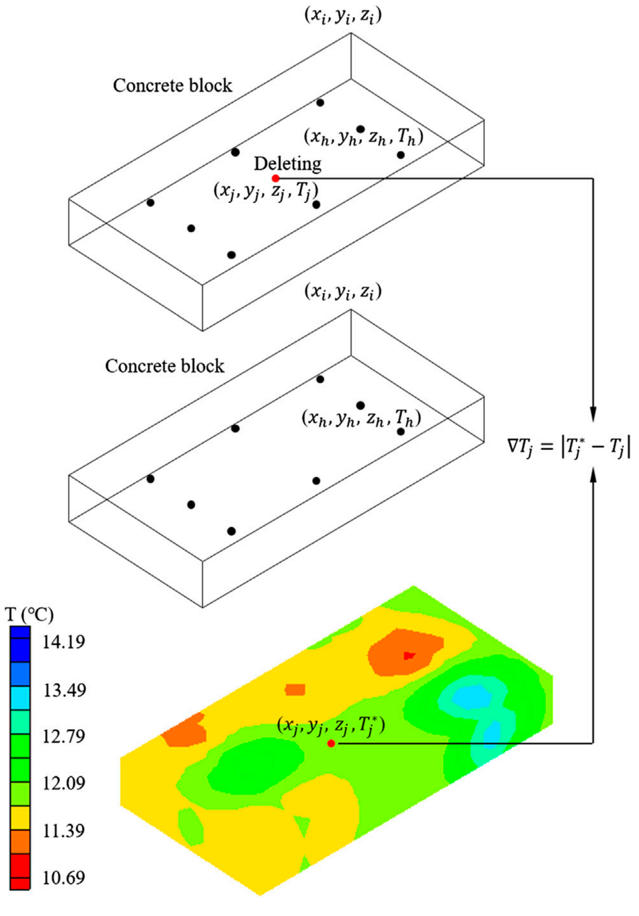

FIGURE 2 | Accuracy of the thermal field judged by the cross-validation method.

are installed at the No. 5 overflow dam monolith of the RCC main dam and the No. 6A of the highest gravity dam monolith. The snake-shaped optical fibers are embedded on the dam pouring layer (Bao et al. 2006). In the Guangzhao Hydropower Station, there are 7 optical fiber loops below EL615.50 m, and 16 optical fiber loops above EL615.50 m. In addition, two vertical optical fibers are arranged from EL560 m to the dam crest to obtain the temperature distribution along the vertical direction. Most optical fibers are buried as a straight line (Jiang and Guo 2008). The Jinghong Hydropower Station is designed to install optical fibers in the dam monoliths 12# and 17# to monitor the concrete temperature. The optical fibers are laid in a "S" shape, with a total length of 1,600 m (Shi 2008). In the Xiluodu arch dam, optical fibers are embedded in 4 dam monoliths 5#, 15#, 16# and 23#, and the total length of fibers is 13500 m. It is generally buried from the upstream or downstream surface to the middle of the concrete blocks, and straight-line layout scheme is usually adopted (Zhou et al. 2017). In the Baihetan arch dam, the optical fibers are embedded in 5 dam monoliths to acquire the concrete temperature and three types of layout schemes on the horizontal surface are applied, including "I", "L", and "Z" shape from upstream surface to downstream surface (Zhou et al. 2019). In the Qianping reservoir, the optical fibers are mainly used to control the temperature cracking of the intake tower. The total length of the mentioned optical fibers is about 4,000 m (Ouyang et al. 2019).

3) infrared thermal imagers for concrete surface temperature measurement. Infrared thermal imaging nondestructive testing technology is usually adopted to obtain the temperature of concrete surface. Based on the surface temperature of concrete piers measured by infrared thermal imagers at different time, Gong et al.(2012) and Chen et al.(2012) acquire the temperature distribution of the concrete structure and calculate the thermal deformation. Chen et al.(2013) obtain the temperature difference of asphalt concrete pavement between the non-manhole position and the manhole position by infrared thermal imagers to facilitate the construction compaction and quality control. Song (2016) monitors the temperature change of the concrete surface by infrared thermal imagers to determine the location and scope of the concrete defect. Zhao et al.(2014) make use of the infrared thermal imagers to monitor the temperature of LNG concrete storage tank and find the fault structure of LNG storage tank according to the thermal field change.

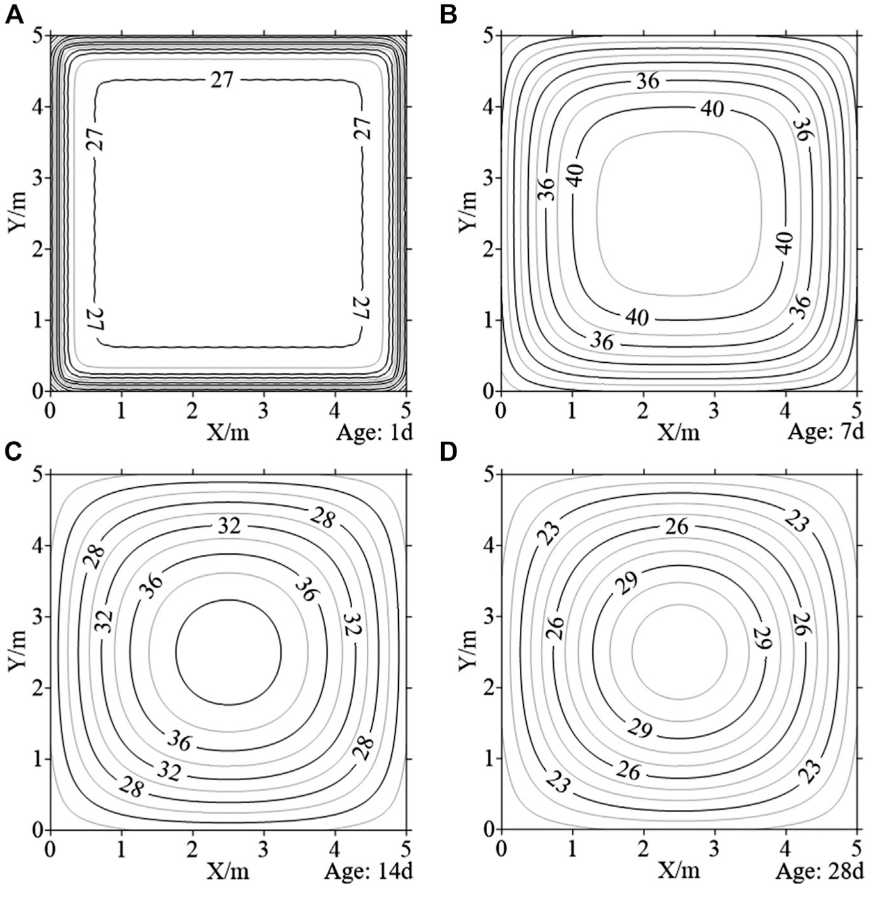

FIGURE 3 | The simulated thermal field of the concrete block: **(A)** 1 day; **(B)** 7 days; **(C)** 14 days; **(D)** 28 days.

Although thermometers and optical fibers have been widely used in concrete dams for temperature monitoring for a long time (Pei et al. 2014), the embedding method and the quantity of thermometers or optical fibers mainly rely on empirical design. Generally, thermometers or optical fibers are embedded in the representative elevation of a typical dam monolith. Moreover, although the infrared thermal imaging nondestructive testing technology has many advantages, such as fast measurement speed, large observation area, non-contact, and high measurement accuracy (Shepard and Steven 1997), this technology has not been widely used in hydropower projects. Therefore, a reasonable design method for the number and positioning of temperature sensors in concrete dams is necessary (Huang et al. 2019). However, this problem is rarely reported in the related literatures. In this study, based on the principle of the cross-validation method, a positioning method of temperature sensors (PMTS) is developed to achieve a scientific and reasonable layout of concrete temperature sensors. Combined with the temperature data measured by the thermometers, optical fibers and infrared thermal imagers in the arch dam, the thermal field of low-heat cement concrete is obtained and analyzed. Finally, the cons and pros, and improvement of the PMTS are further discussed.

POSITIONING METHOD OF TEMPERATURE SENSORS (PMTS)

The Principle of the PMTS

The global thermal field of a concrete dam refers to the real temperature distribution in the entire three-dimensional (3D) space. In order to obtain the global thermal field, the temperature sensors should be embedded reasonably in the dam concrete, including the reasonable quantity and position of the sensors. Excessive temperature sensors would increase unnecessary economic costs, and add a lot of trouble during construction. Few temperature sensors cannot comprehensively monitor the temperature of the dam concrete. When the number of temperature sensors is appropriate, the global thermal field cannot be accurately obtained if the arrangement is unreasonable. Therefore, the principle of the PMTS is proposed to accurately reflect the concrete temperature and get the best economic benefits. Details are as follows:

(1) Considering the economy and technical feasibility, the number of temperature sensors should be as minimal as possible. Generally, about 2–4 thermometers are installed in each concrete block, and the distributed optical fibers are

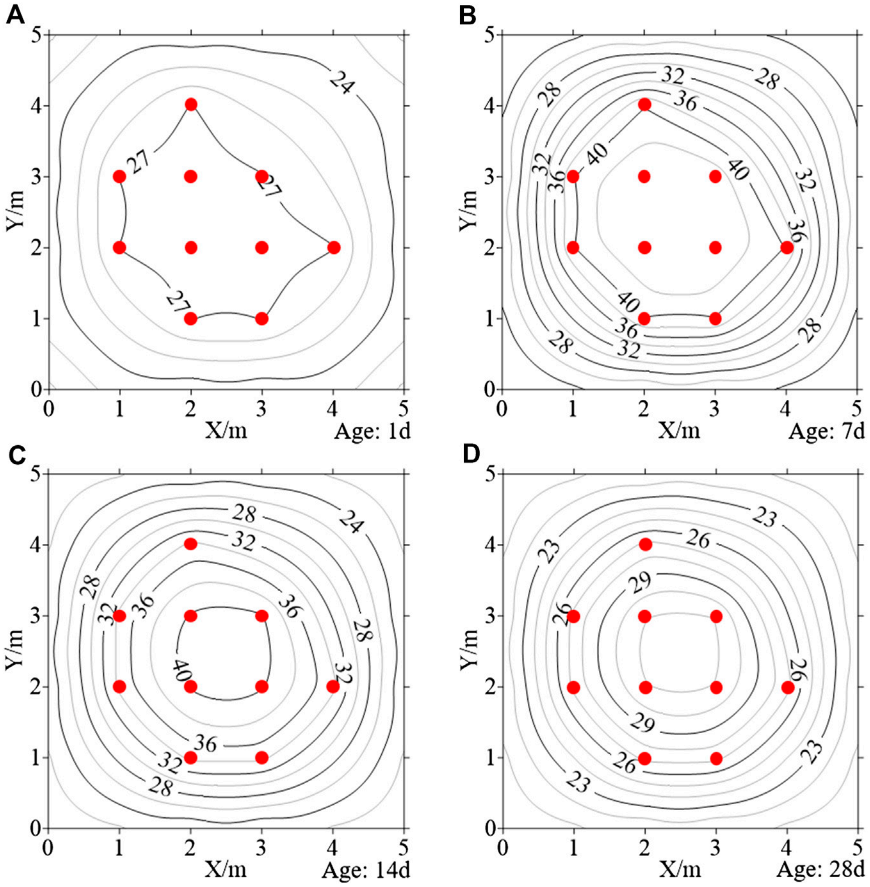

FIGURE 4 | The restructured thermal field of the concrete block based on m = 10: **(A)** 1 day; **(B)** 7 days; **(C)** 14 days; **(D)** 28 days (the red points represent temperature sensors).

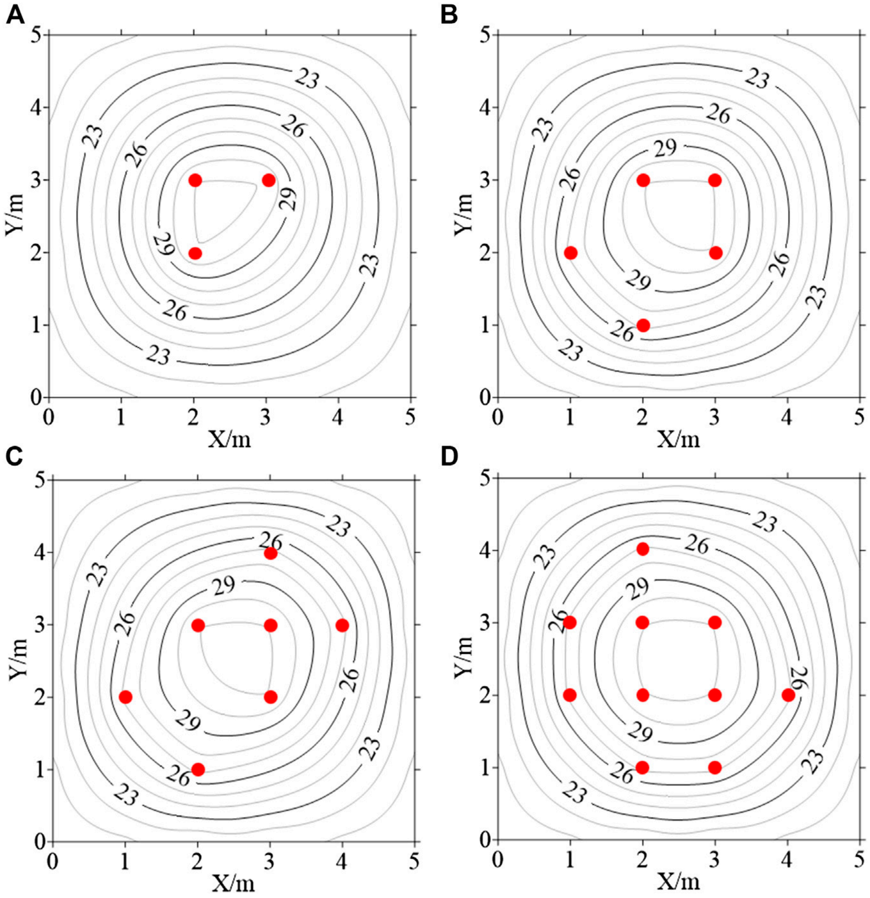

FIGURE 5 | The restructured thermal field of the concrete block: **(A)** *m* = 3; **(B)** *m* = 5; **(C)** *m* = 7; **(D)** *m* = 10 (the red points represent temperature sensors).

embedded in 2–3 dam monoliths of the riverbed and bank slope dam monolith. 2 to 3 infrared thermal imagers are installed to monitor the dam surface temperature.

(2) The embedded position should be reasonable, which can reflect the real concrete thermal field. When the number of sensors is limited, the position must be optimized in order to obtain a more accurate thermal field.

(3) The temperature sensors must have sufficient temperature measurement accuracy to represent the real temperature. Generally, the temperature measurement accuracy of the

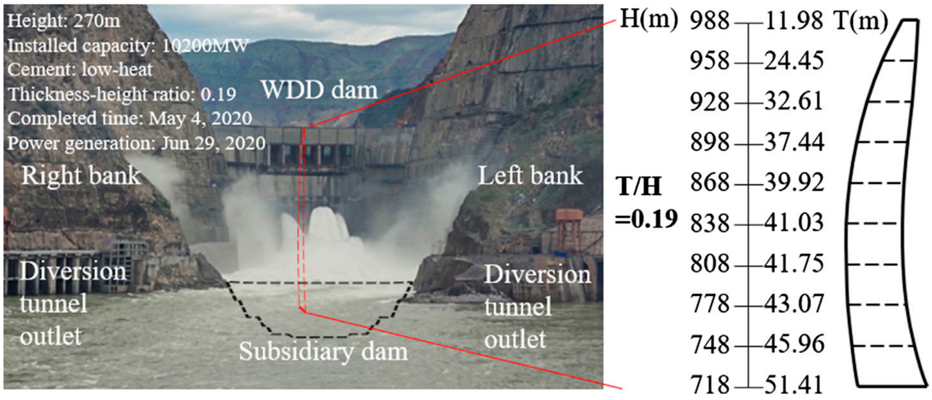

FIGURE 6 | General view of the super-high arch dam.

thermometers, distributed optical fibers and infrared thermal imagers is 0.3°C, 1°C, 1°C–2°C, respectively.

Algorithm Implementation

The positioning steps of the temperature sensors are shown in **Figure 1**. The specific details are as follows:

First, assuming that the coordinates of a dam block vertex are $(x_i,\ y_i,\ z_i)$, $i = 1, 2, 3, \ldots\ldots, n$. Based on the thermodynamic parameters and boundary conditions of the concrete block, the concrete thermal field is simulated, and the temperature of each point inside the concrete is obtained. Then, m points $(x_h,\ y_h,\ z_h)$ $h = 1, 2, 3, \ldots\ldots, m$, are randomly selected inside the dam block. The initial temperature value T_h acquired from the simulation thermal field is assigned to the m points. Therefore, the information of known temperature points $(x_h,\ y_h,\ z_h,\ T_h)$ are obtained. Based on the temperature data of the m points, the natural neighbor interpolation algorithm is used to restructure the thermal field of the dam block. Then, the accuracy of the restructured thermal field by the cross-validation method is judged (**Figure 2**). The details are as follows:

The one deleted point from the initial m temperature points is recorded as $(x_j,\ y_j,\ z_j)$. The other temperature points remain unchanged, and the remaining $(m-1)$ temperature points are used for interpolating the thermal field of the dam block. The

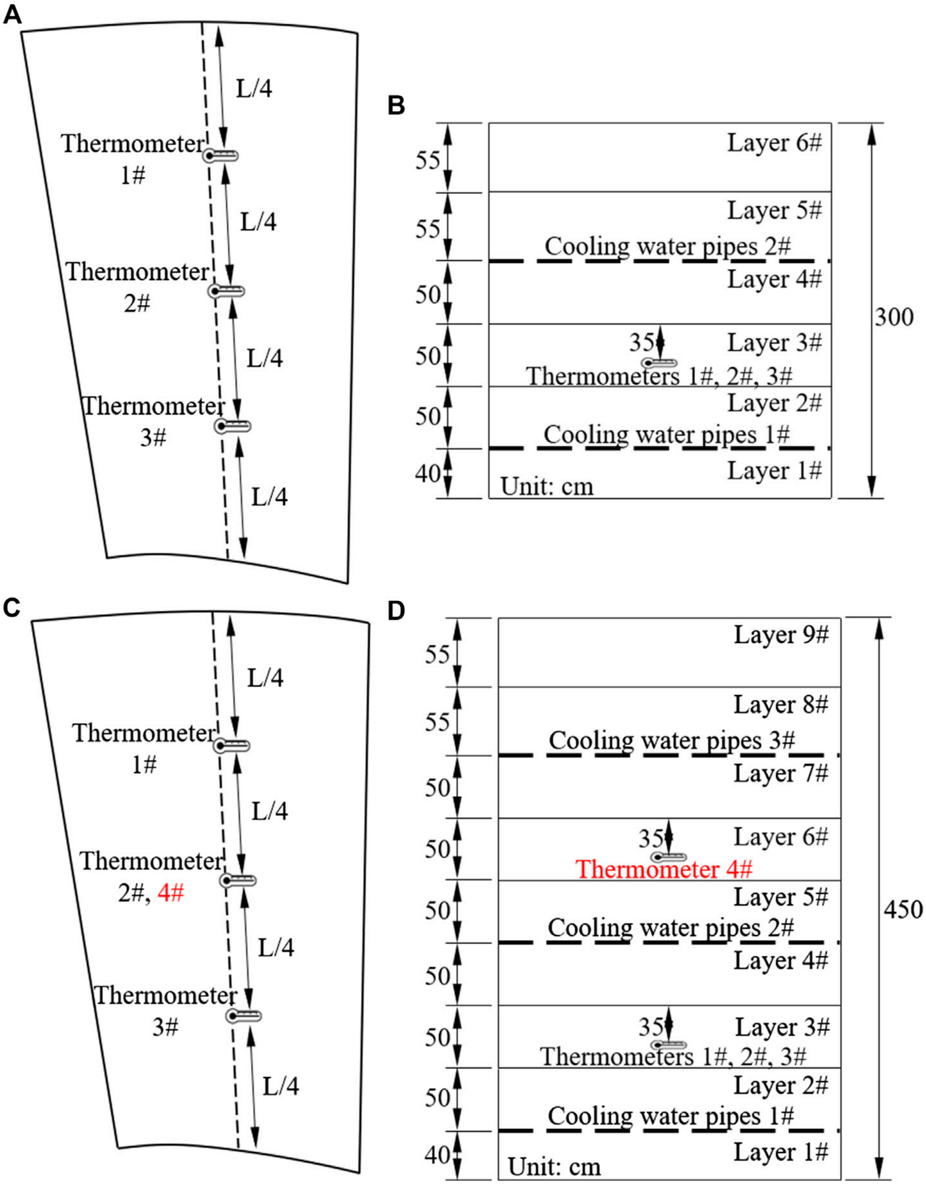

FIGURE 7 | Position of thermometers in concrete blocks below EL910m: **(A)** in horizontal direction (3 m); **(B)** in vertical direction (3 m); **(C)** in horizontal direction (4.5 m); **(D)** in vertical direction (4.5 m).

restructured temperature value T_j^* at (x_j, y_j, z_j) is then compared with the initial value T_j. The absolute difference between them are shown in **Eq. (1)**:

$$\Delta T_j = \left| T_j^* - T_j \right| \tag{1}$$

Next, another point is deleted from the initial temperature points, and the thermal field is restructured by the remaining temperature points. The restructured temperature value is compared with the initial temperature value of this point, and this step is repeated until all temperature points have been compared once. Finally, m absolute difference values ΔT_j are obtained. The average difference is shown in **Eq. (2)**:

$$\overline{\Delta T_j} = \frac{1}{m}\sum_{1}^{m} \Delta T_j \tag{2}$$

The smaller $\overline{\Delta T_j}$ is, the more accurate and reasonable the restructured thermal field is. The number of initial temperature points m and the position of the temperature measurement points (x_h, y_h, z_h) $h = 1, 2, 3, \ldots\ldots, m$, are constantly adjusted to obtain the $\overline{\Delta T_{jMin}}$ in **Eq. (3)**:

$$\overline{\Delta T_{jMin}} = Min\left\{\overline{\Delta T_{j1}}, \overline{\Delta T_{j2}}, \overline{\Delta T_{j3}}, \ldots\ldots, \overline{\Delta T_{jm}}\right\} \tag{3}$$

The number and the position of temperature points related to the $\overline{\Delta T_{jMin}}$ are optimal. Finally, the position of the temperature measurement points constitutes the layout route of the optical

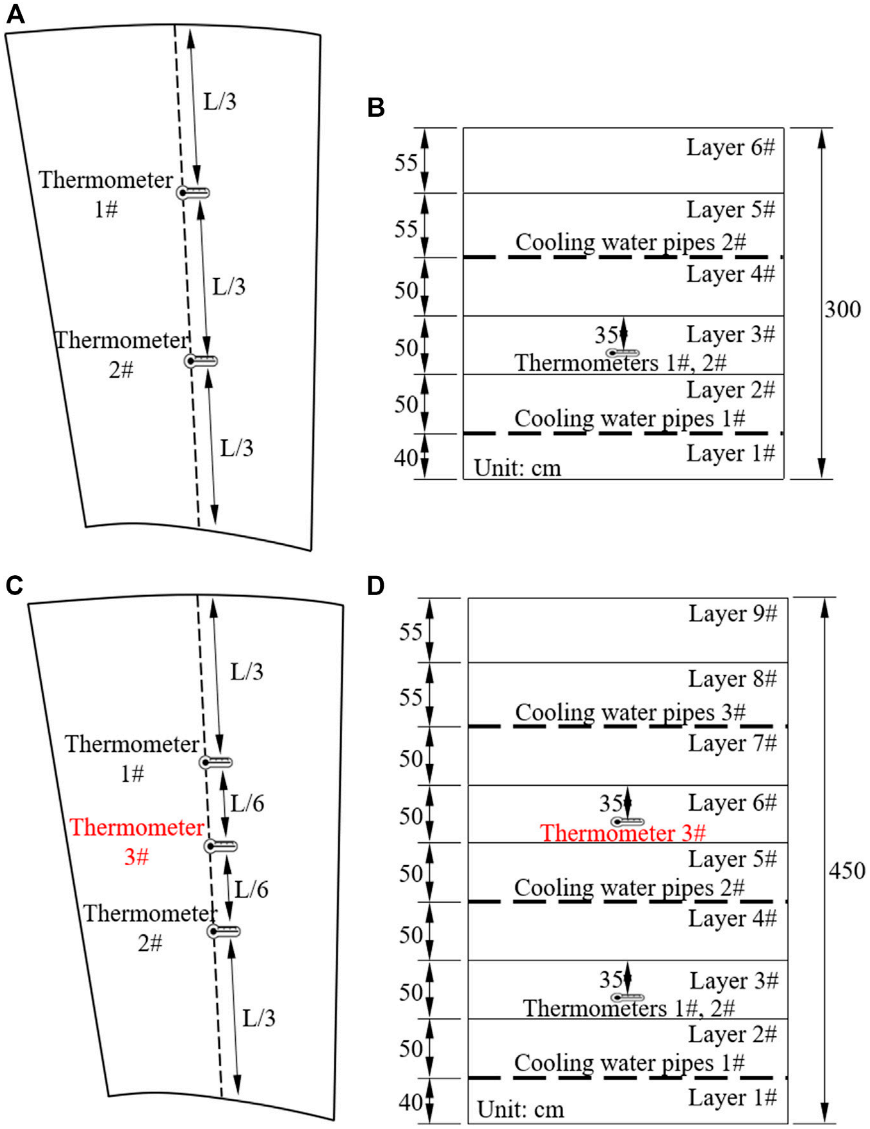

FIGURE 8 | Position of thermometers in concrete blocks above EL910m: **(A)** in horizontal direction (3 m); **(B)** in vertical direction (3 m); **(C)** in horizontal direction (4.5 m); **(D)** in vertical direction (4.5 m).

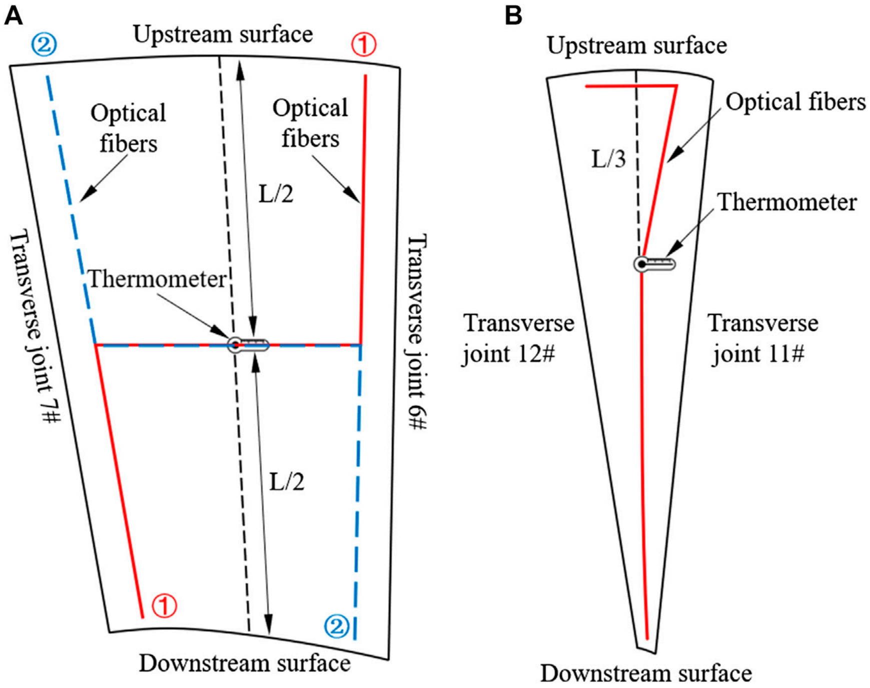

FIGURE 9 | Layout scheme of distributed optical fibers: **(A)** in quadrilateral concrete blocks; **(B)** in triangular concrete blocks.

fibers, that is, the line temperature measurement arrangement is obtained from the point temperature measurement arrangement. The surface temperature measurement is mainly based on the infrared temperature measurement to monitor the temperature of the dam upstream and downstream surfaces.

Calibration of the PMTS

In order to further illustrate the implementation of the PMTS, a square concrete block is selected. This block size and its mesh size are assumed to be 5 m × 5 m and 1 m × 1 m, respectively. First, the concrete block thermal field is simulated according to the thermodynamic parameters of concrete (**Figure 3**). In this case, the concrete thermal conductivity is $\lambda = 7980\, J/(m \cdot h \cdot ℃)$; the concrete specific heat is $c = 1008.6\, J/(kg \cdot ℃)$; the concrete density is $\rho = 2400 kg/m^3$; the convective heat transfer coefficient $\beta = 13\, w/(m^2 \cdot h)$; the coefficient of thermal expansion of concrete is $\alpha = 8 \times 10^{-6}/℃$; the concrete pouring temperature and ambient temperature are assumed to be 20°C; an exponential expression of the adiabatic temperature rise of concrete is shown in **Eq. (4)**:

$$\theta(\tau) = 25\left[1 - \exp\{-0.45(\tau - \tau_0)\}\right] \tag{4}$$

where $\theta(\tau)$ is temperature rise at age of τ; τ is the age of concrete.

The simulated thermal field of the concrete is selected as the initial temperature. Assuming the temperature measurement points $m = 10$, the final optimized position of temperature points is obtained based on the positioning optimization algorithm in *Algorithm Implementation*. According to the position and temperature of the measurement points, the thermal field is restructured at the age of 1, 7, 14, and 28 days, respectively (**Figure 4**). By comparing the restructured thermal field and initial temperature, it can be found that the thermal field distribution law is the same as the simulated field. It is illustrated that with a certain number of the temperature measuring points, the restructured thermal field can reflect the actual concrete temperature distribution based on the PMTS by optimizing the position.

Comparing different temperature measurement points m = 3, 5, 7 and 10, it can be seen that the more temperature monitoring points are arranged, the closer the restructured thermal field is to the initial thermal field (**Figure 5**). However, the number of temperature measurement points should be reasonable and appropriate considering the economic costs and construction interference in actual projects. Therefore, it is particularly important to optimize the position of temperature measurement points. In addition, the construction conditions of the concrete dam are complex, and the temperature sensors are greatly affected by the external factors, such as the influence of the cooling water pipe. In order to avoid the influence of cooling water on the temperature, the temperature sensors are usually as far away as possible from the water pipes. Hence, the layout of temperature monitoring sensors is more complicated in the engineering.

ENGINEERING APPLICATION IN A SUPER-HIGH ARCH DAM

A super-high arch dam studied in this paper is a double-curved concrete dam with a height of 270 m and a thickness-height ratio of 0.19 (**Figure 6**), which is the thinnest 300 m level arch dam in the world. The dam crest elevation is 988 m, and the dam concrete volume is 27 million m3. The whole dam is constructed by low-heat cement concrete, which is the first time in the dam construction history. The dam is located at dry and hot valley. The climate is hot and rainy in summer, dry and windy in winter, and large temperature difference about 14°C during day and night. Hence, it is very difficult to control the arch dam concrete temperature.

Necessity and Challenges of Temperature Monitoring

(1) The thinnest 300 m level arch dam

The thinner the arch dam, the more sensitive it is to air and water temperature, and the greater the temperature change in the dam concrete. For the temperature load, the early calculation is mainly based on the US Bureau of Reclamation's empirical formula (Creager et al., 1945), which is shown in **Eq. (5)**:

$$T_m = 57.57/(L + 2.44) \tag{5}$$

where T_m is the average temperature of the dam cross section (°C), L is the dam thickness (m).

In 1970s, the dam temperature $T(x)$ is decomposed into three parts (Zhu 1999): the average temperature T_m along the thickness direction, equivalent temperature difference T_d, and nonlinear temperature difference T_n, which are shown in **Eq. (6)**:

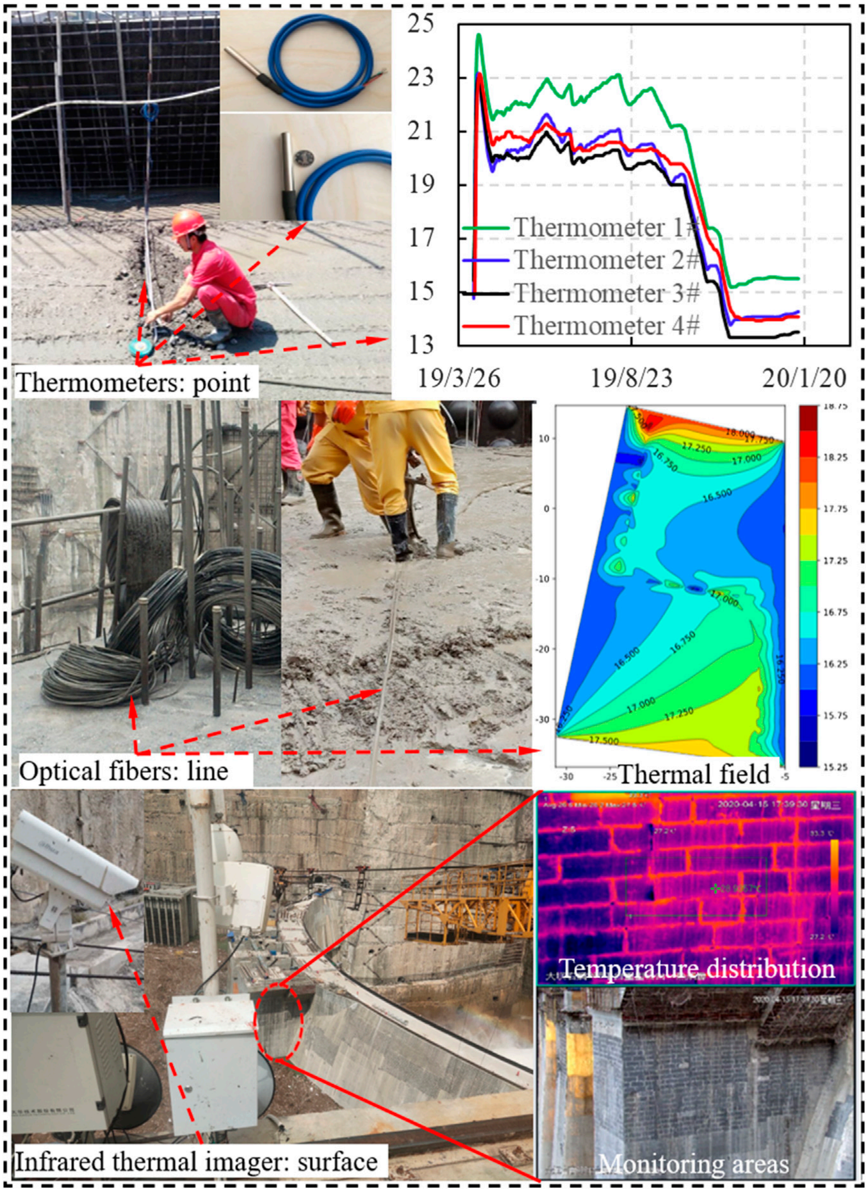

FIGURE 10 | Layout of thermometers, distributed optical fibers and infrared thermal imagers in the super-high arch dam.

$$\begin{cases} \Delta T_m = \dfrac{1}{L}\displaystyle\int_{-L/2}^{L/2} T(x)dx \\ \Delta T_d = \dfrac{12}{L^2}\displaystyle\int_{-L/2}^{L/2} T(x)xdx \\ \Delta T_n = T(x) - T_m - T_d x/L \end{cases} \tag{6}$$

Since the T_n does not affect the displacement and internal force calculation of the dam, only T_m and T_d are usually considered in arch dam design. It can be seen from the **Eqs. (5)** and **(6)** that the thinner the arch dam, the greater the corresponding temperature load.

Except the free boundary at the dam crest, the other three boundaries of the arch dam are constrained by the bedrock, and the temperature deformation is constrained greatly. Therefore, the greater the temperature change of the dam, the greater the thermal stress. As the world's thinnest 300 m level super-high arch dam, the temperature control is particularly significant. Reliable and accurate temperature monitoring is a prerequisite to ensure effective temperature control of the dam concrete.

(2) The whole dam constructed by low-heat cement concrete for the first time

Low-heat cement has the characteristics of slow hydration rate, low hydration heat, high strength in the later period and great durability (Wang et al. 2018). It can effectively improve the crack resistance ability of hydraulic mass concrete and reduce the risk of concrete cracking. The super-high arch dam uses low-heat cement for the construction of the entire dam, which has no precedent in arch dam construction history. The engineering level of this dam is high. The quality of low-heat cement and the construction method are all different from other dams. In addition, the law of low-heat cement hydration and concrete temperature distribution are unclear. In order to obtain the temperature change law of the arch dam concrete, thermometers are embedded in all concrete blocks and the distributed optical fibers are buried in dam monoliths 7# and 12#. Moreover, the infrared thermal imagers are installed on the upstream surface and the right bank abutment platform for temperature monitoring. On this basis, the dam concrete temperature control measures can be optimized and adjusted.

Layout of Temperature Sensors

Based on the optimization principle of the PMTS, the real 3D spatial thermal field of the super-high arch dam studied in this paper is realized by thermometers, distributed optical fibers and infrared thermal imagers.

1) the position of thermometers

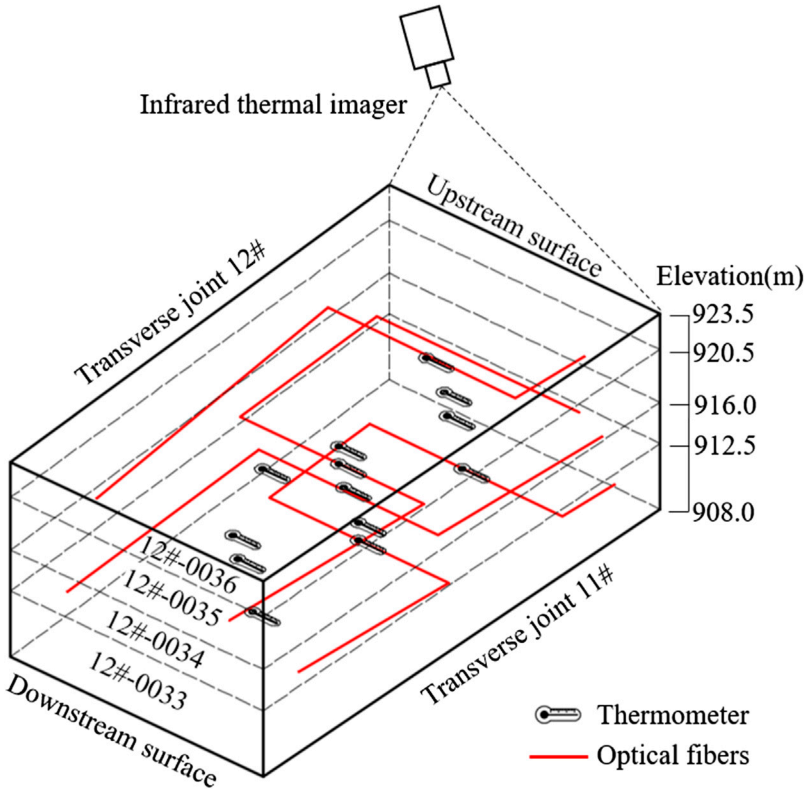

FIGURE 11 | The arrangement of thermometers, distributed optical fibers and infrared thermal imagers in the concrete blocks 12#-0033, 0034, 0035, 0036.

In the arch dam, thermometers are embedded in each concrete block to monitor the concrete temperature. The number and position of thermometers buried in the dam concrete during construction are as follows:

When the elevation of concrete blocks is below EL910 m, 3 and 4 thermometers are embedded in the 3 m and 4.5 m pouring blocks, respectively. When the thickness of concrete blocks is 3 m, thermometers should be arranged in each of the upstream, middle and downstream areas (about 1/4 length of the concrete blocks along the water flow direction) between the two layers of cooling water pipes (**Figures 7A,B**). When the thickness of concrete blocks is 4.5 m, thermometers should be arranged in each of the upstream, middle and downstream areas between the first and second layers of cooling water pipes. There is also a thermometer embedded in the middle area between the second and third layers of cooling water pipes (**Figures 7C,D**).

When the elevation of concrete blocks is above EL910 m, 2 and 3 thermometers are embedded in the 3 m and 4.5 m pouring blocks, respectively. When the thickness of concrete blocks is 3 m, thermometers should be arranged in each of the upstream and downstream areas (about 1/3 length of the concrete blocks along the water flow direction) between the two layers of cooling water pipes (**Figures 8A,B**). When the thickness of concrete blocks is 4.5 m, thermometers should be arranged in each of the upstream, and downstream areas between the first and second layers of cooling water pipes. There is also a thermometer embedded in the middle area between the second and third layers of cooling water pipes (**Figures 8C,D**).

2) the layout of distributed optical fibers

The concrete blocks of the arch dam have two shapes. One is a quadrilateral block, mainly located at the riverbed dam monoliths and the high elevation of bank slope dam monoliths. The other is a triangular block, mainly located at the low elevation of the bank slope dam monoliths.

For quadrilateral concrete blocks, optical fibers are arranged as a "Z" shape and embedded in the same layer with the thermometers. Taking the dam monolith 7# of the arch dam as an example, Z-shaped optical fibers are embedded in two forms (**Figure 9A**), the first of which (①-①) is as follows: the embedded starting point is 1 m and 3 m away from the upstream surface and the transverse joint 6#, respectively. Then, the optical fibers are buried along the water flow direction and turned at the thermometer in the middle of the concrete block. Next, the optical fibers are embedded along the direction transverse to the water flow direction until they are 3 m away from the transverse joint 7#. Finally, the optical fibers are embedded along the water flow direction again and end at

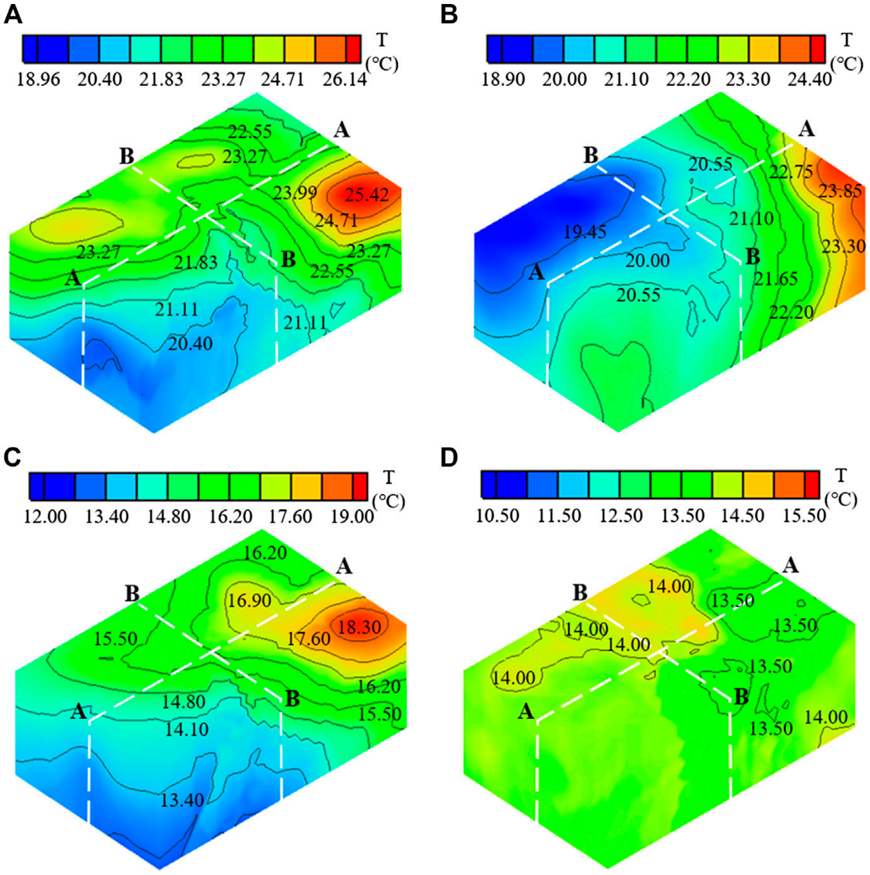

FIGURE 12 | The 3D thermal field in the concrete blocks 12#-0033, 0034, 0035 and 0036: **(A)** May 1, 2019; **(B)** Aug 1, 2019; **(C)** Nov 1, 2019; **(D)** Jan 1, 2020.

the point 1 m away from the downstream surface. The second (②-②) and the first embedded forms are symmetric about the center line of the concrete block. When the two embedded forms alternate along the vertical direction, the optical fibers can be coupled with each other to obtain a more accurate and real thermal field.

For the triangular concrete blocks, due to the short length along the direction transverse to the water flow direction, the optical fibers are embedded as a "7" shape. Taking the dam monolith 12# of the arch dam as an example, the embedded starting point of optical fibers is 1 m and 3 m away from the upstream surface and the transverse joint 12#, respectively. Then, the optical fibers are buried along the direction transverse to the water flow direction, turned to the thermometer in the upstream area of the concrete block. Finally, the optical fibers are embedded along the center line of the concrete block and end at the point 1 m away from the downstream surface (**Figure 9B**).

3) the layout of infrared thermal imagers

The infrared thermal imaging nondestructive testing technology is an indirect temperature measurement and has great advantages, which can overcome the complex environmental influence, e.g. strong wind, fog, high temperature, etc. Moreover, the longest monitoring distance can be up to approximately 300 m, and the temperature accuracy can reach 1°C–2°C. According to the infrared thermal radiation characteristics of the object, an infrared thermal imager is used to receive the thermal radiation of the concrete surface. Considering the monitoring range of the infrared thermal imager, two infrared thermal imagers are installed on the upstream surface and the right bank abutment platform to monitor the surface temperature of the studied super-high arch dam, respectively. The thermometers, optical fibers and infrared thermal imagers installed in the studied super-high arch dam are shown in **Figure 10**.

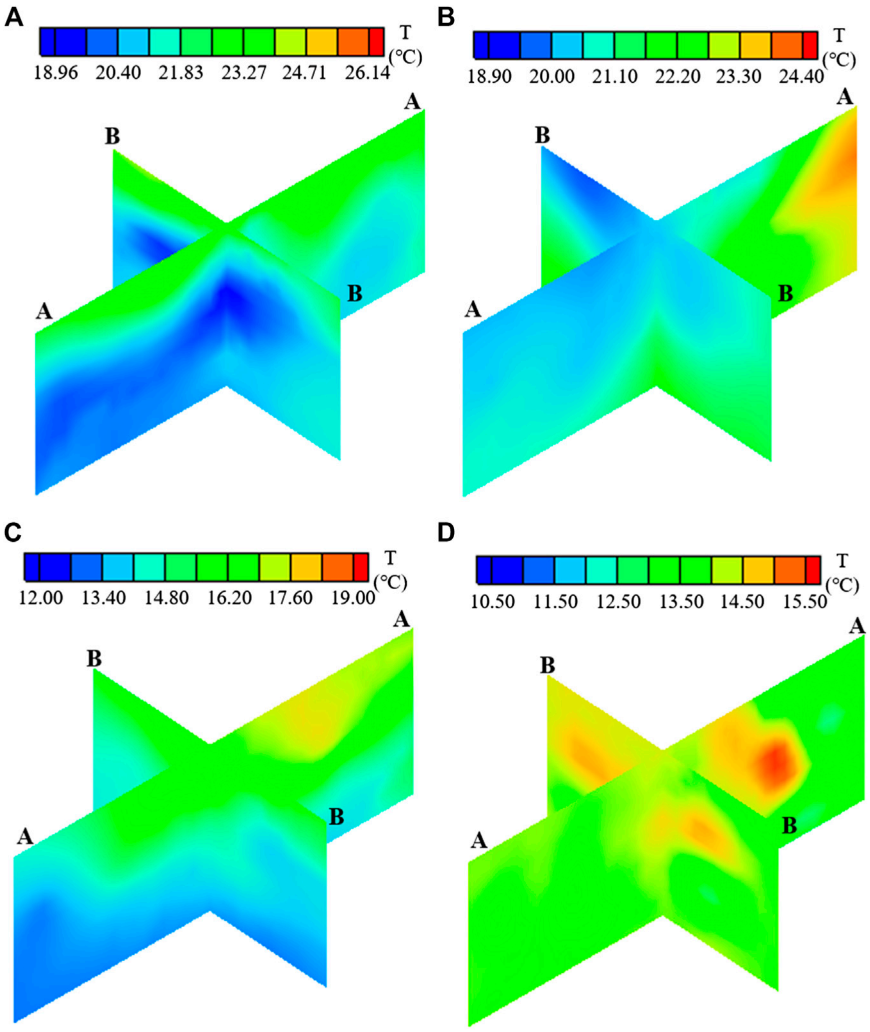

FIGURE 13 | The thermal field in section A-A and B-B in the concrete blocks 12#-0033, 0034, 0035 and 0036: **(A)** May 1, 2019; **(B)** Aug 1, 2019; **(C)** Nov 1, 2019; **(D)** Jan 1, 2020.

Global Thermal Field Realization

According to the temperature measured by thermometers, distributed optical fibers and infrared thermal imagers, the real 3D spatial thermal field is obtained. Illustrated by the example of concrete blocks 12#-0033, 0034, 0035, 0036 (**Figure 11**), the concrete thermal field is restructured on May 1, Aug 1, Nov 1, 2019 and Jan 1, 2020. The restructured 3D thermal fields of different time are shown in **Figures 12**,**13**.

As can be seen from **Figures 12A**,**13A**, on May 1, 2019, the temperature of concrete blocks at the high elevation is higher than that of the concrete blocks at the low elevation. The main reasons are the late pouring time of the high elevation concrete blocks, the great cement hydration heat and the less heat exchange between cooling water and concrete. The concrete temperature of the downstream area is lower than that of the upstream area along the water flow direction. The higher the concrete blocks elevation, the greater the temperature difference between the upstream and downstream area. The temperature difference of the high elevation concrete blocks is about 3°C, whereas the temperature difference of the low elevation concrete blocks is less than 1.5°C.

According to the **Figures 12B**,**13B**, with the increase of concrete age, the concrete temperature decreases due to water cooling and heat dissipation. On Aug 1, 2019, the maximum temperature of concrete blocks 12#-0033, 0034, 0035, 0036 dropped by about 1.6°C compared with that on May 1, 2019. The concrete temperature of the downstream area is lower than that of the upstream area along the water flow direction. For instance, the temperature difference between the upstream and downstream area of the concrete block 12-0036 is about 4.4°C.

t can be seen from **Figures 12C**,**13C** that the maximum concrete temperature on Nov 1, 2019 decreased by about 5.4°C compared with that on Aug 1, 2019. The main reason is that the concrete blocks 12#-0033, 0034, 0035, 0036 are in the initial temperature control stage and the concrete temperature should be controlled at about 22°C–24°C on Aug 1, 2019. However, the concrete blocks 12#-0035, 0036 are in the intermediate temperature control stage and the concrete temperature should be controlled at about 18°C–20°C on Nov 1, 2019. The concrete blocks 12#-0033, 0034 are in the late temperature control stage and the concrete temperature should be controlled at 14°C on Nov 1, 2019. Hence, the temperature decrease is large during this period.

As shown in **Figures 12D**,**13D**, the maximum concrete temperature on Jan 1, 2020 decreased by about 3.5°C compared with that on Nov 1, 2019. The 3D concrete thermal field tends to be uniform, and most of the temperature is approximately 13.5°C–14°C. According to the design standard of the studied super-high arch dam, the concrete blocks 12#-0033, 0034, 0035, 0036 should be in the late temperature control stage on Jan 1, 2020. In order to satisfy the requirement of transverse joints grouting, the temperature should be controlled at about 14°C. It can be seen that the space-time distribution law of the restructured thermal field is consistent with the actual situation of the super-high arch dam.

DISCUSSION

Compared with the method of determining the position of temperature sensors empirically, the PMTS proposed in this study, which can obtain the thermal field of concrete dams more efficiently and provide method support for the arrangement of temperature sensors, is more reasonable and reliable. However, the PMTS may be affected by the complex construction and economic conditions in engineering application. When the thermometers, optical fibers and infrared thermal imagers are arranged mutually, the construction interference is usually large, which reduces the survival rate of the sensors. Moreover, concrete is a relatively complex material and multiple temperature control measures may be applied simultaneously during construction, which result in a particularly complex temperature change and bring great challenges to temperature monitoring.

Under such complex conditions, the PMTS proposed in this paper has been successfully applied to the construction of a super-high arch dam, which provides a basis for the temperature control measures. Up to now, the studied super-high arch dam has not produced a single temperature crack during construction and impounding period. In the PMTS method, the natural neighbor interpolation algorithm and cross-validation are used in this study to restructure the thermal field and verify the accuracy of the restructured thermal field, respectively. However, there are many methods for restructuring and verifying the thermal field. For instance, the restructuring methods of the thermal field include kriging and inverse distance weighting interpolation algorithm. The verification methods can utilize average error or root mean square error methods. Therefore, two key points of the PMTS will be further studied in future research, that is the thermal field restructuring method and the accuracy verification method of restructured thermal field, in order to facilitate the wide engineering application of the PMTS.

CONCLUSIONS

A positioning method of temperature sensors is developed to determine the arrangement of temperature sensors in concrete dams scientifically and quantitatively. The proposed method is then applied to the arrangement of thermometers, distributed optical fibers and infrared thermal imagers in a super-high arch dam for real-time measurement of concrete temperature. According to this study, several conclusions are as follows:

(1) The proposed PMTS based on the natural neighbor interpolation algorithm and the cross-validation is reasonable and reliable, which is illustrated by the accurate acquisition of the super-high arch dam thermal field based on point, line, surface temperature measurement.
(2) The temperature change of the studied super-high arch dam is consistent with the design temperature control process, which indicates that the dam has achieved precise control of concrete temperature.

(3) The PMTS may be affected by the complex engineering site. Therefore, future studies will focus on the application of the PMTS considering construction interference and the integration of the advantages of other thermal field restructuring methods and the accuracy verification methods.

DATA AVAILABILITY STATEMENT

The original contributions presented in the study are included in the article, further inquiries can be directed to the corresponding author.

AUTHOR CONTRIBUTIONS

HP: methodology, and writing original draft. PL, and YX: supervision and writing original draft. WC: algorithm implementation. SZ, NY, and YQ: review and editing. All authors contributed to the final version of the manuscript.

FUNDING

This research work was supported by the National Natural Science Foundation of China (Grant No: 51979146), and the China Three Gorges Corporation Research Program (WDD/0490, BHT/0805).

REFERENCES

Bao, H., Cai, D., Tang, T., and Xu, S. (2006). Design of optical fiber senor network for temperature monitoring and research on its embedded technology in the RCC dam. *Water Power* 32 (2), 26–29. doi:10.3969/j.issn.0559-9342.2006.02.009

Belmokre, A., Mihoubi, M. K., and Santillán, D. (2019). Analysis of dam behavior by statistical models: application of the random forest approach. *KSCE J. Civ. Eng* 23 (2), 4800–4811. doi:10.1007/s12205-019-0339-0

Chen, B., Li, X. J., Pan, H. M., and Zheng, J. (2012). Solar radiation-induced temperature variation of concrete bridge piers. *Appl. Mech. Mater.*, 178–181, 2451–2455. doi:10.4028/www.scientific.net/AMM.178-181.2451

Chen, L. Y., Wang, M. Y., Lin, D. F., and Trsi, S. R. (2013). Assessing the quality of asphalt concrete pavement at special location with infrared thermal imager. *Adv. Mater. Res.* 723, 35–40. doi:10.4028/www.scientific.net/AMR

Creager, W. P., Justin, J. D., and Hinds, J. (1945). *Engineering for dams*. New York, NY: John Wiley & Sons, Inc., 425–558.

Fan, Q., Li, W., Li, X., Chen, G., and Yang, H. (2016). Application of low heat Portland cement concrete in Hoover Dam and its revelation. *Water Power* 42 (12), 46–49+59. doi:10.3969/j.issn.0559-9342.2016.12.012

Gong, P. S., Chen, B., Song, C. F., and Li, X. L. (2012). Assessment on the thermal stresses of concrete bridge piers under solar radiation. *Appl. Mech. Mater.* 204–208, 2045–2050. doi:10.4028/www.scientific.net/AMM.204-208.2045

Huang, Y., Xie, T., Li, C., and Yin, X. (2019). Optimization analysis of the position of thermometers buried in concrete pouring block embedded with cooling pipes. *Math. Probl. Eng.* 2019, 1–13. doi:10.1155/2019/5256839

Jaafar, M. S., Bayagoob, K. H., Noorzaei, J., and Thanoon, W. A. M. (2007). Development of finite element computer code for thermal analysis of roller compacted concrete dams. *Adv. Eng. Softw.* 38 (11–12), 886–895. doi:10.1016/j.advengsoft.2006.08.040

Jiang, J., and Guo, F. (2008). Application discussion on distributed optical fiber temperature measurement in Guangzhao RCC dam. *Water Power* 34 (3), 55–58. doi:10.3969/j.issn.0559-9342.2008.03.017

Lin, P., Guan, J., Peng, H., and Shi, J. (2019). Horizontal cracking and crack repair analysis of a super high arch dam based on fracture toughness. *Eng. Fail. Anal.* 97, 72–90. doi:10.1016/j.engfailanal.2019.01.036

Lin, P., Li, Q., and Hu, H. (2012). A flexible network structure for temperature monitoring of a super high arch dam. *Int. J. Distributed Sens. Netw.* 2012 (4), 1238–1241. doi:10.1155/2012/917849

Lin, P., Li, Q., and Jia, P. (2014). A real-time temperature data transmission approach for intelligent cooling control of mass concrete. *Math. Probl. Eng.* 2014, 1–10. doi:10.1155/2014/514606

Lin, P., Wei, P., Wang, W., and Huang, H. (2018). Cracking risk and overall stability analysis of xulong high arch dam: a case study. *Appl. Sci.* 8 (12), 2555. doi:10.3390/app8122555

Lin, P., Zhou, W., and Liu, H. (2015). Experimental study on cracking, reinforcement, and overall stability of the xiaowan super-high arch dam. *Rock Mech. Rock Eng.* 48 (2), 819–841. doi:10.1007/s00603-014-0593-x

Mata, J., de Castro, A. T., and Costa, J. S. D. (2014). Constructing statistical models for arch dam deformation. *Struct. Control Hlth.* 21 (3), 1–15. doi:10.1002/stc.1575

Mirzabozorg, H., Ghaemian, M., and Roohezamin, A. (2019). The reason of cracking in bottom gallery of SefidRud Buttress Dam and earthquake and post earthquake performance. *Structural Monitoring and Maintenance* 6 (2), 103–124. doi:10.12989/smm.2019.6.2.103

Ouyang, J., Chen, X., Huangfu, Z., Lu, C., Huang, D., and Li, Y. (2019). Application of distributed temperature sensing for cracking control of mass concrete. *Constr. Build. Mater.* 197, 778–791. doi:10.1016/j.conbuildmat.2018.11.221

Pei, H. F., Teng, J., Yin, J. H., and Chen, R. (2014). A review of previous studies on the applications of optical fiber sensors in geotechnical health monitoring. *Measurement* 58 (3), 207–214. doi:10.1016/j.measurement.2014.08.013

Peng, H., Lin, P., Yang, N., Li, M., and Qiao, Y. (2019). Real time thermal field analysis on Wudongde super high arch dam during construction. *Global Energy Interconnection* 2 (3), 264–269. doi:10.1016/j.gloei.2019.07.019

Santillán, D., Salete, E., Vicente, D. J., and Toledo, M. Á. (2014). Treatment of solar radiation by spatial and temporal discretization for modeling the thermal response of arch dams. *J. Eng. Mech.* 140 (11), 05014001. doi:10.1061/(ASCE)EM.1943-7889.0000801

Santillan, D., Saleteb, E., Toledob, M. A., and Granados, A. (2015). An improved 1D-model for computing the thermal behaviour of concrete dams during operation. Comparison with other approaches. *Comput. Concrete* 15 (1), 103–126. doi:10.12989/cac.2015.15.1.103

Schackow, A., Effting, C., Gomes, I. R., Patruni, I. Z., Vicenzi, F., and Kramel, C. (2016). Temperature variation in concrete samples due to cement hydration. *Appl. Therm. Eng.* 103, 1362–1369. doi:10.1016/j.applthermaleng.2016.05.048

Shepard, and Steven, M. (1997). Introduction to active thermography for non-destructive evaluation. *Anti-Corros. Method. M.* 44 (4), 236–239. doi:10.1108/00035599710183199

Shi, L. (2008). Application of temperature measurement technology with optical fiber in jinghong hydropower project. *Water Power* 34 (4), 65–67. doi:10.3969/j.issn.0559-9342.2008.04.021

Song, F. (2016). Experimental study on the quality of concrete strengthened by the means of infrared thermal imager. *Am. J. Civ. Eng.* 4 (2), 55. doi:10.11648/j.ajce.20160402.13

Wang, L., Yang, H. Q., Zhou, S. H., Chen, E., and Tang, S. W. (2018). Mechanical properties, long-term hydration heat, shinkage behavior and crack resistance of dam concrete designed with low heat Portland (LHP) cement and fly ash. *Constr. Build. Mater.* 187, 1073–1091. doi:10.1016/j.conbuildmat.2018.08.056

Zhao, L., Zhang, G. W., Zhang, Q., and Zhang, Y. K. (2014). Multi-point temperature monitoring system for the LNG storage tank. *Appl. Mech.*

Mater. 511–512, 282–285. doi:10.4028/www.scientific.net/AMM.511-512.282

Zhou, H., Pan, Z., Liang, Z., Zhao, C., Zhou, Y., and Wang, F. (2019). Temperature field reconstruction of concrete dams based on distributed optical fiber monitoring data. *KSCE J. Civ. Eng.* 23 (5), 1911–1922. doi:10.1007/s12205-019-0787-6

Zhou, H., Zhou, Y., Zhao, C., Fang, W., and Liang, Z. (2017). Feedback design of temperature control measures for concrete dams based on real-time temperature monitoring and construction process simulation. *KSCE J. Civ. Eng.* 22 (6), 1584–1592. doi:10.1007/s12205-017-1935-5

Zhu, B. (1999). *Temperature stress and temperature control of mass concrete*, China Electric Power Press.

Conflict of Interest: Authors SZ, NY, and YQ are employed by the company China Three Gorges Corporation.

The remaining authors declare that the research was conducted in the absence of any commercial or financial relationships that could be construed as a potential conflict of interest.

frontiers
in Materials

ORIGINAL RESEARCH
published: 28 January 2021
doi: 10.3389/fmats.2020.582635

Prediction of Rubber Fiber Concrete Strength Using Extreme Learning Machine

Jingkui Zhang[1]*, Juncai Xu*[2]**, Changshun Liu*[1] *and Ji Zheng*[1]

[1]Anhui and Huaihe River Institute of Hydraulic Research, Hefei, China, [2]Department of Civil Engineering, Case Western Reserve University, Cleveland, OH, United States

The conventional design method of concrete mix ratio relies on a large number of tests for trial mixing and optimization, and the workload is massive. It is challenging to cope with today's diverse raw materials and the concrete's specific performance to fit modern concrete development. To innovate the design method of concrete mix ratio and effectively use the various complex novel raw materials, the traditional mix ratio test method can be replaced with the intelligent optimization algorithm, and the concrete performance prediction can be realized rapidly and accurately. The mixed ratio of the rubber fiber concrete was designed with its 28-day strength test. Then the range and variance analysis of the orthogonal test results were carried out to determine the optimal mix ratio and its influencing factors. A data set containing 114 sets of valid test data was collected by combining the rubber concrete mix test data published in recent years. Based on this data set, there are six influencing factors; rubber content, rubber particle size, and polypropylene fiber content are considered as the input variables, and the 28-day concrete compression, splitting tensile, and flexural strength are considered as the output variables. A strength prediction model of rubber fiber concrete is established based on the extreme learning machine (ELM). For verifying the ELM prediction model's performance, this article has conducted a comparison experiment between this model and other intelligent algorithm models. The results show that the model has the advantages of high accuracy and high generalization ability compared with other algorithm models such as conventional neural networks. It can be used as an effective method for predicting concrete performance. The method allows for the innovation and development of concrete mixing technology.

Keywords: rubber fiber concrete, mix ratio design, intelligent optimization, concrete strength, extreme learning machine

Edited by:
Bahman Ghiassi,
University of Nottingham,
United Kingdom

Reviewed by:
Warda Ashraf,
University of Texas at Arlington,
United States
Hung-Wei Yen,
National Taiwan University, Taiwan

****Correspondence:***
Juncai Xu
jxx307@case.edu

Specialty section:
This article was submitted to
Structural Materials,
a section of the journal
Frontiers in Materials

Received: *13 July 2020*
Accepted: *10 December 2020*
Published: *28 January 2021*

Citation:
Zhang J, Xu J, Liu C and Zheng J
(2021) Prediction of Rubber Fiber
Concrete Strength Using Extreme
Learning Machine.
Front. Mater. 7:582635.
doi: 10.3389/fmats.2020.582635

INTRODUCTION

With the development and application of green-energy-saving and resource recyclable materials, green and friendly waste rubber fiber concrete, which has excellent physical and mechanical properties, has attracted much attention. Rubber fiber concrete is a kind of engineering composite material made of ordinary concrete as a base material, mixed with waste rubber aggregates and fibers according to a specific ratio. It is solidified and hardened to form a kind of engineering composite material. Rubber fiber concrete has excellent properties such as good toughness, wear-resistance, and frost resistance. Besides, it effectively solves the problem of waste rubber treatment and improves the performance of concrete. So it plays a dual role in resource conservation and environmental protection. Rubber recycled concrete has become a hot topic in the research and development of the concrete industry and contributed to much research (Fang et al., 2001; Topçu and Demir, 2007; Reda Taha et al., 2008; Atahan and Yücel, 2012; Bravo and de Brito, 2012; Richardson et al., 2016). Farhad Aslani et al. prepared a self-compacting rubber fiber concrete. Fibers include polypropylene (PP) fiber and steel fiber, and they studied the influence of different rubber fiber particles' parameters on concrete's mechanical properties (Aslani and Gedeon, 2019). Zahid Hossain et al. studied rubber crumbs (CR), recycled coarse aggregate (RCA) and polypropylene fiber composite concrete, and tested the compressive strength, splitting tensile strength, and bending resistance at different ages (Zahid et al., 2019). Mostafa Jalal et al. prepared high-strength concrete by adding different fine rubber particles and polypropylene fibers. The performance of high-strength concrete (HSC), rubber high-strength concrete (RHSC), polypropylene high-strength concrete (PHSC), and polypropylene rubber high-strength concrete (PRHSC) before and after the high temperature was studied (Jalal et al., 2019a; Jalal et al., 2019b). Jiaqing Wang et al. prepared rubber fiber concrete samples with different rubber volume content and fiber volume fraction and made ordinary concrete samples for comparison. The synergistic effect of polypropylene fiber and rubber concrete was studied in terms of mechanical properties, durability properties, and microstructure (Wang et al., 2019).

Due to low hydrophilicity, the rubber particles have different properties than the concrete particles, and the adhesion between the two kinds of particles is poor. The rubber particles' strength is reduced after the concrete is mixed with the rubber aggregate. The performance of rubber fiber concrete is affected by many factors, and the research on the design of its mix ratio is still developing (Zheng et al., 2008; Skripkiūnas et al., 2009; Richardson et al., 2012). In practical engineering, for the performance of rubber fiber concrete to meet the requirements, a large number of tests are carried out to determine the optimal range of each influencing factor in the design of its mix ratio. This makes the mix ratio design process more complicated. Many workforce and material resources are consumed (Gao, 2018). Although the orthogonal test method has uniform dispersion features in the mix ratio design, it is an efficient and economical test design method. However, it still requires many experiments to get satisfactory results in practical engineering. This situation brings a significant challenge to the mix design. The traditional concrete strength test method is to test the concrete specimens after 28 days of standard curing. Thus, it is difficult to know whether the concrete's strength will meet the design requirements in time for concrete-based construction. If the final test strength of concrete does not meet the design requirements, it will seriously affect the construction period and construction quality. Therefore, how to get the expected 28-day strength of concrete with different mixing ratios in time for construction is a subject worthy of in-depth study. The concrete strength is affected by many factors such as cement strength grade, water-cement ratio, sand ratio, and admixture. There is a complex and highly nonlinear relationship between these influencing factors and concrete strength. So it is difficult to find out the regularity between them by using the traditional regression method. In recent years, the rapid development of machine learning technology has provided a platform for establishing this complicated nonlinear mapping relationship. The application of machine learning technology to establish a prediction model of material performance is a more effective method in improving novel materials development efficiency. It has become a hot international issue (Wu et al., 2019; Li et al., 2020).

In recent years, some scholars have applied machine learning methods such as neural networks (ANN), support vector machines (SVM), deep learning, and gray theory to the prediction of concrete strength. They have even made some valuable achievements (Ni and Wang, 2000; Lim et al., 2004; Topçu and Sarıdemir, 2008; Chou et al., 2014; Xu et al., 2015; Young et al., 2019; Xu and Yu, 2020). Mostafa Jalal et al. used an adaptive neurofuzzy inference system to establish a concrete compressive strength prediction model and studied the influence of cement content, rubber content, silica fume, and sample age on the concrete compressive strength (Jalal et al., 2020). They also used rubber powder and pozzolan to partially replace the aggregate and cement in the concrete raw materials and established three different regression models: linear regression model, logarithmic regression model, and power regression model to predict the compressive strength of concrete (Jalal et al., 2019a; Jalal et al., 2019b). Hesam Madanil et al. tried to use artificial neural methods such as adaptive neurofuzzy inference system (ANFIS), artificial neural network (ANN) technology, and linear and nonlinear regression analysis to predict the compressive strength of cement composite materials and compared the difference of those methods in predicting the strength of the cementitious mixture (Madanil et al., 2020).

However, these methods still have certain limitations. Traditional algorithms such as ANN and SVM are based on the Empirical Risk Minimization (ERM) criterion, which requires a sufficient number of learning samples to obtain a good learning effect. The limitations of the small sample test environment, such as poor adaptability and generalization, affect the prediction accuracy to a certain extent (Yeh, 2006; Li et al., 2015; Xu et al., 2017; Dutta et al., 2018; Prayogo, 2018). Therefore, it is necessary to study a more effective prediction method. Extreme learning machine (ELM) is a particular type of neural network. ELM only needs to set the number of hidden layer nodes of the network. During the algorithm's execution, there is no need to adjust the input weight of the network and the threshold of the hidden element. The weight and threshold can be initialized randomly, and the corresponding output weight can be obtained. It is only necessary to solve a linear least-squares problem. Its solution can be directly generated by the generalized inverse matrix from the hidden layer output matrix, and the optimal solution is unique. Due to this particular network design, ELM has a simple structure and has few training parameters, fast learning speed, and excellent

TABLE 1 | Cement chemical components (%).

Composition	SiO_2	Al_2O_3	Fe_2O_3	CaO	MgO	SO_3	Na_2Oeq
Content	22.51	4.6	3.59	64.18	2.85	0.66	0.58

TABLE 2 | Cement performance index.

Standard consistency water consumption/%	Stability (Boiling method)	Setting time/min		Flexural strength/MPa		Compressive strength (MPa)	
		Initial setting	Final setting	3 d	28 d	3 d	28 d
27.3	Qualified	178	249	4.5	8.3	22.0	49.2

generalization performance compared to other traditional algorithms that pursue infinite training samples. Because of this "ultimate learning speed," it is named the extreme learning machine (Huang et al., 2006; Huang et al., 2011).

Currently, the application of the ELM is mainly focused on fault diagnosis, defect detection, and sound analysis, but rarely in the field of material performance prediction (Bhat et al., 2008; Yaseen et al., 2018). Yaseen et al. proposed a high-precision prediction model of foam concrete compressive strength based on extreme learning machine (ELM) and compared it with multiple adaptive regression spline (MARS), M5 tree model, and support vector regression (SVR) (Yaseen et al., 2018). Jian Tang et al. compared several prediction modeling methods of concrete compressive strength based on extreme learning machine (ELM). The compressive strength of concrete is simulated and verified by various methods (Tang et al., 2014).

The number of data samples in the current literature is relatively small, and the model parameters need to be further optimized. Most approaches are for the strength prediction of ordinary concrete, while rubber fiber concrete with multivariable indicators has not yet been involved. Therefore, it is necessary to establish a prediction model and achieve a more accurate and useful performance prediction of rubber fiber concrete based on ELM. This article, combined with the orthogonal test results of rubber fiber concrete mix, collected relevant concrete mix test data. A prediction model based on ELM was established to predict rubber fiber concrete's mechanical properties and compared with other methods such as BP neural network. The model has high accuracy and robustness. It moves concrete mixing towards high efficiency, intelligence, and generalization. The work further enhances the level of innovation and the application of concrete mixing.

LABORATORY EXPERIMENT

Raw Materials of Rubber Fiber Concrete

As a multicomponent composite material, rubber fiber concrete mainly consists of cement, fly ash, coarse aggregate, fine aggregate, rubber particles, polypropylene fiber, and additives. Cement (P·O 42.5 ordinary Portland cement produced by Conch Cement Co., Ltd.) was used. The chemical composition and performance indexes are shown in **Tables 1** and **2**.

Fly ash: grade II fly ash, material properties shown in **Table 3**.

Coarse aggregates: calcareous gravel, 5–25 mm continuous gradation, apparent density 2,720 kg/m^3.

Fine aggregate: river sand, fineness modulus 2.55, apparent density 2,650 kg/m^3.

Rubber particles: 10 orders (1140 kg/m^3), 20 orders (1120 kg/m^3), 40 orders (1130 kg/m^3).

Polypropylene fiber: single bundle of staple fiber (12 mm).

Admixture: polycarboxylic acid superplasticizer, water reduction rate 20%.

Testing Scheme and Mix Ratio

According to "Specification for Mix Proportion Design of Ordinary Concrete" JGJ55-2011, the mix design of the C40 benchmark concrete was carried out to determine each cubic meter of concrete with a water-cement ratio of 0.4, a sand ratio of 42%, and a slump of 100–120 mm. The rubber aggregate was mixed into the concrete to replace part of the fine aggregate with an equal volume (substitution rate is 10–30%). The polypropylene fiber was added in the way of external reference. For the multi-index mixed design of rubber fiber concrete, it is necessary to investigate the influence of the three factors of rubber content, polypropylene fiber content, and rubber particle size on the mechanical properties of concrete at different levels. The $L9$ (3^3) orthogonal test scheme was used to optimize the mix proportion of the three levels of each influencing factor and seek the optimal level combination. The levels of various factors are shown in **Table 4**.

In **Table 4**, the three levels and the three factors of rubber content, polypropylene fiber content, and rubber particle size are represented by A1, A2, A3, B1, B2, B3, and C1, C2, C3, respectively. The comprehensive combination test was carried out; the total number of mix ratio groups is 27. From the $L9$ (3^3) orthogonal test plan, the number of mix ratio groups obtained is nine groups, as shown in groups 1–9 of **Table 5**. Another nine sets of mix ratio designs were made in work, such as groups 10–18 in **Table 5**.

TABLE 3 | Physical and chemical performance indexes of fly ash.

Loss on ignition/%	Fineness/%	Water requirement ratio/%	Water content/%	Density/kg/m^3	SO$_3$/%	f-CaO/%
2.97	18	92	0.9	2,480	0.51	0.8

TABLE 4 | Factor levels of orthogonal test.

Level	Influencing factors		
	A-Rubber content/%	B-polypropylene fiber content/kg/m^3	C- rubber particle size/orders
1	10	0.6	10
2	20	0.9	20
3	30	1.5	40

TABLE 5 | Mix ratio of rubber fiber concrete.

Group	Water/kg/m^3	Cement/kg/m^3	Fly ash/kg/m^3	Water reducer/kg/m^3	Gravel/kg/m^3	Sand/kg/m^3	Rubber content/kg/m^3	Polypropylene fiber parameters/kg/m^3	Rubber particle size/orders
1-A1B1C1	185	416	46	9.3	1,016	662	30.67	0.6	10
2-A2B1C2	185	416	46	9.3	1,016	589	61.34	0.6	20
3-A3B1C3	185	416	46	9.3	1,016	515	92.01	0.6	40
4-A1B2C2	185	416	46	9.3	1,016	662	30.67	0.9	20
5-A2B2C3	185	416	46	9.3	1,016	589	61.34	0.9	40
6-A3B2C1	185	416	46	9.3	1,016	515	92.01	0.9	10
7-A1B3C3	185	416	46	9.3	1,016	662	30.67	1.5	40
8-A2B3C1	185	416	46	9.3	1,016	589	61.34	1.5	10
9-A3B3C2	185	416	46	9.3	1,016	515	92.01	1.5	20
10-A1B3C1	185	416	46	9.3	1,016	662	30.67	1.5	10
11-A2B2C1	185	416	46	9.3	1,016	589	61.34	0.9	10
12-A3B1C1	185	416	46	9.3	1,016	515	92.01	0.6	10
13-A1B1C2	185	416	46	9.3	1,016	662	30.67	0.6	20
14-A2B3C2	185	416	46	9.3	1,016	589	61.3	1.5	20
15-A3B2C2	185	416	46	9.3	1,016	515	92.01	0.9	20
16-A1B2C3	185	416	46	9.3	1,016	662	30.67	0.9	30
17-A2B1C3	185	416	46	9.3	1,016	589	61.34	0.6	30
18-A3B3C3	185	416	46	9.3	1,016	515	92.01	1.5	30

Testing Content and Method

The testing content considers the 28-day compressive strength, split tensile strength, and flexural strength tests of rubber fiber concrete. According to the mix ratio of each group listed in **Table 5**, the rubber fiber concrete specimens were prepared by referring to "Standard for Test Methods of Mechanical Properties of General Concrete" GB/T 50081-2016. For each mixing ratio of 1–18 groups in **Table 5**, 3 groups of test blocks (3 test blocks for each group) were prepared for compressive, split tensile, and flexural strength tests. The size of the compression and splitting test block is 150 × 150 × 150 mm, and the size of the bending test block is 100 × 100 × 400 mm. The concrete was mixed with a forced mixer. The test piece was vibrated and compacted on the shaker, left to stand for 24 h in the room, and the numbering mark was marked. Then it was put into the standard curing room for 28 days. After that, the concrete strength test was performed. The various test blocks produced are shown in **Figure 1**.

Experimental Results and Analysis

(1) Testing Results

FIGURE 1 | Test block for the strength test.

Three test blocks with the same conditions were taken as a group, and the average of each test value was taken as the strength. The 28-day compressive, split-pull, and flexural strength of each group mix ratio is shown in **Table 6**, and the test process is shown in **Figure 2**.

(2) Orthogonal Range and Variance Analysis

The orthogonal test results (group 1–9) in **Table 6** were analyzed by range and variance. The analysis results are shown in **Table 7**. In **Table 7**, from the range analysis, the three influencing factors of the rubber content (A), polypropylene fiber content (B), and rubber particle size (C) were considered. The rubber content (A) is the largest for the effect of strength. The rubber particle size (C) is the second, and the effect of the polypropylene fiber content (B) is the smallest. The order of each influencing factor is rubber content > rubber particle size > polypropylene fiber content. From the analysis of variance, for the 28-day compressive strength, factor A is highly significant, while the other two factors are not significant. For the 28-day flexural strength, factor A is highly significant, the influence of factor C is significant, and factor B is no significant; for the 28-day tensile strength, factor A is exceptionally significant and factor C is highly significant. The primary and secondary factors influenced by variance analysis are consistent with the results of range analysis.

According to the concrete performance index mentioned above and the comprehensive analysis results of range and variance, it shows that the influence of rubber content A on the three essential indexes of 28-day compressive, flexural, and tensile strength is extremely significant, and A1 is the best. The rubber content selects A1. The fiber content B only has a significant effect on the compression ratio, and it is best when B2 is used. However, there is no significance to the other indicators. The fiber content selects B2. The rubber particle size C has a significant effect on the 28-day flexural and tensile strength, and it is best when C1 is used. Nevertheless, there is also no significance for the other indicators. The rubber particle size selects C1. Therefore, the optimal ratio of rubber fiber concrete obtained by comprehensive analysis is A1B2C1.

INFLUENCE OF VARIOUS FACTORS ON RUBBER CONCRETE PERFORMANCE

From the orthogonal test in **Table 7**, it can be seen that the influencing factors (A, B, C) of different levels (k1, k2, k3) affect the basic mechanical properties of rubber fiber concrete (compressive, flexural, and splitting tensile strength).

Analysis of Influence on Compressive Strength

It can be seen from **Table 7** that the change in the number of rubber particles (A) has a significant effect on the compressive strength of rubber fiber concrete. With the increase in the number of rubber particles (A), the concrete cube's compressive strength shows a significant downward trend. The change of rubber content on the compressive strength of concrete is that the rubber particles are a low-strength organic elastic and hydrophobic material. It has low compatibility with the cement matrix and has a large difference in strength. There is a weak bonding surface inside the concrete, and the effective bearing area is reduced, resulting in decreasing the strength of the concrete.

The most important effect of polypropylene fiber parameter (B) on concrete strength is the weak interface effect and the crack resistance effect. It can be seen from **Table 7** that the change in

TABLE 6 | Testing strength of rubber fiber reinforced concrete.

Orthogonal group	28-day strength index/MPa			Other groups	28-day strength index/MPa		
	Compression	Bending	Tensile		Compression	Bending	Tensile
1-A1B1C1	40.5	5.21	3.11	10-A1B3C1	40.3	5.33	2.99
2-A2B1C2	33.6	4.65	2.62	11-A2B2C1	34.1	4.89	2.67
3-A3B1C3	27.1	3.83	2.17	12-A3B1C1	28.4	4.48	2.49
4-A1B2C2	37.4	5.28	2.93	13-A1B1C2	37.6	5.21	3.02
5-A2B2C3	29.3	4.42	2.45	14-A2B3C2	33.5	4.68	2.50
6-A3B2C1	28.2	4.54	2.38	15-A3B2C2	26.6	4.18	2.33
7-A1B3C3	37.5	4.99	2.73	16-A1B2C3	37.4	5.02	2.81
8-A2B3C1	34.3	4.86	2.58	17-A2B1C3	29.7	4.39	2.58
9-A3B3C2	26.8	4.16	2.24	18-A3B3C3	27.0	3.87	2.04

FIGURE 2 | Specimen strength testing.

TABLE 7 | Range and variance analysis results.

Indicator	Factors	k1	k2	k3	R	Primary and secondary factors	Optimal ratio	Deviation sum of squares	Freedom	Variance	F	Significant	Threshold
Compression strength	A	38.47	31.67	27.37	11.10	A > C > B	A1B1C1	187.94	2	93.97	38.78	**	F0.01 (2, 2) = 9 9.0; F0.05 (2, 2) = 19.0; F0.10 (2, 2) = 9.0
	B	33.73	30.90	32.87	2.83			12.65	2	6.32	2.61		
	C	34.33	32.60	30.57	3.76			21.33	2	10.66	4.40		
Bending strength	A	5.16	4.64	4.18	0.98	A > C > B	A1B2C1	1.45	2	0.725	57.15	**	
	B	4.56	4.75	4.67	0.19			0.05	2	0.025	2.00		
	C	4.87	4.70	4.41	0.46			0.32	2	0.159	12.55	*	
Tensile strength	A	2.92	2.55	2.26	0.66	A > C > B	A1B1C1	0.66	2	0.329	271.3	***	
	B	2.63	2.59	2.52	0.11			0.02	2	0.010	8.54		
	C	2.69	2.60	2.45	0.24			0.09	2	0.044	36.26	**	

concrete compressive strength and fiber content is not a simple linear relationship with the increase of polypropylene fiber content. Generally, it first decreases and then rises. When polypropylene fiber's content increases from level k1 (0.6 kg/m^3) to level k2 (0.9 kg/m^3), the compressive strength is reduced. The weak interface effect of polypropylene fiber is evident at this stage. When the fiber content continues to increase to the level k3 (1.5 kg/m^3), the concrete compressive strength rises again. The crack resistance effect of polypropylene fiber plays a leading role at this stage.

The impact of different rubber particle size (C) on concrete's compressive strength is also apparent. It can be seen from **Table 7** that the compressive strength of the concrete mixed with rubber particles of particle size level k1 (10 mesh) is significantly higher than the particle size level k2 (20 mesh) and level k3 (40 mesh) when the rubber volume is the same. It can be seen that the addition of coarse rubber particles reduces the degree of weakening of the compressive strength of concrete while the specific surface area of fine rubber particles is relatively large. The larger the weak bonding surface formed between the cement matrix, the more unfavorable the compressive strength of concrete.

Analysis of Influence on Flexural Strength

It can be seen from **Table 7** that the increase in the number of rubber particles (A) has a significant adverse effect on the flexural strength of concrete. In addition, the flexural strength of concrete decreases significantly with the decrease of the rubber particle size (C). The magnitude of the decrease in strength is even more remarkable when the rubber particle size changes from level k2 (20 mesh) to level k3 (40 mesh). With the increase of the content of polypropylene fiber (B), the flexural strength of concrete shows a change law that first increases and then gradually decreases. The crack resistance effect of polypropylene fiber is dominant within a particular content range, which strengthens toughness and delays the development of cracks. The flexural strength of concrete increases with the increase of fiber content. However, as polypropylene fiber's content increases, the weaker interfaces in the concrete matrix will increase, and the weak interface effect of polypropylene fibers is more prominent and gradually approaches the crack resistance effect. When the content exceeds the critical value, the polypropylene fiber's weak interface effect plays a leading role. It leads to a decrease in the strength of the concrete matrix, which shows that as the amount of polypropylene fiber increases, the flexural strength of concrete gradually decreases.

Analysis of Influence on Splitting Tensile Strength

It can be seen from **Table 7** that the impact of rubber particle content (A) and rubber particle size (C) on the split tensile strength of concrete is similar to the impact mentioned earlier on flexural and compressive strength. By increasing the rubber particles' content and decreasing the rubber particle size, the splitting tensile strength of concrete shows a significant downward trend. Especially, the change of rubber particle content has a significant impact on the splitting tensile strength of concrete. The polypropylene fiber (B) content has no noticeable effect on the split tensile strength of concrete. The splitting strength of concrete decreases slightly with the increase of fiber content, but the overall change is not significant. Besides, it can be seen that, for the split tensile strength of concrete, the content of rubber particles (A) is hugely significant, the size of rubber particles (C) is significant, and the content of polypropylene fiber (B) is not significant.

STRENGTH PREDICTION MODEL BASED ON EXTREME LEARNING MACHINE

The orthogonal test's optimal mix ratio of rubber fiber concrete was finally determined through the range and variance analysis of the orthogonal test. The influence of various factors on the mechanical properties of concrete was also analyzed. However, the relationship between these influence factors and concrete strength is highly nonlinear. The traditional mixing ratio test method is time-consuming and labor-intensive and difficult to adapt to the requirements of using diverse and differentiated raw materials to prepare new concrete. The extreme learning machine (ELM) has good nonlinear mapping capabilities and reasonable response to the nonlinear relationship between concrete strength and various influencing factors. It can realize rapid and accurate prediction of the strength of rubber fiber concrete. Therefore, ELM modeling will be carried out in this article, and the obtained model will be used for the strength prediction of rubber fiber concrete.

Extreme Learning Machine Principle and Parameter Optimization

Given a set of M training samples (x_i, y_i), $x_i \in R^n$, $y_i \in R$, the number of hidden layer neurons is N in a single-layer feedforward neural network, and the activation function of each hidden layer neuron is f. Then the output of the network can be expressed as follows:

$$\sum_{i=1}^{N} \beta_i f\left(w_i x_j + b_i\right), \qquad j \in [1, M], \tag{1}$$

where w_i and b_i are the weight and bias of the i neuron in the hidden layer, respectively; β_i is the output weights.

To reduce the error between prediction and target, the following relationship can be established:

$$\sum_{i=1}^{N} \beta_i f\left(w_i x_j + b_i\right) = y_j, \qquad j \in [1, M]. \tag{2}$$

Equation (**2**) can be simplified as follows:

$$H\beta = Y, \tag{3}$$

where $\beta = (\beta_{1} \ldots \beta_{N})^{\mathrm{T}}$; $Y = (y_{1} \ldots y_{N})^{\mathrm{T}}$; H is the output matrix of the hidden layer. It can be defined as follows:

$$H = \begin{pmatrix} f\left(w_1 x_1 + b_1\right) & \cdots & f\left(w_N x_1 + b_N\right) \\ \vdots & \ddots & \vdots \\ f\left(w_1 x_M + b_1\right) & \cdots & f\left(w_N x_M + b_N\right) \end{pmatrix}. \tag{4}$$

The output weight β can be obtained from $\beta = \mathrm{H}^{\dagger}\mathrm{Y}$ according to (**3**), where $H^{\dagger}$ is the Moore-Penrose generalized inverse of the matrix H.

Given a training sample set, activation function, and the number of hidden layer neurons, the ELM algorithm's specific steps are as follows:

(1) The hidden layer weight matrix wi and bias matrix bi are from probability distribution random setting.
(2) The hidden layer output matrix H is calculated.
(3) The output weight matrix $\hat{\beta}$ is calculated from $\hat{\beta} = H^{\dagger}Y$.

The hidden layer activation function of extreme learning machine usually chooses the Gaussian radial basis function. The prediction accuracy of the model is related to the selection of hyperparameters. The adjustment and optimization of hyperparameters usually use the Bayesian Optimization Algorithm (BOA). The optimization steps are as follows:

(1) Define the objective function: $X^* = \mathrm{argmax}\, f(x)$.
(2) Randomly generate n initial sample points of hyperparameters. The hyperparameter distribution obeys the Gaussian distribution. Using Gaussian process obtains the prior distribution of the initial hyperparameters.
(3) The acquisition function is based on the principle of maximizing the expected increment and selecting the expected X that maximizes the expected function.
(4) Calculate the actual target value of X. If the conditions are met, output X is the optimal hyperparameter. Otherwise, add X and the real value to the initial sampling point and repeat the previous step.

TABLE 8 | 87 groups of rubber fiber concrete's test data sets.

References	Rubber content/%	Rubber size (mm)	Fiber content/kg/m^3	No. of samples
Chen et al. (2014)	20	1–2	0.6, 1.2	12
Xue et al. (2016)	15	2–4	2, 4, 6, 8, 10	18
Li (2016)	5, 10, 15	0.18, 0.42, 2	0, 1	10
Huang (2017)	2, 5, 8	1.18	2, 4, 6	9
Bai et al. (2018)	4, 10, 15	0.42, 0.84, 2	2, 6, 10	9
Hossain et al. (2019)	5, 10	Maximum size of 4.75	9.1, 18.2	15
Wang et al. (2019)	10, 15	0.6–2.8	4.5	4
Mo et al. (2020)	0, 4.5	0.38	0, 1.6, 3.2, 4, 6	10

TABLE 9 | Input and output variable in the data set.

	Variables	Min	Max	Average
Input	Cement/kg/m^3	262	528	353.72
	W/C ratio	0.35	0.59	0.46
	Fine aggregate/kg/m^3	448	688	573.26
	Rubber content/kg/m^3	0	129.2	28.0
	Rubber particle size/mm	0.18	4.75	1.37
	Fiber content/kg/m^3	0	18.2	4.93
Output	28-day compressive strength	13.3	56.8	31.19
	28-day tensile strength	1.33	3.93	2.51
	28-day flexural strength	1.79	6.84	4.03

Construction of Prediction Model

The orthogonal experiment design adopted a representative factor parameter combination for the experiment, and the resulting sample set was highly representative and comprehensive in the information. The complete sample set met the ELM algorithm's requirements for the representativeness of the training samples, and the accurate prediction model can be obtained through a small number of training samples. This paper combined the 27 sets of data obtained from the above-mentioned orthogonal test of the rubber fiber concrete's mix ratio and used searching engines such as Springer, Google, and CNKI (China National Knowledge Infrastructure) to collect the cement-based rubber data in recent years. The concrete mix ratio test data (a total of 87 data sets as shown in **Table 8**) was established, which contains 114 data sets. The selection of the data set's variable factors is based on the available information of all test data samples. According to the orthogonal test of the rubber fiber concrete's mix ratio, the rubber content, rubber particle size, and polypropylene fiber content are variable factors that affect the strength of concrete and the cement content water-cement ratio factors. The rubber aggregate is mixed in the same volume instead of as part of the fine aggregate, sand changes with the rubber content. Therefore, the data set established includes the above six influencing variables.

The data set's six variables were taken as input parameters with the MATLAB program platform, and 28-day-old concrete compressive, flexural, and tensile strength were taken as output parameters. The rubber fiber concrete's strength prediction model was constructed. Since the established data set is from different researchers, a small part of the data samples lacks concrete flexural strength or tensile strength output variables. For making the data samples in the data set consistent and facilitating the model's training, the statistical regression relationship between the concrete compressive strength and its tensile strength or flexural strength was used based on the relevant literature. For a data sample with incomplete output variables, the tensile or flexural strength can be calculated from the sample's compressive strength. Thus, the three output variables were complemented. The influencing variables and their statistical descriptions are shown in **Table 9**.

To improve the efficiency and generalization characteristics of the model, first, the data set is normalized, and then about 80% of the original data set is randomly selected as the training and validation data set (90 data samples) and 20% as the test data set (24 data samples). A 5-fold cross-validation method is used to train and verify the ELM prediction model. The training and verification data set containing 90 data samples is randomly divided into five parts, and four of them are used as the training set and one as the verification set. The average of the five verification results is used to estimate the accuracy of the algorithm (performance index of the prediction model). Finally, the test data set is used to evaluate or validate the model. When the number of samples is limited, this method can effectively avoid over-learning and under-learning states. Thereby it can obtain a prediction model with good robustness and good generalization ability.

Model Performance Evaluation

In the process of training and testing, this article adopts the correlation coefficient (R^2), relative standard deviation (RSD), and mean relative error (MRE) to evaluate the effectiveness and prediction accuracy of the model. The equation is as follows:

$$R = \frac{\sum_{i=1}^{n}(x_i - \overline{x})(y_i - \overline{y})}{\sqrt{\sum_{i=1}^{n}(x_i - \overline{x})^2}\sqrt{\sum_{i=1}^{n}(y_i - \overline{y})^2}}, \tag{5}$$

$$RSD = \sqrt{\frac{1}{n-1}\sum_{i=1}^{n}\left(\frac{x_i}{y_i} - 1\right)^2} \times 100\%, \tag{6}$$

$$MRE = \frac{1}{n}\sum_{i=1}^{n}\left|\frac{x_i}{y_i} - 1\right| \times 100\%, \tag{7}$$

where x_i is the measured or experimental value of concrete strength, y_i is the predicted value or model output, $\overline{x}$ is the

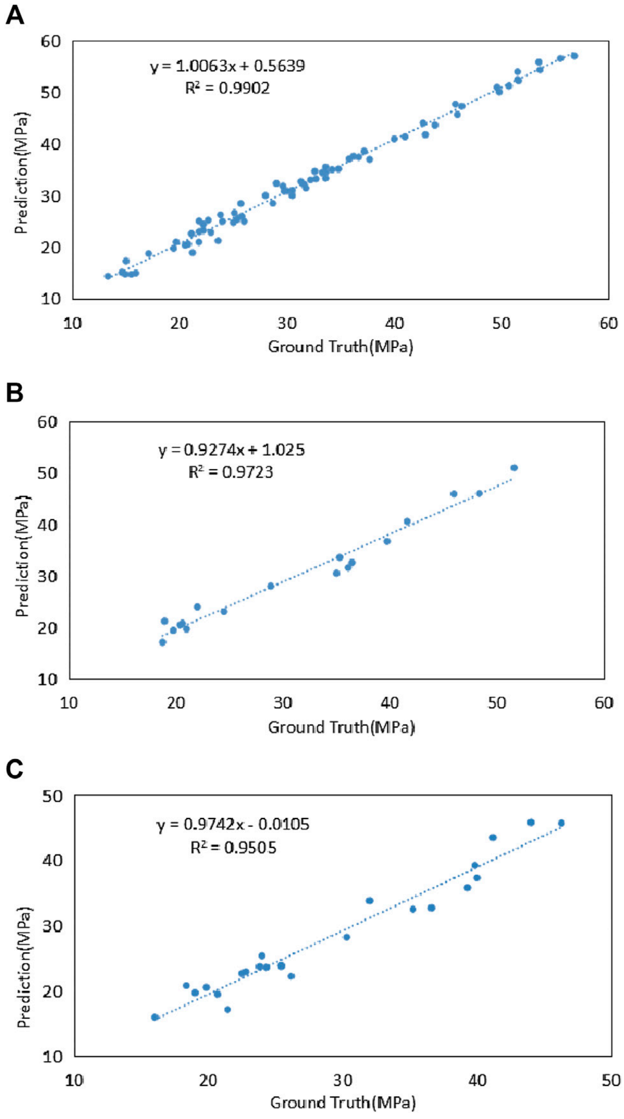

FIGURE 3 | Correlation between predicted and experimental compressive strengths: **(A)** training dataset, **(B)** validation dataset, and **(C)** testing dataset of ELM.

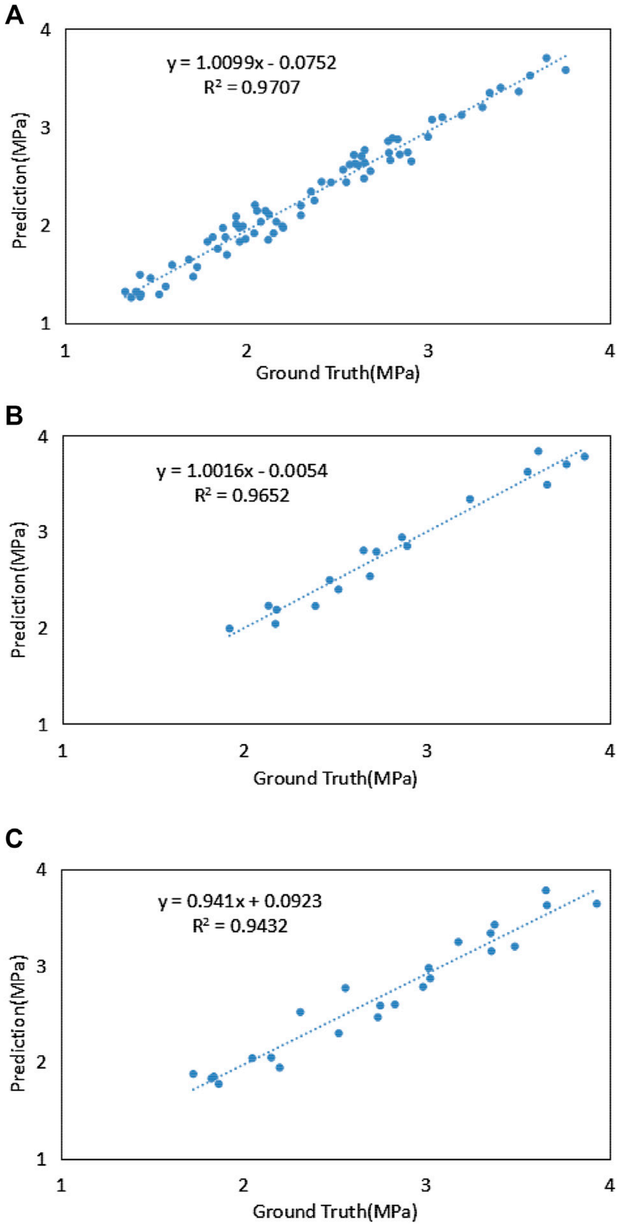

FIGURE 4 | Correlation between predicted and experimental tensile strengths: **(A)** training dataset, **(B)** validation dataset, and **(C)** testing dataset of ELM.

average measured or experimental value, $\bar{y}$ is the average predicted value, and n is the number of collected data samples.

Efficient models with good predictive capabilities have lower RMSE and MAPE values and higher R values. The RSD is not more than 12%, and the MRE is not more than 10%. The accuracy of the model is relatively ideal.

RESULTS AND DISCUSSION

The concrete strength value predicted and the actual concrete strength value in the data set are shown in **Figures 3–5**. Figure (a), (b), and (c) are the linear least squares regression lines between the output predicted value and the actual value of the ELM model for training, verification, and testing. R^2, RSD, and MRE of each linear regression equation are listed in **Table 10**. It can be seen that the prediction of training, verification, and testing of the ELM model are close to the actual values. R^2 values of each data set are relatively high, and the RSD and MRE are less than 10%. In considering multiple influencing parameters, the model can well establish the nonlinear relationship between input and output variables. It has good robustness for predicting the complex behavior of rubber fiber concrete mechanical properties.

According to **Table 10**, the average of the comprehensive performance indicators R^2, RSD, and MRE of each stage of the

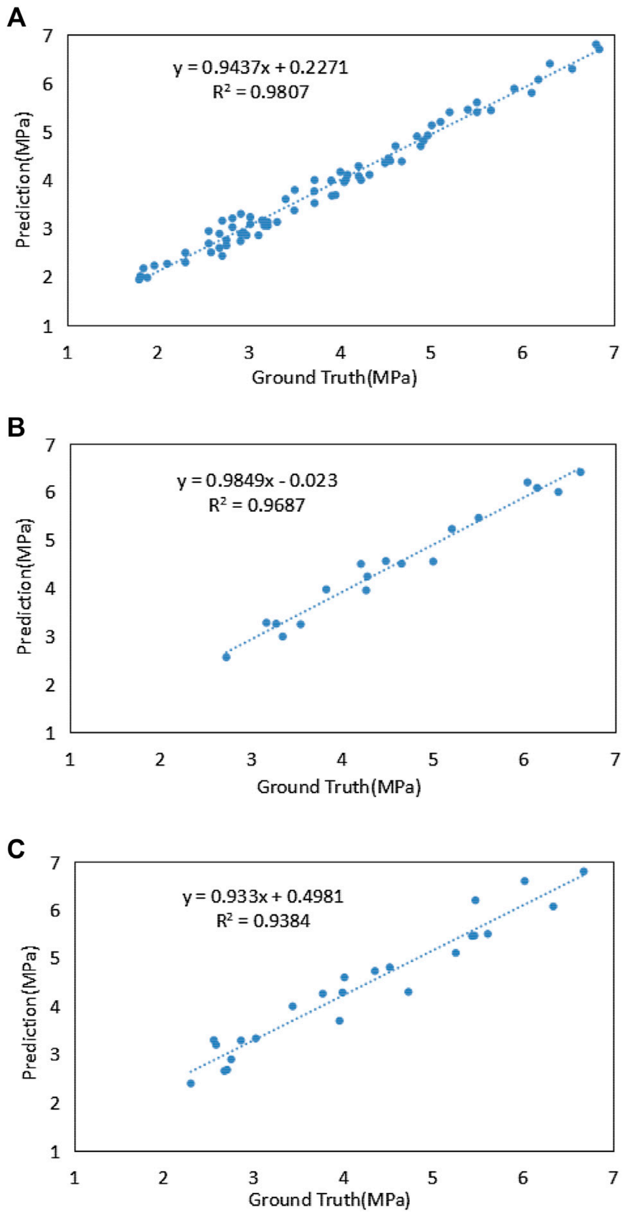

FIGURE 5 | Correlation between predicted and experimental flexural strengths: **(A)** training dataset, **(B)** validation dataset, and **(C)** testing dataset of ELM.

TABLE 10 | Results of performance criteria of the ELM model.

Dataset		R^2	RSD/%	MRE/%
Compressive strengths	Training	0.9902	5.17	3.89
	Validation	0.9723	7.89	6.15
	Testing	0.9505	8.79	6.43
Tensile strengths	Training	0.9707	6.34	4.75
	Validation	0.9652	4.29	3.67
	Testing	0.9432	6.68	5.40
Flexural strengths	Training	0.9807	5.93	4.63
	Validation	0.9687	5.79	4.43
	Testing	0.9384	9.85	7.65

TABLE 11 | Performance criteria comparison of different machine-learning models.

Algorithm	R^2	RSD/%	MRE/%	Running time/s
ELM	0.9644	6.75	5.22	2.5301
BPNN	0.9601	7.66	5.91	30.0715
SVM	0.9489	10.03	7.48	2.8540

ELM model are 0.9644, 6.75%, and 5.22%, respectively. For verifying the ELM's generalization performance and computational efficiency, this study also used BP neural network (BPNN) and support vector machine (SVM) to establish a prediction model and conducted a comparative experiment of the three algorithms.

For obtaining the best structure of the prediction model and ensuring its generalization, it is necessary to optimize the hyperparameters of the model. Levenberg–Marquardt method and Bayesian regularization were used to determine the optimal weight of the ANN model. A 5-fold cross-validation method was used to determine the optimal number of neurons in the network's hidden layer to avoid over-fitting and make the model have a better generalization and minimum prediction bias. The number of neurons in the input layer and the output layer is determined by the input and output parameters. The kernel function is a Gaussian function. For SVM's optimal penalty parameter C and RBF kernel parameter gamma, it is also obtained by optimizing the 5-fold cross-validation method. The cross-validation method can effectively avoid the over-fitting and under-fitting of the model.

The comprehensive performance indicators of each algorithm model are shown in **Table 11**. The training time of the model ignores super-parameter optimization. It can be seen from **Table 11** that the extreme learning machine has the highest prediction accuracy compared with BP neural network and support vector machine. The training time is similar to that of a support vector machine and shorter than the BP neural network. It indicates that the generalization ability of extreme learning machines is more suitable for predicting the strength of rubber fiber concrete. BP neural network has the longest training time, but its accuracy is slightly higher than that of support vector machine.

Wu Xiaoping et al. used Bayesian optimization of the extreme learning machine prediction model to predict concrete compressive strength. The model has higher accuracy and higher efficiency of model training than classic algorithms (Wu et al., 2020). The BP neural network has the highest prediction accuracy in the experiment, but the calculation performance is the worst, and the training time is the longest. The training time of extreme learning and support vector machine is similar, and both are shorter than the BP neural network. Jian Tang et al. compared several concrete compressive strength prediction model methods based on extreme learning machines (ELMs) (Tang et al., 2014). The results show that the conventional ELMs algorithm has fast modeling speed and high prediction accuracy and can be used to predict concrete's compressive strength. Thus, our experimental results are basically consistent with the above-mentioned literature.

CONCLUSIONS

The rubber fiber concrete mix was designed with the orthogonal test method. The rubber fiber concrete's mix test data were collected based on published articles in recent years. A data set containing 114 sets was obtained. Based on the data set and the MATLAB platform, a strength prediction model of rubber fiber concrete was established with ELM. The prediction performance of the model was also verified.

The conclusions can be drawn as follows:

(1) Orthogonal experiment design adopts a representative factor parameter combination for the experiment, and the obtained sample set is highly representative and complete in its information. The orthogonal test method was used to design the mix ratio of rubber fiber concrete and its 28-day strength test for obtaining the complete data sample. The complete sample set meets the ELM algorithm's requirements for representing the training samples, and an accurate prediction model can be obtained through a small number of training samples.

(2) There is a highly nonlinear relationship between rubber fiber concrete's strength and its influencing factors, challenging to deal with using traditional regression methods. With the orthogonal experiment, there are six influencing factors; rubber content, rubber particle size, and polypropylene fiber content are used as input; and 28-day concrete compression, splitting tensile, and flexural strength are used as output. One strength prediction model was established based on ELM. The experimental results show that the model has strong nonlinear mapping ability and high prediction accuracy. It can be used as an effective method for the strength prediction of the rubber fiber concrete.

(3) Since the generalization accuracy of the ELM model is greatly affected by the hyperparameters, the ELM needs further research in the super-parameter optimization method and the reduction of optimization time. It is also difficult to carry out a large number of mix ratio tests in the laboratory. The complete rubber fiber concrete's mix ratio test data samples currently available are limited. Although ELM has outstanding advantages over other small sample modeling methods, the prediction accuracy of this method still depends on the number and quality of learning samples. Therefore, it is necessary to continuously enrich the learning samples to further improve the prediction model's reliability in future practical applications.

DATA AVAILABILITY STATEMENT

The original contributions presented in the study are included in the article/Supplementary Material; further inquiries can be directed to the corresponding author.

AUTHOR CONTRIBUTIONS

JZ (1st author) designed experiments, analyzed data, and wrote the article. JX analyzed data and supervised the project. CL did experiments and collected data. JZ (4th author) did experiments and collected data.

ACKNOWLEDGMENTS

This research was funded by the Open Research Fund of Key Laboratory of Hydraulic and Waterway Engineering of the Ministry of Education (Grant No. SLK2017A02), the Open Research Fund of State Key Laboratory of Simulation and Regulation of Water Cycle in River Basin (Grant No. IWHR-SKL-KF201810) and the Open Research Fund of the Fundamental Science on Radioactive Geology and Exploration Technology Laboratory (Grant No. RGET1502). The authors would like to thank the Associate Editor Bahman Ghiassi, and two reviewers for their constructive comments to improve the early version of this paper.

REFERENCES

Aslani, F., and Gedeon, R. (2019). Experimental investigation into the properties of self-compacting rubberised concrete incorporating polypropylene and steel fibers. *Struct. Concr.* 20, 267–281. doi:10.1002/suco.201800182

Atahan, A. O., and Yücel, A. Ö. (2012). Crumb rubber in concrete: static and dynamic evaluation. *Construct. Build. Mater* 36, 617–622. doi:10.1016/j.conbuildmat.2012.04.068

Bai, C., Ma, F. H., Liu, S. X., and Wang, J. M. (2018). Preparation of plastic steel fiber reinforced rubber concrete and its test analysis of frost resistance. *Non-Metall. Mines.* 41 (2), 35–37. doi:10.16339/j.cnki.jsjsyzdh.202001028

Bhat, A. U., Merchant, S. S., and Bhagwat, S. S. (2008). Prediction of melting points of organic compounds using extreme learning machines. *Ind. Eng. Chem. Res.* 47 (3), 920–925. doi:10.1021/ie0704647

Bravo, M., and de Brito, J. (2012). Concrete made with used tyre aggregate: durability-related performance. *J. Clean. Prod.* 25, 42–50. doi:10.1016/j.jclepro.2011.11.066

Chen, A. J., Chen, M., Wang, D. F., and Hu, F. Q. (2014). Research on the basic properties of the polypropylene fiber rubber recycled concrete. *Concrete* 9, 57–60. doi:10.3969/j.issn.1002-3550.2014.09.014

Chou, J. S., Tsai, C. F., Pham, A. D., and Lu, Y. H. (2014). Machine learning in concrete strength simulations: multi-nation data analytics. *Construct. Build. Mater* 73, 771–780. doi:10.1016/j.conbuildmat.2014.09.054

Dutta, S., Samui, P., and Kim, D. (2018). Comparison of machine learning techniques to predict compressive strength of concrete. *Comput. Concr.* 21 (4), 463–470. doi:10.12989/cac.2018.21.4.463

Fang, Y., Zhan, M., and Wang, Y. (2001). The status of recycling of waste rubber. *Mater. Des.* 22 (2), 123–128. doi:10.1016/S0261-3069(00)00052-2

Gao, W. (2018). Influencing factors and deep learning prediction model of compression strength of recycled concrete. *Concrete* 11, 58–61. doi:10.3969/j.issn.1002-3550.2018.11.015.70

Hossain, F. Z., Shahjalal, M., Islam, K., Tiznobaik, M., and Alam, S. (2019). Mechanical properties of recycled aggregate concrete containing crumb rubber and polypropylene fiber. *Construct. Build. Mater.* 225, 983–996. doi:10.1016/j.conbuildmat.2019.07.245

Huang, G. B., Zhu, Q. Y., and Siew, C. K. (2006). Extreme learning machine: theory and applications. *Neurocomputing* 70 (1-3), 489–501. doi:10.1016/j.neucom.2005.12.126

Huang, G., Zhou, H., Ding, X., and Zhang, R. (2011). Extreme learning machine for regression and multiclass classification. *IEEE Trans. Syst. Man Cybern. Part B (Cybernetics)* 42 (2), 513–529. doi:10.1109/TSMCB.2011.2168604

Huang, J. T. (2017). Research on mix proportion and constitutive relation of plastic steel fiber-rubber concrete used in road. *J. Taiyuan Univ. Technol.* 48 (6), 978–983. doi:10.19540/j.cnki.cjcmm.20190626.501

Jalal, M., Arabali, P., Grasley, Z., and Bullard, J. W. (2019a). Application of adaptive neuro-fuzzy inference system for strength prediction of rubberized concrete containing silica fume and zeolite. *J. Mater. Des. Appl.* 237, 90370. doi:10.1177/1464420719890370

Jalal, M., Nassi, N., and Hamid, J. (2019b). Waste tire rubber and pozzolans in concrete: a trade-off between cleaner production and mechanical properties in a greener concrete. *J. Clean. Prod.* 238, 117882. doi:10.1016/j.jclepro.2019.117882

Jalal, M., Poura, A., Zachary, G., and Jeffrey, W. B. (2020). Application of adaptive neuro-fuzzy inference system for strength prediction of rubberized concrete containing silica fume and zeolite. *Proc. Inst. Mech. Eng.* 234(3), 438–451. doi:10.1177/1464420719890370

Li, K., Hu, C., Liu, G., and Xue, W. (2015). Building's electricity consumption prediction using optimized artificial neural networks and principal component analysis. *Energy Build* 108, 106–113. doi:10.1016/j.enbuild.2015.09.002

Li, R., Xie, L., Wang, W. Y., Liaw, P. K., and Zhang, Y. (2020). High-throughput calculations for high-entropy alloys: a brief review. *Front. Mater* 7, 290. doi:10.3389/fmats.2020.00290

Li, X. H. (2016). Research on mechanical properties and durability of fiber-rubber concrete. *Build. Sci.* 32 (7), 118–122. doi:10.13614/j.cnki.11-962/tu.2016.07.019

Lim, C. H., Yoon, Y. S., and Kim, J. H. (2004). Genetic algorithm in mix proportioning of high-performance concrete. *Cem. Concr. Res.* 34 (3), 409–420. doi:10.1016/j.cemconres.2003.08.018

Madani, H., Kooshafar, M., and Emadi, M. (2020). Compressive strength prediction of nanosilica-Incorporated cement mixtures using adaptive neuro-fuzzy inference system and artificial neural network models. *Struct. Des. Constr.* 25 (3), 04020021. doi:10.1061/(ASCE)SC.1943-5576.0000499

Mo, J., Zeng, L., Liu, Y., Ma, L., Liu, C., et al. (2020). Mechanical properties and damping capacity of polypropylene fiber reinforced concrete modified by rubber powder. *Construct. Build. Mater* 242, 118111. doi:10.1016/j.conbuildmat.2020.118111

Ni, H. G., and Wang, J. Z. (2000). Prediction of compressive strength of concrete by neural networks. *Cem. Concr. Res.* 30 (8), 1245–1250. doi:10.1016/S0008-8846(00)00345-8

Prayogo, D. (2018). Metaheuristic-based machine learning system for prediction of compressive strength based on concrete mixture properties and early-age strength test results. *Civ. Eng. Dimens.* 20 (1), 21–29. doi:10.9744/ced.20.1.21-29

Reda Taha, M. M., El Dieb, A. S., Abd El Wahab, M., and Abdel Hameed, M. (2008). Mechanical, fracture, and microstructural investigations of rubber concrete. *J. Mater. Civ. Eng.* 20 (10), 640–649. doi:10.1061/(ASCE)0899-1561.20082010640

Richardson, A., Coventry, K., Edmondson, V., and Dias, E. (2016). Crumb rubber used in concrete to provide freeze–thaw protection (optimal particle size). *J. Clean. Prod.* 112, 599–606. doi:10.1016/j.jclepro.2015.08.028

Richardson, A. E., Coventry, K. A., and Ward, G. (2012). Freeze/thaw protection of concrete with optimum rubber crumb content. *J. Clean. Prod.* 23 (1), 96–103. doi:10.1016/j.jclepro.2011.10.013

Skripkiūnas, G., Grinys, A., and Miškinis, K. (2009). Damping properties of concrete with rubber waste additives. *Mater. Sci.* 15 (3), 266–272. doi:10.1177/1045389X15586452

Tang, J., Dong, Y., and Zhao, L. (2014). Comparison of several extreme learning machine algorithm for modeling concrete compressive strength. *Appl. Mech. Mater* 548–549, 1735–1738. doi:10.4028/www.scientific.net/AMM.548-549.1735

Topçu, İ. B., and Demir, A. (2007). Durability of rubberized Mortar and concrete. *J. Mater. Civ. Eng.* 19 (2), 173–178. doi:10.1061/(ASCE)0899-1561.2007192173

Topçu, İ. B., and Sarıdemir, M. (2008). Prediction of rubberized concrete properties using artificial neural network and fuzzy logic. *Constr. Build. Mater* 22 (4), 532–540. doi:10.1016/j.conbuildmat.2006.11.007

Wang, J., Dai, Q., Ruizhe, S., and Guo, S. (2019). Mechanical, durability, and microstructural properties of macro synthetic polypropylene (PP) fiber-reinforced rubber concrete. *J. Clean. Prod.* 234, 1351–1364. doi:10.1016/j.jclepro.2019.06.272

Wu, C. T., Chang, H. T., Wu, C. Y., Chen, S. W., et al. (2019). Machine learning recommends affordable new Ti alloy with bone-like modulus. *Mater. Today*. 54, 697. doi:10.1016/j.mattod.2019.08.008

Wu, X., Li, Y., Zhang, Y., Ruan, Y., and Liu, Z. (2020). Prediction of concrete compressive strength based on BOA-ELM. *Comput. Technol. Autom.* 39 (1), 140–144. doi:10.16339/j.cnki.jsjsyzdh.202001028

Xu, J., Ren, Q., and Shen, Z. (2015). Prediction of the strength of concrete radiation shielding based on LS-SVM. *Ann. Nucl. Energy* 85, 296–300. doi:10.1016/j.anucene.2015.05.030

Xu, J., Ren, Q., and Shen, Z. (2017). Sensitivity analysis of the influencing factors of slope stability based on LS-SVM. *Geomech. Eng.* 13 (3), 447–458. doi:10.12989/gae.2017.13.3.447

Xu, J., and Yu, X. (2020). Detection of concrete structural defects using impact echo based on deep networks. *J. Test. Eval.* 49 (1), 801. doi:10.1520/jte20190801

Xue, G., Wu, C. F., and Hu, X. L. (2016). Experiment study on stress-train relationship of plastic fiber reinforced concrete rubber. *Bull. Chin. Ceram. Soc.* 35 (11), 3796–3802. doi:10.16552/j.cnki.issn1001-1625.2016.11.052

Yaseen, Z. M., Deo, R. C., Hilal, A., Abd, A. M., Bueno, L. C., Salcedo-Sanz, S., et al. (2018). Predicting compressive strength of lightweight foamed concrete using extreme learning machine model. *Adv. Eng. Softw.* 115, 112–125. doi:10.1016/j.advengsoft.2017.09.004

Yeh, I. C. (2006). Analysis of strength of concrete using design of experiments and neural networks. *J. Mater. Civ. Eng.* 18 (4), 597–604. doi:10.1061/(ASCE)0899-1561.2006184597

Young, B. A., Hall, A., Pilon, L., Gupta, P., and Sant, G. (2019). Can the compressive strength of concrete be estimated from knowledge of the mixture proportions?: new insights from statistical analysis and machine learning methods. *Cem. Concr. Res.* 115, 379–388. doi:10.1016/j.cemconres.2018.09.006

Zheng, L., Huo, X. S., and Yuan, Y. (2008). Experimental investigation on dynamic properties of rubberized concrete. *Construct. Build. Mater* 22 (5), 939–947. doi:10.1016/j.conbuildmat.2007.03.005

Conflict of Interest: The authors declare that the research was conducted in the absence of any commercial or financial relationships that could be construed as a potential conflict of interest.

Advantages of publishing in Frontiers

OPEN ACCESS
Articles are free to read
for greatest visibility
and readership

FAST PUBLICATION
Around 90 days
from submission
to decision

HIGH QUALITY PEER-REVIEW
Rigorous, collaborative,
and constructive
peer-review

TRANSPARENT PEER-REVIEW
Editors and reviewers
acknowledged by name
on published articles

Frontiers
Avenue du Tribunal-Fédéral 34
1005 Lausanne | Switzerland

Visit us: www.frontiersin.org
Contact us: frontiersin.org/about/contact

REPRODUCIBILITY OF RESEARCH
Support open data
and methods to enhance
research reproducibility

DIGITAL PUBLISHING
Articles designed
for optimal readership
across devices

FOLLOW US
@frontiersin

IMPACT METRICS
Advanced article metrics
track visibility across
digital media

EXTENSIVE PROMOTION
Marketing
and promotion
of impactful research

LOOP RESEARCH NETWORK
Our network
increases your
article's readership